



HAL
open science

Influence of the nonlocal effects on the near-field radiative heat transfer

Farah Singer

► **To cite this version:**

Farah Singer. Influence of the nonlocal effects on the near-field radiative heat transfer. Engineering Sciences [physics]. University of Poitiers, 2014. English. NNT: . tel-01150836

HAL Id: tel-01150836

<https://theses.hal.science/tel-01150836>

Submitted on 12 May 2015

HAL is a multi-disciplinary open access archive for the deposit and dissemination of scientific research documents, whether they are published or not. The documents may come from teaching and research institutions in France or abroad, or from public or private research centers.

L'archive ouverte pluridisciplinaire **HAL**, est destinée au dépôt et à la diffusion de documents scientifiques de niveau recherche, publiés ou non, émanant des établissements d'enseignement et de recherche français ou étrangers, des laboratoires publics ou privés.



Thesis

For obtaining the grade of

DOCTOR OF THE UNIVERSITY OF POITIERS

Ecole Nationale Supérieure d'Ingénieurs de Poitiers

Ecole Doctorale : Ecole Doctorale Sciences et Ingénierie en Matériaux, Mécanique,
Energétique et Aéronautique

Presented by

Farah SINGER

INFLUENCE OF THE NONLOCAL EFFECTS ON THE NEAR-FIELD RADIATIVE HEAT TRANSFER

Director and supervisor of the thesis: **Pr. Karl JOULAIN**

Co-supervisor of the thesis: **Associate Pr. Younès EZZAHRI**

Defended on December 19, 2014 in front of the Commission of examination

JURY

Philippe BEN-ABDALLAH	Senior Researcher at CNRS, Institut d'Optique, Paris	Reviewer
Rodolphe VAILLON	Senior Researcher at CNRS, CETHIL, Lyon	Reviewer
Sebastian VOLZ	Senior Researcher at CNRS, EM2C, Paris	Examiner
Pierre-Olivier CHAPUIS	Researcher at CNRS, CETHIL, Lyon	Examiner
Younès EZZAHRI	Associate Professor at University of Poitiers, PPRIME Institute	Examiner
Karl JOULAIN	Professor at University of Poitiers, PPRIME Institute	Examiner

Abstract

In this thesis, we study the validity of few nonlocal models of the dielectric permittivity in the calculation of the radiative heat transfer coefficient between two semi-infinite parallel dielectric planes separated by a vacuum gap of width d .

In past theoretical studies, it has been shown that upon considering a local model of the dielectric permittivity, near field radiative heat transfer between two dielectric materials follows a $1/d^2$ law when d is of the order or less than few hundreds of nanometers. This nonphysical diverging increase has been the bottleneck of the local model. Overwhelming efforts have been deployed in order to come up with a new model in which the nonlocal effects of the dielectric permittivity are taken into account. To the best of our knowledge, no nonlocal correction to the near field radiative heat transfer has been addressed in the past in the case of dielectrics. In the case of metals however, an important and complete work has been performed using the Lindhard–Mermin nonlocal dielectric permittivity model.

Our work focuses on studying four different nonlocal models of the dielectric permittivity and on using them in the calculation of the radiative heat transfer coefficient between two solid semi-infinite parallel planes of 6H-SiC. For the case of doped semiconductors, we studied the Lindhard–Mermin nonlocal model of the dielectric permittivity to calculate the radiative heat transfer coefficient between two n-doped Si planes. We show that the radiative heat transfer coefficient saturates as the separation distance d tend to zero. The distance at which saturation starts to take place depends on key parameters involved in each model.

Résumé

Dans ce mémoire de thèse, nous étudions la validité de quelques modèles non locaux de la permittivité diélectrique dans le calcul du coefficient de transfert de chaleur par rayonnement entre deux matériaux diélectriques, semi-infinies, plans et parallèles, et séparés par un espace vide de largeur d .

Dans les études théoriques antérieures, il a été montré que lorsque l'on considère un modèle local de la permittivité diélectrique, le transfert de chaleur par rayonnement en champ proche suit une loi $1/d^2$ quand d devient de l'ordre ou inférieure à quelques centaines de nanomètres. Cette divergence non physique constitue la faille majeure du modèle local. Plusieurs efforts ont été fournis afin de développer un nouveau modèle de la permittivité diélectrique qui tient compte des effets nonlocaux. Aucune correction non locale pour le transfert de chaleur par rayonnement en champ proche n'a été abordée dans le passé dans le cas des diélectriques. Cependant dans le cas des métaux, un travail complet a été effectué en utilisant le modèle non local de Lindhard–Mermin de la permittivité diélectrique.

Nos travaux portent sur l'étude de quatre modèles différents de la permittivité diélectrique nonlocale. Nous exploitons ces modèles pour le calcul du coefficient de transfert de chaleur par rayonnement entre deux plans de 6H-SiC. Pour le cas des semi-conducteurs dopés, nous avons étudié le modèle non local de Lindhard–Mermin pour calculer le coefficient de transfert de chaleur par rayonnement entre deux plans de Si n-dopée. Nous montrons que le coefficient de transfert de chaleur par rayonnement sature quand d tend vers zéro. La distance du début de saturation dépend grandement des paramètres clés de chaque modèle.

Acknowledgements

First of all I would like to express my deep gratitude and thanks to my advisors Prof. Karl JOULAIN and Associate Prof. Younès EZZAHRI for their continuous support of my PhD work and research. I deeply appreciate their patience, their encouragement and the immense knowledge they provided me to get well trained as a researcher in the scientific field. I couldn't have imagined a better guidance than theirs, they were real mentors.

My sincere thanks also goes to the jury members Dr. Sebastian VOLZ, Dr. Philippe BEN-ABDALLAH, Dr. Rodolphe VAILLON, and Dr. Pierre-Olivier CHAPUIS for their encouragement, their insightful comments and questions, and their fruitful discussions. I am honored with the participation of each one of them in the jury of my defense.

I would like to thank the friendly and the cheerful team of the TNR laboratory for the unforgettable good days I had with them. They are all amazing in too many ways and I sincerely thank them for helping me since the first day of my arrival to the laboratory. They are not just a laboratory team, they are more like a family and I'll always miss being part of this family.

Last but not least, I would like to thank my parents and my two brothers, my family and my friends for their unconditional support in all ways. You have all been an amazing source of love and energy in the good and the bad days. I love you all so much.

Table of contents

Introduction	1
1. Introduction to Radiative Heat Transfer	4
1.1 Fluctuation-Dissipation Theorem.....	12
1.2 Radiative heat transfer coefficient.....	14
1.2.1 Brief recall of the radiometric approach.....	15
1.2.2 Electromagnetic approach	16
1.3 Theory of the local dielectric permittivity of dielectrics	19
1.3.1 Formalism.....	19
1.3.2 Calculation of the radiative heat transfer coefficient.....	21
1.4 Surface waves.....	24
Conclusions	27
References	28
2. Theory of the nonlocal model of the dielectric permittivity for metals	32
2.1 Recall of the Local dielectric permittivity: Drude model.....	33
2.1.1 Formalism.....	35
2.1.2 Calculation of the radiative heat transfer coefficient.....	35
2.2 Lindhard–Mermin nonlocal model for metals	37
2.2.1 Formalism.....	38
2.2.2 Calculation of the radiative heat transfer coefficient.....	40
Conclusions	44
References	45
3. Nonlocal models of the dielectric permittivity for semiconductors	46
3.1 A suggested nonlocal model of the dielectric permittivity.....	48
3.1.1 Formalism.....	48
3.1.2 Calculation of the radiative heat transfer coefficient.....	50
3.2 A suggested nonlocal model of the dielectric permittivity.....	57
3.2.1 Formalism.....	57
3.2.2 Calculation of the radiative heat transfer coefficient.....	57
3.3 A phenomenological model of the dielectric permittivity.....	65
3.3.1 Formalism.....	67
3.3.2 Calculation of the radiative heat transfer coefficient.....	67
Conclusions	77
References	79

4. Nonlocal model of the dielectric permittivity for dielectrics: Halevi–Fuchs theory.....	80
4.1 Nonlocal macroscopic dielectric permittivity function theory	81
4.2 Formalism.....	83
4.3 Calculation of the radiative heat transfer coefficient.....	90
4.4 Study of the radiative transfer spectrum and the electromagnetic energy density	108
Conclusions	117
References	119
5. Lindhard–Mermin nonlocal model for n-doped semiconductors.....	121
5.1 Theory of the local model of the dielectric permittivity.....	122
5.1.1 Formalism.....	122
5.1.2 Calculation of the radiative heat transfer coefficient.....	122
5.2.3 Study of the contribution of the surface-plasmon polaritons.....	126
5.2 Theory of the nonlocal model of the dielectric permittivity: Lindhard–Mermin nonlocal model	128
5.2.1 Formalism.....	129
5.2.2 Calculation of the radiative heat transfer coefficient.....	130
5.2.3 Study of the spectral radiative heat transfer flux	138
Conclusions	140
References	142
Conclusions.....	143
A. Derivation of the radiative heat transfer coefficient of a system of two interfaces.....	147
A.1 Geometry of the system.....	147
A.2 Sipe formalism for a system of two interfaces: Vectors and notations	147
A.3 Fresnel reflection and transmission factors	149
A.4 Green tensors of a system of two interfaces	150
A.5 Derivation of the Poynting vector from medium (1) to medium (2) and the radiative heat transfer coefficient.....	150
B. The electromagnetic energy density above an interface.....	158
B.1 Geometry of the system	158
B.2 Sipe formalism for a system of one interface: vectors and notations	158
B.3 Fresnel reflection and transmission factors.....	159
B.4 Green tensors of a system of one interface	159
B.5 Deriving the EM energy density above an interface.....	159
C. Electrostatic limits of Fresnel reflection factors	165
C.1 The general case	165

C.1.1 <i>s</i> -polarized EM waves.....	165
C.1.2 <i>p</i> -polarized EM waves	165
C.2 Case of aluminum	166
C.2.1 <i>s</i> -polarized EM waves.....	166
C.2.2 <i>p</i> -polarized EM waves	167
D. Henkel–Joullain approach.....	169
D.1 The correlation equation of the fluctuating currents.....	169
D.2 Derivation of the Poynting vector from medium (1) to medium (2) and the radiative heat transfer coefficient.....	169
E. The polylogarithm function <i>Lisz</i>	173

Table of figures

Figure 1.1: The electromagnetic spectrum.....	5
Figure 1.2: The spectral emissive blackbody power as given by Planck’s law.....	7
Figure 1.3: A schematic diagram of the evanescent waves.....	9
Figure 1.4: A schematic diagram of the geometry of the (1-interface) system.....	13
Figure 1.5: Two parallel semi-infinite planar materials separated by a vacuum gap of width d	14
Figure 1.6: A schematic diagram of a dielectric medium when spatial dispersion is neglected and when spatial dispersion is taken into consideration.....	15
Figure 1.7: Variation of the RHTC between two semi-infinite 6H-SiC parallel planes for the local model case.....	21
Figure 1.8: Behaviors of the spectral energy flux and the spectral EM energy density of the p -polarized evanescent EM waves for the local model of the dielectric permittivity of 6H-SiC planes of average temperature $T=300\text{K}$	24
Figure 1.9: Dispersion relation of surface phonon-polaritons at a SiC-Vacuum interface.....	25
Figure 2.1: Variation of the RHTC between two semi-infinite Al parallel planes, for the local model case.....	36
Figure 2.2: Variation of the RHTC between two semi-infinite Al parallel planes, for the Lindhard–Mermin nonlocal model case.....	41
Figure 2.3: Variation of the RHTC between two semi-infinite Al parallel planes, for the local and the nonlocal model cases.....	41
Figure 2.4: Plot of the transmission coefficient of the p -polarized EM evanescent waves in the plane (ω, K) for the local case and the nonlocal case of Lindhard–Mermin model at a separation distance $d = 10^{-12}m$	42
Figure 3.1: The dispersion relation of surface optical phonons of semi-infinite ionic crystals as given by Kliever and Fuchs.....	48
Figure 3.2: Variation of the RHTC between two semi-infinite 6H-SiC parallel planes, for the suggested nonlocal model case.....	52
Figure 3.3: Variation of the total RHTC between two semi-infinite 6H-SiC parallel planes, for the local and the suggested nonlocal model cases.....	53

Figure 3.4: Variation of $Im(r_{3m}^P)$ as a function of K/k_0 for $\omega = \omega_{T0}$ for the local model case and the suggested nonlocal model case.....	54
Figure 3.5: Plot of the transmission coefficient, for the local case and the suggested nonlocal case	55
Figure 3.6: Variation of the transmission coefficient for $\omega = \omega_{T0}$, for the suggested nonlocal case.....	56
Figure 3.7: Variation of the RHTC between two semi-infinite 6H- SiC parallel planes, for the suggested nonlocal model case.....	60
Figure 3.8: Variation of the total RHTC between two semi-infinite 6H-SiC parallel planes, for the local and the suggested nonlocal model cases.....	60
Figure 3.9: Variation of the total RHTC between two semi-infinite 6H-SiC parallel planes of average temperature $T=300K$, for the first and the second suggested nonlocal models.....	63
Figure 3.10: Plot of the transmission coefficient, for the local case and the suggested nonlocal case.....	64
Figure 3.11: Variation of the transmission coefficient for $\omega = \omega_{T0}$, for the suggested nonlocal model.....	64
Figure 3.12: Plot of the transmission coefficient for the suggested nonlocal model by considering $d=0$ and $K = nq_B$	65
Figure 3.13: Variation of the RHTC between two semi-infinite 6H-SiC parallel planes, for the suggested nonlocal model case when $l = r_0$	69
Figure 3.14: Variation of the total RHTC between two semi-infinite 6H-SiC parallel planes, for the local case and the suggested nonlocal model case when $l = r_0$	69
Figure 3.15: Variation of the total RHTC between two semi-infinite 6H-SiC parallel planes, for the local case and the suggested nonlocal model case when $l = (1,2, \dots 10)r_0$	70
Figure 3.16: Plot of the function $f(\omega, K)$ for the local case ($l=0$) and the suggested nonlocal cases ($l = 1r_0, 3r_0, 6r_0, 8r_0, 10r_0$).....	73
Figure 3.17: Variation of the saturation value of the RHTC between two semi-infinite parallel 6H-SiC planes as function of the coherence parameter l	74
Figure 3.18: Variation of $h_{rad}^{evan p}(T, l)$ as function of the average temperature T for the cases when $l = 1r_0, 5r_0$ and $10r_0$	76

Figure 4.1: A schematic diagram showing the incidence of an EM wave on the interface separating the local medium (vacuum) from the local dielectric medium, and the nonlocal dielectric medium.....	82
Figure 4.2: A schematic diagram showing that an excitation at a point r' produces a response at a point r	85
Figure 4.3: Variation of the RHTC between two semi-infinite 6H-SiC parallel planes of average temperature $T=300\text{K}$, for the nonlocal model of Rimbey–Mahan ABC.....	91
Figure 4.4: Variation of the RHTC between two semi-infinite 6H-SiC parallel planes of average temperature $T=300\text{K}$, for the nonlocal model of Agarwal ABC.....	92
Figure 4.5: Variation of the RHTC between two semi-infinite 6H-SiC parallel planes of average temperature $T=300\text{K}$, for the nonlocal model of Ting ABC.	92
Figure 4.6: Variation of the RHTC between two semi-infinite 6H-SiC parallel planes of average temperature $T=300\text{K}$, for the nonlocal model of Kliewer–Fuchs ABC.....	93
Figure 4.7: Variation of the RHTC between two semi-infinite 6H-SiC parallel planes of average temperature $T=300\text{K}$, for the nonlocal model of Pekar ABC.....	93
Figure 4.8: Variation of the total RHTC between two semi-infinite 6H-SiC parallel planes for the nonlocal model, with the five different sets of the ABC.....	94
Figure 4.9: Variation of the total RHTC between two semi-infinite 6H-SiC parallel planes, for the nonlocal model with the five different sets of the ABC, in comparison with the local model.....	95
Figure 4.10: Plot of the real part and the imaginary part of the nonlocal dielectric permittivity function $\epsilon(\omega, K)$ in the plane (ω, K)	97
Figure 4.11: Variation of the bump in the curve of the contribution of the p -polarized evanescent EM waves to the RHTC, as the value of ω_p changes for the nonlocal model of Kliewer–Fuchs ABC.....	97
Figure 4.12: Variation of the bump in the curve of the contribution of the p -polarized evanescent EM waves to the RHTC, as the value of ω_p changes for the nonlocal model of Ting ABC.....	98
Figure 4.13: Variation of the bump in the curve of the contribution of the p -polarized evanescent EM waves to the RHTC, as the value of the diffusion parameter D changes for the nonlocal model of Kliewer–Fuchs ABC.....	98

Figure 4.14: Variation of the bump in the curve of the contribution of the p -polarized evanescent EM waves to the RHTC, as the value of the diffusion parameter D changes for the nonlocal model of Ting ABC.....	99
Figure 4.15: Variation of the bump in the curve of the contribution of the p -polarized evanescent EM waves to the RHTC, as the value of the losses parameter ν change for the nonlocal model of Kliewer–Fuchs ABC.....	99
Figure 4.16: Variation of the bump in the graph of the contribution of the p -polarized evanescent EM waves to the RHTC, as the value of the losses parameter ν change for the nonlocal model of Ting ABC.....	100
Figure 4.17: Plot of the transmission coefficient for the local model and the nonlocal model of Rimbey–Mahan ABC at different separation distances d	103
Figure 4.18: Plot of the transmission coefficient for the local model and the nonlocal model of Agarwal ABC at different separation distances d	104
Figure 4.19: Plot of the transmission coefficient for the local model and the nonlocal model of Ting ABC at different separation distances d	105
Figure 4.20: Plot of the transmission coefficient for the local model and the nonlocal model of Kliewer–Fuchs ABC at different separation distances d	106
Figure 4.21: Plot of the transmission coefficient for the local model and the nonlocal model of Pekar ABC at different separation distances d	107
Figure 4.22: Plots of the spectral energy flux and the spectral EM energy density for the nonlocal model of Rimbey–Mahan ABC at different distances d and average temperature $T=300K$	109
Figure 4.23: Plots of the spectral energy flux and the spectral EM energy density for the nonlocal case of Agarwal ABC at different distances d of average temperature $T=300K$	110
Figure 4.24: Plots of the spectral energy flux and the spectral EM energy density for the nonlocal case of Ting ABC at different distances d and average temperature $T=300K$	111
Figure 4.25: Plots of the spectral energy flux and the spectral EM energy density for the nonlocal model of Kliewer–Fuchs ABC at different distances d and average temperature $T=300K$	112
Figure 4.26: Plots of the spectral energy flux and the spectral EM energy density for the nonlocal model of Pekar ABC at different distances d and average temperature $T=300K$	113
Figure 4.27: Plots of the spectral energy flux and the spectral EM energy density, for different values of the parameter D for the nonlocal model of Kliewer–Fuchs ABC	114

Figure 4.28: Plots of the spectral energy flux and the spectral EM energy density, for different values of the parameter D for nonlocal model of Rimbey–Mahan ABC	114
Figure 4.29: Plots of the spectral energy flux and the spectral EM energy density, for different values of the parameter D for the nonlocal model of Pekar ABC.....	115
Figure 4.30: Plots of the spectral energy flux and the spectral EM energy density, for different values of the parameter D for the nonlocal model of Ting ABC.....	115
Figure 4.31: Plots of the spectral energy flux and the spectral EM energy density, for different values of the parameter D for the nonlocal model of Agarwal et al ABC.....	116
Figure 5.1: Resistivity of Si at $T=300\text{K}$ as a function of acceptor and donor concentration.	123
Figure 5.2: Variation of the RHTC between two semi-infinite n-doped Si parallel planes of doping concentration $N = 10^{19}\text{cm}^{-3}$ for the local model.....	123
Figure 5.3: Variation of the RHTC between two semi-infinite n-doped Si parallel planes of doping concentration $N = 10^{20}\text{cm}^{-3}$, for the local model case.....	124
Figure 5.4: Variation of the RHTC between two semi-infinite n-doped Si parallel planes of doping concentration $N = 10^{21}\text{cm}^{-3}$, for the local model case.....	124
Figure 5.5: Variation of the total RHTC between two semi-infinite n-doped Si parallel planes of doping concentration $N = 10^{19}\text{cm}^{-3}, 10^{20}\text{cm}^{-3}$ and 10^{21}cm^{-3} , for the local model case.....	125
Figure 5.6: Variation of $\delta G(T, N)$ as function of the average temperature T for the three different doping concentrations considered in the calculation of the RHTC between the n-doped Si semi-infinite parallel planes.....	127
Figure 5.7: Variation of $\delta G(T, N)$ as function of the doping concentration for different average temperatures T	127
Figure 5.8: Variation of the RHTC between two semi-infinite n-doped Si parallel planes of doping concentration $N = 10^{19}\text{cm}^{-3}$, for the nonlocal model case.....	131
Figure 5.9: Variation of the RHTC between two semi-infinite n-doped Si parallel planes of doping concentration $N = 10^{20}\text{cm}^{-3}$, for the nonlocal model case.....	131
Figure 5.10: Variation of the RHTC between two semi-infinite n-doped Si parallel planes of doping concentration $N = 10^{21}\text{cm}^{-3}$, for the nonlocal model case.....	132
Figure 5.11: Variation of the total RHTC between two semi-infinite n-doped Si parallel planes of doping concentration $N = 10^{19}\text{cm}^{-3}, 10^{20}\text{cm}^{-3}$ and 10^{21}cm^{-3} , for the nonlocal model case.....	132

Figure 5.12: Variation of the total RHTC between two semi-infinite n-doped Si parallel planes of doping level $N = 10^{19} \text{cm}^{-3}$, 10^{20}cm^{-3} and 10^{21}cm^{-3} , for the local and the nonlocal model cases.....	133
Figure 5.13: Variation of the saturation value of the RHTC graph as the doping concentration varies between 10^{19}cm^{-3} and 10^{21}cm^{-3} for the nonlocal model case where the average temperature of the system is considered $T=300\text{K}$	134
Figure 5.14: Plot of the transmission for the local case and the nonlocal case for the doping level $N = 10^{19} \text{cm}^{-3}$ and at different separation distances d	135
Figure 5.15: Plot of the transmission coefficient for the local model and the nonlocal model for the doping level $N = 10^{20} \text{cm}^{-3}$ and at different separation distances d	136
Figure 5.16: Plot of the transmission coefficient for the local model and the nonlocal model for the doping level $N = 10^{21} \text{cm}^{-3}$ and at different separation distances d	137
Figure 5.17: Variation of the spectral radiative heat transfer flux Φ of the p -polarized EM evanescent waves as ω varies for different doping concentrations N in the nonlocal model case and for a separation distance $d = 10^{-12} \text{m}$	138
Figure A.1: Geometry of the system considered (2–interfaces).....	147
Figure A.2: Presentation of the different vectors of the EM waves of s and p polarizations, introduced in the formalism of Sipe 1987 for the 2–interfaces system.....	148
Figure B.1: Geometry if the system considered (1–interface).....	158
Figure B.2: Presentation of the different vectors introduced in the formalism of Sipe 1987 for the 1–interface system.....	158

List of Abbreviations

6H-SiC	6H-type Silicon Carbide
ABC	Additional boundary conditions
DRHF	Density of the radiative heat flux
EM	Electromagnetic
FFRHT	Far-field radiative heat transfer
FDT	Fluctuation-dissipation theorem
FBZ	First Brillouin zone
IR	Infrared
LDOS	Local density of states
MIT	Massachusetts Institute of Technology
n-Si	n-doped Silicon
NFRHT	Near-field radiative heat transfer
NSOM/SNOM	Near-field Scanning Optical Microscopy ()
PINEM	Photon-induced near-field electron microscopy
RHT	Radiative heat transfer
RHF	Radiative heat flux
RHTC	Radiative heat transfer coefficient
RPA	Random phase approximation
STM	Scanning Tunneling Microscopy
STM	Scanning Tunneling Microscope
SFM	Scanning Force Microscopy
SSP	Surface scattering parameters
UV	Ultraviolet

List of symbols

Greek Letters

Γ	Normalized damping factor
$\Pi(\mathbf{r}, \omega)$	Poynting vector ($J \cdot s^{-1} \cdot m^{-2}$)
\mathbb{P}	Excitation polarization (C/m^2)
Φ	Exchanged radiative heat flux ($W \cdot m^{-2}$)
Φ	Spectral flux energy density ($J \cdot m^{-2} \cdot rad^{-1}$)
Ω	Normalized frequency factor
γ	Normal wavevector component m^{-1}
$\delta_{k,l}$	Kronecker symbol
δ	Dirac delta function
δ	Skin depth (m)
ϵ	Emissivity
ε	Dielectric permittivity function
ε_∞	Infinite frequency permittivity
ε_0	Dielectric permittivity of vacuum ($F \cdot m^{-1}$)
θ	Mean energy of the harmonic oscillator in (J)
κ	Thermal conductivity ($W \cdot m^{-2} \cdot K^{-1}$)
λ	Wavelength of thermal radiation (m)
λ_{max}	Wien's wavelength in (m)
μ_0	Vacuum permeability ($H \cdot m^{-1}$)
ν	Frequency of thermal radiation (H_z)
ν	Damping factor ($rad \cdot s^{-1}$)
ρ	Reflectivity

ρ	Polarization at an interface (C/m^2)
ρ	Electric resistivity ($\Omega \cdot cm$)
σ	Stefan–Boltzmann constant in ($W \cdot m^{-2} \cdot K^{-4}$)
τ	Relaxation time (s)
τ	Transmission coefficient of the electromagnetic wave
v_F	Fermi velocity ($m \cdot s^{-1}$)
$\tilde{\chi}$	Susceptibility tensor
ω	Angular frequency ($rad \cdot s^{-1}$)
ω_p	Plasma frequency ($rad \cdot s^{-1}$)
ω_L	Optical longitudinal angular frequency ($rad \cdot s^{-1}$)
ω_T	Optical transverse angular frequency ($rad \cdot s^{-1}$)
ω_{sp}	Surface plasmon-polaritons excitation frequency ($rad \cdot s^{-1}$)

Latin letters

A	Adjusted constant
B	Adjusted constant
C_1	First radiation constant ($W \cdot \mu m^4 / m^2$)
C_2	Second radiation constant ($\mu m \cdot K$)
C_3	Third radiation constant ($\mu m \cdot K$)
D	Constant related to a diffusion phenomenon of the carriers ($m^2 \cdot s^{-2}$)
D	Displacement vector ($A \cdot m^{-1}$)
E	Electric field ($V \cdot m^{-1}$)
$E_{\lambda,b}$	Spectral emissive power of a blackbody ($W/m^2 \cdot \mu m$)
\vec{G}	Green tensor
J	Radiative heat flux between two real opaque bodies ($W \cdot m^{-2}$)
J_{bb}	Radiative heat flux between two blackbodies ($W \cdot m^{-2}$)
K	Parallel wavevector component (m^{-1})
L_ω^0	Monochromatic specific intensity of radiation of a blackbody ($J \cdot s^{-1} \cdot m^{-3} \cdot Sr^{-1}$)

N	Doping concentration (cm^{-3})
N_c	Effective density of states in the conduction band (cm^{-3})
T	Temperature (K)
U	Surface scattering parameters
Z	Surface impedance ($m \cdot s^{-1}$)
c	Speed of light in vacuum ($m \cdot s^{-1}$)
d	Distance (m)
d_c	Critical distance (m)
e	Electron charge (C)
g_0	Quantum of the thermal conductance ($J \cdot s^{-1} \cdot K^{-1}$)
h	Planck's constant in ($J \cdot s$)
\hbar	Reduced Planck constant (or Dirac constant) ($J \cdot s$)
h^0	Derivative of the black body specific intensity of radiation with respect to temperature (Planck's law) ($J \cdot s^{-1} \cdot m^{-2} \cdot K^{-1}$)
h_{rad}	Radiative heat transfer coefficient ($W \cdot m^{-2} \cdot K^{-1}$)
$j(\mathbf{r}, \omega)$	Current density at point r in ($A \cdot m^{-2}$)
k_B	Boltzmann constant in ($J \cdot K^{-1}$)
\mathbf{k}	Total wavevector of the EM wave in (m^{-1})
k_0	Total wavevector in vacuum (m^{-1})
k_F	Fermi wavevector (m^{-1})
l	Coherence length of the thermal EM field (m)
l_{TF}	Thomas–Fermi length (m)
m_e	Electron mass (Kg)
m_h	Hole mass (Kg)
m^*	Electron effective mass (Kg)
q	Tangential wavevector component (m^{-1})
q_B	Perpendicular wavevector at the limit of the first Brillouin zone (m^{-1})

r	Reflection coefficient of the EM wave
r_0	Lattice constant (m)
u	Energy density ($J.m^{-3}.rad^{-1}.s$)

Introduction

This thesis is devoted to the study of the influence of the nonlocal effects on the near-field radiative heat transfer. Conducting this study for a system consisting of two semi-infinite parallel solid dielectric planes, we present the consequences of accounting for the nonlocal effects in the dielectric permittivity model on the exchanged radiative heat flux. One of the major consequences is the saturation of the radiative heat transfer coefficient, which replaces the non-physical divergence obtained upon using a local model of the dielectric permittivity.

The originality of this work consists in three main points. The first point is suggesting four different nonlocal models of the dielectric permittivity for dielectrics, which take into consideration the spatial dispersion and the nonlocal effects. Throughout the past few decades, most of the theoretical studies of the radiative heat transfer between two objects involved local models of the dielectric permittivity and nonlocal effects were not included. Obtaining some results that could not be considered physical, such as the infinity diverging radiative heat transfer coefficient as the inter-planar distance decreases, the authors conducting these studies suggested that considering a nonlocal model of the dielectric permittivity could be the solution. As far as we know, the nonlocal models of the dielectric permittivity that were suggested after that were complicated as to be handled analytically and numerically. For this reason, the second point that constitutes the originality of our work is the simplicity of our suggested nonlocal models of the dielectric permittivity. We will show throughout the different aspects of our work the simple mathematical and analytical treatment of these models, as well as the clarity of the different physical notions portrayed in their expressions. The third point would definitely relate to the results; obtaining saturation of the radiative heat transfer coefficient as the inter-planar distance decreases between the dielectric planes constitutes one main original point. Our suggested nonlocal dielectric models lead to replacing the nonphysical divergence with a finite saturation, backed up with the analytical calculations, the numerical simulations, the physical interpretations and the supporting references.

This work is detailed and presented in five chapters:

- Chapter 1 presents an introduction to the different aspects of our work. Starting with the description of the thermal energy and the radiative heat transfer, we demonstrate the characteristics of the far-field radiative heat transfer and the near-field radiative heat transfer, along with their physical differences. Showing the importance of the near-field radiative heat transfer in the different technological domains, and explaining the physical phenomena dominating this transfer, we highlight the physical bases needed to conduct our work. We then present the detailed near-field radiative heat transfer study for a system of two semi-infinite parallel 6H-SiC planes using a local model of the dielectric permittivity. We show how the radiative heat transfer diverges as the inter-planar distance decreases.
- Chapter 2 is dedicated to studying the near-field radiative heat transfer for a system of two semi-infinite parallel metallic planes using a local model of the dielectric permittivity. We then proceed by repeating the complete work of Chapuis et al. to perform the same study as the previous section, using a nonlocal model of the dielectric permittivity.
- Chapter 3 includes the detailed study of three of our suggested nonlocal models of the dielectric permittivity for dielectrics. Considering the same system as in the local study in chapter 1, we present each model along with the validity conditions and the related results. We also compare between the different results and features. We show that saturation of the radiative heat transfer coefficient is attained in the three models.
- Chapter 4 presents the fourth suggested nonlocal model of the dielectric permittivity for dielectrics. It is based on the macroscopic theory of Halevi and Fuchs. This theory considers spatial dispersion and electromagnetic excitation at the surface of the dielectrics. We will show that the latter of these assumptions necessitates some additional boundary conditions. We will consider five different sets of these ABC and use them in the study of the near-field radiative heat transfer for the same 6H-SiC system. Saturation and other different interesting physical features are obtained, and consequently explained throughout the chapter.
- Chapter 5 is devoted to studying the near-field radiative heat transfer for a system of two n-doped silicon planes. We start with performing this study using a local model of the dielectric permittivity. The nonphysical divergence is obtained, and for this reason we repeat in the second section the same study using a nonlocal model of the dielectric permittivity. The model used is the same one considered in chapter 2 for the metallic planes case. We will show that the saturation of the radiative heat transfer coefficient

is obtained. Different physical features are presented and interpreted with respect to the variation of the doping concentration, and the average temperature of the system. The last part is dedicated to the conclusions and the future perspectives; followed by the appendices *A*, *B*, *C*, *D* and *E* demonstrating in details the necessary derivations mentioned throughout the report.

Chapter 1

1. Introduction to Radiative Heat Transfer

Introduction

Thermal radiation is a well-known physical phenomenon that was described since the beginning of the last century by Planck [1] and Einstein [2,3]. It is defined as the radiant energy emitted by a medium and that is due solely to the temperature of this medium, i.e. it is the temperature of the medium that governs the emission of thermal radiation. We refer by thermal radiation or radiative heat transfer (RHT) to the phenomenon describing the heat transfer due to the propagation of electromagnetic (EM) waves. Unlike the other two mechanisms of energy transfer, conduction and convection, RHT requires no intervening medium to propagate which makes it of great importance for many applications in different fields [4–6]. Very often, the RHT from cooler bodies can be neglected in comparison with convection and conduction; but heat transfer processes that occur at high temperature, or with conduction or convection suppressed by evacuated insulations (different kinds of insulations evacuated from gas), usually involve a significant fraction of radiation. RHT plays an important role in the transfer of heat in the furnaces and the combustion chambers; as well as in the energy emission of nuclear explosions. In general, heat transfer considerations are important in almost all the domains of technology; heat transfer involves a great variety of physical phenomena and engineering systems [7].

In the EM radiation spectrum, the thermal radiation at usual temperatures lies in the intermediate portion extending from $0.1 \mu\text{m}$ to $100 \mu\text{m}$ including a part of the ultraviolet (UV) range, all the visible range and all the infrared (IR) range; see Fig. 1.1 [4]. Thermal radiation exhibits the same wavelike properties as light or radio waves where each quantum of radiant energy has a wavelength “ λ ” and a frequency “ ν ” associated with it.

Any material of finite temperature emits and absorbs continuously heat radiation in all directions due to the molecular and atomic motions associated with its internal energy.

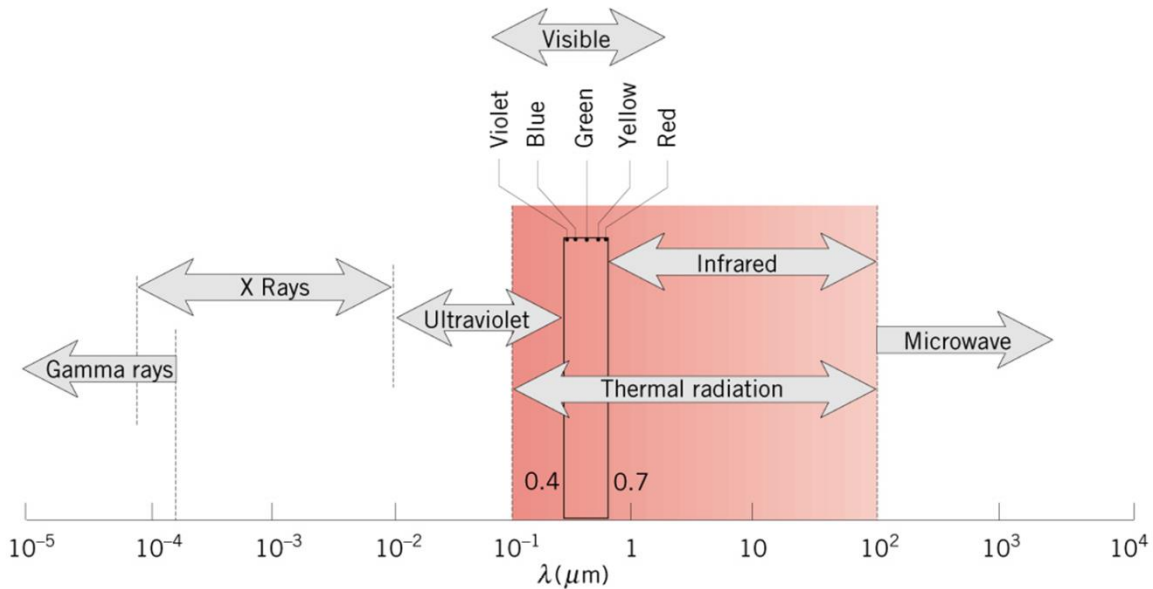


Figure 1.1: The electromagnetic spectrum [4].

The strength of the emission depends on the temperature and all real bodies emit and absorb heat less than a blackbody at the same temperature. The blackbody is considered as the standard against which the behavior of all real radiating materials is estimated and compared; and its properties are well-defined in theory. In general, it is defined as a surface or volume that absorbs all incident radiation at every wavelength and from any direction, and it is considered also as the best possible emitter of radiation, at every wavelength and in every direction. As a consequence, any real material will reflect some of the incident radiation and therefore it will absorb energy less than that absorbed by the ideal blackbody; similarly, a real body will emit energy less than emitted by the ideal blackbody [4–6].

Since the end of the nineteenth century, scientists had tried for many years to predict the spectrum of the blackbody emission, starting from Wilhelm Wien 1896 [8] who used thermodynamic arguments along with some experimental data to propose a spectral distribution of the blackbody emissive power; a large part of this spectrum was accurately correct. Lord Rayleigh and Sir Jeans derived a spectral distribution of the blackbody emissive power based on the assumption that the equipartition theorem of energy is valid [7,9]; they expressed the energy density as the product of the number of standing waves, which were considered as oscillators, and the average energy of an oscillator. They found the average energy of an oscillator of temperature T to be independent of the frequency and equal to $k_B T$, where $k_B = 1.380648 \times 10^{-23} \text{J} \cdot \text{K}^{-1}$ is Boltzmann constant. This Rayleigh–Jeans law agreed well with the experimental observations for small frequencies, but for large

frequencies, i.e. for the ultraviolet range, this law gave results that were very different from the experimental results. This error in the values of Rayleigh–Jeans law is known as the ultraviolet catastrophe.

In 1900, based on his work on quantum statistics, Planck [1] published the correct spectral emissive power spectrum of a blackbody where he assumed that a molecule can emit photons only at distinct energy levels. The spectral emissive power (in $W/m^2 \cdot \mu m$) is given by the following equation [1, 4–6]:

$$E_{\lambda,b}(\lambda, T) = \frac{C_1}{\lambda^5 [e^{C_2/\lambda T} - 1]} \quad (1.1)$$

λ is the wavelength, T is the absolute temperature, $C_1 = 2\pi hc^2 = 3.742 \times 10^8 W \cdot \mu m^4/m^2$ and $C_2 = hc/k_B = 1.439 \times 10^4 \mu m \cdot K$ are the first and the second radiation constants, respectively. $h = 6.626069 \times 10^{-34} J \cdot s$ is Planck's constant and $c = 2.998 \times 10^8 m \cdot s^{-1}$ is the speed of light in vacuum.

Wien's displacement law [8] published in 1891 independently and well before Planck's law allows calculating at any temperature T , the wavelength λ_{max} at which the emitted power of the blackbody is maximal. This law is given by the following equation [4,5,6,10,11]:

$$\lambda_{max} = \frac{C_3}{T} \quad (1.2)$$

where $C_3 = 2898 \mu m \cdot K$ is the third radiation constant. In Fig. 1.2 we present the emissive power spectrum obtained from Planck's equation Eq. (1) along with the locus of Wien's equation Eq. [2], where we observe that the power increases and λ_{max} shifts to smaller values as the temperature increases [4].

Followed by the work of Einstein [2,3] in 1907 and 1916 that generalized Planck's law and gave clear definitions, the notions associated to thermal radiation were well presented and thus well-understood since then.

One of the typical studies of the RHT phenomenon is the study of the energy transfer exchanged between two bodies of different temperatures. When the bodies are separated by a vacuum gap of width d , the heat flux exchanged between them is only due to RHT.

Classical RHT between two semi-infinite bodies does not depend on the distance between them, but on the optical properties of the bodies. More recently, it has been shown that the radiative heat flux (RHF) transferred between two bodies increases and reaches values of several orders of magnitude larger than the classical RHT as the gap distance decreases.

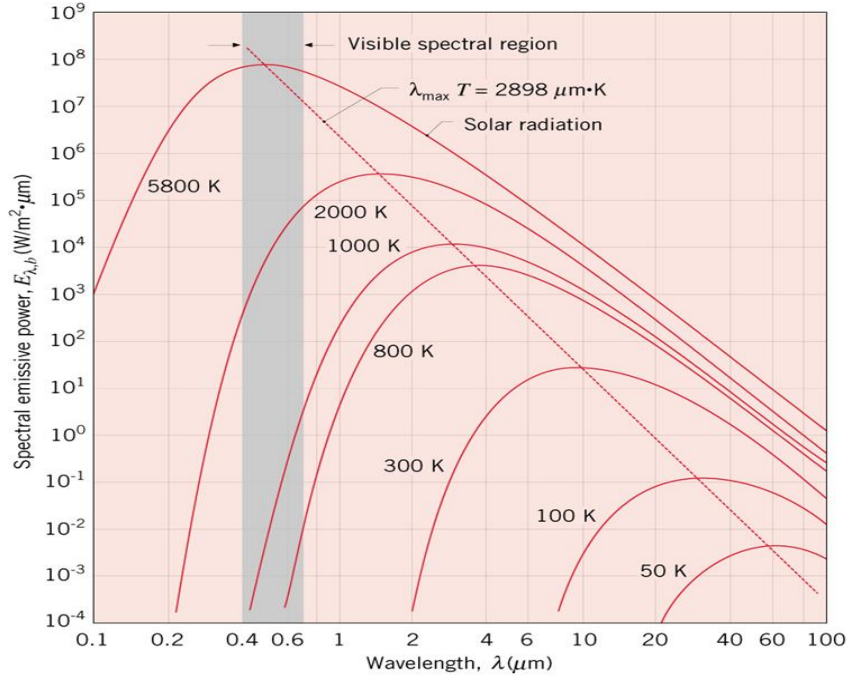


Figure 1.2: The spectral emissive blackbody power as given by Planck's law [4]. The straight line connecting the peaks of the graphs corresponds to the locus of the wavelength given by Wien's displacement law.

This happens when the typical gap distance becomes much smaller than the thermal wavelength λ_{max} ; i.e. this typical wavelength separates the far-field range where the classical RHT is valid, from the near-field range where the wave effects come into play [12,13].

In the past years the importance of studying and evaluating the heat transfer in the near-field has significantly increased due to particular technological challenges [14]. The recent development of micro and nanotechnologies posed new fundamental and technological problems as the dissipated power per unit volume in these devices is becoming increasingly important due to the reduced size and the increased performance of such systems. Nevertheless, the evacuation of this power is also increasingly difficult leading to undesired consequences as the heating of many electronic or optoelectronic components affects their performance and their life span [15]. The need to solve these problems or at least to limit their consequences had led to the importance of measuring and controlling the temperature and the radiated energy at micro and nano-scales.

We start by recalling the far-field radiative heat transfer (FFRHT) using the classical theory of heat radiation. For a system consisting of two bodies of temperatures T_1 and T_2 separated by a vacuum gap of width $d \gg \lambda_{max}$, the heat radiation exchanged between them is due to the EM waves travelling through the vacuum gap. When the two bodies are considered

as perfect absorbers, i.e. when they act as blackbodies [1, 16], the RHT flux between them is maximal and by Stefan–Boltzmann law it is given as follows [17]:

$$J_{bb} = \sigma(T_1^4 - T_2^4) \quad (1.3)$$

where $\sigma = \pi^2 k_B^4 / 60 \hbar^3 c^2 = 5.67 \times 10^{-8} \text{Wm}^{-2} \text{K}^{-4}$ is the Stefan–Boltzmann constant and $\hbar = 1.054571 \times 10^{-34} \text{J.s}$ is the reduced Planck constant (or Dirac constant). We notice from Eq. (1.3) that the RHT flux density is independent of the gap distance d between the bodies and it depends on the difference of their absolute temperatures each raised to the fourth power. For real opaque bodies the Stefan–Boltzmann law is modified and the RHT flux density is given as follows:

$$J = \sigma \epsilon_{12} (T_1^4 - T_2^4) \quad (1.4)$$

where ϵ_{12} is effective emissivity that depends on the emissivities of the bodies ϵ_1 and ϵ_2 and a corrective factor called the view factor F_{12} . The emissivity of a body is defined as its ability to emit radiation compared to the ideal emission of a blackbody at the same temperature. This implies that for real bodies, the values acquired by ϵ are given by: $0 < \epsilon < 1$. For the special case where the opaque bodies are two semi-infinite parallel plates, Eq. (1.4) reduces to the following form:

$$J = \sigma \frac{\epsilon_1 \epsilon_2}{1 - \rho_1 \rho_2} (T_1^4 - T_2^4) \quad (1.5)$$

where ρ is the reflectivity of the body defined as the fraction of the incident radiative energy reflected by this body.

For the near–field radiative heat transfer (NFRHT), the classical theory does not apply as in this case the gap distance d considered is of the order of or smaller than Wien’s wavelength λ_{max} . It had been shown by many studies that the near-field radiation allows heat to propagate across a small vacuum gap at rates several orders of magnitude higher than that of the far-field blackbody radiation [12,13,17–23].

Cravalho et al. [12] and Polder and Van Hove [13] presented the pioneering work of studying the radiative heat transfer in the near-field by showing the RHF significant increase when the bodies are approached, until this flux reaches values of many orders higher than that between two blackbodies [1,24]. This increase in the NFRHF was interpreted to be due to different complex physical wave phenomena [9,13,18–21,24,25] taking place at small

distances. The phenomena playing the most important role are the interference effects in the waves between the two surfaces and the tunneling evanescent waves.

Evanescent waves are EM waves that dominate the RHT at small distances. They tunnel between two surfaces, and their contribution increases as the separation distance decreases, and they decay exponentially as the distance increases [12,13,21–26]. In general, the first recognition of the existence of evanescent electromagnetic waves was probably the analysis of the skin depth effect at metallic surfaces [17–31]. Years later, following the work of Cravalho et al. [12] and Polder and VanHove [13], a lot of theoretical and experimental research had been devoted to the study of NFRHT between bodies of different materials and different geometrical configurations as this heat transfer mechanism exhibits complex wave phenomena [12,13,21,24–28]. As it is shown in Fig. 1.3 [30], when two surfaces are approached to each other, some of the photons tunnel between the two mediums; new channels of transfer are open corresponding to modes of large wavevectors parallel to the surface by which heat transfer is enhanced.

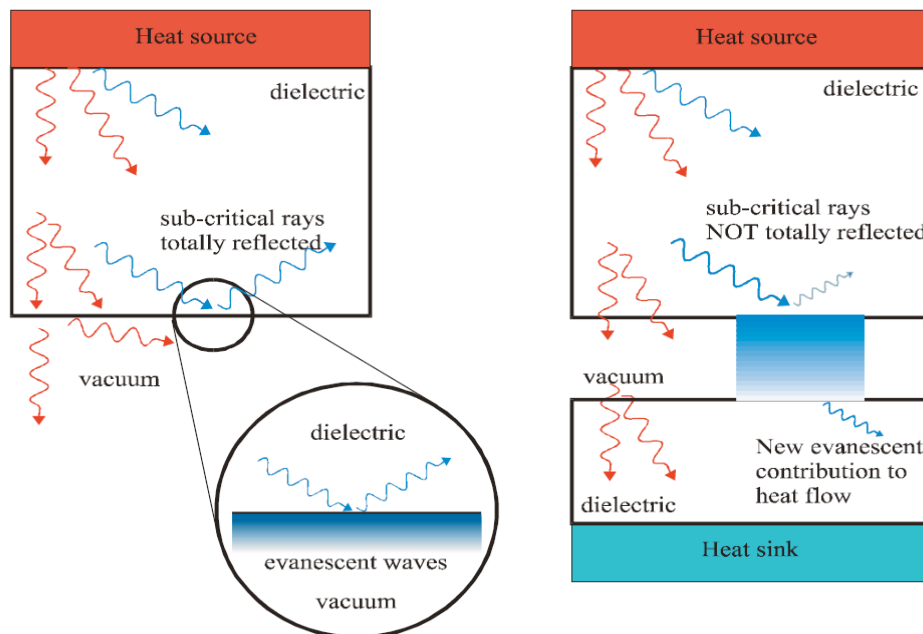


Figure 1.3: Evanescent waves decay exponentially away from the surface and play important role when two planes approach each other as they tunnel between the surfaces of the two planes and contribute effectively to the heat transfer at small separation distances [32].

The science of the EM evanescent waves had drawn a lot of attention because of the different promising technological enhancements that could be achieved using the properties of these waves. As an example, some researchers at the Massachusetts Institute of Technology

(MIT) had proposed a plan for wireless power transfer based on the idea that evanescent wave coupling describes how electromagnetic energy can be sent from one device to another by the way of a decaying electromagnetic field. They were driven by their interest in using wireless technology to charge or power devices which led them to greater understanding of the principles of wireless evanescent coupling. They demonstrated a way to wirelessly send and receive power from a local transmitter to a receiver that is in the vicinity of the device, and in 2007 they showed how a 60 Watt light bulb could be powered up from a distance of 2 meters. They used a technology termed “WiTricity” as an abbreviation of “wireless electricity” to describe this phenomenon of evanescent wave coupling at resonance [33].

The practical exploitations of the evanescent waves, their decaying characteristic and the exponential nature of their wavefunction were undeveloped for a long time until the emergence of local probe-based methods (Scanning Tunneling Microscopy (STM), Scanning Force Microscopy (SFM), and Near-field Scanning Optical Microscopy (NSOM/SNOM)) in the early 1980s with the beginning of the actual investigation of the near-field physics [34–37]. This was followed by many studies at subnanoscale resolution that were achieved due to the evanescent waves effects [38]. Almost two decades later, the research team of A. Zewail exploited the characteristics of the evanescent waves to invent a new type of imaging technique that combines the best qualities from electron microscopy and light microscopy; they called it photon-induced near-field electron microscopy (PINEM) [39]. Nevertheless, superluminal effects of evanescent waves have been revealed in photonic tunneling experiments in both the optical and the microwave domains [39–47].

On the other hand, and due to its different characteristics, NFRHT became crucial in the development of potential applications in numerous technologies such as solar cells and thermophotovoltaic sources [26,49–51], nanolithography [51,52] and sub-wavelength light sources [53].

A lot of theoretical studies were carried out for systems consisting of two semi-infinite plane-parallel solid surfaces. These studies aimed to calculate the NFRHT between the two planes using a local dielectric permittivity function, as the optical response of the material was considered local i.e. $\varepsilon = \varepsilon(\omega)$, where ω is the angular frequency of the EM wave. These studies have shown different behaviors according to the type of the considered material.

For dielectrics, the NFRHT follows a $1/d^2$ law starting at distances as large as few hundreds of nm [13,21,24,26].

For metals, it was shown that the transfer seems to saturate at distances below the material skin depth and then diverges with a $1/d^2$ law at extremely small separation distance d below 1 nm [28,54,55]. We will present in chapter 2 our study of the RHT between two semi-infinite parallel metallic planes where we demonstrate and discuss these results.

Following these theoretical predictions, some experimental studies were carried out to study the RHT between different bodies as the separation distance decreases [55–59]. The obtained results confirmed the enhancement of the RHTF in the nanometer regime due to the tunneling of evanescent waves at the surfaces. Nevertheless, some of the experimental studies have roughly confirmed the $1/d^2$ law mostly at micrometric distances [58]. In the following sections (and chapters) we will present these studies, their results and their discussions in details.

The $1/d^2$ diverging law as the separation distance d is reduced cannot be followed at extremely small distances as no heat transfer can become infinite. Moreover, the continuous behavior of matter does not exist at the atomic scale so that matter response inevitably changes for high spatial frequency. This leads to the need of a nonlocal description of the matter response as suggested by various authors [21,24,61]. In this case, the dielectric permittivity function will be not only frequency dependent but also wavevector dependent.

This constitutes the main subject of this thesis, as we study the validity of few nonlocal models of the dielectric permittivity in the calculation of the radiative heat transfer coefficient (RHTC) between two semi-infinite parallel dielectric planes. For the case of two metallic planes, Chapuis et al. [54] have studied the Lindhard–Mermin nonlocal dielectric permittivity function model and showed that the NFRHT saturated at distances of the order of the Thomas–Fermi length and also suppressed the $1/d^2$ divergence that occurred at extremely small distances. In chapter 2 we present these results along with their detailed explanation.

In the following sections we will present in details the study of the RHT between two solid semi-infinite parallel planes. We will start by presenting the main ideas that allow treating the RHT in electromagnetism in sections 1.1 and 1.2: the Fluctuation-dissipation theorem, the thermodynamic equilibrium and the correlation equation of the fluctuating currents needed in the derivation of the RHTC equation. In section 1.3 we show our calculations of the RHTC between two 6H-type Silicon Carbide semi-infinite parallel planes as the distance between them approaches zero, using a local model of the dielectric permittivity. Section 1.4 will be devoted to the conclusions of this chapter.

1.1 Fluctuation-Dissipation Theorem

In the far-field the emitted electromagnetic field is well described using radiometry theory that is based on the geometrical optics, while in the near-field this theory ceases to be valid as it does not take into consideration the evanescent waves that play an important role in the NFRHT. This leads to the necessity of deriving a formalism that describes well the EM field at small distances. Therefore, one has to use Maxwell equations to calculate the EM field emitted by a body of temperature T . This is the aim of the Fluctuational Electrodynamics formalism, first suggested by Rytov [21, 27,62].

The Fluctuational Electrodynamics states that a body of temperature $T > 0 K$ in local thermodynamical equilibrium radiates thermal energy due to the fluctuations of random currents generated by the random thermal motion of the charges of the body. These charges are electrons in metals and ions in polar materials. The properties of these currents are given by the fluctuation-dissipation theorem (FDT) relating the currents correlation function to the medium radiative losses. These currents radiate an EM field related to the currents by the Green's tensors of the system. This implies that knowing the properties of the random currents and the radiation of a volume element below the interface is essential to determine the statistical properties of the radiated field. Defining the density of the fluctuating current at any point in the medium and substituting it in Maxwell's equations enable us to treat the thermal radiation in electromagnetism [21].

Formalism

The overall current correlation function is a non-zero average and is given by the FDT. We consider a nonmagnetic material body described from an electromagnetic point of view by its dielectric constant $\epsilon(\omega)$. We assume that the dielectric permittivity is local, i.e. the polarization at a certain point of the medium is directly proportional to the electric field at this point, and does not directly depend on the field of other points. Moreover, the body is assumed to be in local thermodynamic equilibrium, i.e. at any instant the temperature of any point of the material is T .

Considering these assumptions as basic, we define the two current densities at points \mathbf{r} and \mathbf{r}' situated in the medium by $j(\mathbf{r}, \omega)$ and $j(\mathbf{r}', \omega')$, oscillating at frequencies ω and ω' respectively, as shown in Fig.1.4.

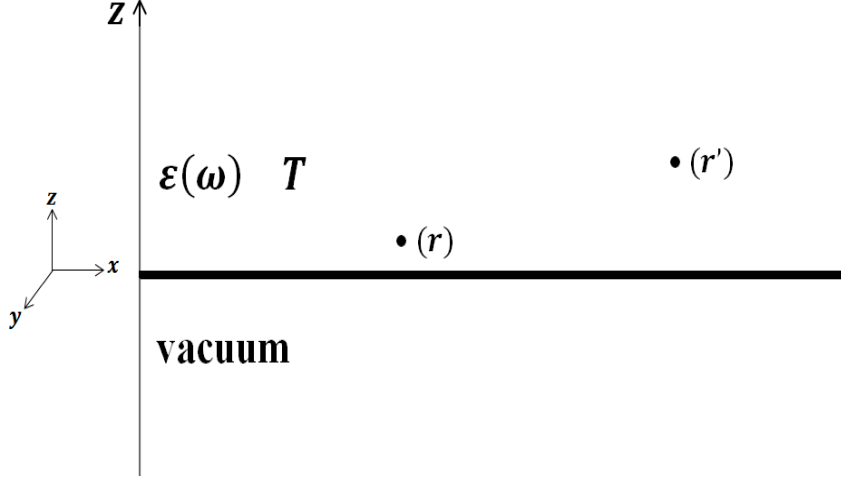


Figure 1.4: A schematic diagram of the geometry of the system.

The FDT then defines the correlation equation of the currents as follows:

$$\langle j_k(\mathbf{r}, \omega) j_l^*(\mathbf{r}', \omega') \rangle = \frac{\omega \varepsilon_0}{\pi} \text{Im}(\varepsilon(\omega)) \Theta(\omega, T) \delta_{k,l} \delta(\mathbf{r} - \mathbf{r}') \delta(\omega - \omega') \quad (1.6)$$

where $\langle \dots \rangle$ indicate an ensemble average. $k, l = x, y, z$ correspond to the different spatial components (in Cartesian coordinates) of the currents. $\varepsilon_0 = 8.85417 \times 10^{-12} \text{ F.m}^{-1}$ is the dielectric permittivity of vacuum and $\text{Im}(\varepsilon(\omega))$ is the imaginary part of the material's dielectric permittivity. $\delta_{k,l}$ is Kronecker symbol and δ is Dirac delta function. $\Theta(\omega, T) = \{(\hbar\omega/2) + [\hbar\omega/(e^{\hbar\omega/k_B T} - 1)]\}$ is the mean energy of the harmonic oscillator of frequency ω at temperature T and $\hbar\omega/2$ represents the vacuum energy, called the zero-point energy. The latter term vanishes from the final results in the case of radiative energy transfer [21]. A simple interpretation would be that we suppose that the medium considered is the only source of fluctuating fields. However the fluctuations of vacuum exist in the presence and absence of the medium, and whether the temperature is zero or not. Therefore, we consider that at any instant, the zero-point energy emitted by a volume element is compensated by an absorbed flux coming from the rest of the space, leading to equilibrium [21].

From Eq. (1.4) we deduce that the fluctuating currents are δ -correlated in space (spatial locality of the dielectric constant) and the fluctuation amplitude is directly related to the losses in the system given by the term $\text{Im}(\varepsilon(\omega))$. Furthermore, understanding how the medium radiates EM waves into space is achieved when the dielectric permittivity of the medium is known. Propagation of waves from the sources (currents) to the observation point is given by the knowledge of the Green function depending on the geometry and the optical properties ($\varepsilon(\omega)$).

The FDT is considered the starting point for the derivation of the RHTC exchanged between two bodies, as it will be presented in the following section.

1.2 Radiative heat transfer coefficient

In this section we will use the FDT to derive the equation of the RHTC exchanged between two semi-infinite parallel planes of temperatures T_1 and T_2 [13,17,18,21,23,63–65], see Fig. 1.5.

The system considered is divided into three media subspaces: the first subspace corresponding to $z < 0$ is occupied by medium (1) whose properties are described by the dielectric permittivity ϵ_1 and similarly, the second subspace corresponding to $z > d$ is occupied by medium (2) and described by the dielectric permittivity ϵ_2 ; subspace (3) corresponds to $0 < z < d$ and is occupied by vacuum described by the dielectric permittivity ϵ_3 . At this stage of our study the nature of the media (metals, dielectrics ...) does not affect the derivation and so it will not be specified.

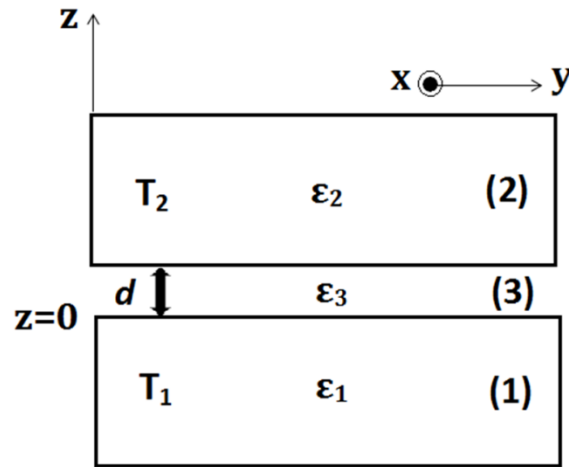


Figure 1.5: Two parallel semi-infinite material planes separated by a vacuum gap of width d .

In the most general sense, constitutive relations in a medium that relate bound charges to the electric field depend on the wave vector and the frequency so that for example $\mathbf{D}(\mathbf{k}, \omega) = \epsilon(\mathbf{k}, \omega)\mathbf{E}(\mathbf{k}, \omega)$, where $\mathbf{D}(\mathbf{k}, \omega)$ is the displacement vector and $\mathbf{E}(\mathbf{k}, \omega)$ is the electric field. When the EM field varies on a spatial scale larger than the microscopic characteristic lengths of the propagation medium, the medium is referred to as local so that the characteristic quantities of the medium are frequency-dependent only, i.e. $\mathbf{D}(\mathbf{r}, \omega) = \epsilon(\mathbf{r}, \omega)\mathbf{E}(\mathbf{r}, \omega)$. When this is not the case, the medium is said to be nonlocal, i.e. the optical properties depend on the

wavevector of the EM field [21,24]. In other words, we can say that in the case of nonlocality, the polarization at one point in the nonlocal medium depends not only on the electric field at that point, but also on the electric fields at the surrounding points. To illustrate this condition clearly, for the case of dielectrics for example, a so-called single-oscillator nonlocal model of the dielectric permittivity $\epsilon(\mathbf{k}, \omega)$ [66] is used (this model is represented in details in chapter 4) where the spatial dispersion, and eventually the nonlocality condition, is presented schematically in Fig. 1.6. We will discuss the nonlocality case in details in the following chapters.

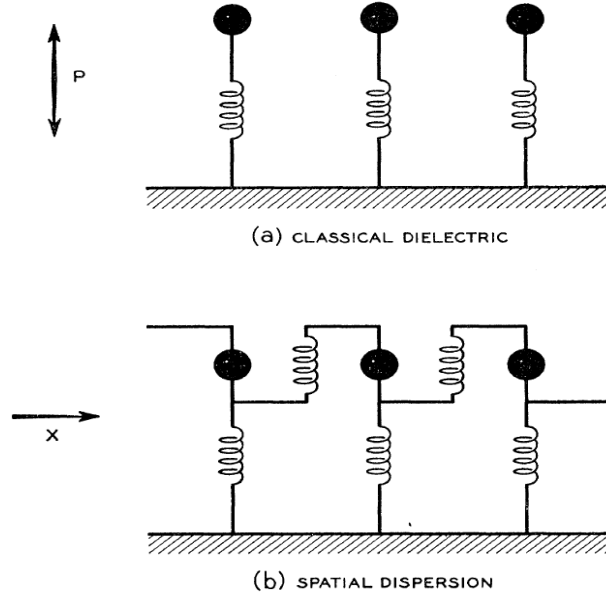


Figure 1.6: A schematic diagram of a dielectric medium when spatial dispersion is neglected (a) and when spatial dispersion is taken into consideration (b) [66].

1.2.1 Brief recall of the radiometric approach

This approach is based on two main concepts: the geometrical optics and the luminous ray nature of the radiation. The exchanged energy flux originates due to the multiple reflections of the radiation in vacuum at the interfaces of planes 1 and 2. Performing few simple algebraic steps we obtain finally the following expression for the exchanged RHF between the two planes separated by vacuum [21,67]:

$$\Phi_{1,2} = \int_0^{2\pi} \cos \theta \, d\Omega \int_0^{\infty} d\omega \frac{\epsilon'_{1\omega} \epsilon'_{2\omega}}{1 - \rho'_{1\omega} \rho'_{2\omega}} [L_{\omega}^0(T_1) - L_{\omega}^0(T_2)] \quad (1.7)$$

where Ω is the solid angle considered to study the radiation in a direction of angle θ with respect to the z axis. $\epsilon'_{1\omega}$ and $\epsilon'_{2\omega}$ are the directional monochromatic emissivities of media (1)

and (2), respectively. $L_{\omega}^0(T) = \hbar\omega^3/[4\pi^3c^2(e^{\hbar\omega/k_B T} - 1)]$ is the monochromatic specific intensity of radiation of a blackbody of temperature T as given by Planck's law.

For the study of the radiation in the near field, this approach is not valid anymore. Regarding the concept, this approach does not take into account the wave nature of the radiation which leads to neglecting the interference phenomena in the studies. Another important negative point of this approach is the total neglecting of the role of the tunneling evanescent waves between the two interfaces because tunneling is a consequence of the wave behavior of radiation. The role of evanescent waves becomes dominant in the small distance range, and neglecting their role in the near-field leads to huge error in the study of the RHT.

This imposed the importance of having a different approach taking into consideration the different phenomena appearing at small distances, in addition to the tunneling EM evanescent waves. The EM approach presented in the following section solves these problems and accounts for the different near-field properties.

1.2.2 Electromagnetic approach

The emitted radiative flux is given by the Poynting vector $\langle \Pi(\mathbf{r}, \omega) \rangle = 4 \times \frac{1}{2} \text{Re}[\langle \mathbf{E}(\mathbf{r}, \omega) \times \mathbf{H}^*(\mathbf{r}, \omega) \rangle]$ [21, 51,65], where $\mathbf{E}(\mathbf{r}, \omega)$ and $\mathbf{H}(\mathbf{r}, \omega)$ are the electric field and magnetic field Eqs. (6) and (7), respectively [37,53]. The factor “4” comes from the fact that the signals considered here have positive frequencies only, so that the fields are analytic signals [21].

$$\mathbf{E}(\mathbf{r}, \omega) = i\omega\mu_0 \int \vec{\mathbf{G}}^E(\mathbf{r}, \mathbf{r}', \omega) \cdot \mathbf{j}_f(\mathbf{r}', \omega) d^3\mathbf{r}' \quad (1.8)$$

$$\mathbf{H}(\mathbf{r}, \omega) = \int \vec{\mathbf{G}}^H(\mathbf{r}, \mathbf{r}', \omega) \cdot \mathbf{j}_f(\mathbf{r}', \omega) d^3\mathbf{r}' \quad (1.9)$$

\mathbf{r}' corresponds to the “source point” situated in the plane (2) and \mathbf{r} is the observation point situated in plane (2). $\vec{\mathbf{G}}^E(\mathbf{r}, \mathbf{r}', \omega)$ and $\vec{\mathbf{G}}^H(\mathbf{r}, \mathbf{r}', \omega)$ are the Green tensors of the medium.

The Green function equations are used to link the EM field at the point \mathbf{r} to the current density at point \mathbf{r}' . Their expressions along with the explanations are given in Appendix A.

It follows that

$$\langle E_x H_y^* \rangle = \iint G^E_{12x\alpha}(\mathbf{r}, \mathbf{r}', \omega) G^{H*}_{12y\beta}(\mathbf{r}, \mathbf{r}'', \omega) \langle j_{f\alpha}(\mathbf{r}', \omega) j_{f\beta}^*(\mathbf{r}'', \omega) \rangle d^3\mathbf{r}' d^3\mathbf{r}'' \quad (1.10)$$

where $\langle j_{f\alpha}(\mathbf{r}', \omega) j_{f\beta}^*(\mathbf{r}'', \omega) \rangle$ is given by the FDT.

Proceeding with the derivation we obtained the final form of the pointing vector Eq. (1.11) (the detailed derivation steps are given in Appendix A).

$$\begin{aligned} \langle \pi_z(d, \omega) \rangle = \pi L_\omega^0(T_1) & \left\{ \int_0^{\frac{\omega}{c}} \frac{K dK}{\omega^2/c^2} \left[\frac{(1 - |r_{31}^s|^2)(1 - |r_{32}^s|^2)}{|1 - r_{31}^s r_{32}^s e^{2i\gamma_3 d}|^2} \right. \right. \\ & + \left. \frac{(1 - |r_{31}^p|^2)(1 - |r_{32}^p|^2)}{|1 - r_{31}^p r_{32}^p e^{2i\gamma_3 d}|^2} \right] \\ & + \int_{\frac{\omega}{c}}^\infty \frac{K dK}{\omega^2/c^2} \left[\frac{4 \operatorname{Im}(r_{31}^s) \operatorname{Im}(r_{32}^s) e^{-2\gamma_3'' d}}{|1 - r_{31}^s r_{32}^s e^{-2\gamma_3'' d}|^2} \right. \\ & \left. \left. + \frac{4 \operatorname{Im}(r_{31}^p) \operatorname{Im}(r_{32}^p) e^{-2\gamma_3'' d}}{|1 - r_{31}^p r_{32}^p e^{-2\gamma_3'' d}|^2} \right] \right\} \quad (1.11) \end{aligned}$$

r_{3m}^s and r_{3m}^p are the reflection factors for the EM waves of polarization $\alpha=s, p$ incident from medium 3 and reflected on media $m=1$ and $m=2$, respectively. K and $\gamma_3 = \sqrt{\omega^2/c^2 - K^2}$ are the wavevector components parallel and normal to the surface in vacuum, respectively. γ_3'' denotes the imaginary part of γ_3 .

When the temperature difference is small $(T_1 - T_2)/T_1 \ll 1$, the density of the radiative heat flux (DRHF) ϕ Eqs. (10) can be linearized and written as a RHTC h_{rad} multiplied by the temperature difference [21, 67]

$$\left\{ \begin{array}{l} \phi(T, d) = h_{rad} \delta T \\ h_{rad} = \int_0^\infty d\omega h_\omega^R(T, d) \\ h_\omega^R(T, d) = \lim_{T_2 \rightarrow T_1} \langle \Pi(d, \omega) \rangle / (T_1 - T_2) \end{array} \right\} \quad (1.12)$$

where $h_\omega^R(T, d)$ is the monochromatic RHTC.

Proceeding with the derivation and considering $k_0^2 = \omega^2/c^2$, we obtain finally the expression of the RHTC Eqs. (1.13):

$$\left\{ \begin{array}{l} h_{rad}(T, d) = \sum_{\alpha=S,P} \int_0^{+\infty} d\omega [h_{prop}^{\alpha}(T, d, \omega) + h_{evan}^{\alpha}(T, d, \omega)] \\ h_{prop}(T, d, \omega) = h^0(T, \omega) \times \int_0^{k_0} \frac{KdK}{k_0^2} \frac{(1 - |r_{31}^{\alpha}|^2)(1 - |r_{32}^{\alpha}|^2)}{|1 - r_{31}^{\alpha} r_{32}^{\alpha} e^{2i\gamma_3 d}|^2} \\ h_{evan}(T, d, \omega) = h^0(T, \omega) \times \int_{k_0}^{+\infty} \frac{KdK}{k_0^2} \frac{4Im(r_{31}^{\alpha})Im(r_{32}^{\alpha})e^{2i\gamma_3 d}}{|1 - r_{31}^{\alpha} r_{32}^{\alpha} e^{2i\gamma_3 d}|^2} \end{array} \right\} \alpha = s, p \quad (1.13)$$

where $h^0(T, \omega)$ is the derivative of the black body specific intensity of radiation with respect to temperature (Planck's law) given by the following equation:

$$h^0(T, \omega) = \frac{\hbar\omega^3}{4\pi^2 c^2} \frac{\hbar\omega}{k_B T^2} \left[2 \sinh\left(\frac{\hbar\omega}{2k_B T}\right) \right]^{-2} \quad (1.14)$$

Eqs. (1.13) show that the RHTC is the sum of the contributions of propagative ($K < k_0$) and evanescent ($K > k_0$) waves of s and p polarizations. The propagative waves have small wavevectors and dominate in the far field while the evanescent waves acquire large wavevectors and dominate in the near field and decay exponentially away from the surface.

As we saw previously, these transmission coefficients can be identified with an emissivity [21]. It is worth mentioning here that the formula of the flux for the propagating EM waves and the classical expression for the radiative flux between two semi-infinite materials are similar, even though the denominator seems different. Upon considering a small range of the frequency, the exponential function $e^{2i\gamma_3 d}$ varies with ω much faster than the Fresnel factors. Therefore, the integration over this range would lead to obtaining an average value of $|1 - r_{31}^{\alpha} r_{32}^{\alpha} e^{2i\gamma_3 d}|^2$ which is equal to $1 - |r_{31}^{\alpha}|^2 |r_{32}^{\alpha}|^2$ [23]. Then, by identifying the reflectance with the squared modulus of the Fresnel reflection factor, it follows that the expression for the classical radiative transfer between media 1 and 2 Eq. (1.5) is equal to the contribution of the propagating waves to this transfer [21].

Another important feature shown by Eqs. (1.13) is their dependence on the separation distance d through an exponential term. This d dependence is one of the major differences between the RHF in the near field and the far field and this emphasizes the concept of different behaviors of the RHT in the near and the far fields.

The reflection factors are given by the general equations Eqs. (1.15) and they depend on the surface impedances $Z_m^p = E_x(0^+)/B_y(0^+)$ and $Z_m^s = -E_y(0^+)/B_x(0^+)$ between media 3 and m which are defined as the ratio of the parallel component of the electric field on the parallel component of the magnetic field Eqs. (1.16) [52,66].

$$\left\{ \begin{array}{l} r_{3m}^p = \frac{\gamma_3 - \varepsilon_3 \omega Z_m^p}{\gamma_3 + \varepsilon_3 \omega Z_m^p} \\ r_{3m}^s = \frac{c^2 \gamma_3 Z_m^s - \omega}{c^2 \gamma_3 Z_m^s + \omega} \end{array} \right\} \quad (1.15)$$

$$\left\{ \begin{array}{l} Z_m^p = \frac{2i}{\pi\omega} \int_0^{+\infty} \frac{dq}{k^2} \left[\frac{q^2}{\varepsilon_t(k, \omega) - (ck/\omega)^2} + \frac{K^2}{\varepsilon_l(k, \omega)} \right] \\ Z_m^s = \frac{2i}{\pi\omega} \int_0^{+\infty} \frac{dq}{\varepsilon_t(k, \omega) - (ck/\omega)^2} \end{array} \right\} \quad (1.16)$$

where $k^2 = K^2 + q^2$, $\varepsilon_t(k, \omega)$ and $\varepsilon_l(k, \omega)$ are the transverse and longitudinal components of the dielectric permittivity of the medium.

1.3 Theory of the local dielectric permittivity of dielectrics

We proceed with the RHT calculations by considering two semi-infinite 6H-type Silicon Carbide (6H-SiC) parallel planes of temperatures $T_1 = 299.5 \text{ K}$ and $T_2 = 300.5 \text{ K}$ so that the average temperature of the system is $T = 300 \text{ K}$.

6H-SiC is a non-magnetic polar material characterized by a hexagonal crystal structure and a lattice constant ratio $c/a \approx 4.9$ where c and a are the lattice parameters; c is the tetrahedron height and a is the length of the Si-Si bond or the C-C bond. The crystallographic configuration of SiC is widely used in research and studied especially at high temperatures. It had received a lot of attention in theoretical and experimental research due to its different physical, semiconducting and heat-resistant properties [69]. The optical properties of SiC have been studied since the late fifties [70–72]. Many investigations concentrated on its electronic structure [73] while Raman spectroscopy experiments were performed to better understand its phonon-related properties and its polytypism [74,75]. The most significant properties of SiC are the high thermal conductivity [76], the excellent thermo-stability [77] and its mechanical stability [78]. All these characteristics lead SiC to be a very promising material for future work in different domains of high-temperature devices [30], electronic and optoelectronic devices [77].

1.3.1 Formalism

In this section we will calculate the RHTC as a function of the distance d by considering the theory of the local dielectric permittivity. As we mentioned previously, when

the medium is referred to as being local, the dielectric permittivity is of frequency dependence only, i.e. $\varepsilon = \varepsilon(\omega)$.

For the case of dielectrics, and specifically SiC, the optical response in the local case is well described by a single oscillator model and presented by Lorentz–Drude local dielectric function Eq. (1.17) [21,72].

$$\varepsilon(\omega) = \varepsilon_{\infty} \left(1 + \frac{\omega_p^2}{\omega_T^2 - \omega^2 - i\nu\omega} \right) \quad (1.17)$$

where $\varepsilon_{\infty} = 6.7$ is the infinite frequency permittivity representing the contribution of the ions of the crystal lattice to the polarization. $\omega_p = 1.049 \times 10^{14} \text{rad.s}^{-1}$ is the plasma frequency defined as $\omega_p^2 = \omega_L^2 - \omega_T^2$, where $\omega_L = 1.821 \times 10^{14} \text{rad.s}^{-1}$ and $\omega_T = 1.495 \times 10^{14} \text{rad.s}^{-1}$ are the optical longitudinal angular frequency and the optical transverse angular frequency of phonons, respectively. $\nu = 8.972 \times 10^{11} \text{rad.s}^{-1}$ is the damping factor accounting for the losses in the medium [71].

We substituted with the dielectric permittivity equation in the general equations of the surface impedances Eqs. (1.16) by assuming that the longitudinal and the transverse components of the dielectric function are equal in the static limit ($\varepsilon(\omega) = \lim_{k \rightarrow 0} \varepsilon_t(k, \omega) = \lim_{k \rightarrow 0} \varepsilon_l(k, \omega)$). For the surface impedance of waves of s -polarization we obtained $Z_m^s = \frac{2i\omega}{\pi c^2} \int_0^{\infty} \frac{dq}{\gamma_m^2 - q^2}$ which gives finally $Z_m^s = \omega/\gamma_m c^2$, where $\gamma_m = \sqrt{\varepsilon_m \omega^2 / c^2 - K^2}$ is the wavevector component normal to the surface of this medium, and $\varepsilon_m = \varepsilon(\omega)$ represents the dielectric permittivity of the medium..

For the surface impedance of p -polarized waves, the expression is developed to $Z_m^p = \frac{2i}{\pi\omega} \left\{ \int_0^{\infty} \frac{q^2 \omega^2 / c^2 dq}{(q^2 + K^2)(\gamma_m^2 - q^2)} + \int_0^{\infty} \frac{K^2 dq}{\varepsilon_m (q^2 + K^2)} \right\}$ and by using the residue theorem we obtain finally $Z_m^p = \gamma_m / \omega \varepsilon_m$.

By substituting the final expressions obtained for the surface impedances in the expressions of the reflection factors as given by Eqs. (1.15), we obtain straightforwardly the classical Fresnel reflection factors for the waves of s and p polarizations:

$$\left\{ \begin{array}{l} r_{3m}^p = \frac{\varepsilon_m \gamma_3 - \varepsilon_3 \gamma_m}{\varepsilon_m \gamma_3 + \varepsilon_3 \gamma_m} \\ r_{3m}^s = \frac{\gamma_3 - \gamma_m}{\gamma_3 + \gamma_m} \end{array} \right\} \quad \text{Eqs. (1.18)}$$

This result was expected because the Fresnel reflection factors are local and they are standard local reflection factors describing a local plane interface.

1.3.2 Calculation of the radiative heat transfer coefficient

To calculate the RHTC, we replace Eqs. (1.16) into the expression given by Eqs. (1.13) to obtain the RHTC as function of the separation distance d . By numerically calculating the obtained equation, we plot in Fig. 1.7 the different contributions of the waves of s and p polarization to the RHTC.

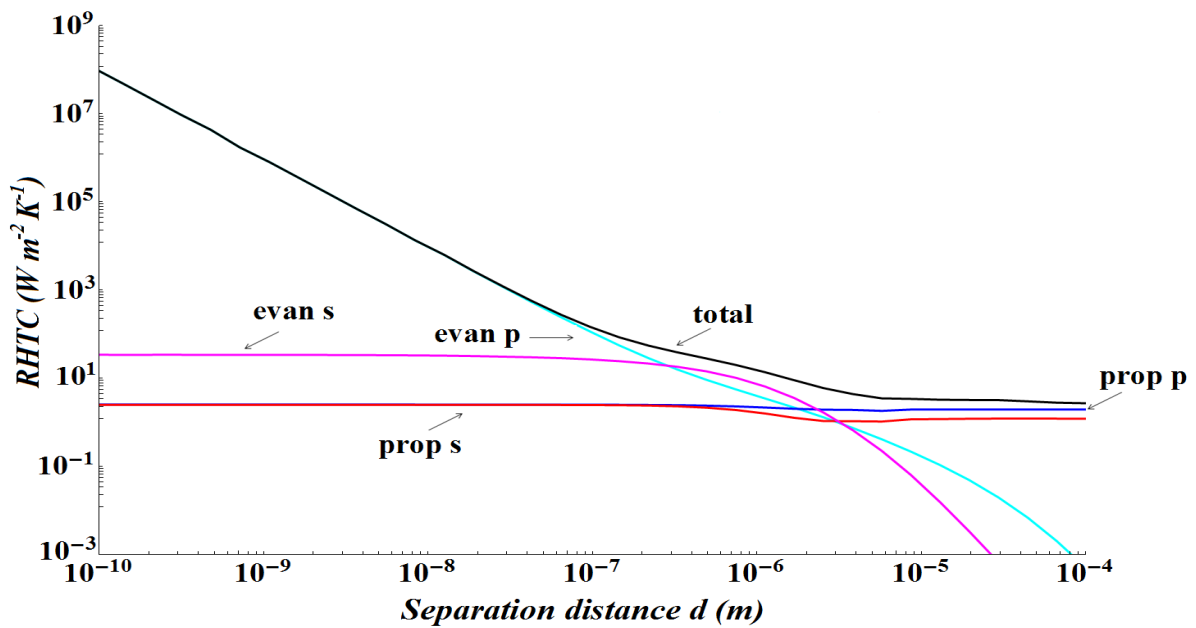


Figure 1.7: Variation of the radiative heat transfer coefficient (contributions of the evanescent and propagative EM waves of s and p polarizations) between two semi-infinite 6H-SiC parallel planes of average temperature $T=300\text{K}$, for the local model case.

Fig. 1.7 shows the graphs of the contributions of the evanescent and propagative EM waves of s and p polarization to the RHTC. We also plotted the total contribution which is the sum of all the four contributions as to compare between the graphs.

From these graphs, we observe that the contributions of the propagative EM waves of both s and p polarizations dominate at large distances and did not change a lot for submicronic distances as they saturate for small distances. Propagative waves dominate at large distances because in the far field the evanescent waves rapidly decrease as the separation distances is large compared to λ_{max} , and by this the value of the RHTC is limited to the contribution of propagative waves and is somewhat less than the value $4\sigma T^3$ [9,10,20,21] which is the standard heat transfer coefficient for a blackbody. This is due to the fact that SiC is highly absorbing over a wide spectral range, except around $10.6\mu\text{m}$ where it is reflective. We also

notice in Fig. 1.6 that the contribution of the p polarized propagative waves gives values slightly higher than those of the s polarized propagative waves; this is explained as being due to the existence of the Brewster angle for which the reflection contribution of the p polarized waves is zero and thus allows for a greater absorption.

To better interpret the obtained results, it is essential to emphasize that the heat transfer is mainly governed by the product of the mean energy of an oscillator at frequency ω and at temperature T and by the density of EM states. It follows that the propagative contributions of s and p polarizations did not change significantly at small distances because the density of EM propagative states at these distances scales does not change significantly [21]. Regarding the contributions of the evanescent EM waves, we observe that at large distances they are negligible compared to the contributions of the propagative waves. This is due to the fact that the evanescent waves decay exponentially away from the surface so that at large distance their decaying rate is large. At sub-wavelength distances, evanescent waves decaying rate is small so that these waves can tunnel between the surfaces and their contributions to the RHTC become dominant. The evanescent contribution of s polarization shows negligible contribution in the far-field and saturates when the distance is smaller than the skin depth [54]. This contribution of the s -polarized evanescent waves could be attributed to the presence of eddy currents on a typical distance equal to the skin depth. When the distance is smaller than the skin depth, the transfer saturates to a value given by a distribution of the current in all the material.

To better understand the results obtained for the evanescent waves contributions it is important to highlight the role of the imaginary part of the reflection factor in the RHTC equation. From Eqs. (1.13) we notice that the evanescent term is proportional to the square of the imaginary part of the reflection factor for identical materials which leads to the importance of studying the variation of the latter to interpret the variation of the RHTC. Thus, to explain the saturation of the evanescent term of s polarization at small distances and for large K , we derived the electrostatic limit of the reflection factor for large K . The latter limit is valid when the separation distance becomes much smaller than the dominant wavelength. In this case, the retardation effects become negligible [21]. Starting with the expression given in Eqs. (1.18) we obtained $r_{3m}^S = (\varepsilon - 1)/4(K/k_0)^2$ which tends to zero for $K \geq k_0$; and since the skin depth is defined as $\delta \approx 1/k_0 \text{Im}(\varepsilon)$, we deduce that the contribution of s -polarized evanescent waves to the RHTC saturate at distances smaller than the skin depth [21,54].

The evanescent p term is the only term that did not saturate as d decreased but on the contrary it showed the well-known divergence behaving as $1/d^2$. This increase in the magnitude of the evanescent p contribution had been described in many articles starting from the first studies that concentrated on the RHT in the near field [21, 54,56,61]. It had been shown that the presence of surface phonon-polaritons that contribute to the transfer lead to the increase of the density of the EM energy Eq. (1.19) close to the surface and consequently to the divergence of the RHTC [21]. We derived the expression of the EM energy density for the p -polarized waves (check appendix B for details) and we obtained the following equation:

$$u_{EM}^{evan p}(d, \omega, T) = \frac{\omega^2 \Theta(\omega, T)}{\pi^2 c^3} \left\{ 4 \int_{k_0}^{\infty} \frac{K^3 dK}{k_0^3 |\gamma_3|} \left[\frac{Im(r_{31}^p)}{2} \right] e^{-2\gamma_3'' d} \right\} \quad (1.19)$$

From this equation we notice that at small distances and large K , $K \approx 1/d$ and $|\gamma_3| \approx K$ lead to the increase of $u_{EM}(d, \omega, T)$ as $1/d^2$. This fact explains the asymptotic increase of the RHTC as $1/d^2$.

We also studied the electrostatic limit of the reflection factor r_{3m}^P where for large K we obtained $r_{3m}^P \approx (\varepsilon - 1)/(\varepsilon + 1)$ which gives a finite non-zero value, and reaches very large values when $\varepsilon = -1$; this corresponds to the resonance frequency of the surface waves [20]. These two limits of the EM energy density and the reflection factor explain the sharp divergence obtained for the graph of the p -polarized evanescent waves' contribution to the RHTC shown in Fig. 1.6.

An important step in our interpretation of the obtained results is to study the variation of the EM spectral energy density Eq. (1.19) and the spectral flux energy density Eq. (1.20) of the p -polarized evanescent waves as the frequency varies.

$$\Phi_{\omega}^{evan p} = h^0(T, \omega) \times \int_{k_0}^{+\infty} \frac{K dK}{k_0^2} \frac{4 [Im(r_{31}^p)]^2 e^{2i\gamma_3 d}}{|1 - (r_{31}^{\alpha})^2 e^{2i\gamma_3 d}|^2} \quad (1.20)$$

Fig. 1.8 shows the plot of the variations of $\Phi_{\omega}^{evan p}$ and $u_{EM}^{evan p}$ as a function of the frequency at two distances $d_1=10^{-5}$ m and $d_2=10^{-7}$ m.

The plots of Fig. 1.8 represent the radiative transfer spectrum (a) and the EM energy density spectrum (b). As the distance decreases three main features are revealed, where we observe that around the specific frequency ω_s which is equal to $\omega_s = 1.784 \times 10^{14} rad.s^{-1}$ (the solution of the equation $\varepsilon = -1$), the spectra show a strong peak, their magnitudes increase by few orders and the thermal emission becomes monochromatic. As ω_s is related to the surface waves, we deduce that the formation of the peak is due to the excitation of surface

phonon-polariton waves which emphasizes the fact that the increase of the RHT is due to the contribution of surface waves.

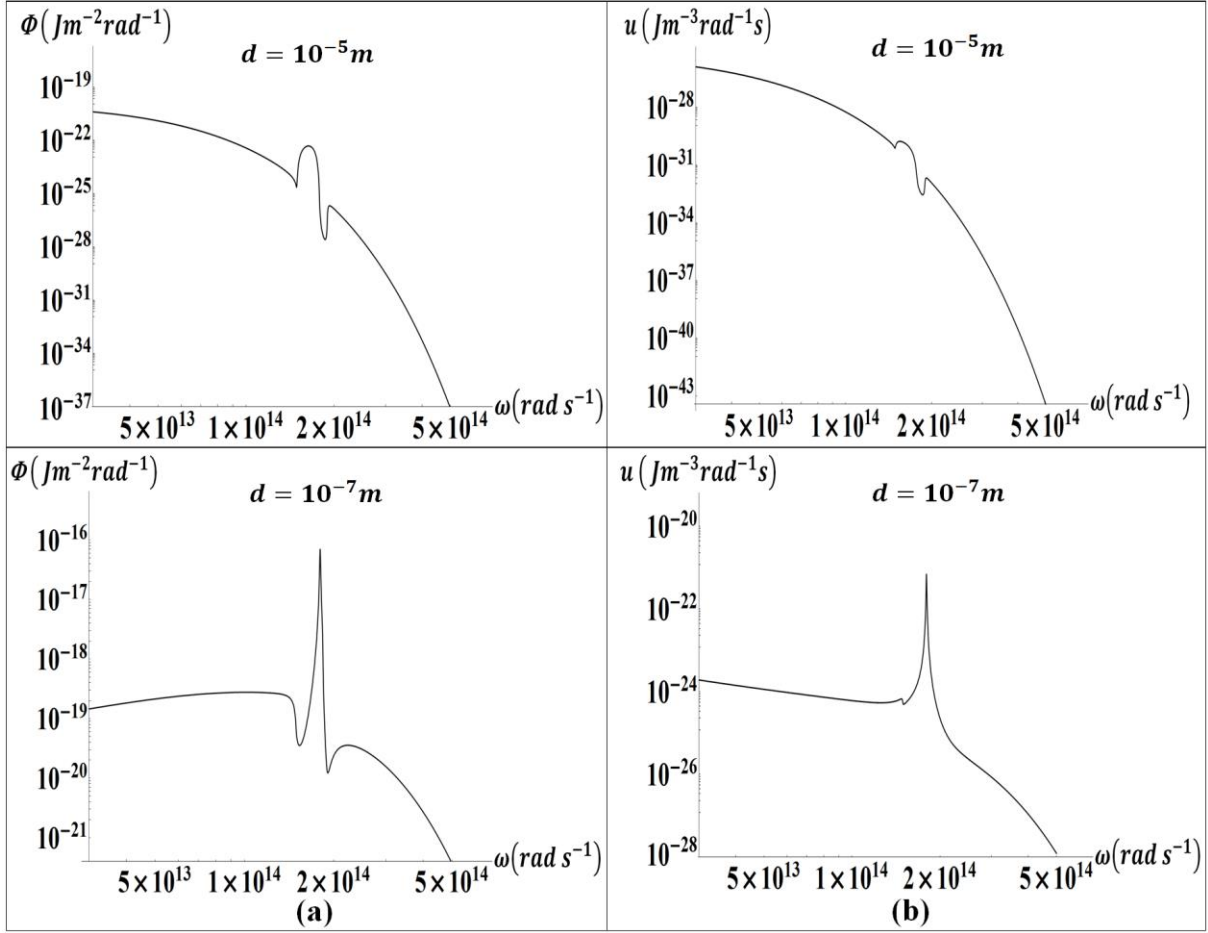


Figure 1.8: Behaviors of the spectral energy flux (a) and the spectral EM energy density (b) of the p -polarized evanescent EM waves as function of the angular frequency at different distances d , for the local model of the dielectric permittivity of 6H-SiC planes of average temperature $T=300\text{K}$.

1.4 Surface waves

The surface waves appear at the interface between two media; in our case they appear at the planar interface (interface-vacuum). They are solutions of Maxwell's equations corresponding to waves propagating parallel to the interface acquiring exponentially decaying amplitude as the distance from the interface increases in the perpendicular direction; for this reason these waves are often called surface waves as they are known to exist in the vicinity of the interface [21]. Surface waves exist due to a coupling between the EM field and a resonant polarization oscillation in the material.

When the material considered is a metal, the surface waves at its interface are charge density waves or plasmons; they are therefore called surface-plasmon polaritons. When the considered material is a dielectric, the surface waves are due to the coupling of optical phonons with the EM field; they are called surface-phonon polaritons.

For the case where the interface considered is a material-vacuum one, the dispersion relation for the p -polarization is given by [21]:

$$K = \frac{\omega}{c} \sqrt{\frac{\varepsilon_m(\omega)}{\varepsilon_m(\omega) + 1}} \quad (1.21)$$

where $\varepsilon_m(\omega)$ is the dielectric permittivity function of the material. From this equation we conclude that the wavevector is larger than $k_0 = \omega/c$ when $\varepsilon_m(\omega) < -1$. By considering the interface SiC-vacuum, Eq. (1.19) represents then the dispersion relation for the surface phonon-polaritons and the previous equality implies that K is large for $\omega_s = 1.784 \times 10^{14} \text{ rad.s}^{-1}$. Plotting equation (1.19) shows that the light line $\omega = ck$ separates between the upper region where the propagative waves ($K < k_0$) exist and the lower region where the evanescent waves exist ($K > k_0$), see Fig 1.9.

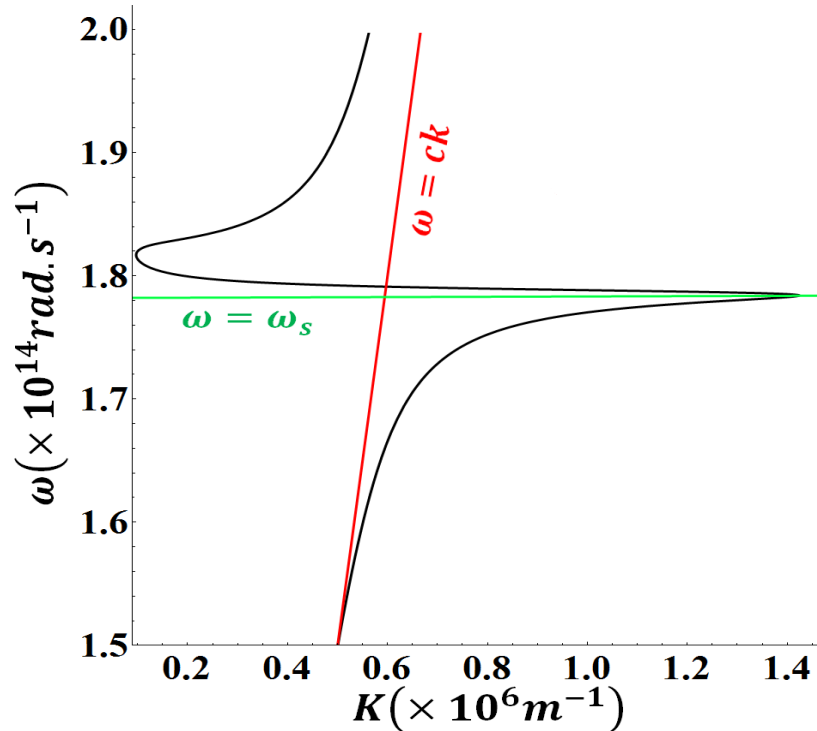


Figure 1.9: Dispersion relation for surface phonon-polaritons at a SiC–vacuum interface.

The real part of K is represented. The horizontal asymptote is situated at $\omega_s = 1.784 \times 10^{14} \text{ rad.s}^{-1}$. The oblique line represents the light line above which a wave is propagative ($K < k_0$) and below which a wave is evanescent ($K > k_0$).

We would like to end this chapter by recalling that the infinite divergence of the evanescent p polarization contribution cannot be physical at extremely small distances at which the EM fields begin to feel the microscopic variations of the matter properties. As few authors did before, This led us to take into account the nonlocal behavior of matter by introducing a nonlocal dielectric permittivity function in order to overcome this problem [17,21,23,25].

Conclusions

In this chapter we described the thermal energy and the RHT and we showed their importance in the different applications of the physical and the technological domains. We presented also the different historical attempts that aimed to predict the blackbody spectrum. We showed that Planck's law predicts correctly this spectrum and we defined Wien's law that allows calculating the wavelength at which the spectrum reaches its maximum, at any temperature T .

We continued by highlighting the importance of studying the RHT between two bodies separated by a distance d . We showed that in the far-field, i.e. when d is much larger than Wien's wavelength, the RHT is dependent on the difference of the temperatures of the bodies, to the power four. Classically, this heat transfer is maximal when the bodies act as blackbodies.

In the near-field different physical phenomena come into play and dominate the transfer, such as the tunneling evanescent waves that exist at the surface and decay in the perpendicular direction away from the surface. A consequence, the RHT between the bodies depends in this case on the separating distance d and the formula obtained for the far-field is no longer valid. Due to the different applications in the technological domains, the studies of the near-field radiative heat transfer have gained an increasing attention during the last years.

We proceeded by deriving the radiative heat flux using the radiometry approach in the far field. Then we derived the formula of the RHTC between two semi-infinite parallel planes using the fluctuation dissipation theorem. We showed that the obtained formula in the near field consists of two terms related to the contributions of the evanescent and propagative EM waves.

We then studied the variation of the RHTC between two semi-infinite parallel planes of 6H-SiC using Lorentz-Drude local model of the dielectric permittivity. We showed that the RHTC due to the p -polarized EM evanescent waves diverged as $1/d^2$ when the distance d decreases; which represents a non-physical result. We also studied the variation of the spectral energy flux and the spectral EM energy density of the p -polarized EM evanescent waves and we showed that the spectra exhibit a strong peak around the specific frequency of the surface waves, their magnitudes increase by few orders and the thermal emission becomes monochromatic as the distance d decreases. We deduced that this peak is due to the excitation of surface phonon-polariton waves which lead to the increase of the RHT.

References

1. M. Planck, *Verh. D. Phys. Ges. Berlin* **2**, 237 (1900).
2. A. Einstein, *Ann. der Phys.* **22**, 180 (1907).
3. A. Einstein, *Grundlage der allgemeinen Relativitätstheorie* (1916).
4. T. Bergman, A. Lavne, F. Incropera and D. Dewitt, “*Fundamentals of Heat and Mass Transfer*”, John Wiley & Sons Inc., Seventh Edition (2011) .
5. W. Rohsenow, J. Hartnett, Y. Cho, “*Handbook of Heat Transfer*”, McGraw-Hill Education (1998).
6. M. F. Modest, “*Radiative heat transfer*, third edition ”, Academic Press (2003).
7. R. Siegel and J. Howell, “*Thermal Radiation Heat Transfer*, fourth edition”, Taylor and Francis (2002).
8. W. Wien, *Annalen der Physik* **58**, 662-669 (1896).
9. R. Serway, C. Moses and Curt Moyer, “*Modern Physics*”, Third edition (2005).
10. P. Ben-Abdallah and K. Joulain, *Phys. Rev.B* **82**, 121419(R), (2010).
11. W. Wien, *Annalen der Physik* **52**, pp. 132-165 (1894).
12. E.G. Carvalho, C.L. Tien, and R.P. Caren, *J. Heat Transfer* **89**, 351-357 (1967).
13. D. Polder and M. Van Hove; *Phys. Rev. B* **4**, 3303-3314 (1971).
14. A. Abramson and C. Tien, *Microscale Thermophys. Eng.* **3**, 229- 244 (1999).
15. P. Galtier, Thermométrie à haute résolution ; application aux mesures thermiques sub-microniques sur composants. Paris France. Journée thématique de la SFT « Transferts radiatifs et conductifs aux courtes échelles : de l'énergétique aux nanotechnologies » (2002).
16. M. Planck; *The Theory of Heat Radiation* “Dover, New York”, Ch. 1, p:1-21 (1959).
17. A. Volokitin and B. Persson, *Phys. Rev. B* **63**, 205404 (2001).
18. J. J. Loomis and H. J. Maris, *Phys. Rev. B* **50**, 18517- 18 524 (1994).
19. A.V. Shchegrov, K. Joulain, R. Carminati, J.-J. Greffet; *Phys. Rev. Lett.* **85**, 1548-1551 (2000).
20. A. I. Volokitin and B. N. J. Persson; *Phys. Rev. B* **69**, 045417 (2004).
21. K. Joulain, J.-P. Mulet, F. Marquier, R. Carminati, and J.-J. Greffet, *Surf. Sci. Rep.* **57**, 59-112 (2005).
22. J.-P. Mulet, K. Joulain, R. Carminati, and J.-J. Greffet, *Microscale Therm. Eng.* **6**, 209–222 (2002).
23. G. Chen, *Microscale Therm. Eng.* **1**, 215-224 (1997).

24. A. Volokitin and B. Persson, *Rev. Mod. Phys.* **79**, 1291-1329 (2007).
25. C. J. Fu and Z. M. Zhang, *Int. J. Heat Mass Transfer* **49**, 1703-1718 (2006).
26. S. Basu, Z. M. Zhang, and C. J. Fu, *Int. J. Energy Res.* **33**, 1203-1232 (2009).
27. S. M. Rytov et al, *Principles of Statistical Radiophysics* “Springer, New York”, Vol. 3 (1989).
28. Z. M. Zhang, *Nano/Microscale Heat Transfer* “McGraw-Hill, New York” (2007).
29. J. Zenneck, *Ann. Phys., Lpz.* IV **23**, 846 (1907).
30. A. Sommerfeld, *Ann. Phys., Lpz.* IV **28**, 665–737 (1909).
31. C. Girard, C. Joachim and S. Gauthier, *Rep. Prog. Phys.* **63**, 893–938 (2000).
32. J. Pendry, *J. Phys. Condens. Matter* **11**, 6621-6633 (1999).
33. G. DeJean, *Wireless Evanescent Coupling and its Connection to the Latest Developments Presented by Researchers at MIT*, Microsoft Research September 27, 2007.
34. G. Binnig, H. Rohrer, C. Gerber, and E. Weibel, *Phys. Rev. Lett.* **49**, 57(1982).
35. G. Binnig and H. Rohrer, *Helv. Phys. Acta* **55** 726–30 (1982).
36. D. Pohl D, W. Denk and M. Lanz, *Appl. Phys. Lett.* **44** 651–3 (1984).
37. R. Behm, N. Garcia and H. Rohrer H (eds) 1990, *Scanning Tunnelling Microscopy and Related Methods* (NATO ASI vol E 184) (Dordrecht: Kluwer).
38. P. Descouts, H. Siegenthaler (Eds.), *Ultramicroscopy*, 42–44 (1992).
39. B. Barwick, D. Flannigan and A. Zewail, *Nature letters* **462**, 902 (2009).
40. A. Steinberg, P. Kwiat and R. Chiao, *Phys. Rev. Lett.* **71**, 708 (1993).
41. A. Enders G. and Nimtz, *J. Phys. I* (France) **2**, 1693 (1992).
42. A. Enders G. and Nimtz, *Phys. Rev. E* **48**, 632 (1993).
43. D. Mugnai, A. Ranfagni and L. Schulman, *Phys. Rev. E* **55**, 3593 (1997).
44. D. Mugnai, A. Ranfagni and L. Ronchi, *Phys. Lett. A* **247**, 281 (1998).
45. Ph. Balcou and L. Dutriaux, *Phys. Rev. Lett.* **78**, 851 (1997).
46. I. Alexeev, K. Kim and H. Milchberg, *Phys. Rev. Lett.* **88**, 073901 (2002).
47. G. Nimtz and W. Heitmann, *Prog. Quant. Electr.* **21**, 81 (1997).
48. B. Guha, C. Otey, C. B. Poitras, S. Fan, and M. Lipson; *Nano Lett.* **12**, 4546-4550 (2012).
49. J. L. Pan, H. K. Choy, and C. G. Fonstad, *IEEE Trans. Electron Devices* **47**, 241 –249 (2000).
50. M. Laroche, R. Carminati, and J.-J. Greffet; *J. Appl. Phys.* **100**, 063704 (2006).
51. W. Srituravanich, N. Fang, C. Sun, and X. Zhang; *Nano Lett.* **4**, 1085-1088 (2004).

52. B. J. Lee, Y. B. Chen, and Z. M. Zhang, *J. Quant. Spectrosc. Radiat. Transfer* **109**, 608-619 (2008).
53. L. Martin-Moreno, F. J. García-Vidal, H. J. Lezec, A. Degiron, and T. W. Ebbesen, *Phys. Rev. Lett.* **90**, 167401 (2003).
54. P. O. Chapuis, S. Volz, C. Henkel, K. Joulain and J.-J. Greffet; *Phys. Rev. B* **77**, 035431 (2008).
55. C. M. Hargreaves, *Phys. Lett.* **30A**, 491 (1969).
56. E. Rousseau et al, *Nat. Photonics* **3**, 514-517 (2009).
57. L. Hu, A. Narayanaswamy, X. Chen and G. Chen, *Appl. Phys. Lett.* **92**, 133106 (2008).
58. G. A. Domoto, R. F. Boehm, and C. L. Tien, *J. Heat Transfer* **92**, 412-416 (1970).
59. A. Kittel, W. Müller-Hirsch, J. Parisi, S.A. Biehs, D. Reddig, and M. Holthaus, *Phys. Rev. Lett.* **95**, 224301 (2005).
60. T. Kralik, P. Hanzelka, M. Zobac, V. Musilova, T. Fort, and M. Horak, *Phys. Rev. Lett.* **109**, 224302 (2012).
61. C. Henkel and K. Joulain, *Appl. Phys. B* **84**, 61-68 (2006).
62. S. Rytov, *Sov. Phys. JETP* **6**, 130-140 (1958).
63. M. Levin, V. Polevoi, and S. Rytov, *Sov. Phys. JETP* **52**, 1054 (1981).
64. I. Dorofeev, *Tech. Phys. Lett.* **23**, 109 (1997).
65. J. Pendry, *J. Phys. Condens. Matter* **11**, 6621-6633 (1999).
66. J. J. Hopfield and D. G. Thomas, *Phys. Rev.* **132**, 563 (1963).
67. K. Joulain, "Radiative Transfer on Short Length Scales", Part II in "Microscale and Nanoscale Heat Transfer" Ed. by S. Volz, Springer (2007).
68. K. L. Kliewer and R. Fuchs; *Advance in Chemical Physics*, Volume XXVII .Ed. by I. Prigogine, Stuart A. Rice, John Wiley & Sons. Inc. (1974).
69. R. Willardson and E. Weber, *SiC Materials and Devices*, Vol. **52** (1998).
70. W. G. Spitzer, D. Kleinman, and D. Walsh, *Phys. Rev.* **113**, 127(1959).
71. W.J. Choyke and L. Patrick, in *Silicon Carbide*(1973), ed. R. C. Marshall, J. W. Faust, Jr. and C. E. Ryan, University of South Carolina Press, Columbia, SC (1974), p. 261.
72. E. Palik, *Handbook of Optical Constants*, Vol. **1** (1985).
73. W.J. Choyke and R.P. Devaty, *Diamond and Related Materials* **6**, 1243-1248 (1997).
74. D.W. Feldman, J.H. Parker, W.J. Choyke and L. Patrick, *Phys.Rev.* **170**, 698-704(1968).

75. D.W. Feldman, J.H. Parker, W.J. Choyke and L. Patrick, *Phys.Rev.* **173**, 787-793 (1968).
76. Landoldt-Bornstein, in *Numerical Data and Functional Relationships in Science and Technology*, Vol. **22a**, ed. O. Madelung, Springer, Berlin (1986).
77. *Thermophysical Properties of High Temperature Solid Materials*, Vol. **5**, ed. Y. S. Touloukian; The Macmillan Company, New York, NY (1969).
78. Crystal Lattice Dynamics of Various Silicon-Carbide Polytypes (*International Conference on Solid State Crystals 2000: Growth, Characterization, and Applications of Single Crystals Held in Zakopane, 2000*).

Chapter 2

2. Theory of the nonlocal model of the dielectric permittivity for metals

Introduction

In this chapter, we recall the calculations performed by Chapuis et al. [1] to study the RHT between two metallic semi-infinite parallel planes using a nonlocal dielectric model as the inter-planar distance tends to zero.

In the first section we recall the calculations of the RHTC between two aluminum (Al) semi-infinite parallel planes separated by a gap distance d , upon using a local model of the dielectric permittivity (Drude model). We show that the contribution of the p -polarized evanescent waves to the RHTC diverges as $1/d^2$ when d tends to zero. The contribution of the s -polarized evanescent waves to the RHTC is dominant and saturates starting from distances of the order of the skin depth. These obtained results are in agreement with those obtained from the experimental studies carried by Kittel et al. [2]. These experiments studied the near field radiation transfer between a tip and a metallic plane and showed that for metals the RHTC saturates at a distance of the order of some tens of nanometer. This confirms the dominance of the contribution of the s polarization.

In the second section we will repeat the calculations using the Lindhard-Mermin nonlocal model of the dielectric permittivity that account for the spatial dispersion. We show that the contribution of the p -polarized evanescent waves to the RHTC deviates from the diverging graph of the local model at distances of the order of the Thomas-Fermi length; after which saturation takes place.

2.1 Recall of the Local dielectric permittivity: Drude model

The early studies of the RHT between two metallic materials had shown divergence of the radiative flux as the distance between the materials decreases. Similar to the dielectrics case, local models of the dielectric permittivity of metals were considered and the large increase of the RHT was attributed to the tunneling evanescent waves between the surfaces of the considered metallic materials.

Polder and Van Hove [3] were among the first to study theoretically the RHT in the near-field especially for the case of two macroscopic metallic bodies separated by a distance d . They followed the same formalism of Rytov [4,5] i.e. the fluctuational electrodynamics and their study showed that the RHT between closely spaced bodies differs significantly from that when the separation distance is large; they also showed that for metallic bodies the dominant mechanism of energy transfer is the tunneling evanescent waves giving rise to a strong increase of RHT as d decreases. Polder and Van Hove compared their results to the experimental results obtained by C. M. Hargreaves [6] as their measurements show the existence of a proximity effect on the RHT between two Chromium coated plates due to the dominance of the near-field coupling over cut-off effects at small distances.

Loomis and Maris [7] have shown that for sufficiently small distances d the heat flow is enhanced by the contribution of the tunneling evanescent waves, and varies as $1/d^2$ in the limit of very small d . Volokitin and Persson [8] studied the RHT between two bodies and its dependence on the dielectric properties of the media and they found that the RHF significantly enhanced at short distances between bodies, as compared to the blackbody radiation. As for metals, they showed that the radiated flux is enhanced when the metallic surfaces support low-frequency surface plasmons. Mulet et al. [9] and Joulain et al. [10] had shown that in the near-field the RHT is enhanced due to the tunneling of the EM evanescent waves. The density of the EM energy increases in the near field due to the contribution of surface waves and the local treatment of the NFRHT leads to obtaining the infinitely diverging RHTC between two bodies. Francoeur et al. [11] have shown that the NFRHT is enhanced around resonance of surface phonon polaritons for thin film emitters due to the surface wave coupling and consequently the total radiative heat flux increases in a very narrow spectral range as compared to a bulk emitter.

Kittel et al. [2] studied the NFRHT experimentally using the scanning thermal microscope (STM). They measured the NFHT between a metallic tip and a metallic planar surface as they

varied the distance between them. They showed that for distances larger than 10 nanometers their results were in good agreement with theoretical predictions of the RHT using the macroscopic theory based on fluctuational electrodynamics. For distances below $10^{-8}m$, their results differed significantly from the predictions of the macroscopic theory as their measurements showed saturation of the RHT in the extreme near-field limit, contrary to the infinite divergence obtained by the macroscopic theory. They explained that these differences are due to the existence of a material-dependent small length scale below which the macroscopic description of the dielectric properties fails; they mentioned that nonlocal effects should be taken into consideration by representing them in a nonlocal model of the dielectric permittivity. Few years later it was shown by Chapuis et al. [1] that the contribution of the s-polarized EM waves to the RHTC between two metallic planes had saturated in a behavior and at a scale similar to those reported by Kittel et al. [2] experimental results. Chapuis et al. showed that this saturation occurred upon considering local model of the dielectric permittivity, i.e. nonlocal effects are not important to obtain these results.

Narayanaswamy et al. [12] presented another sensitive technique of measuring near-field radiative transfer between a Silica microsphere and a flat substrate, which was considered a glass microscope slide. Their measurements lead to concluding that strong near-field effects result in the enhancement of the heat transfer over the predictions of the Planck blackbody radiation theory.

Rousseau et al. [13] conducted an experimental work involving a sphere-plane geometry of two dielectric polar materials that allows measuring the conductance for gaps varying between 30 nm and 2.5 mm. They have shown that their obtained results agreed well with the theory in the considered gap range, which confirms the significant enhancement of the radiative heat transfer at nano-scaled distances.

These results supported the fact that the RHT is enhanced in the near field and diverged till exceeding the far-field limit by many orders of magnitude. This also provoked the idea that the infinite divergence of the RHTC between two planes obtained at extremely small distances should be investigated with an appropriate theoretical model in order to obtain a physical finite saturation. Therefore, saturation of the RHTC between two parallel metallic planes could be attained upon considering a nonlocal model of the dielectric permittivity in the theoretical study. This will be done in section two; in this section, we study the RHTC between two Al semi-infinite parallel planes separated by a gap distance d , using the local Drude model for the dielectric permittivity expression. We will show via this study the huge

increase of the RHF between the two planes as the distance decreases below the thermal wavelength.

2.1.1 Formalism

We will carry on our study of the RHT by considering two semi-infinite parallel Aluminum planes separated by a vacuum gap of width d (see Fig. 1.5) where the average temperature of the system is $T=300K$ ($T_1 = 300.5K$ and $T_2 = 299.5K$).

Similar to the case of dielectrics, considering the medium to be local implies using a frequency-dependent dielectric permittivity function that describes the local optical response of the medium.

From a classical point of view, the frequency-dependent dielectric permittivity of metals can be described with a Drude model which determines the material's dielectric response by considering the motion of the free electrons with respect to a background of positive ion cores. The dielectric permittivity is then expressed as [1,10,14]:

$$\varepsilon(\omega) = \varepsilon_b - \frac{\omega_p^2}{\omega(\omega + i\nu)} \quad (2.1)$$

where $\omega_p = 2.24 \times 10^{16} s^{-1}$ is the plasma frequency which is a material property that is based on the density of conduction electrons. ε_b is a corrective constant that accounts for the background electron screening at high frequency and in the case of Aluminum it is equal to 2. $\nu = 1.22 \times 10^{14} s^{-1}$ is the damping factor accounting for losses as it represents the scattering frequency of the electron as it travels through the metal [1].

2.1.2 Calculation of the radiative heat transfer coefficient

Calculating the RHTC requires the substitution with the equations of the reflection factors of the EM waves at the interfaces. The surface impedances and the reflection factors general expressions are given in chapter one by Eqs. (1.16) and Eqs. (1.15), respectively. As we showed in the local case of dielectrics in the previous chapter, these equations are simplified due to the locality condition considering the static limit ($\varepsilon(\omega) = \lim_{k \rightarrow 0} \varepsilon_t(k, \omega) = \lim_{k \rightarrow 0} \varepsilon_l(k, \omega)$). This will eventually lead to obtaining Fresnel reflection factors Eqs. (1.18). Substituting with the reflection factor equations and the dielectric permittivity equation in the RHTC expression Eq. (1.13), we obtained the graphs representing the different contributions of s and p polarized EM waves to the RHTC.

In Fig. 2.1 we present the different contributions of the EM waves of both s and p polarizations to the RHTC for the local case.

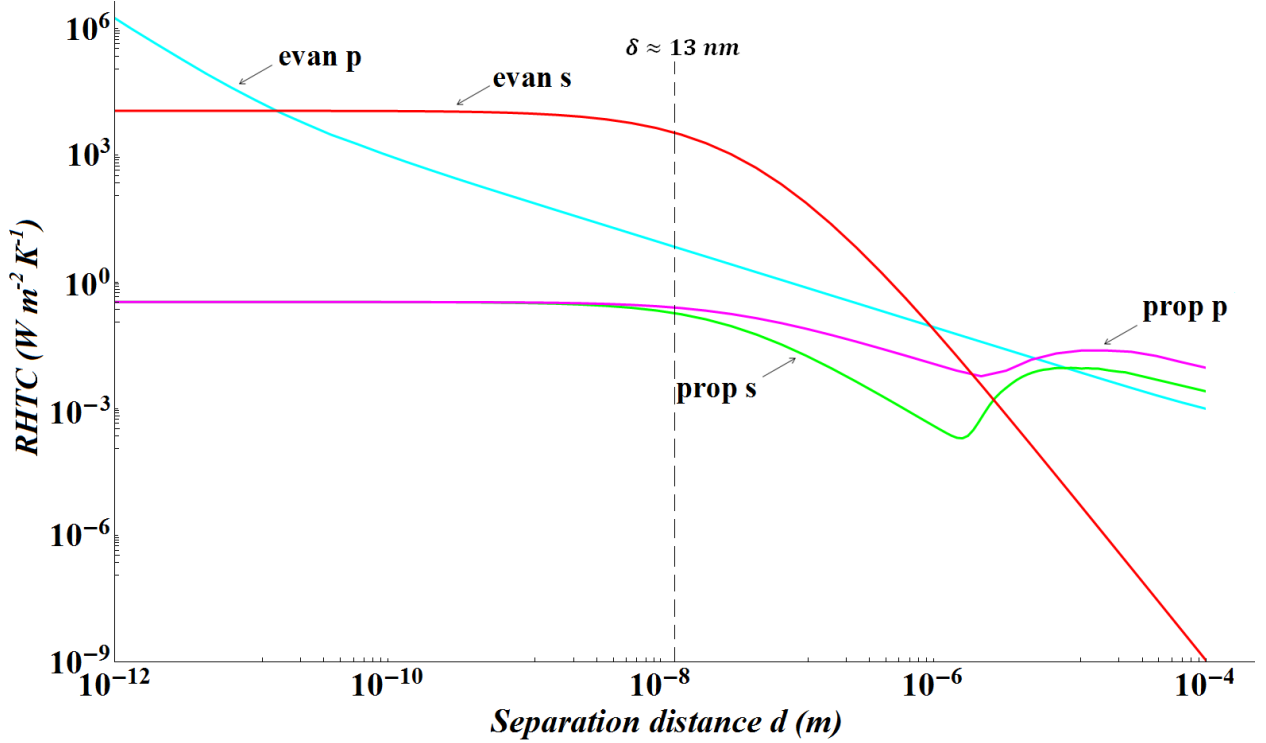


Figure 2.1: Variation of the radiative heat transfer coefficient (contributions of evanescent and propagative EM waves of s and p polarizations) between two semi-infinite Al parallel planes of average temperature $T=300\text{K}$, for the local model case. The contribution of the s -polarized evanescent waves saturates at a distance d of the order of the skin depth $\delta \approx c/\omega_p = 13 \text{ nm}$.

We observe in Fig. 2.1 that the contributions of the propagative waves of both s and p polarizations saturate as the distance decreases. At large distances, the transmission factor of these waves $\frac{(1-|r_{31}^\alpha|^2)(1-|r_{32}^\alpha|^2)}{|1-r_{31}^\alpha r_{32}^\alpha e^{2i\gamma_3 d}|^2}$ is independent of d , and for small distances where the wavelength is much larger than d , $\gamma_3 \approx \text{Re}(\gamma_3)$ which implies that $e^{2i\gamma_3 d} \approx e^{-2\gamma_3'' d} \approx 1$ and their contribution saturate with values relatively small, compared to the evanescent waves contribution.

On the other hand, we observe in this figure that the contribution of the s -polarized evanescent waves dominates the transfer till reaching distances as short as 0.01 nm below which the contribution of the evanescent EM waves of p -polarization dominates. The former saturated at short distances, while the latter diverged. To interpret these results, we derived the limits of the reflection factors as K increases because the RHTC is dominated by the imaginary parts of the reflection factors. Starting with Fresnel reflection equation of the s -

polarized waves we obtained $r_{3m}^S \approx \omega^2 \omega_p^2 \nu / [4c^2 K^2 \omega (\omega^2 + \nu^2)]$ which shows the same dependence on K (at large K) as the general limit obtained in chapter 1: $r_{3m}^S = (\varepsilon - 1)/4(K/k_0)^2$ (see Appendix C for derivation). From this expression we deduce that the imaginary part of r_s tends to zero as $1/K^2$ which explains the saturation of the contribution of the s-polarized evanescent waves to the RHTC at small distances. We notice in Fig 2.1 that this saturation starts at a distance d of the order of the skin depth $\delta \approx c/\omega_p = 13 \text{ nm}$ [1]. This could be deduced analytically by considering the general equation of the parallel wavevector in the medium: $K^2 + \gamma_1^2 = \varepsilon(\omega)k_0^2$. There exists a cutoff value of K after which saturation of the RHTC takes place, and by denoting it as K_c , saturation takes place for all wavevectors $K \geq K_c$. As we mentioned before, at small distances the waves with large wavevectors K dominate the transfer, i.e. $K^2 \approx \varepsilon(\omega)k_0^2$, so that $K_c \approx k_0 \sqrt{|\varepsilon(\omega)|}$ leading finally to obtaining $K_c \approx \frac{\omega_p}{c} \sqrt{\omega/|\omega + i\nu|}$. From this equation we deduce that the cutoff wavevector value after which saturation of the contribution of the s-polarized waves takes place for all larger wavevectors, is proportional to the inverse of the skin depth δ and the distance at which this saturation starts is of the order of the skin depth i.e. $d_c \approx \delta$. This result is consistent with the experimental result obtained by Kittel et al. [2] where the distances at which a cutoff of the diverging RHT was observed are of the order of the skin depth.

Furthermore, to interpret the divergence of the contribution of the p-polarized evanescent waves, we calculate the limit of the reflection factor r^P for large K . We obtained $r_{3m}^P \approx \omega \nu \omega_{sp}^2 (R + 1) / [(\omega_{sp}^2 - \omega^2)^2 + \omega^2 \nu^2]$ where $\omega_{sp} = \omega_p / \sqrt{2}$ is the surface plasmon-polariton excitation frequency, $R = (\varepsilon_b - \varepsilon_3) / (\varepsilon_b + \varepsilon_3)$ and $\varepsilon_3 = 1$ in our case. From this expression we deduce that the reflection factor is finite for large K . It follows eventually that the imaginary part of this reflection factor is also finite, and since it dominates the transmission factor of the p-polarized evanescent waves, their contribution to the RHTC diverges at small distances.

2.2 Lindhard–Mermin nonlocal model for metals

In this section we will follow the same procedure of section 2.1.1 but with a nonlocal model of the dielectric permittivity accounting for spatial dependence in the medium in which the dielectric permittivity function is of frequency and wavevector dependence i.e. $\varepsilon = \varepsilon(\omega, k)$.

The model used is the Lindhard–Mermin nonlocal model extended by Mermin [15] from the longitudinal dielectric constant derived by Lindhard [16]. This longitudinal term is considered collisionless, and that’s what drove Mermin to use the relaxation-time approximation to account for the collisions in the electron gas. The longitudinal term expression obtained by Mermin combined with the transverse term derived by Ford and Weber [17] form the nonlocal dielectric model used in this chapter.

Ford and Weber [17] then showed how this model is suitable to describe the nonlocality of a metallic medium when they applied it in their study of the EM interactions of molecules with metal surfaces. They showed that the expression of the dielectric permittivity given by this nonlocal model is deduced when considering the quantum infinite barrier model of the metal in their studies. It is a generalized extension of the semi-classical infinite barrier model in which the equations of the latter are obtained from those of the former by considering the semi-classical limit ($k \rightarrow 0$).

We will show that the unphysical divergence of the RHTC at small distances obtained in the local case is removed in the nonlocal case as saturation is obtained for all the contributions of the waves of s and p polarizations.

2.2.1 Formalism

Considering the classical EM theory in their study, Ford and Weber [17] aimed to describe the EM interactions of molecules with metal surfaces. In their discussion of the reflection of EM waves at a plane interface, they imposed the necessity of extending the classical Fresnel formulas to the case of a nonlocal medium, which is considered as the basic theoretical concept in the discussion of different various phenomena explained in their review. To calculate the surface response of a metal, they considered first the semi-classical infinite barrier model, in which the electron density is uniform up to the barrier, where it abruptly goes to zero. In this model, specular reflection of the conduction electrons at the metal surface is considered, as well as the anomalous skin effect. The conduction electrons are then treated as a classical ideal gas, but with Fermi–Dirac statistics. The behavior of a metal with conditions of purity and low temperature that the high-frequency oscillations of the electric field and current are confined within a surface layer of thickness much smaller than the mean free path of electrons is called the anomalous skin effect. The field strength decays steadily within a depth called the skin depth and is denoted by δ . The value of δ differs from one metal to the other [18,19].

Due to this nonlocal model, they needed to derive the appropriate generalized formulas of the classical Fresnel formulas by introducing the concept of surface impedances, which are then used to construct the reflection coefficients suitable for the nonlocal model of a metal. Ford and Weber used the surface impedances defined by Landau and Lifshitz [20] and by Garcia-Moliner and Flores [21] that depend on the description of the considered nonlocal medium. To continue their calculations, it was essential to use nonlocal equations of the dielectric permittivity in which they chose the Lindhard-Mermin equations simplified in the semi-classical limit.

Extending their study to the quantum infinite barrier model, in which the electron density undergoes Friedel-type oscillations near the surface and goes smoothly to zero at the barrier, they used the general equations of the Lindhard-Mermin nonlocal dielectric permittivity model as to well describe the system. Friedel-type oscillations take place due to localized perturbations in a metallic system caused by a defect in the Fermi gas or Fermi Liquid, where the decay of the oscillations density is induced by the defect. They could be defined as being the formation of a rippling pattern of electrons around a stationary charge. They can be observed on metal surfaces using STM [22].

The Lindhard-Mermin nonlocal model of the dielectric permittivity consists of two separate components, longitudinal and transversal, both of spatial and temporal dependence. By following Ford and Weber notations [17] they are defined as:

$$\left\{ \begin{array}{l} \varepsilon_{LM}^l(\omega, z) = \varepsilon_b + \frac{3\omega_p^2}{\omega + i\nu} \frac{u^2}{\{\omega + i\nu [f_l(z, u)/f_l(z, 0)]\}} \\ \varepsilon_{LM}^t(\omega, z) = \varepsilon_b - \frac{\omega_p^2}{\omega^2(\omega + i\nu)} \{\omega [f_t(z, u) - 3z^2 f_l(z, u)] + i\nu [f_t(z, 0) - 3z^2 f_l(z, 0)]\} \end{array} \right\} \quad (2.2)$$

with

$$\left\{ \begin{array}{l} z = k/2k_F \\ u = (\omega + i\nu)/kv_F \\ f_l(z, u) = 1/2 + [1 - (z - u)^2/8z] \ln(z - u + 1/z - u - 1) + \\ \quad [1 - (z + u)^2/8z] \ln(z + u + 1/z + u - 1) \\ f_t(z, u) = 3/8 (z^2 + 3z^2 + 1) - \{3 [1 - (z - u)^2]^2/32z\} \ln(z - u + 1/z - u - 1) - \\ \quad \{3 [1 - (z + u)^2]^2/32z\} \ln(z + u + 1/z + u - 1) \\ f_l(z, 0) = 1/2 + (1 - z^2/4z) \ln|z + 1/z - 1| \\ f_t(z, 0) = 3/8 (z^2 + 1) - [3(1 - z^2)^2/16z] \ln|z + 1/z - 1| \end{array} \right\} \quad (2.3)$$

Where k_F and v_F are the Fermi wavevector and the Fermi velocity, respectively. For the case of Al, $k_F \approx 10^{10} m^{-1}$ and $v_F \approx 2.03 \times 10^6 m.s^{-1}$ ($\frac{c}{v_F} = 148$) [1,23]. These equations were first obtained by Lindhard [16] for the special case $\nu = 0$ and $\varepsilon_b = 1$.

We note here that for small k limit, the Lindhard–Mermin equations give the local equations in which we retrieve the local Drude model given in section 2.1.1 Eq. (2.1) as the spatial dependence is eliminated in this case.

2.2.2 Calculation of the radiative heat transfer coefficient

The equations of the impedances and the reflection factors needed to perform the calculations of the RHTC, are those considered in chapter 1 (Eqs. (1.15) and Eqs. (1.16), respectively), as they are the general equations including temporal and spatial dependence and accounting for the specular reflection of the conduction electrons.

By substituting these equations in the expression of the RHTC Eqs. (1.13) we calculated the different contributions of s and p polarizations to the RHTC between the two semi-infinite parallel Al planes as the distance between them tends to zero.

In Fig. 2.2 we present the contributions of the evanescent EM waves of s and p polarizations to the RHTC using the nonlocal Lindhard–Mermin dielectric permittivity model. The first thing to notice in this figure is that both evanescent contributions saturate to a finite value. The contribution of the evanescent waves of s polarization saturates as in the local case with almost no change in values. This implies that the nonlocality imposes no significant changes on the s -polarized evanescent waves as they are dominant at relatively large distances. The saturation obtained for the p -polarized evanescent waves replaces the infinite divergence obtained in the local case, as we showed in Fig. 2.1, and this result is considered the most important feature revealed by Fig. 2.2. Before we interpret this result, we will examine the differences between the graphs obtained in the local and the nonlocal cases by plotting them in the same figure, Fig 2.3.

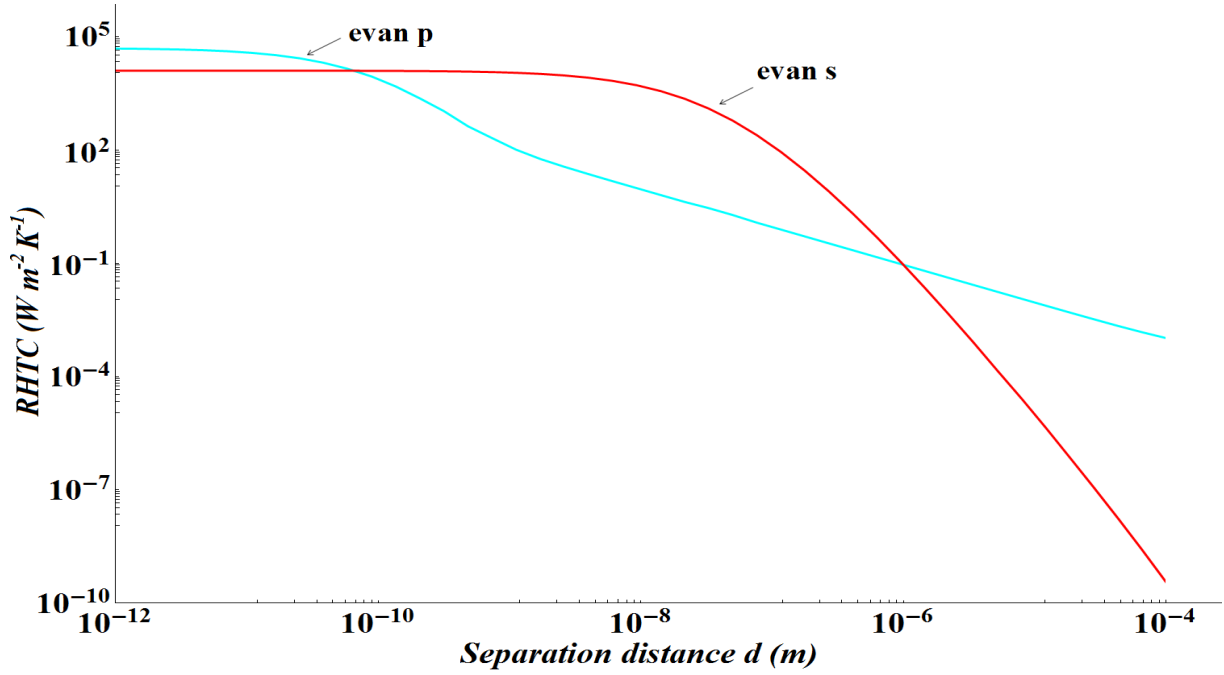


Figure 2.2: Variation of the radiative heat transfer coefficient (contributions of the evanescent EM waves of s and p polarizations) between two semi-infinite Al parallel planes of average temperature $T=300K$, for the Lindhard–Mermin nonlocal model case.

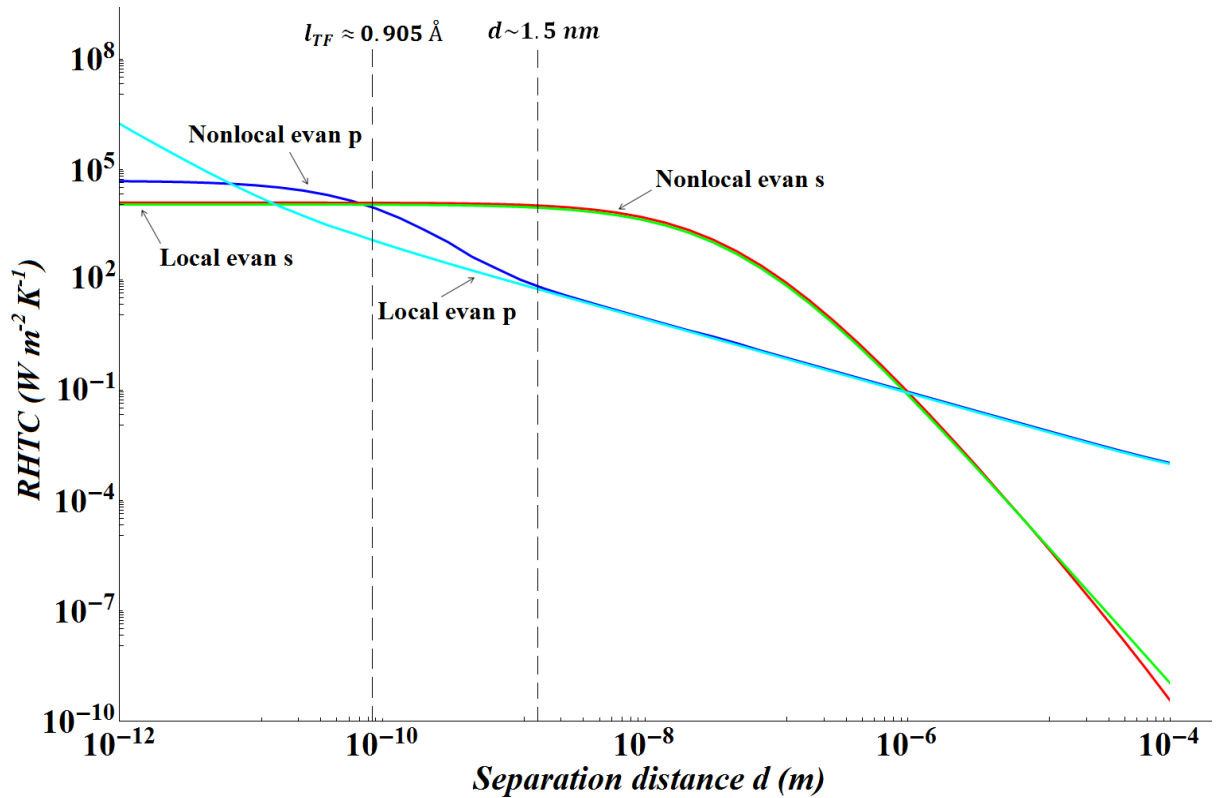


Figure 2.3: Variation of the radiative heat transfer coefficient (contributions of evanescent EM waves of s and p polarizations) between two semi-infinite Al parallel planes of average temperature $T=300K$, for the local and the nonlocal model cases. The graphs of both models overlap up to a distance d of the order of 1.5 nm , and the graph of the nonlocal model saturates starting from a distance of the order of the Thomas–Fermi length $l_{TF} = 0.905\text{ \AA}$.

It is important to note that representing our results for distances as small as $10^{-12}m$ is just to show that our nonlocal model would lead mathematically to saturation at these small distances scales. We are aware that from a physical point of view, for distances of the order of few angstroms and less where quantum effects appear [24], a correct study must take these effects into consideration. Regarding this thesis, we are only interested in the EM approach that is sufficient for distances larger than few angstroms. We notice in Fig. 2.3 that up to a distance d of the order of 1.5 nm the graphs of the contributions of the evanescent EM waves of p -polarization of both the local and the nonlocal models overlap, after which the graph of the nonlocal model deviates from the local graph and it saturates starting from a distance of the order of the Thomas–Fermi length $l_{TF} = v_F/\omega_p = 0.905 \text{ \AA}$.

To give a better interpretation of the obtained results, we study the plot of the transmission coefficient of the p -polarized EM evanescent waves $4(Im(r_{31}^P))^2 e^{2i\gamma_3 d} / |1 - (r_{31}^P)^2 e^{2i\gamma_3 d}|^2$ in the local and the nonlocal cases at a distance $d = 10^{-12}m$ Fig. 2.4.

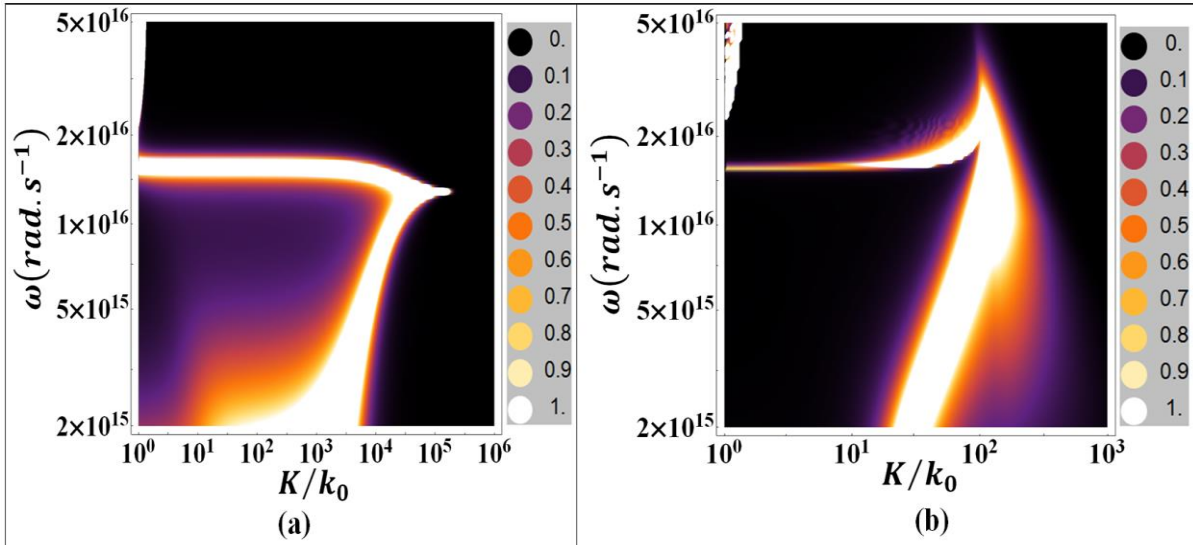


Figure 2.4: Plot of the transmission coefficient $4(Im(r_{31}^P))^2 e^{2i\gamma_3 d} / |1 - (r_{31}^P)^2 e^{2i\gamma_3 d}|^2$ of the p -polarized EM evanescent waves in the plane (ω, K) for the local model case (a) and the nonlocal case of Lindhard–Mermin model (b) at a separation distance $d = 10^{-12}m$.

From Fig. 2.4, we notice in the local case that the graph is wide and as K increases its values increase. This implies that as K increases, the number of modes contributing to the transfer increases also. The transmission factor acquires high values even for relatively very large wavevectors K . This explains the divergence of the RHTC due to the contribution of the p -polarized EM evanescent waves at small distances. In the nonlocal case we notice that the

graph is relatively narrow and it shows an increase in the values as K increases, but when K is of the order of the inverse of the Thomas–Fermi length ($K \cong 2 \times 10^2 k_0 \approx K_{TF} \approx 1.105 \times 10^{10} m^{-1}$), a cutoff removes the continuous increase of the transmission factor spectrum. For further increase in the values of K , the spectrum acquires negligible values. This cutoff confirms the saturation of the RHTC shown in Fig 2.3 starting from distances of the order of l_{TF} .

Conclusions

We presented in this chapter the study of the RHTC between two semi-infinite parallel aluminum planes separated by a vacuum gap of width d .

In the first section, we considered the local Drude model in which the dielectric permittivity is of temporal dependence and we showed that by substituting with this equation in the RHTC expression, the evanescent term of p polarization diverges as $1/d^2$ in an unphysical infinite tendency while all other contributions saturate as the distance d decreased. The saturation of the contribution of the evanescent waves of s polarization starts at a distance of the order of the skin depth.

In the second section, we repeated the calculations using the Lindhard–Mermin nonlocal model for the dielectric permittivity. This model is of temporal and spatial dependence and by applying it to the study of the RHTC, we obtained saturation of the evanescent p term while all other terms showed no significant change in values. We observed that the nonlocal contribution of the p -polarized evanescent waves coincides with that of the local contribution until reaching a distance of the order of 1.5 nm, and the saturation takes place for distances smaller than Thomas–Fermi length.

We compared also between the plots of the transmission factors of the evanescent p terms in both the local and the nonlocal cases to better examine the differences. We observed a continuous increase of the spectrum in the local case whereas the nonlocal spectrum increases until it reaches a cutoff at a K value of the order of the inverse of the Thomas–Fermi length which explains the saturation obtained for the RHTC at distances of the order of Thomas–Fermi length.

References

1. P. O. Chapuis, S. Volz, C. Henkel, K. Joulain and J.-J. Greffet; *Phys. Rev. B* **77**, 035431 (2008).
2. A. Kittel, W. Müller-Hirsch, J. Parisi, S.A. Biehs, D. Reddig, and M. Holthaus, *Phys. Rev. Lett.* **95**, 224301 (2005).
3. D. Polder and M. Van Hove, *Phys. Rev. B* **4**, 3303-3314 (1971).
4. S. Rytov, *Sov. Phys. JETP* **6**, 130-140 (1958).
5. S. M. Rytov et al, *Principles of Statistical Radiophysics* “Springer, New York”, Vol. 3 (1989).
6. C. M. Hargreaves, *Phys. Lett.* **30A**, 491 (1969).
7. J. J. Loomis and H. J. Maris, *Phys. Rev. B* **50**, 18517- 18 524 (1994).
8. A. I. Volokitin and B. N. J. Persson, *Phys. Rev. B* **69**, 045417 (2004).
9. J. P. Mulet, K. Joulain, R. Carminati, and J.-J. Greffet, *Microscale Thermophys. Eng.* **6**, 209-222 (2002).
10. K. Joulain, J.-P. Mulet, F. Marquier, R. Carminati, and J.-J. Greffet, *Surf. Sci. Rep.* **57**, 59-112 (2005).
11. M. Francoeur, M. Pinar Mengüç, and R. Vaillon, *Appl. Phys. Lett.* **93**, 043109 (2008).
12. A. Narayanaswamy, S. Shen and G. Chen, *Phys. Rev. B* **78**, 115303 (2008).
13. E. Rousseau et al, *Nat. Photonics* **3**, 514-517 (2009).
14. E. Palik, *Handbook of Optical Constants*, Vol. 1 (1985).
15. N. D. Mermin, *Phys. Rev. B* **1**, 2362 (1970).
16. J. Lindhard, Kgl. Danske Videnskab. Selskab, *Mat.-Fys. Medd.* **28**, 8 (1954).
17. G. W. Ford and W. H. Weber, *Phys. Rep.* **113**, 195 (1984). We note a mistake in formula 2.29 corrected, for example, in Ref. 25.
18. G. Reuter and E. Sondheimer, *Proc. R. Soc. Lond. A* **195**, 336(1948).
19. A. Pippard, *Proc. R. Soc. Lond. A* **224**, 273(1954).
20. L.D. Landau and E.M. Lifshitz, *Electrodynamics of Continuous Media* (Pergamon Press, Oxford,1960).
21. F. Garcia-Moliner and F. Flores, *Introduction to the theory of solid surfaces*, Cambridge U. Press, Cambridge (1979).
22. W. A. Harrison, *Solid State Theory*, New York: Dover Publication (1979).
23. N. W. Ashcroft and N. D. Mermin, *Solid State Physics*, Holt, Rinehart and Winston, New York, (1976).
24. H. Duan, A. I. Fernandez-Domínguez, M. Bosman, S. Maier, and J. Yang, *Nano Lett.* **12**, 1683 (2012).
25. R. Esquivel and V. B. Svetovoy, *Phys. Rev. A* **69**, 062102 (2004).

Chapter 3

3. Nonlocal models of the dielectric permittivity for semiconductors

Introduction

In Chapter 1, we presented the study of the RHT between two semi-infinite parallel solid 6H-SiC planes separated by a vacuum gap of width d , using a local model of the dielectric permittivity. We showed that as the separation distance decreases till reaching few nanometers, the RHTC diverged as $1/d^2$. As we explained in chapter 1, this infinite divergence of the RHTC as d tends to zero is considered nonphysical because the transfer of energy between two bodies could not be infinite. We have also shown that this infinite divergence is obtained due to the local model of the dielectric permittivity used; which leads us to consider applying a nonlocal model of the dielectric permittivity as to obtain saturation of the RHTC.

This is therefore the aim of the work presented in this chapter, where we present three different nonlocal models of the dielectric permittivity of relatively simple nonlocality concepts. We then show that applying these models in the calculation of the RHTC between the two 6H-SiC planes leads to the saturation of the RHTC in the three different cases.

For the case of dielectrics, only few nonlocal models of the dielectric permittivity were suggested, and as far as we know, our proposed models are the first to well apply in the RHT study and to lead to a RHT saturation. Our models are the first to be based on simple physical nonlocal concepts, and the first to be handled in a simple algebraic and analytic way.

The authors who worked on proposing a suitable nonlocal model of the dielectric permittivity for dielectrics aimed in the first place to include the spatial dispersion effects in the equations of the dielectric permittivity or the inverse of the dielectric permittivity; thus the concluded expressions were of ω and k dependences [1–6]. Different basis were set for these different proposed nonlocal models such as the random phase approximation (RPA) [2,3] where the Lindhard dielectric equation is used throughout some modelings [1], and the

quantum mechanical perturbation theory [4], etc. Some of these models have not been given a clear derivation, while one common thing among all of them is the complexity of their structure which led to the difficulty of handling them algebraically and numerically in our study. For this reason, we aimed to suggest simple nonlocal models of the dielectric permittivity, which allow us to calculate in an easy numerical and analytical way the RHTC between two dielectric semi-infinite parallel planes in general and in particular the case of our study, the 6H-SiC planes.

This chapter will be divided into three sections; each one will be devoted to the study of the RHTC between two semi-infinite parallel planes of 6H-SiC using one of the three suggested nonlocal models of the dielectric permittivity function.

3.1 A suggested nonlocal model of the dielectric permittivity

This model is relatively simple and it was inspired from the nonlocal model derived by Kliewer and Fuchs [5].

In their review, Kliewer and Fuchs considered the surface of the semi-infinite medium to scatter the field specularly and they aimed in the first place to analyze the dispersion relation of surface optical phonons of semi-infinite ionic crystals Eq. (3.1).

$$\omega = \omega_{TO} \sqrt{A + B \left(\cos \left(\frac{\pi q}{q_B} \right) - 1 \right)} \quad (3.1)$$

where $\omega_{TO} = 1.49 \times 10^{14} \text{rad.s}^{-1}$ is the transverse optical phonon frequency, $q_B = \pi/r_0$ is the value of the perpendicular wavevector at the limit of the first Brillouin zone (FBZ) and $r_0 \approx 1.5 \text{ nm}$ is the lattice constant. The plot of the dispersion relation Eq. (3.1) is shown in Fig 3.1.

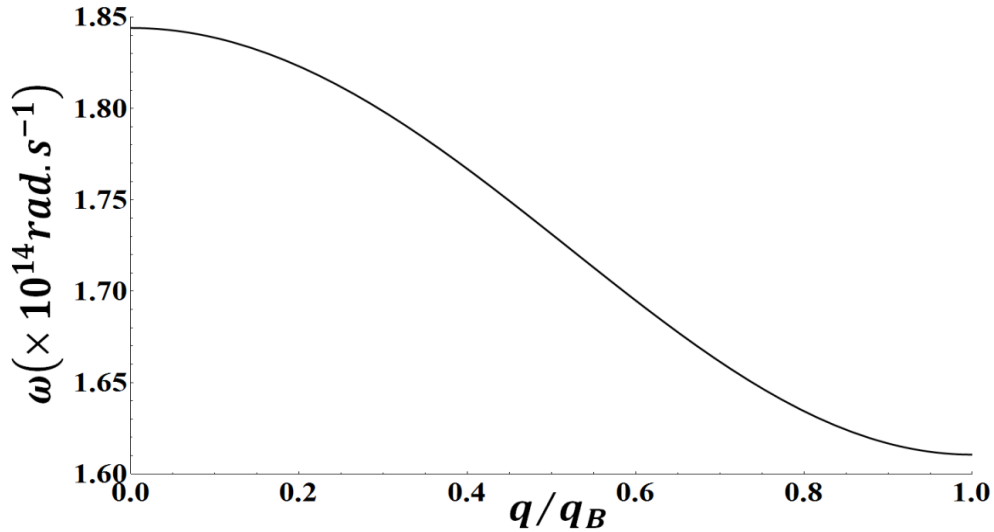


Figure 3.1: The dispersion relation of surface optical phonons of semi-infinite ionic crystals as given by Kliewer and Fuchs [5].

3.1.1 Formalism

Considering the dielectric permittivity of the semi-infinite medium to consist of two terms, longitudinal and transverse, they suggested the following model, Eqs. (3.2), from which the dispersion equation is deduced.

$$\left\{ \begin{array}{l} \varepsilon_t(\omega) = \varepsilon_{local} = 1 + \frac{A - 1}{1 - \Omega(\Omega + i\Gamma)} \\ \varepsilon_l(k, \omega) = 1 + \frac{A - 1}{1 - \Omega(\Omega + i\Gamma) + B \left(\cos\left(\frac{\pi q}{q_B}\right) - 1 \right)} \end{array} \quad \forall q \leq q_B \right\} \quad (3.2)$$

where $\Omega = \omega/\omega_{TO}$, $\Gamma = \nu/\omega_{TO}$ is the normalized damping factor, $A=1.522$ and $B=0.185$ are two constants adjusted by this model. We obtained their values by fitting the dispersion equation to experimental values given in reference [6]. We should note here that by expanding the expression of the local dielectric permittivity (ε_{local}) given Eq. (3.2), we end up with the Lorentz–Drude expression of the dielectric permittivity model (Eq. (1.17)), defined using ω_p , ω_{TO} and ω_{LO} .

Eqs. (3.2) show that the transverse term is local, as it is of frequency dependence only, while the longitudinal term is considered nonlocal as it is dependent on the frequency and the wavevector.

We notice that the longitudinal term is valid as long as the value of the total wavevector k is inferior or equal to the value q_B ; and since these conditions that are set on the range of values of k as to ensure the validity of the model do not apply in our calculations, this model failed to suit our study of the NFRHT between two 6H-SiC. In our study, as we explained before, we aim to obtain saturation of the RHTC at small distance where the dominant contribution to the RHTC is due to EM waves of large wavevectors, i.e. wavevectors larger than q_B ; which implies that in the range of k values that we are interested in, the model is not valid. For this reason, we continue our work by modifying the model as to reflect the characteristics and the limits of our system more accurately. And for this, we defined the following model:

$$\left\{ \begin{array}{l} \varepsilon_t(\omega) = 1 + \frac{A - 1}{1 - \Omega(\Omega + i\Gamma)} \quad \forall q \\ \varepsilon_l(\omega) = \left\{ \begin{array}{l} \varepsilon_t(\omega) \text{ for } q \leq q_B \\ 1 \quad \text{for } q > q_B \end{array} \right\} \end{array} \right\} \quad (3.3)$$

We kept the same expression for the transverse term as it is local and defined for every value of the z -component of the wavevector, q . We modified the longitudinal term by changing its expression and dividing it into two different terms depending on the range of q . For all values of q inferior to q_B , the longitudinal term is given by the same local term as the transverse component. For all values of q equal to or larger than q_B , the longitudinal component is equal to 1. To suggest this model we rely on the fact that as long as the spatial

wavelength of the plane wave is large compared to the lattice constant, the plane wave is described over distances spatially larger than the lattice constant; the optical response of the medium may then be considered as continuous and local and for this reason we represent it by the local equation of the dielectric permittivity. When the spatial wavelength approaches the lattice constant, the plane wave is considered sensitive to the lattice structure and this implies that for large wavevectors, i.e. larger than q_B , the medium might, grossly approximated of course, regarded as vacuum for the longitudinal waves.

3.1.2 Calculation of the radiative heat transfer coefficient

To proceed in calculating the RHTC, we should follow the same steps as in the previous chapters, where we have to substitute the expressions of the dielectric permittivity in the equations of the surface impedances. Then we use the surface impedances equations to calculate the reflection factors needed to calculate the RHTC. The surface impedances and the reflection factors are given by the general equations Eqs. (1.16) and Eqs. (1.15) defined in chapter 1. As we mentioned before, these expressions are general and they will be applied in the different models. For the EM waves of s polarization, the surface impedance Z_m^s is dependent on the transverse component of the dielectric permittivity $\varepsilon_t(\omega)$. As we showed in section 1.3 in chapter 1, upon substituting the local dielectric equation in Z_m^s and performing some simple algebraic steps we obtain finally $Z_m^s = \omega/\gamma_m c^2$. Substituting the final form of Z_m^s in the general equation of r_{3m}^s will lead finally to the Fresnel reflection factor Eqs. (1.18) as explained in section 1.3.

The general expression of the surface impedance of the p -polarized EM waves Z_m^p is dependent on both the longitudinal and the transversal components of the dielectric permittivity. Taking into consideration the different values of the longitudinal component $\varepsilon_l(\omega)$, we divided the range of the integral into two regions $q < q_B$ and $q \geq q_B$:

$$Z_m^p = \frac{2i}{\pi\omega} \int_0^{+\infty} \frac{dq}{k^2} \left[\frac{q^2}{\varepsilon_t(k, \omega) - (ck/\omega)^2} + \frac{K^2}{\varepsilon_l(k, \omega)} \right] =$$

$$\frac{2i}{\pi\omega} \int_0^{+\infty} \frac{dq}{k^2} \frac{q^2}{\varepsilon_t(k, \omega) - (ck/\omega)^2} + \frac{2i}{\pi\omega} \int_0^{q_B} \frac{dq}{k^2} \frac{K^2}{\varepsilon_l(k, \omega)} + \frac{2i}{\pi\omega} \int_{q_B}^{+\infty} \frac{dq}{k^2} \frac{K^2}{\varepsilon_l(k, \omega)} \quad (3.4)$$

To simplify this expression we will proceed by calculating each term separately where we consider $Z_m^p = Z_m^{p1^{st}} + Z_m^{p2^{nd}} + Z_m^{p3^{rd}}$. The first term on the right hand-side would give the following expression:

$$Z_m^{p1^{st}} = \frac{2ik_0^2}{\pi\omega} \left\{ \int_0^\infty \frac{q^2 dq}{(q^2 + K^2)(\gamma_m^2 - q^2)} \right\} \quad (3.5)$$

By applying the residue theorem, we obtain finally:

$$Z_m^{p1^{st}} = \frac{\gamma_m}{\omega\varepsilon_t(\omega)} - \frac{iK}{\omega\varepsilon_t(\omega)} \quad (3.6)$$

In the second term $Z_m^{p2^{nd}}$ we will replace $\varepsilon_l(k, \omega)$ with $\varepsilon_t(\omega)$ as given by Eq. (3.3) for the range $q < q_B$. Since $\varepsilon_t(\omega)$ is local and independent of the wavevector, $Z_m^{p2^{nd}}$ reduces to the following expression:

$$Z_m^{p2^{nd}} = \frac{2i}{\pi\omega\varepsilon_t(\omega)} \int_0^{q_B} \frac{K^2 dq}{q^2 + K^2} \quad (3.7)$$

The final expression of $Z_m^{p2^{nd}}$ is then given by the following equation:

$$Z_m^{p2^{nd}} = \frac{2iK}{\pi\omega\varepsilon_t(\omega)} \text{Arctan} \left[\frac{q_B}{K} \right] \quad (3.8)$$

In the third expression of Z_m^p and due to the range of the q values $q \geq q_B$, the longitudinal component of the dielectric permittivity is equal to 1 and by this the third expression of the surface impedance is simplified to the following reduced equation :

$$Z_m^{p3^{rd}} = \frac{2i}{\pi\omega} \int_{q_B}^\infty \frac{K^2 dq}{q^2 + K^2} \quad (3.9)$$

which is easily calculated and so the final form of this term is given as:

$$Z_m^{p3^{rd}} = \frac{2iK}{\pi\omega} \left(\frac{\pi}{2} - \text{Arctan} \left[\frac{q_B}{K} \right] \right) \quad (3.10)$$

Combining the final three terms we obtain the simplified total expression of the surface impedance of the p -polarized EM waves:

$$Z_m^p = \frac{\gamma_1}{\varepsilon_t(\omega)\omega} - \frac{iK}{\varepsilon_t(\omega)\omega} + \frac{2iK}{\pi\omega} \left[\left(\frac{1}{\varepsilon_t(\omega)} - 1 \right) \text{Arctan} \left[\frac{q_B}{K} \right] + \frac{\pi}{2} \right] \quad (3.11)$$

We then substitute this equation in the general equation of the reflection factor r_{3m}^p , which will remain in this case nonlocal as it is of frequency and wavevector dependence. By substituting with the obtained expressions of the reflection factors in the RHTC equation given in chapter 1 Eqs. (1.15), we calculated and plotted in Fig. 3.2 the different contributions of the EM waves of s and p polarization to the RHTC between the two 6H-SiC semi-infinite parallel planes. Fig. 3.2 shows the propagative and evanescent contributions of the waves of s and p polarizations to the RHTC for the nonlocal model considered above.

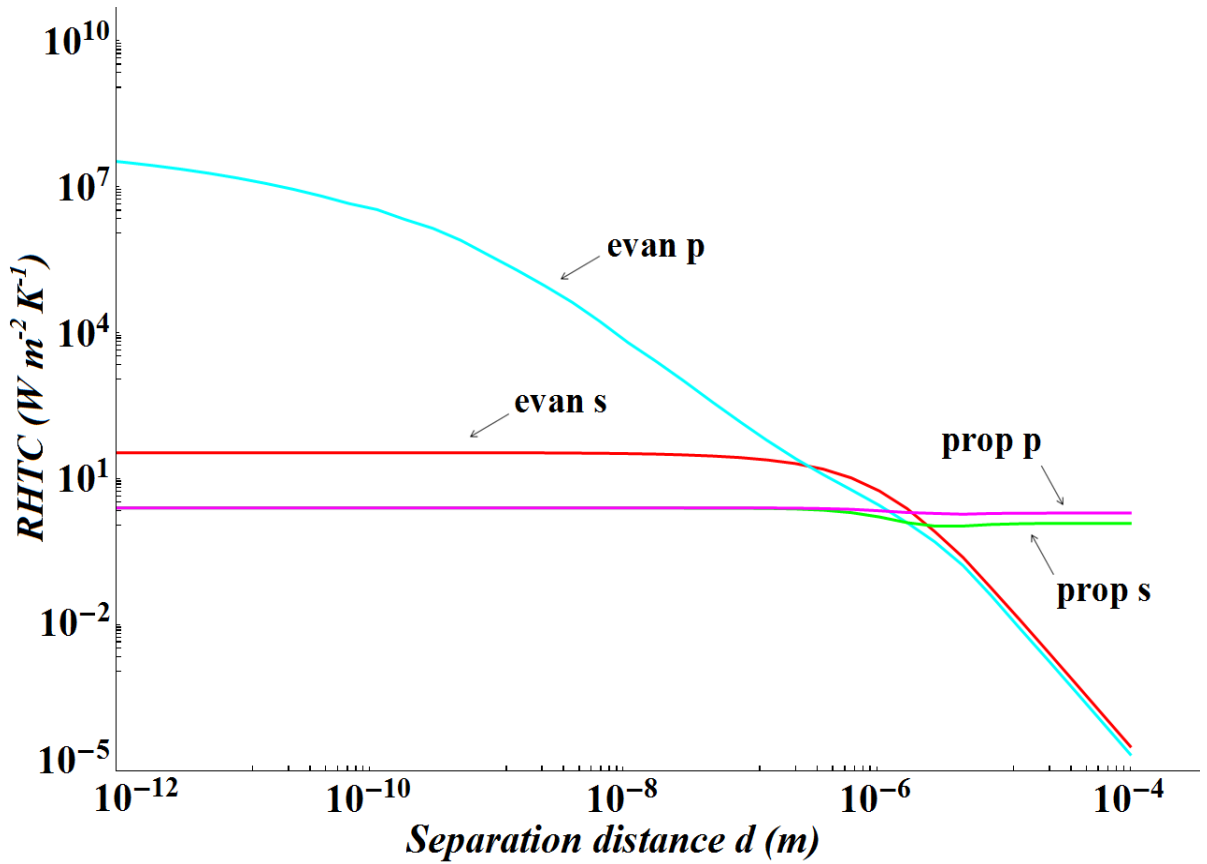


Figure 3.2: Variation of the radiative heat transfer coefficient (contributions of evanescent and propagative EM waves of s and p polarizations) between two semi-infinite 6H-SiC parallel planes of average temperature $T=300\text{K}$, for the 1st suggested nonlocal model case.

Regarding the contributions of propagative contributions of s and p polarizations, the same argument given in section 1.4 in chapter 1 applies in this case also. As we mentioned before, this is due to the fact that the propagative terms of the RHTC dominate at large distances as they acquire small wavevectors, and their behaviors are unaffected by the nonlocality of the system presented in the nonlocal dielectric permittivity equations. On the other hand, the evanescent term of the s -polarized waves is also relatively not affected by the nonlocality as it

saturates in the local and the nonlocal cases, with slight insignificant difference in the values between the two cases. This was also explained in the discussion given in section 1.4.

The important result obtained is thus the change in the shape of the graph of the contribution of the evanescent p -polarized waves, which has shown infinite divergence in the local case. We observe that the infinite divergence is replaced by a “logarithmic-like” divergence, or an incomplete saturation, as d decreases. We should note here that this logarithmic increase could not be shown analytically as the equations employed in this model did not simplify to a simple analytical expression reflecting the logarithmic behavior of the obtained plot. To compare between the local and the nonlocal cases, we plot the total contribution (sum of all different contributions of s and p polarizations) for both cases on the same graph Fig. 3.3.

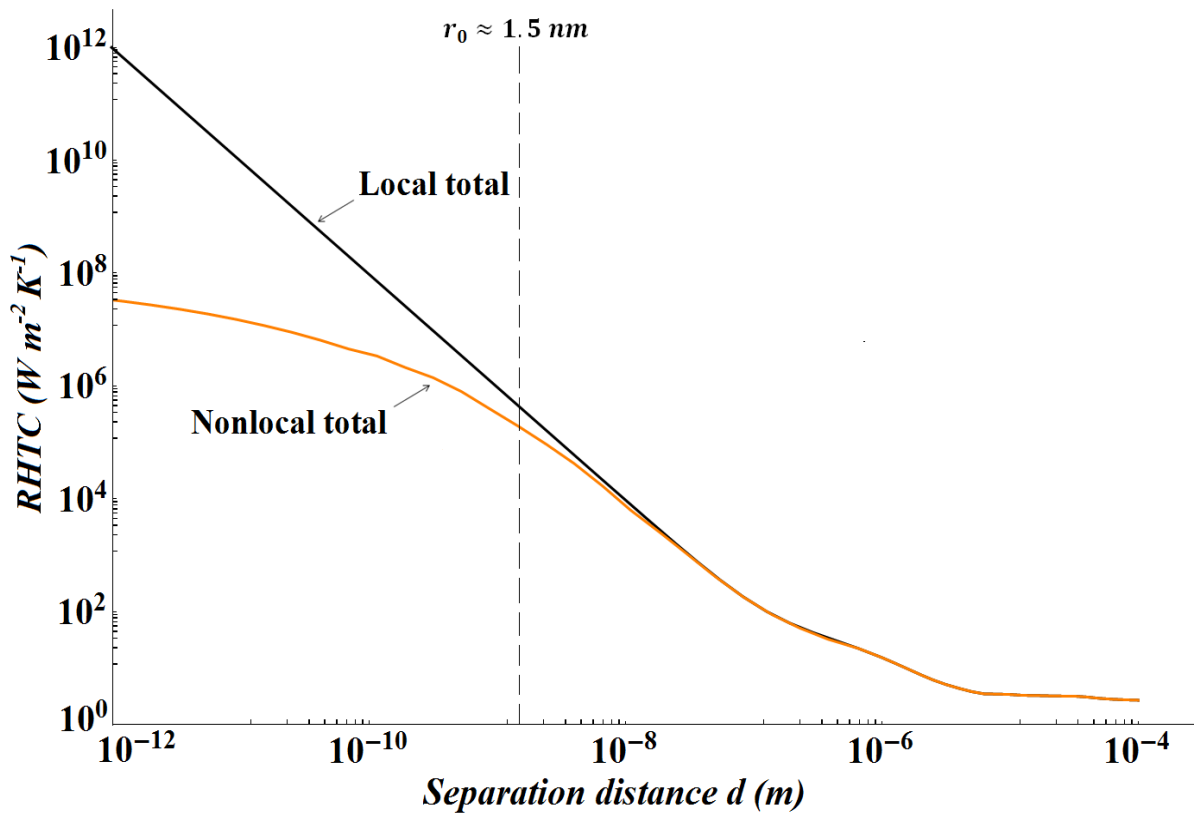


Figure 3.3: Variation of the total radiative heat transfer coefficient (summation of the evanescent and propagative contributions of s and p polarizations) between two semi-infinite 6H-SiC parallel planes of average temperature $T=300\text{K}$, for the local and the first suggested nonlocal model cases.

We should note that as in the case of metals, our results are represented for distances as small as 10^{-12}m just to show that mathematically the nonlocal model leads to this incomplete saturation as these distances scales. Physically, at sub-nm scale quantum effects should be taken into consideration in the full heat transfer study as it was reported that they dominate at

such scales in semiconductors. [7–10]. As this work limits itself to radiative heat transfer, this quantum treatment is beyond the scope of this thesis.

In Fig. 3.3, we observe that at large distances the curves of the local and the nonlocal cases coincided and their values were equal to those given by the propagative contributions. This is not surprising, because at large distances the contributions of the propagative waves of both s and p polarizations dominate and their summation constitutes almost the total contribution, as the contributions of the evanescent waves of both s and p polarizations are negligible. At small distances where the contributions of the evanescent waves dominate, the magnitude of the plots increase by few orders compared to the values at larger distances. We notice that at distances of the order of the lattice constant r_0 , the curve of the nonlocal model deviates from the $1/d^2$ diverging slope of the local graph and the graph continues to increase in a logarithmic way which is considered as an incomplete saturation.

As we mentioned before, the behavior of the curve of the RHTC could be deduced from the values of the imaginary part of the reflection factor for large K values and small distances d . We examined then the variation of $Im(r_{3m}^P)$ as K increases by plotting the graph of the imaginary parts of the reflection factors for the local and the nonlocal cases Fig. 3.4.

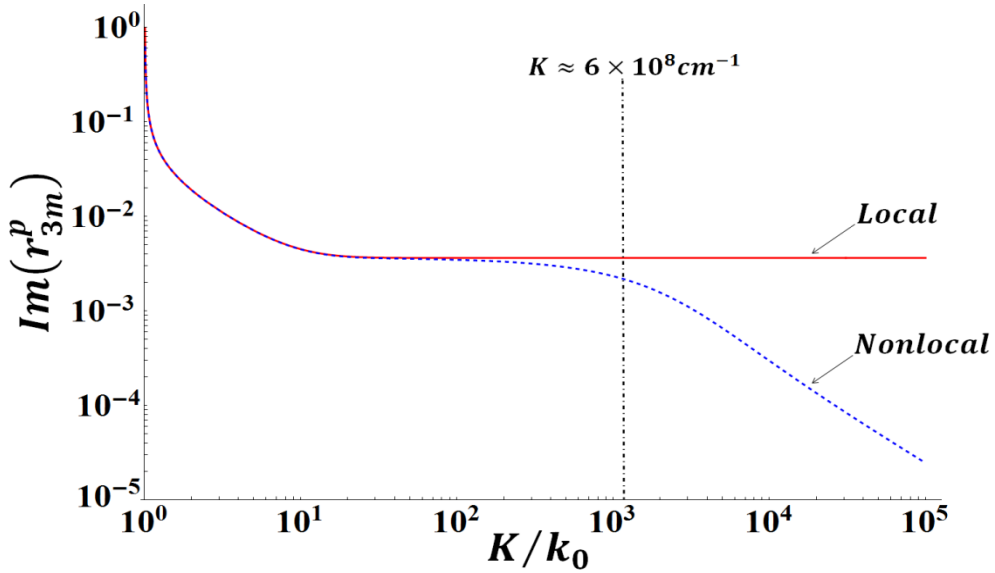


Figure 3.4: Variation of $Im(r_{3m}^P)$ as a function of K/k_0 for $\omega = \omega_{TO}$ for the local model case and the first suggested nonlocal model case. The curve of the local case acquires constant value as K increases while the curve of the nonlocal case shows a continuous decrease which explains the saturation of the RHTC.

Fig. 3.4 compares between the variations of $Im(r_{3m}^P)$ as K increases for the local and the nonlocal cases. We observe that in the local case the curve remained constant with the increase of the wavevector K values, and this explains the steep divergence of the RHTC as

the distance decreases. We showed in section 1.4 in chapter 1 that the limit of the expression of $Im(r_{3m}^P)$ tends to a finite value in the local case, which explains the constant value acquired at large K in Fig. 3.4. The curve of the nonlocal model coincided with that of the local model for all $K/k_0 < 5 \times 10^2$ and when K is of the order of the inverse of the lattice constant, i.e. $K \approx 6 \times 10^8 m^{-1}$, the curve deviates in a decreasing manner to become of negligible values as the wavevector continues to increase in magnitude. This interprets the deviation of the RHTC graph in the nonlocal case from the infinite diverging manner starting at distances of the order of the lattice constant.

An important step in the interpretation of the results is the study of the variation of the transmission coefficient of the p -polarized EM evanescent waves $f(K, \omega) = 4(Im(r_{31}^P))^2 / |1 - (r_{31}^P)^2|^2$ and for this reason we analyzed its variation for $d=0$. We plot $f(K, \omega)$ then in the (K, ω) plane for the local and the nonlocal cases Fig. 3.5.

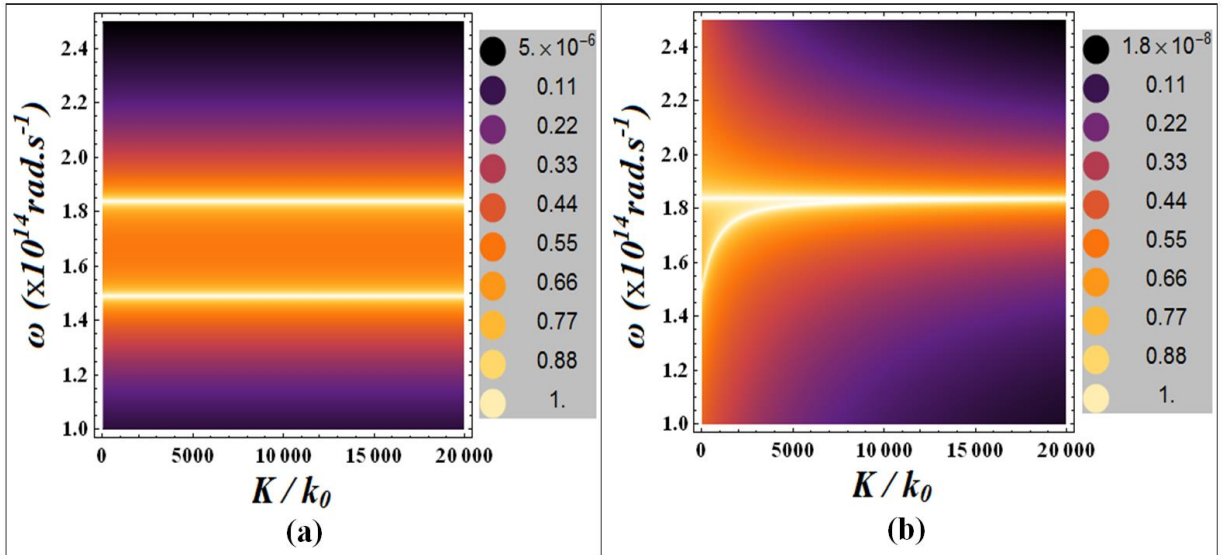


Figure 3.5: Plot of the transmission coefficient $f(K, \omega) = 4(Im(r_{31}^P))^2 / |1 - (r_{31}^P)^2|^2$ of the p -polarized EM evanescent waves in the plane (ω, K) by considering $d=0$, for the local case (a) and the first suggested nonlocal case (b).

Fig. 3.5 shows that as ω increases, the values of the spectrum of the local model increase till reaching the maximum for $\omega = \omega_{TO}$, after which the values decrease. The spectrum reaches its maximum again for $\omega = \omega_{LO}$, above which the values of the transmission coefficient decrease gradually. On the other hand, as K increases, the values and the width of the spectrum remain constant. In the spectrum of the nonlocal model, the maximum values are attained for $\omega = \omega_{TO}$ and $\omega = \omega_{LO}$, and starting from $K \approx 1000k_0$ the width of the spectrum decreases and its values decreased in a slow rate as K increases which is coherent with the

results observed in the RHTC graph. Therefore, it is clear from Fig. 3.5 that in the local case the number of modes contributing to the transfer increases, which explains the divergence of the RHTC, while in the nonlocal case the number of modes that are able to well couple to the transfer decreases as K increases and as the distance decreases explaining by that the deviation of the RHTC plot from the infinite diverging curve of the local case.

We wanted to study the variation of the transmission factor at a specific frequency so we plot $f(K, \omega)$ for $\omega = \omega_{T0}$ as K increases Fig. 3.6.

Fig. 3.6 shows that $f(K, \omega = \omega_{T0})$ varies and increases in value until reaching a maximum value when K is of the order of the inverse of the lattice constant ($K \sim 1/r_0$), after which the graph decreases till reaching very small values for large K values. This behavior of the transmission factor is coherent with the behavior of the RHTC observed in Fig. 3.2.

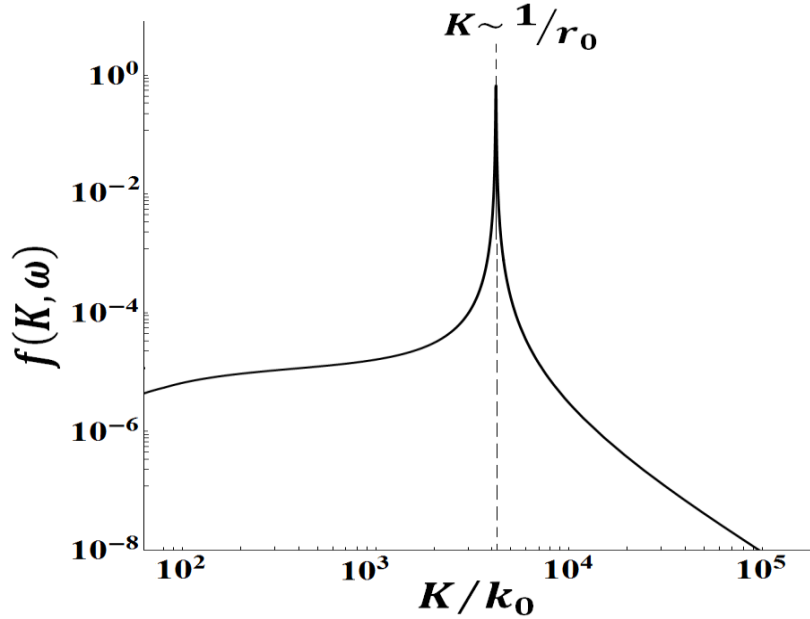


Figure 3.6: Variation of the transmission coefficient of the p -polarized EM evanescent waves for $f(K, \omega = \omega_{T0}) = 4(Im(r_{31}^P))^2 / |1 - (r_{31}^P)^2|^2$ by considering $d=0$, for the first suggested nonlocal case.

Through this model we have shown that the nonphysical infinite divergence of the RHTC between two parallel SiC planes is not obtained upon considering different optical responses of the medium depending on the spatial scale considered. When the wavelength of the plane wave vary on a scale larger than the lattice constant, the medium is seen continuous and reflecting by this wave; when the wavelength is of the order of the lattice constant, the discrete nature of the medium dominates and the medium is thus seen as transparent to this

wave, leading to a huge reduction of its reflectivity as the wavelength decreases compared to the lattice constant scale.

Since we do not obtain a complete saturation by using the above model, we suggested another nonlocal model of the dielectrics permittivity and we present it in the following section.

3.2 A suggested nonlocal model of the dielectric permittivity

In this section we present our study of the RHTC between two 6H-SiC planes (same as those considered in the previous section) using a second nonlocal model of the dielectric permittivity. We will be following the same procedure as before. We will show that incomplete saturation of the RHTC is attained in this case also; the obtained results are quite similar to those presented in the previous section.

3.2.1 Formalism

This model is also a simplified version of the model presented by Kliewer and Fuchs [5], where we consider in this case that the longitudinal and transverse components of the dielectric permittivity are equal for any value of the z -component of the wavevector q . We define the dielectric permittivity ε as follows:

$$\varepsilon_t(\omega) = \varepsilon_l(\omega) = \begin{cases} 1 + \frac{A-1}{1-\Omega(\Omega+i\Gamma)} & \forall q \leq q_B \\ 1 & \forall q > q_B \end{cases} \quad (3.12)$$

Eqs. 3.12 show that the range of the values of q is divided with respect to the value of the wavevector at the edge of the first Brillouin zone, i.e. q_B . We consider the optical response of the medium to be local for every q less than or equal to q_B , and to be equal to 1 for all q larger than q_B . This model is more general than the one proposed in the previous section as we generalized the condition on q for both the transverse and the longitudinal components of ε .

3.2.2 Calculation of the radiative heat transfer coefficient

The surface impedances equations needed to calculate the RHTC, are those defined in chapter 1, i.e. Eqs. (1.16) and their general forms will be definitely modified upon substituting with the expressions of the dielectric permittivity. The integrals of the surface impedances

will be divided into two terms depending on the range of the q values. The surface impedance of the EM waves of s polarization will be given as:

$$Z_m^s = \frac{2i}{\pi\omega} \int_0^{q_B} \frac{dq}{\varepsilon_t(k, \omega) - (k/k_0)^2} + \int_{q_B}^{\infty} \frac{dq}{\varepsilon_t(k, \omega) - (k/k_0)^2} \quad (3.13)$$

Upon substituting with the expressions of the dielectric permittivity, Z_m^s reduces to the following form:

$$Z_m^s = \frac{2ik_0^2}{\pi\omega} \int_0^{q_B} \frac{dq}{\gamma_m^2 - q^2} + \frac{2ik_0^2}{\pi\omega} \int_{q_B}^{\infty} \frac{dq}{\gamma_3^2 - q^2} \quad (3.14)$$

The term on the right-hand side cannot be solved analytically as depending on the frequency ω , the poles of the denominators might lie within the integration interval. Therefore the s -polarized surface impedance equation could not be further modified and it will be calculated numerically.

The general expression of the surface impedance of the p -polarized EM waves on the other hand is also modified by dividing the integrals according to the range of the q values. It is then given by:

$$Z_m^p = \frac{2i}{\pi\omega} \int_0^{q_B} \frac{1}{k^2} \frac{q^2 dq}{\varepsilon_t(\omega) - (k/k_0)^2} + \frac{2i}{\pi\omega} \int_{q_B}^{\infty} \frac{1}{k^2} \frac{q^2 dq}{\varepsilon_t(\omega) - (k/k_0)^2} + \frac{2i}{\pi\omega} \int_0^{q_B} \frac{dq}{k^2} \frac{K^2}{\varepsilon_l(k, \omega)} + \frac{2i}{\pi\omega} \int_{q_B}^{+\infty} \frac{dq}{k^2} \frac{K^2}{\varepsilon_l(k, \omega)} \quad (3.15)$$

Upon substituting with the dielectric permittivity expressions, Z_m^p becomes:

$$Z_m^p = \frac{2ik_0^2}{\pi\omega} \left\{ \int_0^{q_B} \frac{1}{(K^2 + q^2)} \frac{q^2 dq}{(\gamma_m^2 - q^2)} + k_0^2 \int_{q_B}^{\infty} \frac{1}{(K^2 + q^2)} \frac{q^2 dq}{(\gamma_3^2 - q^2)} + \int_0^{q_B} \frac{1}{(K^2 + q^2)} \frac{K^2 dq}{\varepsilon_l(k, \omega)} + \int_{q_B}^{\infty} \frac{K^2 dq}{(K^2 + q^2)} \right\} \quad (3.16)$$

The first two terms on the right-hand side could not be solved analytically and we will calculate them numerically while the third and fourth terms are solved analytically and the final form of the surface impedance is thus given by:

$$Z_m^p = \frac{2ik_0^2}{\pi\omega} \left\{ \int_0^{q_B} \frac{1}{(K^2 + q^2)} \frac{q^2 dq}{(\gamma_m^2 - q^2)} + \int_{q_B}^{\infty} \frac{1}{(K^2 + q^2)} \frac{q^2 dq}{(\gamma_3^2 - q^2)} \right\} + \frac{2iK}{\pi\omega} \left\{ \left(\frac{1}{\epsilon_t(\omega)} - 1 \right) \text{Arctan} \left[\frac{q_B}{K} \right] + \frac{\pi}{2} \right\} \quad (3.17)$$

By substituting these equations in the general equations of the reflection factors Eqs. (1.15) we obtain the nonlocal expressions of the reflection factors that we then substitute in the RHTC equations Eqs. (1.13) to calculate the different contributions of the EM waves of s and p polarizations.

Fig. 3.7 shows the evanescent and propagative contributions of the EM waves of s and p polarizations to the RHTC using the nonlocal model proposed above. With respect to the contributions of the propagative EM waves of s and p polarizations and the evanescent waves of s polarization, the discussion presented in sections 1.4 and 2.3 applies here also. We will focus then on the contribution of the evanescent EM waves of p -polarization. We plot in Fig. 3.8 the total contribution to the RHTC in the local and the nonlocal models as to compare between them. We notice from this figure that the graph of the second nonlocal model deviated from the infinite diverging graph as the distance decreased and the non-infinite divergence obtained in the local case was no more attained. The deviation of the graph of the nonlocal model started at a distance of the order of the lattice constant r_0 , and a logarithmic-like divergence or an incomplete saturation starts to take place. This is thus consistent with the argument given in the first model. To better interpret the “logarithmic-like” behavior we should derive the analytic expression supporting it. The deviation of the RHTC from the infinitely diverging graph indicates that the imaginary part of the p -polarized evanescent waves tends to zero upon using the nonlocal equations of the dielectric permittivity and to check this tendency we derive the limit of this factor for large K values. To do so, we start by deriving a simplified form of Z_m^p for large K values.

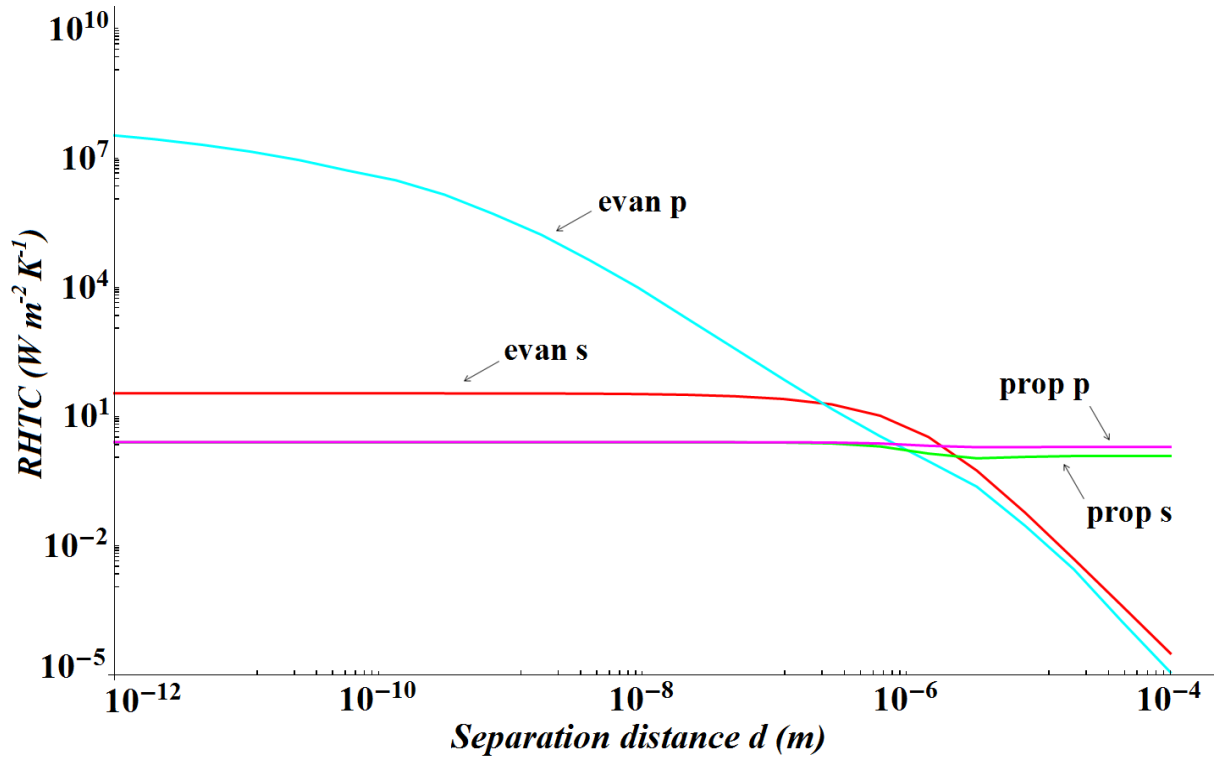


Figure 3.7: Variation of the radiative heat transfer coefficient (contributions of the evanescent and propagative EM waves of s and p polarizations) between two semi-infinite 6H-SiC parallel planes of average temperature $T=300K$, for the second suggested nonlocal model case.

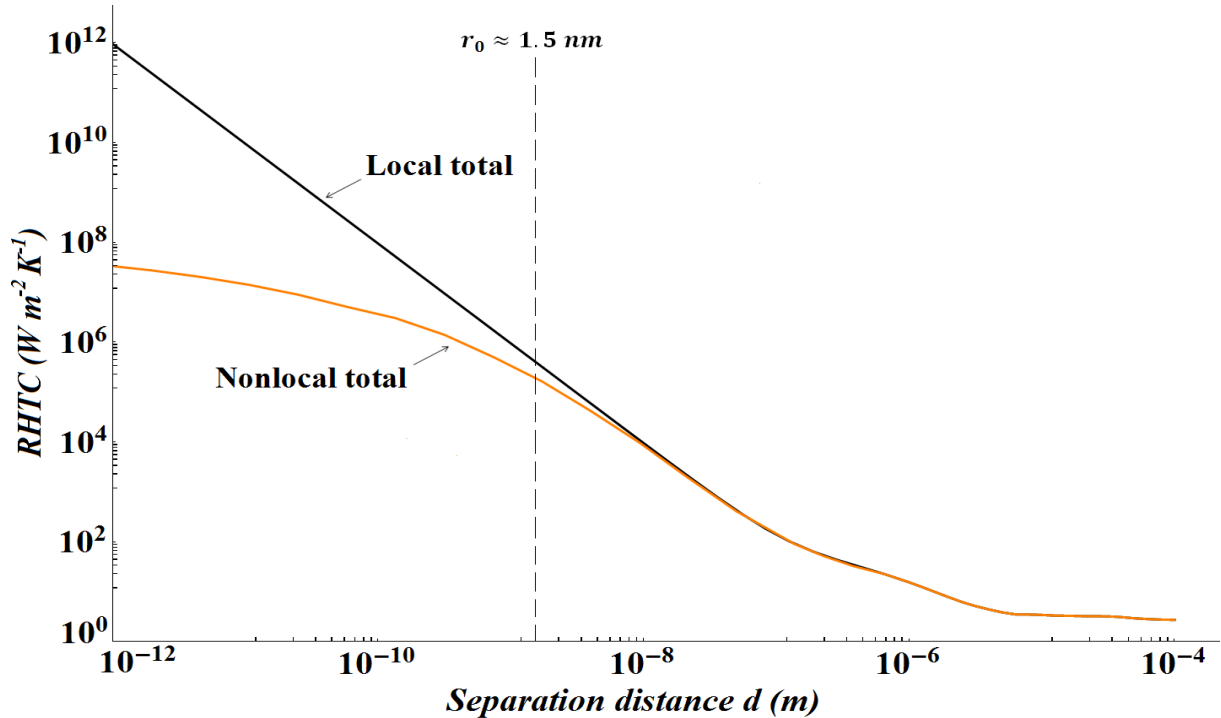


Figure 3.8: Variation of the total radiative heat transfer coefficient (summation of the contributions of the evanescent and propagative EM waves of s and p polarizations) between two semi-infinite 6H-SiC parallel planes of average temperature $T=300K$, for the local and the second suggested nonlocal model cases.

Taking into consideration that for large K , the first term on the right-hand side of Eq. (3.17) will become:

$$Z_m^{p1^{st}} \approx \frac{2ik_0^2}{\pi\omega} \int_0^{q_B} \frac{-q^2 dq}{(K^2 + q^2)^2} \quad (3.18)$$

solving the integral will give:

$$Z_m^{p1^{st}} = \frac{i\omega}{\pi c^2} \left\{ \frac{q_B}{K^2 + q_B^2} - \frac{\text{Arctan}[q_B/K]}{K} \right\} \quad (3.19)$$

Taking the expansion limit of the Arctan function, $Z_m^{p1^{st}}$ will reduce to the following form:

$$Z_m^{p1^{st}} = \frac{i\omega}{\pi c^2} \left\{ \frac{q_B}{K^2 + q_B^2} - \frac{q_B}{K^2} + \frac{q_B^3}{K^4} \right\} \quad (3.20)$$

Following the same procedure with second term on the right-hand side of Eq. (3.17):

$$Z_m^{p2^{nd}} \approx \frac{2i}{\pi\omega} \int_{q_B}^{\infty} \frac{1}{k^2} \frac{q^2 dq}{1 - (k/k_0)^2} \quad (3.21)$$

we obtain the following reduced form:

$$Z_m^{p2^{nd}} \approx \frac{i\omega}{\pi c^2} \left\{ \frac{-\pi}{2K} - \frac{q_B}{K^2 + q_B^2} + \frac{q_B}{K^2} - \frac{q_B^3}{K^4} \right\} \quad (3.22)$$

For the third term on the right-hand side of Eq. (3.17) we use the expansion form of the Arctan function:

$$Z_m^{p3^{rd}} = \frac{2iK}{\pi\omega} \left\{ \left(\frac{1}{\varepsilon_t(\omega)} - 1 \right) \text{Arctan} \left[\frac{q_B}{K} \right] + \frac{\pi}{2} \right\} \quad (3.23)$$

we obtain the reduced form given by Eq. (3.24)

$$Z_m^{p3^{rd}} = \frac{2iK}{\pi\omega} \left\{ \frac{q_B}{K\varepsilon_t(\omega)} - \frac{q_B^3}{K^3\varepsilon_t(\omega)} - \frac{q_B}{K} + \frac{q_B^3}{K^3} + \frac{\pi}{2} \right\} \quad (3.24)$$

Adding the obtained terms, we obtain the final simplified form of Z_m^p for the limit of large K :

$$Z_m^p \approx \frac{-i\omega}{2K\pi c^2} + \frac{iK}{\omega} + \frac{2iK}{\pi\omega} \left\{ \frac{q_B}{K\varepsilon_t(\omega)} - \frac{q_B^3}{K^3\varepsilon_t(\omega)} - \frac{q_B}{K} + \frac{q_B^3}{K^3} \right\} \quad (3.25)$$

Substituting Eq. 3.25 in the general equation of the reflection factor, we obtain for large K limit:

$$r_{3m}^p \approx \frac{\frac{i\omega}{2K\pi c^2} - \frac{2iq_B}{\pi\omega} \left(\frac{1}{\varepsilon_t(\omega)} - 1 \right)}{\frac{2iK}{\pi\omega} - \frac{i\omega}{2K\pi c^2} + \frac{2iq_B}{\pi\omega} \left(\frac{1}{\varepsilon_t(\omega)} - 1 \right)} \quad (3.26)$$

Performing few trivial simplifying steps we finally obtain the following reduced form of r_{3m}^p for the large K limit:

$$r_{3m}^p \approx \frac{q_B(\varepsilon_t(\omega) - 1)}{\varepsilon_t(\omega)K\pi} \quad (3.27)$$

From this expression we notice that the reflection factor varies as $1/K$ and tends to zero for large K which leads to the deviation of the RHTC graph from the infinitely divergent graph of the local model as shown in Figs. 3.7 and 3.8. From Eq. (3.27) we can deduce that the imaginary part of the reflection factor is:

$$\text{Im}(r_{3m}^p) \approx \frac{q_B \text{Im}(\varepsilon_t(\omega))}{K\pi|\varepsilon_t(\omega)|^2} \quad (3.28)$$

It follows that by using Eqs. (1.13) we can write in the electrostatic limit:

$$h_{evan}(T, d, \omega) \approx h^0(T, \omega) \times \frac{4}{k_0^2} \int_{k_0}^{+\infty} \frac{\text{Im}(r_{3m}^p) e^{-2Kd} K dK}{|1 - (r_{3m}^p)^2 e^{-2Kd}|^2} \quad (3.29)$$

Considering Eq. (3.29) and $(r_{3m}^p)^2 \sim 1/K^2$, we obtain finally:

$$h_{evan}(T, d, \omega) \approx h^0(T, \omega) \times \frac{4q_B^2 [\text{Im}(\varepsilon_t(\omega))]^2}{\pi^2 |\varepsilon_t(\omega)|^2 k_0^2} \int_{k_0}^{+\infty} \frac{e^{-2Kd} dK}{K} \quad (3.30)$$

Therefore, the obtained integral of the exponential function of K in the expression of the contribution of the p -polarized evanescent waves leads to a plot acquiring a logarithmic-like behavior, as shown in plots of the RHTC. To compare between the results obtained in this nonlocal model and the previous nonlocal model, we plot the total contribution to the RHTC for the two cases in Figure 3.9. From this figure we notice that the two curves totally overlap. This leads us to conclude that the two suggested models of the dielectric permittivity give the same results regardless of the difference in the conditions on the dielectric permittivity

expressions. In other words, the nonlocality condition of the transverse component of the dielectric permittivity leads to no change in the RHTC and it is all due to the nonlocality of the longitudinal component that the infinite divergence is replaced by the logarithmic-like divergence.

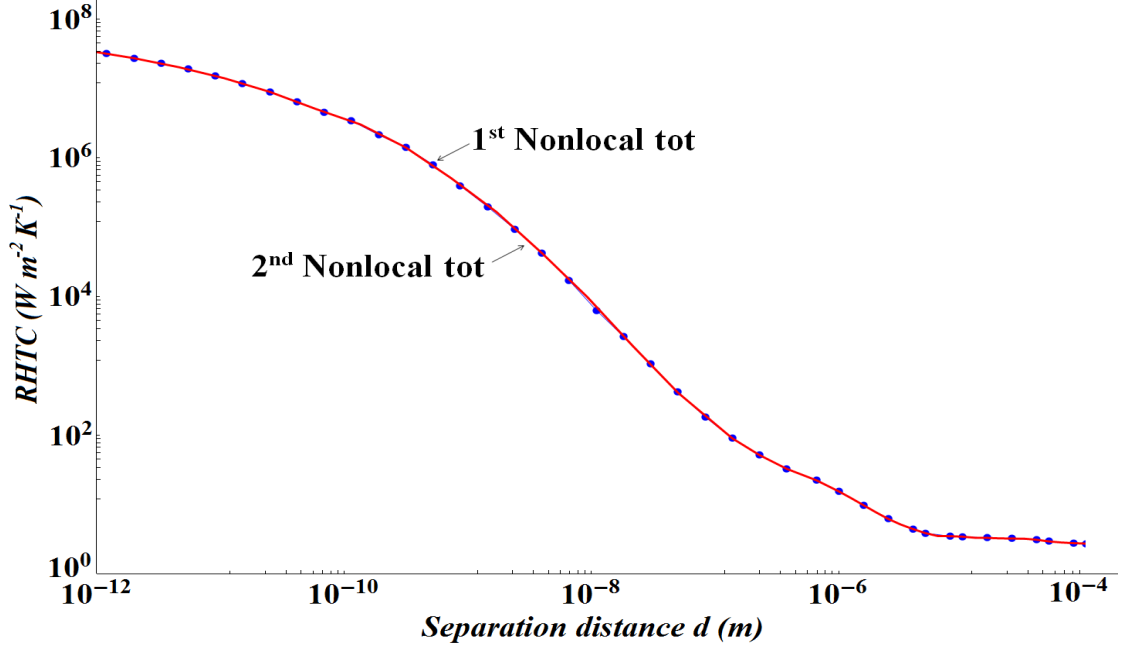


Figure 3.9: Variation of the total radiative heat transfer coefficient (summation of the contributions of the evanescent and propagative EM waves of s and p polarizations) between two semi-infinite 6H-SiC parallel planes of average temperature $T=300K$, for the first suggested nonlocal model (dotted blue curve) and the second suggested nonlocal model (red curve).

Similar to the previous cases, we are interested in studying the variation of the transmission factor for $d=0$, $f(K, \omega) = 4(Im(r_{31}^p))^2 / |1 - (r_{31}^p)^2|^2$ so we plotted it in the (ω, K) plane for the nonlocal case and we compared it to that of the local case, as shown in Fig. 3.10.

From Fig. 3.10 we notice that the width and magnitude of the spectrum of the transmission factor for $d=0$ in the nonlocal model decrease as K increases which leads to the logarithmic divergence of the RHTC, while in the local case the magnitude of the spectrum remained constant as K increases and showed no decrease which explains the infinite divergence shown by the RHTC graph. In fact, the detailed discussion given in the previous section of the chapter for the spectrum of the 1st suggested nonlocal model applies for the spectrum of this model as well. We also plotted $f(K, \omega)$ for $\omega = \omega_{TO}$ as K increases in Fig. 3.11, where we noticed that the graph increased and reached its maximum when $K/k_0 \approx 3 \times 10^1$, after which it decreased as K continues to increase. The variations of the graphs obtained in Figs. 3.10 and 3.11 are coherent with the variation of the RHTC.

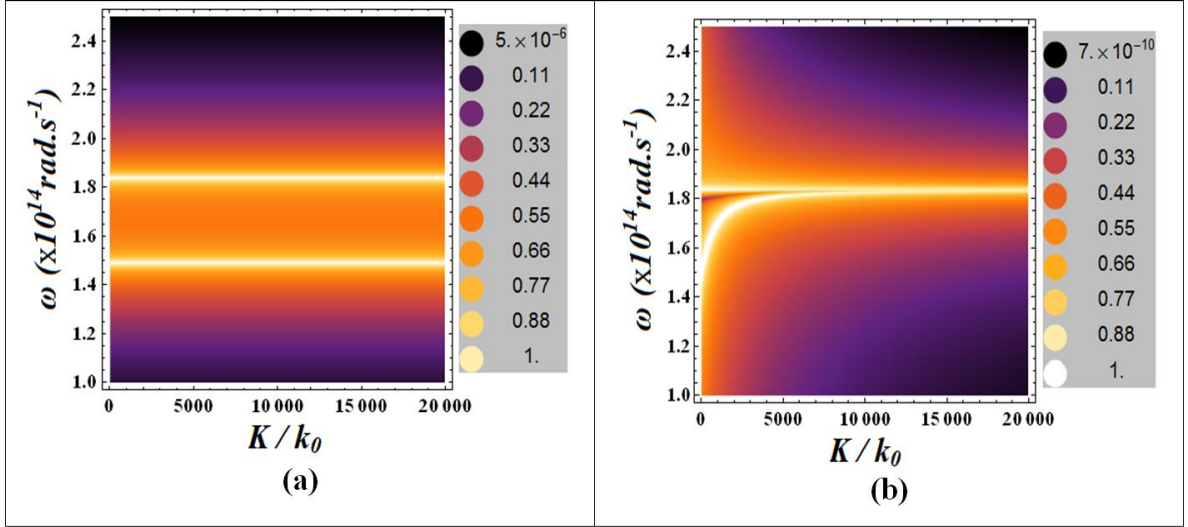


Figure 3.10: Plot of the transmission coefficient for $d=0$, $f(K, \omega) = 4(\text{Im}(r_{31}^P))^2 / |1 - (r_{31}^P)^2|^2$ of the p -polarized EM evanescent waves in the plane (ω, K) for the local case (a) and the second suggested nonlocal case (b).

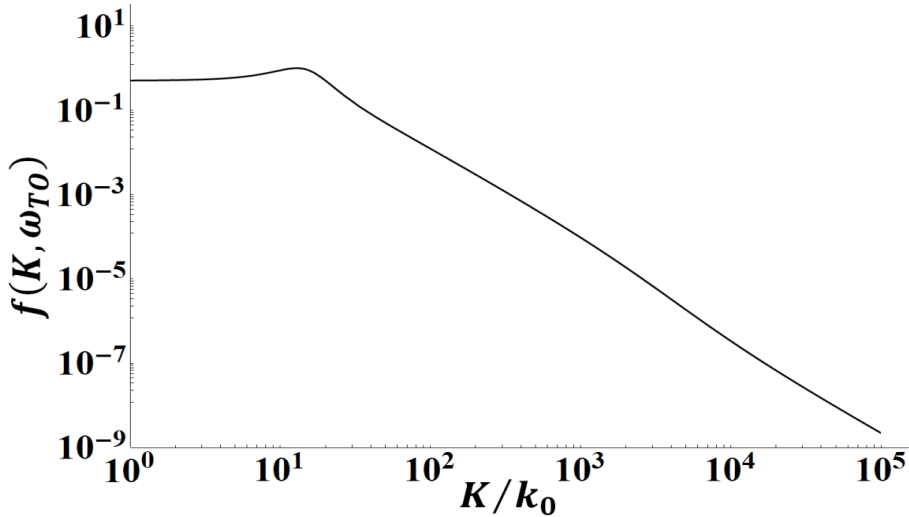


Figure 3.11: Variation of the transmission coefficient of the p -polarized EM evanescent waves $f(K, \omega = \omega_{T0}) = 4(\text{Im}(r_{31}^P))^2 / |1 - (r_{31}^P)^2|^2$ by considering $d=0$, as function of K for the second suggested nonlocal model.

We wanted to check the effect of changing the value of q at which the dielectric permittivity components change their values, on the cutoff value of K at which the transmission factor deviates from the infinitely diverging graph. For this reason, in the limit $d=0$ we considered, for one case, the limiting value of q to be $q = 5q_B$. For another case, we considered the limiting value to be $q = 10q_B$. For each case, we calculated the transmission factor $f(K, \omega)$ for $d=0$ by considering $K = nq_B$. In Fig. 3.12 we show the plots of $f(K/q_B, \omega = \omega_{T0})$ along with the original case considered, i.e. $q = q_B$. We observe from this figure that in each case

the graph starts to decay and decreases drastically in magnitude when the wavevector K is equal to the limiting value of q . This emphasizes our obtained results and our conclusions that the limit at which the optical response of the medium changes from being local to nonlocal sets the limit to the infinite divergence of the RHTC and leads to its logarithmic divergence.

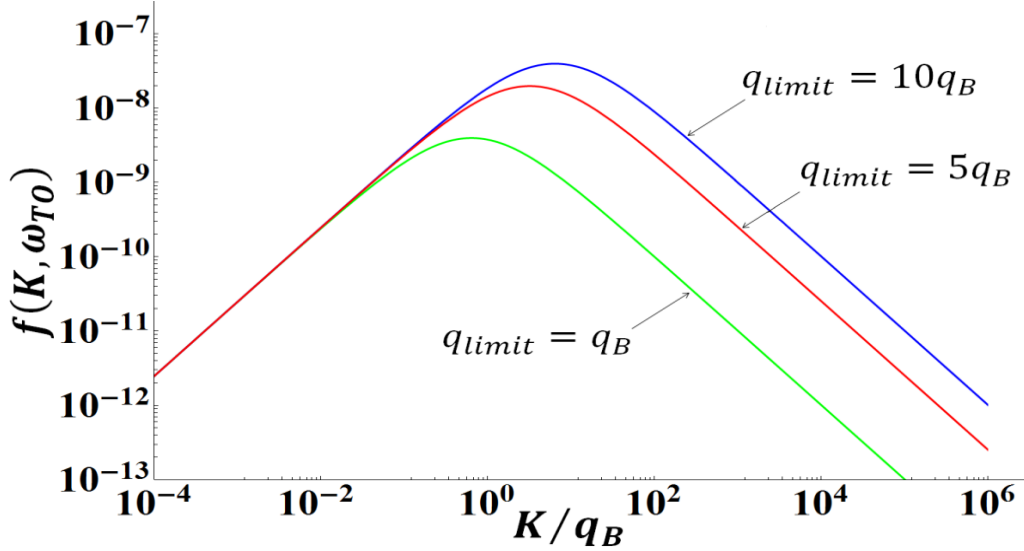


Figure 3.12: Plot of the transmission factor of the p -polarized EM evanescent waves $f(K, \omega = \omega_{TO}) = 4(\text{Im}(r_{31}^P))^2 / |1 - (r_{31}^P)^2|^2$ by considering $d=0$ and $K = nq_B$. The green plot corresponds to the model considered where ϵ_l changes values at $q = q_B$ and the cutoff occurs at $K = q_B$. The red plot corresponds to the case where the longitudinal component of the dielectric permittivity ϵ_l changes values for $q = 5q_B$. We notice that the cutoff shifts to $K = 5q_B$. The blue plot corresponds to the case where ϵ_l changes values at $q = 10q_B$; we notice that the cutoff occurs at $K = 10q_B$.

3.3 A phenomenological model of the dielectric permittivity

The nonlocal model proposed in this section and used in our calculation of the RHTC between the two 6H-SiC planes is inspired from the work of Henkel and Joulain [11]. Based on the idea that the coherence length of the thermal EM field near a planar surface is related to the nonlocal dielectric response of the material, Henkel and Joulain [11] defined a parameter l as being the minimum coherence length of the EM field. The minimum value of this parameter is related to the nature of the considered material (polar or metallic) and its different physical parameters. By introducing this parameter in the equations, they calculated the local density of states (LDOS) and the field's degree of spatial coherence above a polar material surface and a metallic surface and they showed that these quantities depend on the coherence length l .

Henkel and Joulain [11] carried out their calculations using the Lindhard–Mermin nonlocal dielectric model of the dielectric permittivity for metals, and for the polar materials they posed a nonlocality condition by introducing l as a correlation distance in the correlation equation Eq. (1.4) of the fluctuating currents that generate the radiation field in the medium.

One condition on the value of l is that it is not considered physical for it to be smaller than the lattice constant, and so it was chosen to be of the order of or higher than the lattice constant of the dielectric material; indeed, the source or currents in dielectrics being the ions in the crystals, the currents can hardly be uncorrelated at distances smaller than the lattice constant. Introducing the parameter l and proceeding in calculating the RHTC and the density of EM waves at the surface along with some explicit asymptotic formulas allowed Henkel and Joulain to identify in a semi-quantitative way the scale for the coherence length of the EM field above the surface supporting surface waves.

For metals, they showed that the field’s coherence length is limited by the Thomas–Fermi screening length, even though significant deviations from the local description occur already on a scale of the order or larger than the electron mean free path. For polar materials, they showed through the performed calculations that the radiation generated outside the surface acquires a minimum coherence length given by l , which cuts off the $1/d^2$ divergence of the RHTC and the LDOS obtained in the local description of the material.

As in our work we are considering systems of 6H-SiC planes, we will be more interested in the calculations performed for the polar materials. We will use the modified correlation equation of the currents proposed by Henkel and Joulain [11] to repeat the derivation of the RHTC. Then, using the local dielectric function $\varepsilon(\omega)$ Eq. (1.17) we will proceed to calculate the different contributions of s and p polarized EM waves to the RHTC between two semi-infinite parallel planes of 6H-SiC as functions of their separation distance d . We will show that saturation of the RHTC is obtained upon performing these calculations, and the distance at which this saturation starts to occur is related directly to the value of the correlation length l .

Our results will lead us to conclude that defining a finite correlation length for the sources of the EM field will set this length as a minimum for the coherence length of the field and will impose a cutoff on the RHTC and the LDOS.

3.3.1 Formalism

The correlation length l is introduced in the correlation equation of the fluctuating currents Eq. (1.4) given in chapter 1, this equation is modified and becomes:

$$\begin{aligned} \langle j_m(\mathbf{r}', \omega) j_n^*(\mathbf{r}'', \omega') \rangle \\ = 2 \omega \varepsilon_0 \text{Im}(\varepsilon(\omega)) \left[e^{-(\mathbf{r}' - \mathbf{r}'')^2 / l^2} / \pi^{3/2} l^3 \right] \theta(\omega, T_1) \delta_{kl} \delta(\omega' - \omega'') \end{aligned} \quad (3.28)$$

Comparing this equation with Eq. (1.4) we notice that the authors introduced an exponential term decaying as function of l^2 and they smoothed the spatial delta function into a Gaussian. The modified correlation equation of the fluctuating currents is dependent on l through two terms, one to the power three of l , and the other to the power two in the argument of the exponential function in the numerator. It is important to note here that upon considering $l=0$, the Gaussian reads as a delta function so that we retrieve. (1.4). The Gaussian expresses the fact that the currents are not completely spatially correlated, but exhibit on the contrary a distance on which the currents are correlated.

3.3.2 Calculation of the radiative heat transfer coefficient

Starting from the modified equation on the spatial correlation function of the currents Eq. (3.28), we proceed in the derivation of the RHTC following the same steps as the derivation performed before (see Appendix for complete derivation steps). We obtain an equation similar to Eqs. (1.13) but with an additional term ($e^{-[Re^2(\gamma_2) + K^2]l^2/4}$) found in the numerators of the transmission factors of the propagative and the evanescent terms consisting of the multiplication of two exponential terms depending on the square of the correlation length l :

$$\left\{ \begin{aligned} h_{rad}(T, d) &= \sum_{\alpha=S,P} \int_0^{+\infty} d\omega [h_{prop}^\alpha(T, d, \omega) + h_{evan}^\alpha(T, d, \omega)] \\ h_{prop}(T, d, \omega) &= h^0(T, \omega) \times \int_0^{k_0} \frac{K d K (1 - |r_{31}^\alpha|^2)(1 - |r_{32}^\alpha|^2) \times e^{-[Re^2(\gamma_2) + K^2]l^2/4}}{k_0^2 |1 - r_{31}^\alpha r_{32}^\alpha e^{2i\gamma_3 d}|^2} \\ h_{evan}(T, d, \omega) &= h^0(T, \omega) \times \int_{k_0}^{+\infty} \frac{K d K 4 \text{Im}(r_{31}^\alpha) \text{Im}(r_{32}^\alpha) e^{2i\gamma_3 d} \times e^{-[Re^2(\gamma_2) + K^2]l^2/4}}{k_0^2 |1 - r_{31}^\alpha r_{32}^\alpha e^{2i\gamma_3 d}|^2} \end{aligned} \right\} \quad (3.29)$$

It is important to mention that by assuming $l=0$, we retrieve the equation obtained in chapter 1, i.e. Eqs. (1.13).

The presence of the additional term in the numerators of the transmission factors assures the dependence of the RHF on the correlation length l where we expect that the behavior and the tendencies of graphs should show dependence on l . To calculate the RHTC as function of the separation distance d and since we consider that the nonlocality is included in the correlation equation of the fluctuating currents, we use in this case the Fresnel reflection factors, i.e. the local equations of the reflection factors Eqs. (1.18).

One important step in our calculations is specifying a value for the correlation l . As we mentioned in the introduction, the minimum value of l should be that of the lattice constant, and for this reason we assign different values for l : $l = (1,2, \dots 10)r_0$, where $r_0 \approx 1.5nm$ is the lattice constant of 6H-SiC. We then substitute with the Fresnel reflection factors in Eq. (3.29) to calculate in each case and for each value of l the different contributions to the RHTC of the EM waves of s and p polarizations as functions of d .

We present in Fig. 3.13 the different contributions to the RHTC for the case of $l = r_0$. We notice that the saturation of the evanescent contribution of the p -polarized EM waves was obtained, replacing by that the infinite divergence obtained in the local case. We also notice that the propagative contributions of s and p -polarized EM waves and the contribution of the s -polarized evanescent EM waves were similar to those obtained in the local case, and their interpretations given in section 1.4 still apply here. To compare the variations of the graphs of the contributions of the evanescent waves for the different cases with the local case, we plot in Fig. 3.14 the total contribution of the nonlocal and the local cases; and in Fig. 3.15 we plot the total contributions for the nonlocal cases corresponding to the different values of l ($l = (1,2, \dots 10)r_0$) along with the total contribution of the local case. We observe in Fig.3.14 that at large distances the graphs coincide and at distances of the order of the lattice constant r_0 the nonlocal graph deviates from the diverging slope of the local case and saturation starts to take place as l/K . On the other hand, in Fig. 3.15 we observe that for all l , the saturation occurs in a tendency sharper than that obtained in the first and the second models. As the value of l increases, the saturation value decreases and the distance at which the graph deviates from that of the local case, increases. By examining the distances at which saturation in each case occurs we found that they are of the order of the values of the coherence parameter l . This lead us to conclude that the coherence parameter l acts as a cutoff to the RHF exchanged

between the two 6H-SiC planes; it hence defines a finite value of the maximum RHF exchanged. The results of Henkel and Joulain [11] had led to the same conclusion.

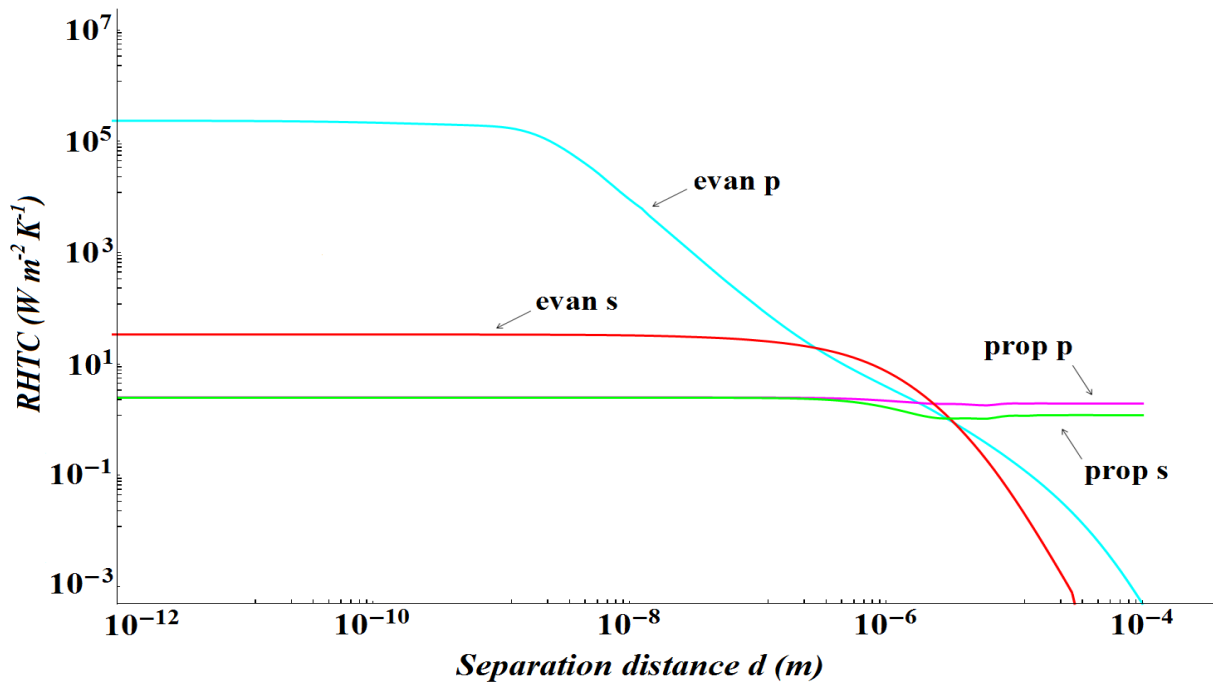


Figure 3.13: Variation of the radiative heat transfer coefficient (contributions of evanescent and propagative EM waves of s and p polarizations) between two semi-infinite 6H-SiC parallel planes of average temperature $T=300\text{K}$, for the third suggested nonlocal model case when $l = r_0$.

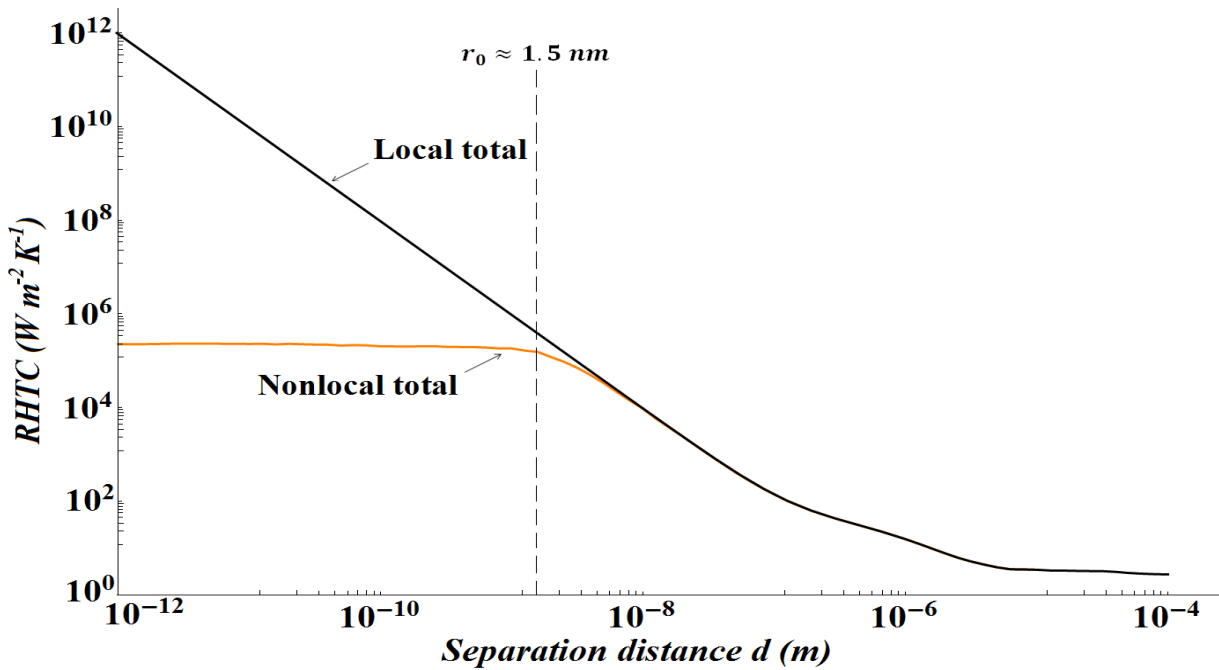


Figure 3.14: Variation of the total radiative heat transfer coefficient (summation of the contributions of evanescent and propagative EM waves of s and p polarizations) between two semi-infinite 6H-SiC parallel planes of average temperature $T=300\text{K}$, for the local case and the third suggested nonlocal model case when $l = r_0$.

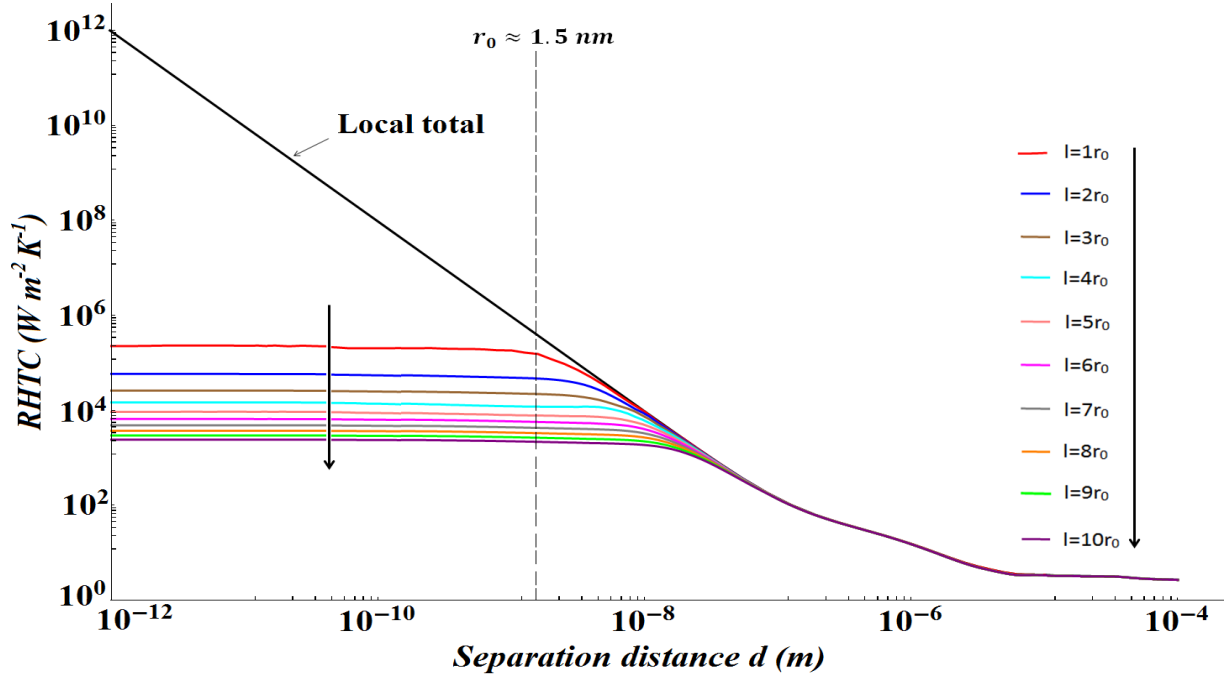


Figure 3.15: Variation of the total radiative heat transfer coefficient (summation of the contributions of evanescent and propagative EM waves of s and p polarizations) between two semi-infinite 6H-SiC parallel planes of average temperature $T=300\text{K}$, for the local case and the third suggested nonlocal model case when $l = (1, 2, \dots, 10)r_0$. The arrow indicates the increasing order of the value of l , as well as the order of the corresponding graphs.

Since the arguments of all the cases are similar, we will give the full interpretation of the results obtained only for the case $l = r_0$. Mathematically, the saturation is caused by the cutoff imposed by the additional exponential term $e^{-K^2 l^2/4}$ which converges as K increase. From a physical point of view, the correlation length for the currents sets a cutoff for the divergence of the RHTC at K of the order of the inverse of this correlation length. This is due to the fact that the correlation of the currents at a certain scale leads to the correlation of the EM fields at a similar scale and the saturation of the RHF starting from distances of the order of and smaller than this correlation length. This implies that the contribution of the EM evanescent waves of large wavevectors such that $K \geq 1/l$ saturates and leads to the saturation of the total RHTC.

The radiative transfer spectrum shows a behavior similar to that of the EM energy density spectrum (and specifically the electric energy density spectrum) since the latter diverges as $1/d^2$ as d decreases Eq. (1.19). This implies that in the nonlocal case saturation is expected. Henkel and Joulain [11] studied the variation of the electric energy density and they showed that it saturated upon introducing the coherence length l . In the local case (also corresponds to

the case $l=0$) the electric energy density is given by the following equation (see Appendix D for full derivation steps):

$$u^E(z, \omega, T) = \frac{\omega^2 \Theta(\omega, T)}{\pi^2 c^3} \left\{ \int_0^{k_0} \frac{K dK}{k_0 |\gamma_3|} \left[\frac{(1 - |r_{31}^s|^2) + (1 - |r_{31}^p|^2)}{2} \right] + 4 \int_{k_0}^{\infty} \frac{K^3 dK}{k_0^3 |\gamma_3|} \left[\frac{Im(r_{31}^s) + Im(r_{31}^p)}{2} \right] e^{-2\gamma_3'' z} \right\} \quad (3.30)$$

By assuming that l is different from zero, we repeat the derivation of the electric density starting from the correlation equation of the fluctuating currents given by Eq. (3.28) where we obtain finally the following form (see Appendix D for full derivation):

$$u^E(z, \omega, T, l) = \frac{\omega^2 \Theta(\omega, T)}{\pi^2 c^3} \left\{ \int_0^{k_0} \frac{K dK}{k_0 |\gamma_3|} \left[\frac{(1 - |r_{31}^s|^2) + (1 - |r_{31}^p|^2)}{2} \right] \times e^{-[Re^2(\gamma_2) + K^2]l^2/4} + 4 \int_{k_0}^{\infty} \frac{K^3 dK}{k_0^3 |\gamma_3|} \left[\frac{Im(r_{31}^s) + Im(r_{31}^p)}{2} \right] e^{-2\gamma_3'' z} \times e^{-[Re^2(\gamma_2) + K^2]l^2/4} \right\} \quad (3.31)$$

By comparing Eq. (3.30) and Eq. (3.31) we notice that they only differ by the presence of the term $e^{-[Re^2(\gamma_2) + K^2]l^2/4}$ as in Eq. (3.29). This additional term ensures the dependence of the electric energy density on the coherence length l . We note that by considering $l=0$ in Eq. (3.31) we retrieve Eq. (3.30) corresponding to the local case.

To study the variation of $u^E(z, \omega, T, l)$ for large K and at small distances we derive the limit of Eq. (3.31) for these conditions. For large K , the limit of the electric energy density is dominated by the contribution of the evanescent waves, and the following limits should be considered:

$$\left\{ \begin{array}{l} \lim_{K \rightarrow \infty} r_{31}^s = \frac{\epsilon_1 - 1}{4(K/k_0)^2} \\ \lim_{K \rightarrow \infty} r_{31}^p = \frac{\epsilon_1 - 1}{\epsilon_1 + 1} \\ |\gamma_3| \approx K \\ e^{-2\gamma_3'' z} \approx 1 \end{array} \right\} \quad (3.32)$$

where the limits of the exponential functions in Eqs. (3.32) are obtained upon considering Taylor's expansion. By substituting Eqs. (3.32) in Eq. (3.31), the electric energy density reduces into the following form:

$$u^E(z, \omega, T, l) = \frac{\Theta(\omega, T)}{\pi^2 \omega} \text{Im} \left(\frac{\varepsilon_1 - 1}{\varepsilon_1 + 1} \right) \int_{k_0}^{\infty} K^2 e^{-K^2 l^2 / 4} dK \quad (3.33)$$

Considering now the following equalities:

$$\left\{ \begin{array}{l} \int \int K^2 e^{-K^2 l^2 / 4} dK \rightarrow \int x^2 e^{-ax^2} dx = \frac{1}{4} \sqrt{\frac{\pi}{a^3}} \text{erf}(x\sqrt{a}) \\ a = \frac{l^2}{4} \\ \text{erf}(\infty) = 1 \end{array} \right\} \quad (3.34)$$

We obtain finally the following form of the electric energy density for large K values and small gap distances:

$$u^E(z, \omega, T, l) = \frac{2\Theta(\omega, T)}{\pi^2 \omega l^3} \text{Im} \left(\frac{\varepsilon_1 - 1}{\varepsilon_1 + 1} \right) \quad (3.35)$$

From Eq. (3.35) we notice the inverse dependence on l^3 which leads us to conclude that the electric energy density will saturate as $1/l^3$ at short distances.

To better interpret the obtained results, we plot the function $f(\omega, K) = 4\text{Im}(r_{31}^P)^2 e^{-[\text{Re}^2(\gamma_2) + K^2]l^2/4} / |1 - (r_{31}^P)^2|^2$ by considering $d=0$ for the local case ($l=0$) and the cases where $l = 1r_0, 3r_0, 6r_0, 8r_0$ and $10r_0$, as shown in Fig. 3.16. We note that the case when $l=0$ corresponds to the local case. Comparing the graph of the local case and that of the case when $l = r_0$, we notice that for both spectrums the maximum values are obtained for $\omega = \omega_{TO}$ and $\omega = \omega_{LO}$. As K increases, the spectrum of the local case increases while that of the nonlocal case ($l = r_0$) decreases in magnitude as K increases explaining by that the saturation obtained by the RHTC graph. Examining the other curves we notice that for any l , the maximum values of the spectrum are always obtained for $\omega = \omega_{TO}$ and $\omega = \omega_{LO}$ and the spectrum decrease as K increases. On the other side, we also notice that as l increases the range of values of the spectrum's magnitude decreases; this implies that the saturation takes place at smaller K and larger distances, which explains the increase of the distance at which saturation of the RHTC starts (Fig. 3.15).

As we have shown above, the saturation of the RHTC depends on the value of l where the distance at which the saturation started is of the order of the value of l . In order to check the relation between the value of the RHTC at saturation and the coherence length l , we plot the variation of the saturation values of the RHTC as l varies Fig. 3.17.

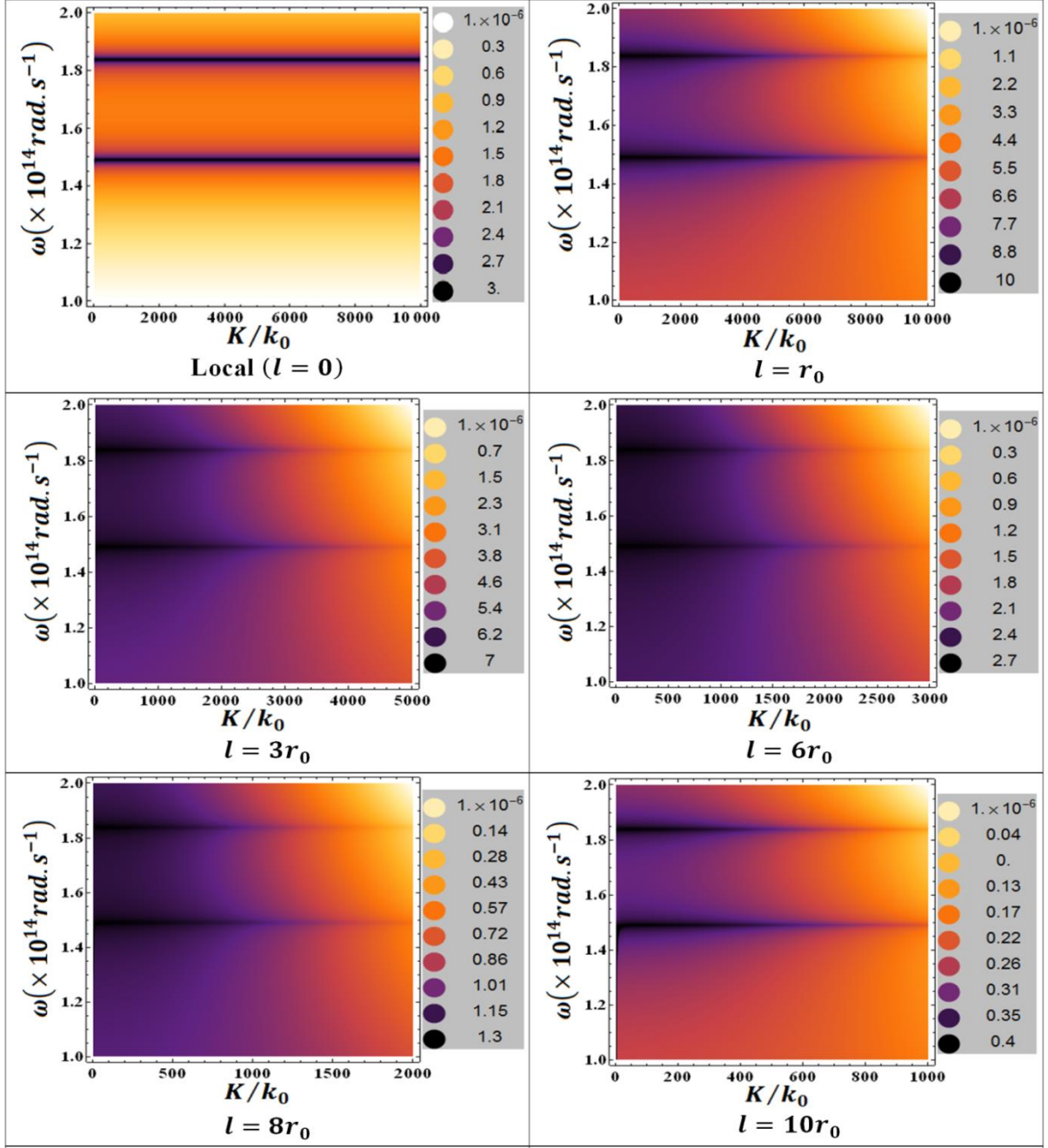


Figure 3.16: Plot of the function $f(\omega, K) = 4Im(r_{31}^P)^2 e^{-[Re^2(\gamma_2)+K^2]l^2/4} / |1 - (r_{31}^P)^2|^2$ of the p -polarized evanescent EM waves in the plane (ω, K) for the local case ($l=0$) and the third suggested nonlocal cases ($l = 1r_0, 3r_0, 6r_0, 8r_0$ and $10r_0$).

From the plot of Fig. 3.17 we are able to deduce a relation between the saturation value of the RHTC and l , depending on the inverse of l^2 :

$$h_{rad} \approx 5.25 \times 10^{-13} / l^2 \quad (3.36)$$

We notice from Fig. 3.17 that the saturation value decreases as l increases. This would lead us to conclude that the coherence length would not only affect the distance at which the saturation of the RHTC occurs, but it also affects the value of this saturation.

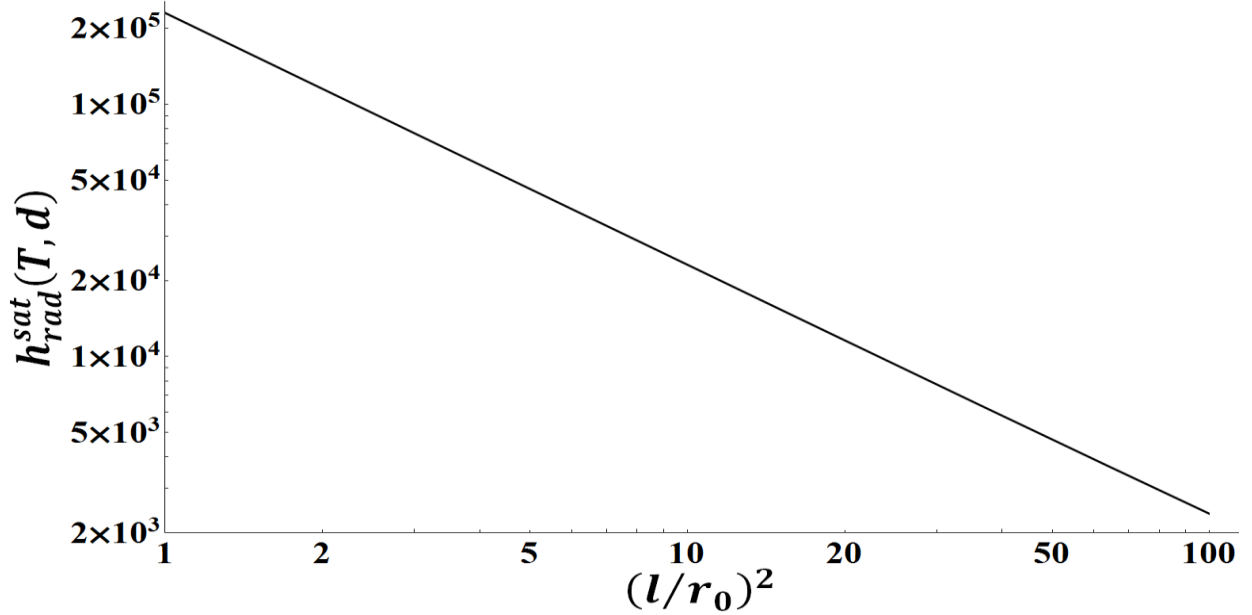


Figure 3.17: Variation of the saturation value of the RHTC between two semi-infinite parallel 6H-SiC planes of average temperature $T=300\text{K}$, as function of the coherence parameter l .

We are interested in the study of the variation of the RHTC of the contribution of the evanescent EM waves of p polarization in the large K limit. For this reason we derived analytically the limit of this coefficient for large K values as to finally obtain a simplified expression depending on the temperature parameter T and the coherence length l . Starting from Eq. (3.29):

$$h_{evan}^p(T, \omega, d, l) = h^0(T, \omega) \times \int_{k_0}^{+\infty} \frac{Kdk 4[Im(r_{3m}^p)]^2 e^{2i\gamma_3 d} \times e^{-[Re^2(\gamma_2)+K^2]l^2/4}}{k_0^2 |1 - (r_{3m}^p)^2 e^{2i\gamma_3 d}|^2} \quad (3.37)$$

and taking into account the following limits:

$$\left\{ \begin{array}{l} d \approx 0 \\ K \gg k_0 \\ Re^2(\gamma_2) \ll K \\ r_{3m}^p \approx \frac{\epsilon_m - 1}{\epsilon_m + 1} \end{array} \right\} \quad (3.38)$$

Eq. (3.37) becomes:

$$h_{evan}^p(T, \omega, l) \approx h^0(T, \omega) \times \frac{4[Im(r_{3m}^p)]^2}{k_0^2 |1 - (r_{3m}^p)^2|^2} \int_0^{+\infty} Kdk e^{-K^2 l^2/4} \quad (3.39)$$

Solving the integral we obtain:

$$h_{evan}^p(T, l) \approx \int_0^{+\infty} d\omega h^0(T, \omega) \times \frac{8[Im(r_{3m}^p)]^2}{l^2 k_0^2 |1 - (r_{3m}^p)^2|^2} \quad (3.40)$$

Substituting with the expression of the reflection factor:

$$h_{evan}^p(T, \omega, l) \approx \frac{8}{l^2} \int_0^{+\infty} d\omega \frac{h^0(T, \omega)}{k_0^2} \times \frac{\left[Im\left(\frac{\varepsilon_m - 1}{\varepsilon_m + 1}\right)\right]^2}{\left|1 - \left(\frac{\varepsilon_m - 1}{\varepsilon_m + 1}\right)^2\right|^2} \quad (3.41)$$

To simplify the term involving the dielectric permittivity expression, we assume that generally

ε_m is given as a complex expression defined as $\varepsilon_m = \varepsilon_{Re} + i\varepsilon_{Im}$. This lead us to obtain:

$$\frac{\left[Im\left(\frac{\varepsilon_m - 1}{\varepsilon_m + 1}\right)\right]^2}{\left|1 - \left(\frac{\varepsilon_m - 1}{\varepsilon_m + 1}\right)^2\right|^2} = \frac{[Im(\varepsilon_m)]^2}{4|\varepsilon_m|^2} \quad (3.42)$$

The final form obtained for the RHTC of the contribution of the EM evanescent waves of p polarization, for the limits of large K and zero distance is:

$$h_{rad}^{evan p}(T, l) \approx \frac{8}{l^2} \int_0^{+\infty} d\omega \frac{h^0(T, \omega)}{k_0^2} \times \frac{[Im(\varepsilon_m)]^2}{4|\varepsilon_m|^2} \quad (3.43)$$

Eq. (3.43) shows that the simplified form of the saturation value of the RHTC depends on the average temperature of the system T and the coherence length l . In Fig. 3.18, we show the plot of $h_{rad}^{evan p}(T, l)$ expressed in $W m^{-2} K^{-1}$ as function of the temperature average T for the cases where $l = 1r_0, 5r_0$ and $10r_0$. From this figure, we note that for a certain value of l , $h_{rad}^{evan p}(T, l)$ increases as the temperature increases. Comparing the plots for different values of l , we note that for the same range of temperature variation, the magnitude of $h_{rad}^{evan p}(T, l)$ decreases as the value of the coherence length l increases. This result is expected as we can see in Eq. (3.43) that $h_{rad}^{evan p}(T, l)$ is inversely proportional to l^2 .

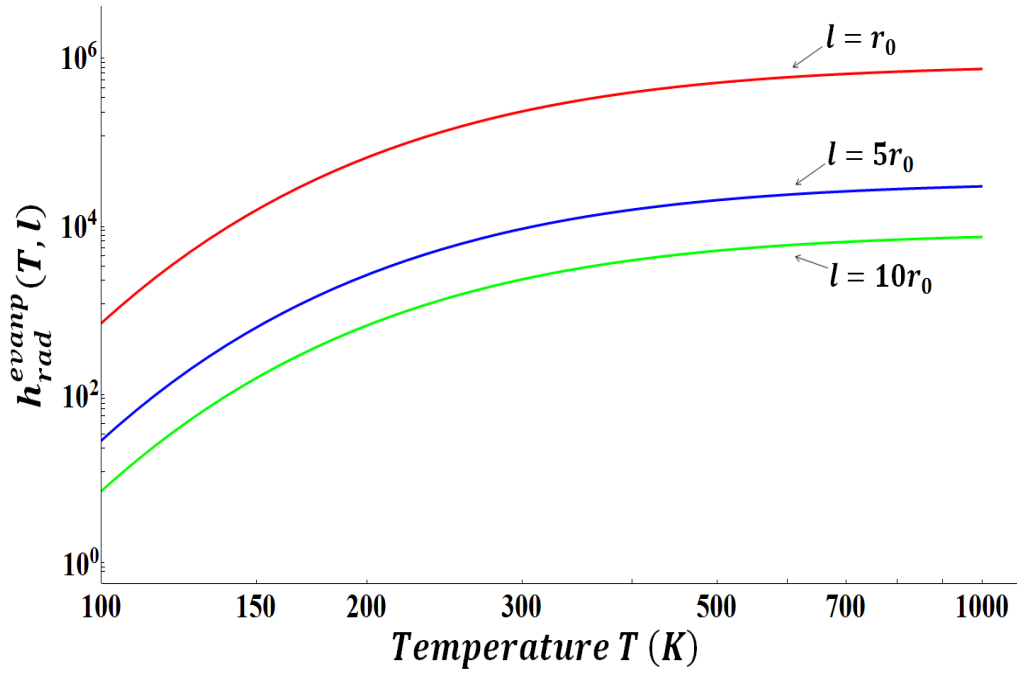


Figure 3.18: Variation of $h_{rad}^{evap}(T, l)$ as function of the average temperature T for the cases when $l = 1r_0, 5r_0$ and $10r_0$.

Conclusions

We have shown in this chapter that applying a nonlocal model of the dielectric permittivity in the study of the RHTC between two semi-infinite parallel planes of 6H-SiC would lead to incomplete saturation that replaces the $1/d^2$ nonphysical infinite divergence obtained using the local model as the separation distance d decreases. The first and the second nonlocal models were inspired from the model of Kliewer and Fuchs [5]. We considered in the first model that the transverse component of the dielectric permittivity is local, while the longitudinal term is local for all wavevectors smaller than the limit of the first Brillouin zone (FBZ), and for larger wavevectors, the longitudinal response was considered equal to one. In the second model a similar formalism was considered in which the transverse and the longitudinal components were considered equal and local for all wavevectors smaller than the limit of the FBZ, and considered equal to one for larger wavevectors.

The results of these models were similar and the graph of the RHTC due to the contribution of the evanescent EM waves of p -polarization deviated from the infinite diverging graph obtained in the local case, but it showed a logarithmic divergence as the distance d decreases. We noticed that the limit of the FBZ affects the distance at which this deviation takes place where in the first model it starts at distances of the order of the lattice constant, and in the second model it starts at distances just before the lattice constant. The plots of the transmission factors in the (ω, K) plane for $d=0$ confirmed the obtained results and showed that the number of modes contributing to the transfer decreases (in a slow rate) as K increases in the nonlocal cases. We also showed that upon changing the value of the limiting perpendicular wavevector q after which the optical response changes from local to nonlocal, the value of the wavevector at which the transmission factor for $d=0$ decreases drastically, shifts in a way that it is always equal to this limiting value of q .

The third nonlocal model was inspired from the work of Henkel and Joulain [11] where it is supposed that the EM field above the dielectric medium acquires a coherence length l of the order or larger than the lattice constant. We showed that upon introducing this length in the correlation equation of the fluctuating currents, the derived RHF equation was dependent on l and the RHTC between the two 6H-SiC planes saturated at distances of the order of the coherence length l . Upon changing the value of l the saturation distance changed but in all cases it was equal to l . We showed that the value of the saturated RHTC decreases as the

value of l increases. We derived also an analytic simplified form of the saturation value of the RHTC due mainly to the contribution of the evanescent EM waves of p polarization. We found that this saturation value is inversely proportional to l^2 with a T -dependent coefficient. We found that as l increases, the values attained by the spectrum as function of T decrease. On the other hand, we showed that the electric energy density is dependent on l and saturates as $1/l^3$ at very small distances.

References

1. Z. Levine and S. Louie, *Phys. Rev. B* **25**, 10 (1982).
2. H. Rodríguez-Coppola, L. M. Gaggero-Sager, M. E. Mora-Ramos, and R. Pérez-Álvarez, *J. Appl. Phys.* **108**, 083717 (2010).
3. E. H. Hwang and S. Das Sarma, *Phys. Rev. B* **75**, 205418 (2007).
4. O. Jenkins and K. Hunt, *J. Chem. Phys.* **119**, 8250 (2003).
5. K. L. Kliewer and R. Fuchs, Theory of dynamical properties of dielectric surfaces, *Advance in Chemical Physics*, Vol. XXVII, ed. I. Prigogine, Stuart A. Rice by John Wiley & Sons. (1974).
6. Crystal Lattice Dynamics of Various Silicon-Carbide Polytypes *International Conference on Solid State Crystals 2000: Growth, Characterization, and Applications of Single Crystals Held in Zakopane, Poland on 9-12 October 2000*.
7. H. Duan, A. I. Fernández-Domínguez, M. Bosman, S. A. Maier and J. K. W. Yang, *Nano Lett.*, **12**, 1683 (2012).
8. J.A. Scholl, A.I. Koh and J.A. Dionne, *Nature*, **483**, 421 (2012).
9. F. Javier Garcia de Abajo, *Nature*, **483**, 417 (2012).
10. S. Xiong, K. Yang, Y. A. Kosevich, Y. Chalopin, R. D'Agosta, P. Cortona and S. Volz, *Phys. Rev. Lett.*, **112**, 114301 (2014).
11. C. Henkel and K. Joulain, *Appl. Phys. B* **84**, 61-68 (2006).

Chapter 4

4. Nonlocal model of the dielectric permittivity for dielectrics: Halevi–Fuchs theory

Introduction

In this chapter we present a fourth nonlocal model of the dielectric permittivity for dielectrics. We study the RHT between two semi-infinite 6H-SiC parallel planes using a macroscopic nonlocal dielectric permittivity theory suggested by Halevi and Fuchs [1]. According to this theory, the nonlocal dielectric function is described by a Lorentz–Drude like single oscillator model, in which the spatial dispersion effects are represented by an additional term depending on the square of the total wave vector k . The theory takes into account the scattering of the EM excitation at the surface of the dielectric material, which leads to the need of additional boundary conditions (ABC) in order to solve Maxwell’s equations and treat the EM transmission problem. These ABC lead to the introduction of additional surface scattering parameters (SSP) in the expressions of the surface impedances. Different sets of the SSP were suggested by different authors and used in the derivation of the expressions of the surface impedances and the reflection factors of the EM at the surface of the dielectrics. By using these derived expressions, we will show that the nonlocal modeling deviates from the classical $1/d^2$ law in the nanometer range at distances larger than the ones where quantum effects are expected to come into play. It is shown that at ultimately small distances the flux saturates.

In the first section we will explain the foundation of this model and we will present in details its formalism. The following section will be devoted to the results obtained along with the interpretations and the discussions. The conclusions will be presented in the last section.

4.1 Nonlocal macroscopic dielectric permittivity function theory

The theory proposed by Halevi and Fuchs is based on two main physical phenomena: the spatial dispersion and the EM excitation at the surface of the dielectric medium. Each of these phenomena imposes different conditions on the equations applied in this model.

The spatial dispersion effects affect in a direct way the expression of the dielectric permittivity considered in the study. One of the simplest modeling of the latter is to use the single oscillator model in combination with the so-called hydrodynamic model [2,3]. The latter model has been used in a large variety of forms and in the case considered by Halevi and Fuchs the dielectric permittivity is expressed as a sum over resonances, each resonance occurring at a particular frequency; the spatial dispersion effects, i.e. the nonlocal dielectric behavior, are considered as the effect of the wave-vector dependence of the resonant frequencies on optical properties. By this, the spatial dispersion effects were represented in the dielectric function expression as an additional term dependent on the square of the total wavevector k (Eq. 4.1). In Halevi–Fuchs modeling, a spatial dispersion parameter $D = \hbar\omega_T/(m_e + m_h)$ is introduced, where ω_T is the frequency of an isolated transition (for example an exciton), and m_e and m_h are the electron and hole masses, respectively. D is typically related to a diffusion phenomenon of the carriers in the medium and it is homogeneous to the square of a velocity. Under these assumptions, the nonlocal dielectric permittivity equation is given as:

$$\varepsilon(\omega, k) = \varepsilon_\infty \left(1 + \frac{\omega_p^2}{\omega_T^2 - \omega^2 - i\nu\omega + Dk^2} \right) \quad (4.1)$$

where $\varepsilon_\infty = 6.7$ is the infinite frequency permittivity representing the contribution of the ions of the crystal lattice to the polarization for SiC. k is the total wavevector such that $k^2 = K^2 + q^2$, K and q are, respectively, the parallel and perpendicular wavevector components to the dielectric material interface. The frequency ω_p is a measure of the oscillator strength and ν represents the losses parameter. In the case of 6H-SiC, the parameters in Eq. (4.1) are assigned the following values: $D = 1.77 \times 10^{10} m^2 \cdot s^{-2}$, $\omega_p = 1.049 \times 10^{14} rad \cdot s^{-1}$, $\omega_T = 1.49 \times 10^{14} rad \cdot s^{-1}$ and $\nu = 8.97 \times 10^{11} rad \cdot s^{-1}$ [4].

Taking into consideration the EM excitation at the surface and the nonlocality, Halevi and Fuchs showed that an incoming transverse EM wave gives birth not only to a single transverse wave in the material, as in the local case, but also to a second transverse wave and a supplementary longitudinal wave (Fig. 4.1). In this case, the usual boundary conditions on the

continuity of the tangential components of the electric field \mathbf{E} and the magnetic field \mathbf{H} , are not sufficient to solve the transmission problem of Maxwell's equations [1,5]. To better explain this idea, we will discuss both the local and the nonlocal cases separately as it is first considered that the solutions of Maxwell's equations in the nonlocal medium are plane waves, and the fields depend on the vertical distance z above the nonlocal medium through the exponential term $\exp(iqz)$.

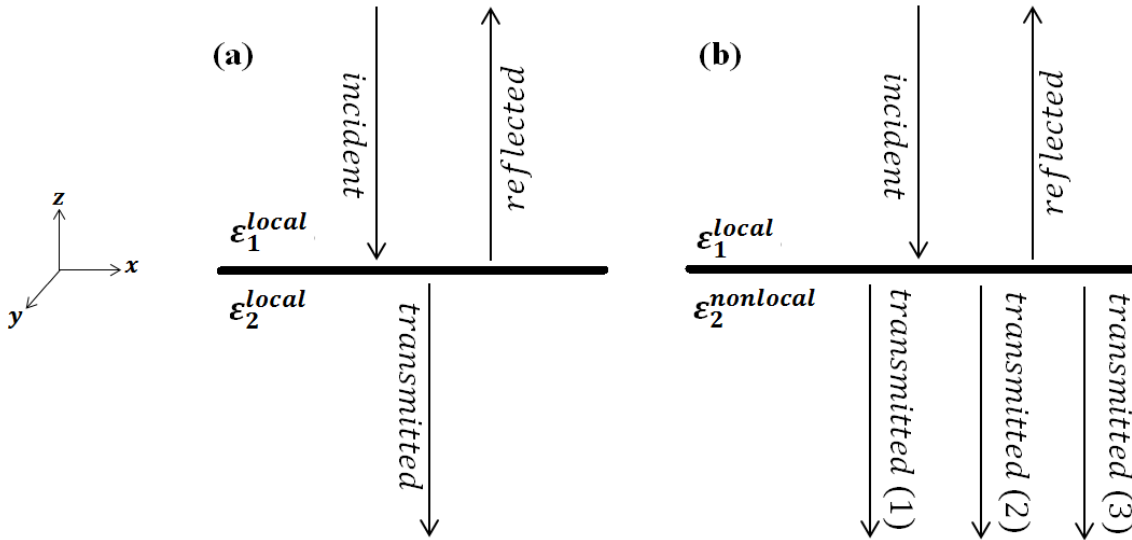


Figure 4.1: A schematic diagram showing the incidence of an EM wave on the interface separating the local medium (vacuum) from the local dielectric medium (a), and the nonlocal dielectric medium (b). In the former case where $D=0$, the incident EM wave gives birth to one transmitted transverse wave. In the latter case where $D \neq 0$, the incident wave gives birth to two transmitted transverse wave and one additional longitudinal wave (if the incident wave is p -polarized).

In the local case, where $D=0$ in Eq. 4.1, there is only one solution for q corresponding to a transverse wave with $\nabla \cdot \mathbf{E} = 0$; and therefore solving for the amplitudes of the reflected and the transmitted waves is done using the very known Maxwell boundary conditions, i.e. the continuity of the tangential components of \mathbf{E} and \mathbf{H} across the interface.

In the nonlocal case where $D \neq 0$, two transverse waves are born in the non-local medium, and if the incident wave is p -polarized there is in addition a longitudinal wave with $\nabla \times \mathbf{E} = 0$. In this case, Maxwell boundary conditions considered in the local case are insufficient to solve for the unknown amplitudes of the reflected wave and the three transmitted waves. This leads to the importance of having additional relations between the amplitudes. These relations are then given as ABC.

4.2 Formalism

In the literature, several ABC have been proposed. Halevi and Fuchs [1] have suggested a theory in which all ABC, typically conditions on the component of polarization or its derivatives at the boundary, developed by different authors are included. The advantage of this theory is that it includes the main nonlocal modeling developed in literature. The ABC take the following forms as conditions on the polarization $\boldsymbol{\rho}$ at the interface [1] which allows obtaining relations between the amplitudes of the waves (three transmitted waves and one reflected wave). For the p -polarized EM, waves the ABC are given (in SI units) by:

$$\left\{ \begin{array}{l} \alpha_j \mathbb{P}(0^+) + \beta_j \frac{\partial \mathbb{P}_j(0^+)}{\partial z} = 0 \quad j = x, z \\ \mathbb{P} = \boldsymbol{\rho} - \varepsilon_0(\varepsilon_\infty - 1)\mathbf{E} \end{array} \right\} \quad (4.2)$$

where \mathbb{P} denotes the excitation polarization (for example an exciton or any resonance). It represents the scattered polarization components, excluding the dielectric polarization of the background. For s -polarized EM wave, one has a similar equation for $\rho_y(z)$. These ABC therefore necessitate a choice of the ratio α_i/β_i of the parameters α_i and β_i . Different choices correspond to different SSP, imposed in the expressions of the surface impedances and the reflection factors coefficients of the system Eq. (4.3). These parameters are related to the complex reflection amplitude from the surface, and they depend on the nature of the polarization of the EM field where U_y is defined for the EM waves of s polarization, while U_x and U_z are defined for the EM waves of p polarization. The U parameters have a direct physical interpretation as they are considered complex numbers that describe the way in which the excitation is reflected by the surface. Halevi and Fuchs have made a correspondence between the SSP values and the ABC given by different authors (see Table 1 on page 97).

$$\left\{ \begin{array}{l} \frac{\alpha_j}{\beta_j} = i\Gamma \frac{1 - U_j}{1 + U_j} \quad j = x, z \\ \Gamma = [(\omega^2 - \omega_T^2 + i\nu\omega - DK^2)/D]^{1/2} \end{array} \right\} \quad (4.3)$$

The importance of these suggested SPP lies in the dependence of the expressions of the reflection factors and the surface impedances on their values.

We proceed now to derive these expressions by first defining the wave equation given by:

$$\nabla \times (\nabla \times \mathbf{E}) + \mu_0 \frac{\partial^2 \mathbf{D}}{\partial t^2} = 0 \quad (4.4)$$

with its plane-wave solution given by

$$\mathbf{E} = E_0 e^{i(\mathbf{k}\cdot\mathbf{r}-\omega t)} \quad (4.5)$$

while the frequency and the wavevector must satisfy the following dispersion relations for the transverse waves ($\mathbf{E} \cdot \mathbf{k} = 0$) and the longitudinal waves ($\mathbf{E} \times \mathbf{k} = 0$), respectively:

$$\left\{ \begin{array}{l} \varepsilon(\omega, \mathbf{k}) = \frac{k^2}{k_0^2} = \frac{K^2 + q^2}{k_0^2} \\ \varepsilon(\omega, \mathbf{k}) = 0 \end{array} \right\} \quad (4.6)$$

In the local case where $D=0$, only the transverse mode is excited so that the transverse waves equation will give one solution for q and the longitudinal waves equation will give no solutions. In this case and as we mentioned before, Maxwell's continuity conditions are sufficient for the calculation of the electric field amplitude. In the nonlocal case where $D \neq 0$, the first equation gives two solutions, q_1 and q_2 , while the second equation gives an additional third solution q_3 . The electric field in the non-local medium is thus given as a linear combination of three partial waves with q_1 , q_2 and q_3 :

$$\mathbf{E}(\mathbf{r}, t) = [\mathbf{E}^{(1)} e^{iq_1 z} + \mathbf{E}^{(2)} e^{iq_2 z} + \mathbf{E}^{(3)} e^{iq_3 z}] e^{i(Kx - \omega t)} \quad (4.7)$$

In this case Maxwell's continuity conditions are insufficient to calculate the ratios of the amplitudes needed for the calculation of the reflection factors. This leads to the need of proposing ABC.

As we mentioned in the introduction, the proposed ABC and the nonlocality are presented in the equations as SSP on which the amplitudes of the electric field depend. To define these SSP, we first substitute in the wave equation Eq. (4.4) with the displacement vector using the following equation $\boldsymbol{\rho} = \mathbf{D} - \varepsilon_0 \mathbf{E}$:

$$\nabla^2 \mathbf{E} - \frac{1}{c^2} \frac{\partial^2 \mathbf{E}}{\partial t^2} = \mu_0 \frac{\partial^2 \boldsymbol{\rho}}{\partial t^2} \quad (4.8)$$

The linear response relation between \mathbf{E} and $\boldsymbol{\rho}$ is given by:

$$\left\{ \begin{array}{l} \boldsymbol{\rho}(z) = \int_0^\infty \varepsilon_0 \tilde{\chi}(z, z') \mathbf{E}(z') dz' \\ \tilde{\chi}_{ij}(z, z') = [\chi(z - z') + U_i \chi(z + z')] \delta_{ij} \\ \chi(\zeta) = \frac{1}{2\pi} \int_{-\infty}^\infty \chi(q) e^{iq\zeta} dq \quad \zeta = z \pm z' \\ \chi(q) = \frac{\varepsilon(\omega, \mathbf{k})}{\varepsilon_0} - 1 \end{array} \right\} \quad (4.9)$$

where $\tilde{\chi}(z, z')$ is the explicit form of the susceptibility tensor. It depends on the model considered in the study and for this model it is defined as a function of the Fourier transforms of the bulk susceptibility $\chi(q)$, $\chi(z - z')$ and $\chi(z + z')$.

$\chi(z - z')$ depends only on the distance between the points r and r' and it refers to the non-local bulk response where the surface shows no effect when an excitation propagates directly from r' to r . $\chi(z + z')$ on the other hand refers to the nonlocal response of the surface as it depends on the distances from the surface to r and r' . In this case the excitation propagates from the point r' towards the surface, where it is reflected, and then continues to the point r , as illustrated in Fig. 4.2 [1].

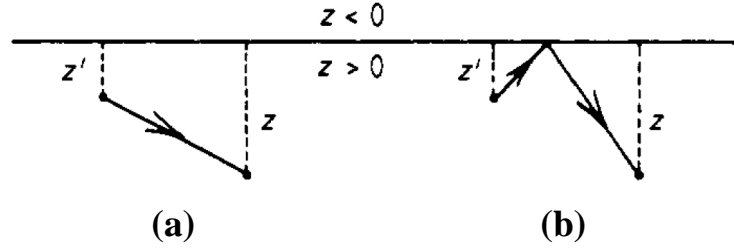


Figure 4.2: A schematic diagram showing that an excitation at a point r' produces a response at a point r . The bulk response (a) is direct and depends on $z - z'$. The surface response (b) is indirect and depends on $z + z'$ [1].

Eqs. (4.9) reflect the physical interpretation of the SSP and their contribution to the formalism as they appear in the susceptibility $\tilde{\chi}_{ij}$ and the dependence of the amplitudes needed on the values of these parameters U .

Using the nonlocal expression of the dielectric permittivity Eq. (4.1) allows calculating easily q_1 , q_2 and q_3 , and simplifying the expressions of $\chi(q)$ and $\chi(\zeta)$:

$$\left\{ \begin{array}{l} \chi(q) = \left(\frac{\epsilon_\infty}{\epsilon_0} - 1 \right) + \frac{\omega_p^2 \epsilon_\infty / \epsilon_0 D}{q^2 - \Gamma^2} \\ \chi(\zeta) = \left(\frac{\epsilon_\infty}{\epsilon_0} - 1 \right) \delta(\zeta) + \frac{i\omega_p^2 \epsilon_\infty / \epsilon_0}{2D\Gamma} e^{i\Gamma|\zeta|} \end{array} \right\} \quad (4.10)$$

We proceed now in the calculations to derive the reflection factors, of both the waves of s and p polarization.

p-polarized EM wave

For the EM waves of p-polarization the following conditions apply:

$$\left\{ \begin{array}{l} E_x \neq 0 \\ E_y = 0 \\ E_z \neq 0 \end{array} \right\} \quad (4.11)$$

Substituting these equations in the expression of Eq. (4.7) and calculating then $\boldsymbol{\rho}$ of Eq. (4.9) using Eq. (4.10) we obtain :

$$\rho_j(z) = \int_0^\infty \left[\varepsilon_0 \left(\frac{\varepsilon_\infty}{\varepsilon_0} - 1 \right) \delta(z - z') + \frac{i\omega_p^2 \varepsilon_\infty}{2D\Gamma} e^{i\Gamma|z-z'|} + U_j \frac{i\omega_p^2 \varepsilon_\infty}{2D\Gamma} e^{i\Gamma|z+z'|} \right] \\ \times \sum_{\eta=1}^3 E_j^{(\eta)} e^{iq_\eta z'} dz' \quad j = x, z \quad (4.12)$$

For the second term on the left-hand side we split the range of integration into two parts: from 0 to z , and from z to ∞ . This allows us to obtain:

$$\rho_j(z) = \sum_{\eta=1}^3 \left(\varepsilon_\infty - \varepsilon_0 + \frac{\omega_p^2/D}{q_\eta^2 - \Gamma^2} \right) E_j^{(\eta)} e^{iq_\eta z} - \frac{\omega_p^2 \varepsilon_\infty}{2D\Gamma} \sum_{\eta=1}^3 \left(\frac{1}{q_\eta - \Gamma} + \frac{U_j}{q_\eta + \Gamma} \right) E_j^{(\eta)} e^{i\Gamma z} \quad j \\ = x, z \quad (4.13)$$

We continue by substituting Eqs. (4.7) and (4.13) in Eq. (4.8) while taking into consideration that the coefficient of the exponential term $e^{i\Gamma z}$ must vanish as for Eq. (4.8) to be satisfied for any z , we obtain the following equation representing the ABC allowing to calculate the amplitude ratios $E_j^{(\eta)}$:

$$\sum_{\eta=1}^3 \left(\frac{1}{q_\eta - \Gamma} + \frac{U_j}{q_\eta + \Gamma} \right) E_j^{(\eta)} = 0 \quad j = x, z \quad (4.14)$$

The polarization Eq. (4.13) and the excitonic polarization Eq. (4.2) could be then written as:

$$\left\{ \begin{array}{l} \boldsymbol{\rho}(z) = \sum_{\eta=1}^3 \varepsilon_0 \chi(q_\eta) \mathbf{E}^{(\eta)} e^{iq_\eta z} \\ \mathbb{P}(z) = \varepsilon_\infty (1 - \varepsilon_0) \sum_{\eta=1}^3 \mathbf{E}^{(\eta)} e^{iq_\eta z} + \frac{\varepsilon_\infty \omega_p^2}{D} \sum_{\eta=1}^3 \frac{1}{q_\eta^2 - \Gamma^2} \mathbf{E}^{(\eta)} e^{iq_\eta z} \end{array} \right\} \quad (4.15)$$

By using these equations we can easily deduce the following alternative form of the ABC equations:

$$i\Gamma(1 - U_j)\mathbb{P}_j(0^+) + (1 + U_j) \frac{d\mathbb{P}_j(0^+)}{dz} = 0 \quad j = x, z \quad (4.16)$$

To proceed in our derivation it is important to mention that the surface impedance of the p -polarized waves is defined as being the ratio of the electric field and the magnetic field at the interface:

$$Z_p = \frac{E_x(0^+)}{B_y(0^+)} \quad (4.17)$$

Substituting Eqs. (4.7) and the expression of $\rho(z)$ given by Eq. (4.15) in the wave equation Eq. (4.8) we obtain its x and z components given as:

$$\left\{ \begin{array}{l} \sum_{\eta=1}^3 \left\{ \left[k_0^2 (1 + \chi(q_\eta)) - q_\eta^2 \right] E_x^{(\eta)} + K q_\eta E_z^{(\eta)} \right\} e^{iq_\eta z} = 0 \\ \sum_{\eta=1}^3 \left\{ \left[k_0^2 (1 + \chi(q_\eta)) - K^2 \right] E_z^{(\eta)} + K q_\eta E_x^{(\eta)} \right\} e^{iq_\eta z} = 0 \end{array} \right\} \quad (4.18)$$

Taking into account that these equations must be valid for any z and making use of the relation Eq. (4.19) between the dielectric permittivity and the susceptibility, Eqs. (4.18) are simplified as follows:

$$\frac{\varepsilon_\eta}{\varepsilon_0} \equiv \frac{\varepsilon(q_\eta)}{\varepsilon_0} = 1 + \chi(q_\eta) \quad \eta = 1,2,3 \quad (4.19)$$

$$\left\{ \begin{array}{l} \left(k_0^2 \frac{\varepsilon_\eta}{\varepsilon_0} - q_\eta^2 \right) E_x^{(\eta)} + K q_\eta E_z^{(\eta)} = 0 \\ K q_\eta E_x^{(\eta)} + \left(k_0^2 \frac{\varepsilon_\eta}{\varepsilon_0} - K^2 \right) E_z^{(\eta)} = 0 \end{array} \right\} \quad \eta = 1,2,3 \quad (4.20)$$

For each value of η the determinant of Eqs. (4.20) must vanish since $E_x^{(\eta)}$ and $E_z^{(\eta)}$ are *nonzero*:

$$\varepsilon_\eta \left(k_0^2 \frac{\varepsilon_\eta}{\varepsilon_0} - K^2 - q_\eta^2 \right) = 0 \quad \eta = 1,2,3 \quad (4.21)$$

Taking into account that in this model the dielectric permittivity is given by Eq. (4.1):

$$\left\{ \begin{array}{l} k_0^2 \frac{\varepsilon_\eta}{\varepsilon_0} - K^2 - q_\eta^2 = 0 \quad \eta = 1,2 \\ \varepsilon_3 = 0 \end{array} \right\} \quad (4.22)$$

Using Eqs. (4.22) we simplify Eqs. (4.20) into the following forms:

$$\left\{ \begin{array}{l} E_z^{(\eta)} = -\frac{K}{q_\eta} E_x^{(\eta)} \\ E_z^{(3)} = \frac{q_3}{K} E_x^{(3)} \end{array} \right\} \quad \eta = 1,2 \quad (4.23)$$

which correspond to the following conditions for the transverse waves and the longitudinal waves, respectively:

$$\left\{ \begin{array}{l} \mathbf{q}^{(\eta)} \cdot \mathbf{E}^{(\eta)} = 0 \quad \eta = 1,2 \\ \mathbf{q}^{(3)} \times \mathbf{E}^{(3)} = 0 \end{array} \right\} \quad (4.24)$$

Using the Faraday law (Eq. (4.25)) we calculate the magnetic field, and since for p -polarized waves the y -component is the only non-vanishing term given by Eq. (4.26):

$$\nabla \times \mathbf{E} = -\frac{\partial \mathbf{B}}{\partial t} \quad (4.25)$$

$$B_y(z) = -\frac{i}{\omega} \left(\frac{dE_x(z)}{dz} - iKE_z(z) \right) \quad (4.26)$$

Using Eqs. (4.7), (4.22) and (4.23) we obtain:

$$B_y(z) = \frac{k_0^2}{\varepsilon_0 \omega} \sum_{\eta=1}^2 \frac{\varepsilon_\eta}{q_\eta} E_x^{(\eta)} e^{iq_\eta z} \quad (4.27)$$

Since the longitudinal wave is not accompanied by a magnetic field the term $\eta = 3$ is not given in Eq. (4.27). Substituting Eqs. (4.7) and (4.27) in the expression of the surface impedance Eq. (4.18) we obtain:

$$Z_p = \frac{E_x^{(1)} + E_x^{(2)} + E_x^{(3)}}{\frac{\varepsilon_1}{\varepsilon_0} \left(\frac{k_0}{q_1} \right) E_x^{(1)} + \frac{\varepsilon_2}{\varepsilon_0} \left(\frac{k_0}{q_2} \right) E_x^{(2)}} \quad (4.28)$$

Eq. (4.28) is the general form of the surface impedance. In the local medium where only transverse waves are found $E_x^{(2)} = E_x^{(3)} = 0$, which implies:

$$Z_p^{local} = \frac{q_1}{k_0 \frac{\varepsilon^{local}}{\varepsilon_0}} = \frac{\left(\frac{\varepsilon^{local}}{\varepsilon_0} - \frac{K^2}{k_0^2} \right)^{1/2}}{\varepsilon^{local} / \varepsilon_0} \quad (4.29)$$

where $\varepsilon^{local} = \varepsilon(k=0, \omega)$. To calculate Z_p for the nonlocal medium, we substitute Eqs. (4.23) in the ABC equations Eq. (4.14) as to first express $E_x^{(2)}$ and $E_x^{(3)}$ in terms of $E_x^{(1)}$ to obtain finally:

$$\left\{ \begin{array}{l} \sum_{\eta=1}^3 a_\eta E_x^{(\eta)} = 0 \\ \sum_{\eta=1}^3 b_\eta E_x^{(\eta)} = 0 \end{array} \right\} \quad (4.30)$$

where

$$\left\{ \begin{array}{l} a_\eta = \frac{1}{q_\eta - \Gamma} + \frac{U_x}{q_\eta + \Gamma} \\ b_\eta = \left(\frac{1}{q_\eta - \Gamma} + \frac{U_z}{q_\eta + \Gamma} \right) \mu_\eta \quad l = 1, 2, 3 \\ \mu_1 = -\frac{K}{q_1}, \mu_2 = -\frac{K}{q_2}, \mu_3 = \frac{q_3}{K} \end{array} \right\} \quad (4.31)$$

Solving Eqs. (4.30) for the field ratios we obtain:

$$\left\{ \begin{array}{l} \frac{E_x^{(2)}}{E_x^{(1)}} = \frac{(3,1)}{(2,3)} \\ \frac{E_x^{(3)}}{E_x^{(1)}} = \frac{(1,2)}{(2,3)} \\ (i,j) = a_i b_j - b_i a_j \end{array} \right\} \quad (4.32)$$

Substituting these equations in Eq. (4.28) we obtain the following form of the nonlocal surface impedance of p -polarized EM waves:

$$Z_p = \frac{(1,2) + (2,3) + (3,1)}{\frac{\varepsilon_1}{\varepsilon_0} \left(\frac{k_0}{q_1} \right) (2,3) + \frac{\varepsilon_2}{\varepsilon_0} \left(\frac{k_0}{q_2} \right) (3,1)} \quad (4.33)$$

The reflection factor of the p -polarized EM waves is given by the following expression:

$$r_p = \frac{Z_p - Z_p^{Local}}{Z_p + Z_p^{Local}} \quad (4.34)$$

By substituting Eqs. (4.29) and (4.33) in Eq. (4.34) we are able to calculate the reflection factor at the surface of the nonlocal medium.

s -polarized EM waves

For the EM waves of s polarization we repeat the same procedure as for the p -polarized EM waves except that we should consider $j=y$ and $\eta = 1,2$ and we obtain the following expressions for the ABC:

$$\left\{ \begin{array}{l} \sum_{\eta=1}^2 \left(\frac{1}{q_\eta - \Gamma} + \frac{U_y}{q_\eta + \Gamma} \right) = 0 \\ i\Gamma(1 - U_y)\mathbb{P}_y(0^+) + (1 + U_y) \frac{d\mathbb{P}_y(0^+)}{dz} = 0 \end{array} \right\} \quad (4.35)$$

To proceed in the derivation of the surface impedance expression, we should mention first that longitudinal waves are absent for s polarization which implies that $E^{(3)} = 0$. Taking into consideration Eqs. (4.36), the magnetic field is given as follows:

$$\left\{ \begin{array}{l} E_x = 0 \\ E_y \neq 0 \\ E_z = 0 \end{array} \right\} \quad (4.36)$$

$$B_x(z) = \frac{i}{\omega} \frac{dE_y(z)}{dz} = -\frac{q_1}{\omega} E_y^{(1)} e^{iq_1 z} - \frac{q_2}{\omega} E_y^{(2)} e^{iq_2 z} \quad (4.37)$$

Using Eqs. (4.7) and (4.37), the surface impedance is given by:

$$Z_s = -\frac{E_y(0^+)}{B_x(0^+)} = \frac{k_0(E_y^{(1)} + E_y^{(2)})}{q_1 E_y^{(1)} + q_2 E_y^{(2)}} \quad (4.38)$$

In the local medium $E_y^{(2)} = 0$, this implies that:

$$Z_s^{Local} = \frac{k_0}{q_1} \quad (4.39)$$

Using the ABC equation we calculated the needed amplitude ratio:

$$\frac{E_y^{(2)}}{E_y^{(1)}} = -\frac{a_1}{a_2} \quad (4.40)$$

Substituting this equation in Eq. (4.38) we obtain the general form of the surface impedance of the nonlocal medium Eq. (4.41) which we substitute then in the expression of the reflection factor Eq. (4.42) to calculate its value:

$$Z_s = \frac{k_0(a_1 - a_2)}{q_2 a_1 - q_1 a_2} \quad (4.41)$$

$$r_s = \frac{Z_s - Z_s^{Local}}{Z_s + Z_s^{Local}} \quad (4.42)$$

4.3 Calculation of the radiative heat transfer coefficient

As we obtained the expressions of the reflection factors of the EM waves of s and p polarizations in the previous section, we substitute them in Eqs. (1.13) to calculate the different contributions to the RHTC between two solid semi-infinite parallel planes of 6H-SiC as the distance between them decreases. In our calculations, we substituted with the SSP values given in Table 1. This table gathers the different values proposed by the different authors mentioned in the review paper of Halevi and Fuchs [1]. Then we repeat the RHTC calculation for each set of values.

In figures 4.3–4.7 we present the plots obtained for the different contributions to the RHTC using the five ABC sets proposed by the different authors, and the plots of the total contribution to the RHTC for each ABC set in comparison with the plot of the local model.

Table 1 : Five different sets of surface scattering parameters proposed in literature.

ABC	U_x	U_y	U_z
Kliwer and Fuchs [6–10]	1	1	−1
Rimbey and Mahan [11–15]	−1	−1	1
Pekar [16–19]	−1	−1	−1
Ting et al. [9]	1	1	1
Agarwal et al. [20–29]	0	0	0

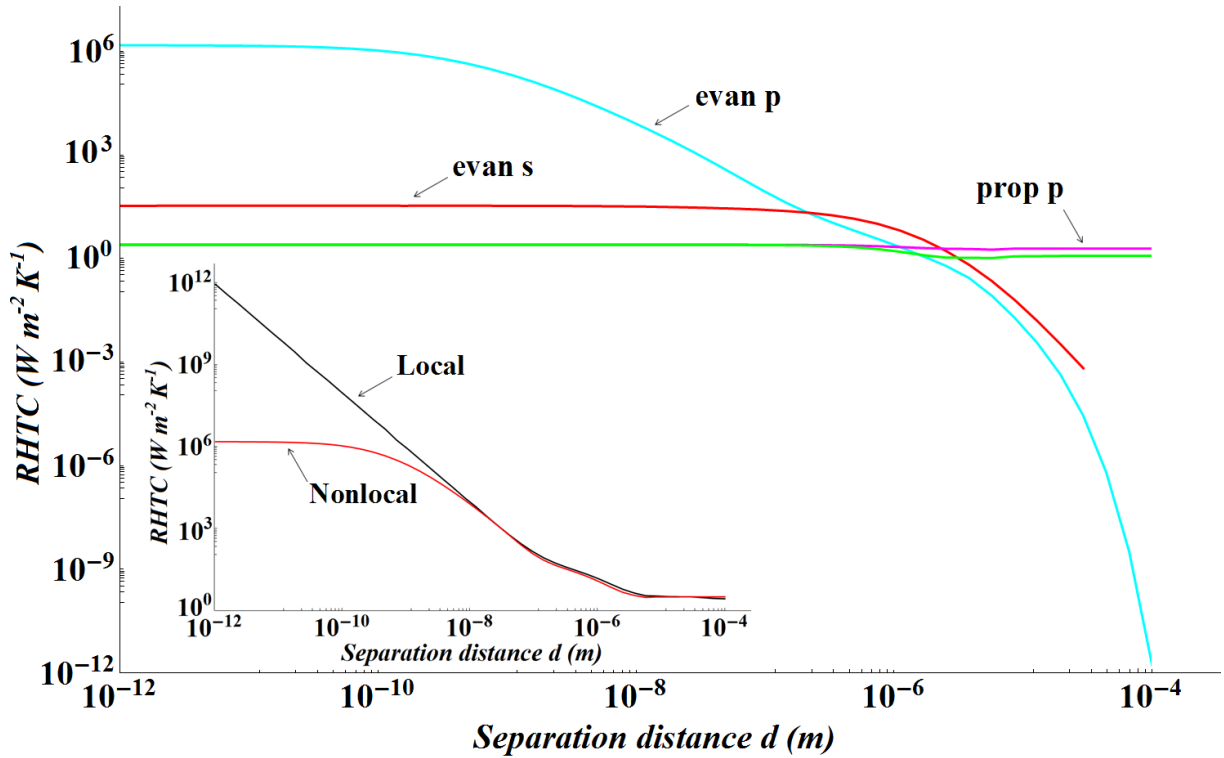


Figure 4.3: Variation of the RHTC (contributions of the evanescent and propagative EM waves of s and p polarizations) between two semi-infinite 6H-SiC parallel planes of average temperature $T=300K$, for the nonlocal model of Rimbey–Mahan ABC. Inset: variation of the total RHTC for the nonlocal model of Rimbey–Mahan ABC in comparison with the local model.

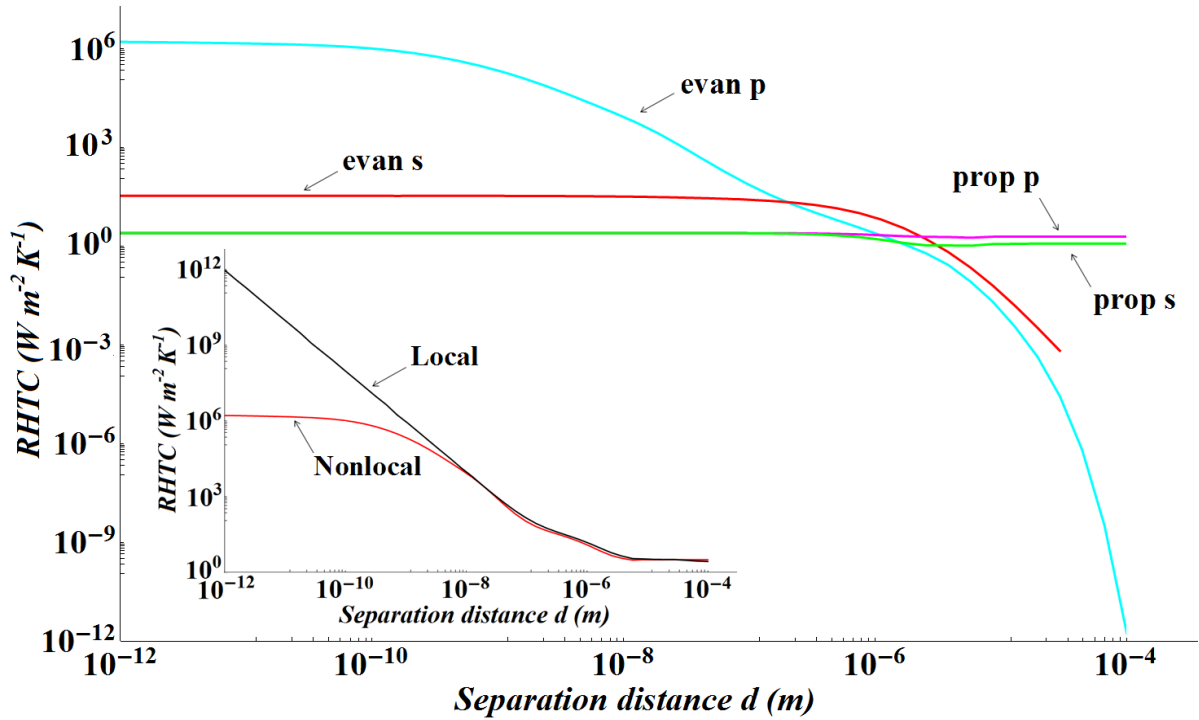


Figure 4.4: Variation of the RHTC (contributions of the evanescent and propagative EM waves of s and p polarizations) between two semi-infinite 6H-SiC parallel planes of average temperature $T=300\text{K}$, for the nonlocal model of Agarwal ABC. Inset: variation of the total RHTC for the nonlocal model of Agarwal ABC in comparison with the local model.

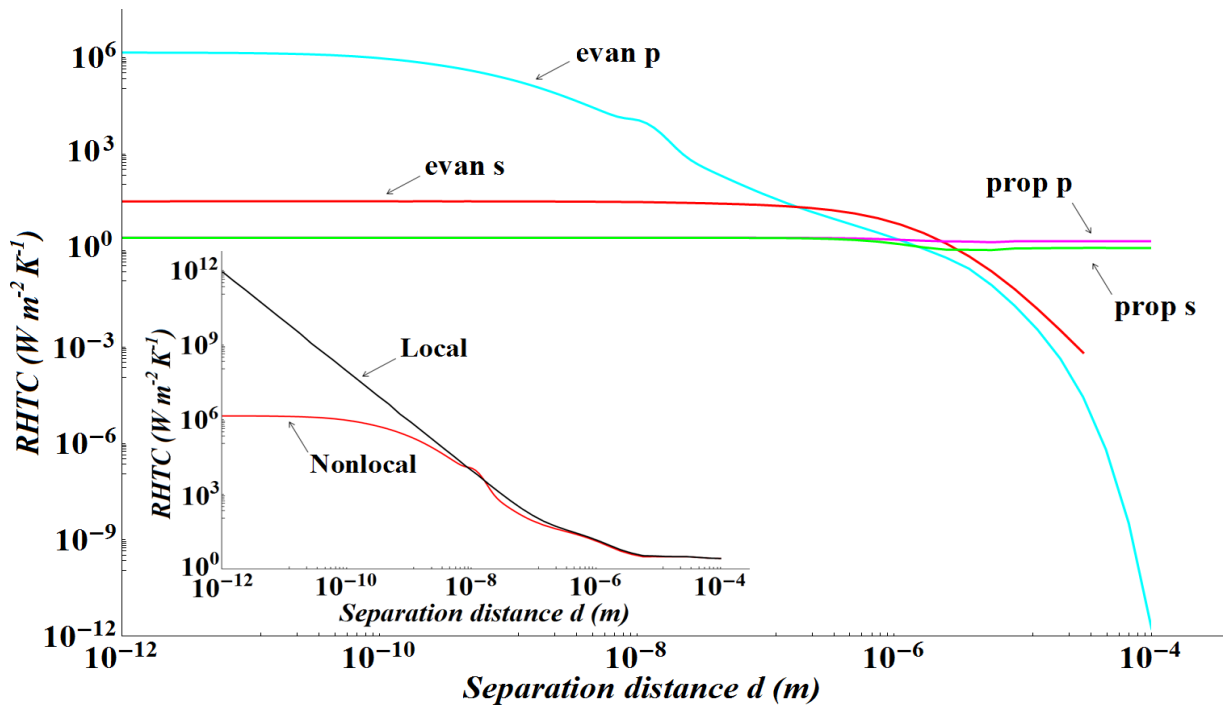


Figure 4.5: Variation of the radiative heat transfer coefficient (contributions of the evanescent and propagative EM waves of s and p polarizations) between two semi-infinite 6H-SiC parallel planes of average temperature $T=300\text{K}$, for the nonlocal model of Ting ABC. Inset: variation of the total RHTC for the nonlocal model of Ting ABC in comparison with the local model.

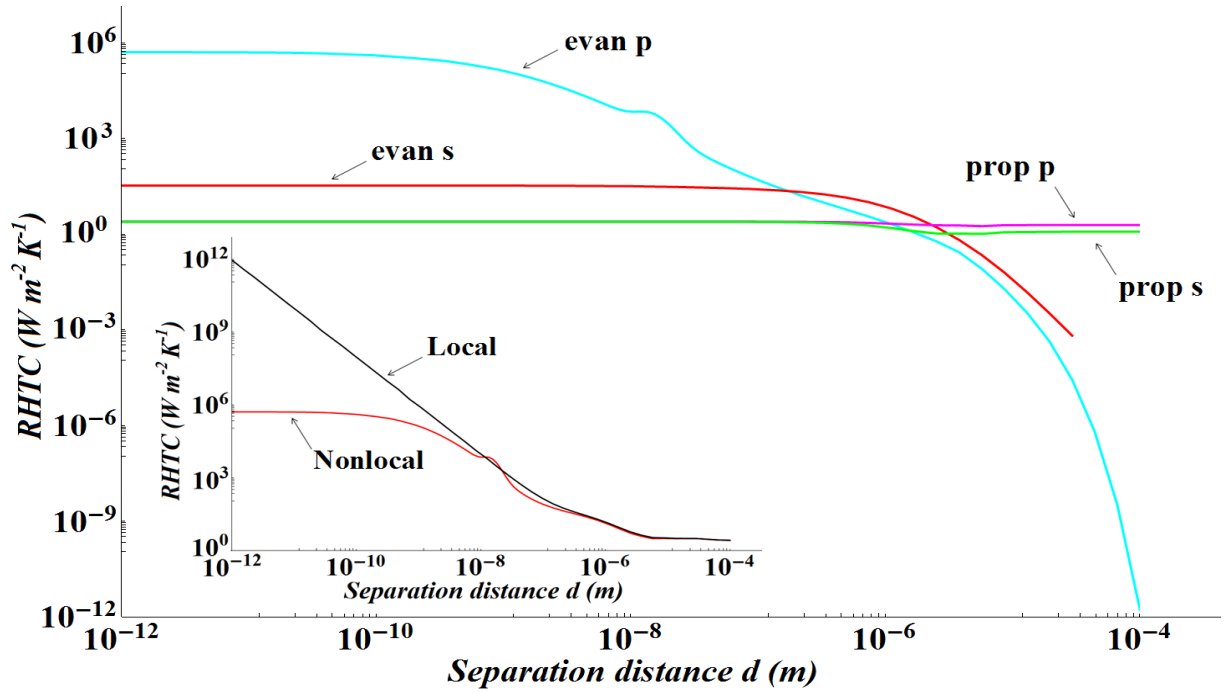


Figure 4.6: Variation of the radiative heat transfer coefficient (contributions of the evanescent and propagative EM waves of s and p polarizations) between two semi-infinite 6H-SiC parallel planes of average temperature $T=300\text{K}$, for the nonlocal model of Kliewer-Fuchs ABC. Inset: variation of the total RHTC for the nonlocal model of Kliewer-Fuchs ABC in comparison with the local model.

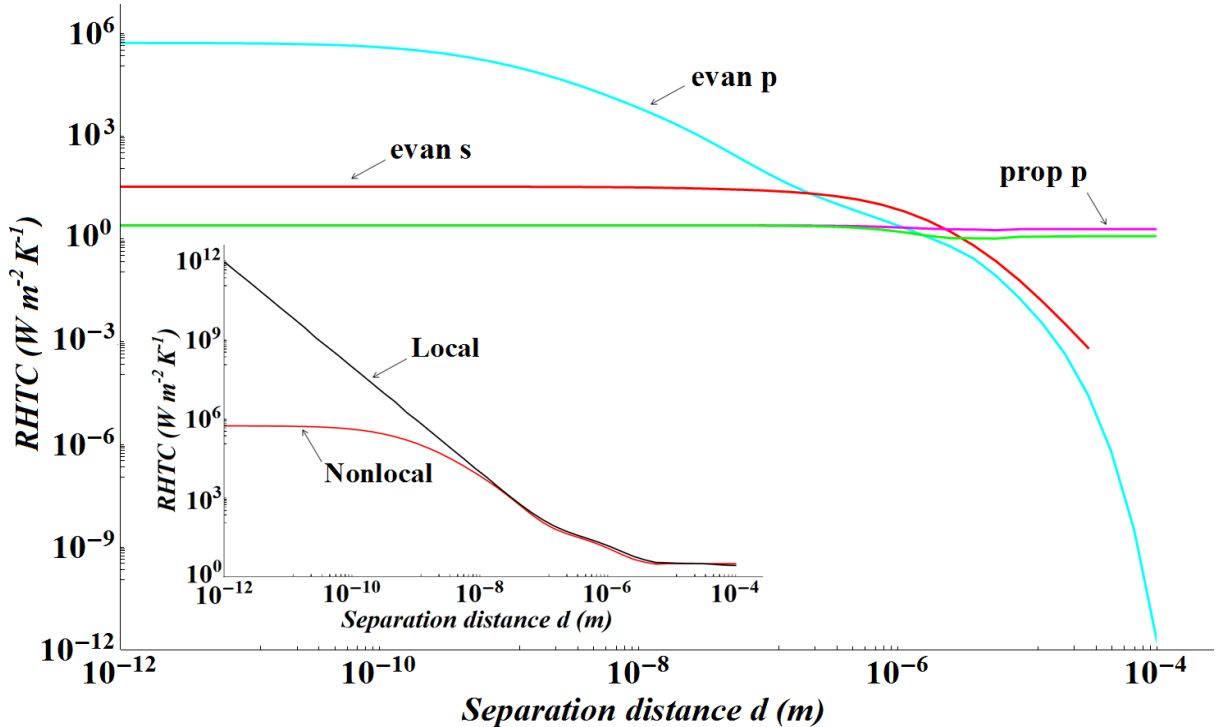


Figure 4.7: Variation of the radiative heat transfer coefficient (contributions of the evanescent and propagative EM waves of s and p polarizations) between two semi-infinite 6H-SiC parallel planes of average temperature $T=300\text{K}$, for the nonlocal model of Pekar ABC. Inset: variation of the total RHTC for the nonlocal model of Pekar ABC in comparison with the local model.

From these figures we observe that the saturation of the contribution of the p -polarized evanescent EM waves was attained in the five different models. We note here that as for the previous models, the ultimately small values of the separation distance (10^{-12} m) taken in the plots are nonphysical but they are considered just to show that the nonlocal matter description mathematically leads to a saturation value in the radiative heat transfer when the separation distance tends to zero.

As we mentioned before, the contributions of the propagative waves of both s and p polarizations dominate at large distances only and the discussion presented in the previous chapters applies here also. The s -polarized evanescent term saturates in all cases and acquires values similar to those of the local case.

We will be focusing on the behavior of the evanescent p term which dominates the transfer at small distances and for this reason we present in Fig. 4.8 the graphs obtained of the total contribution term for the five different sets of the ABC as to compare between them, and in Fig. 4.9 we plot these graphs along with the graph of the total contribution in the local case.

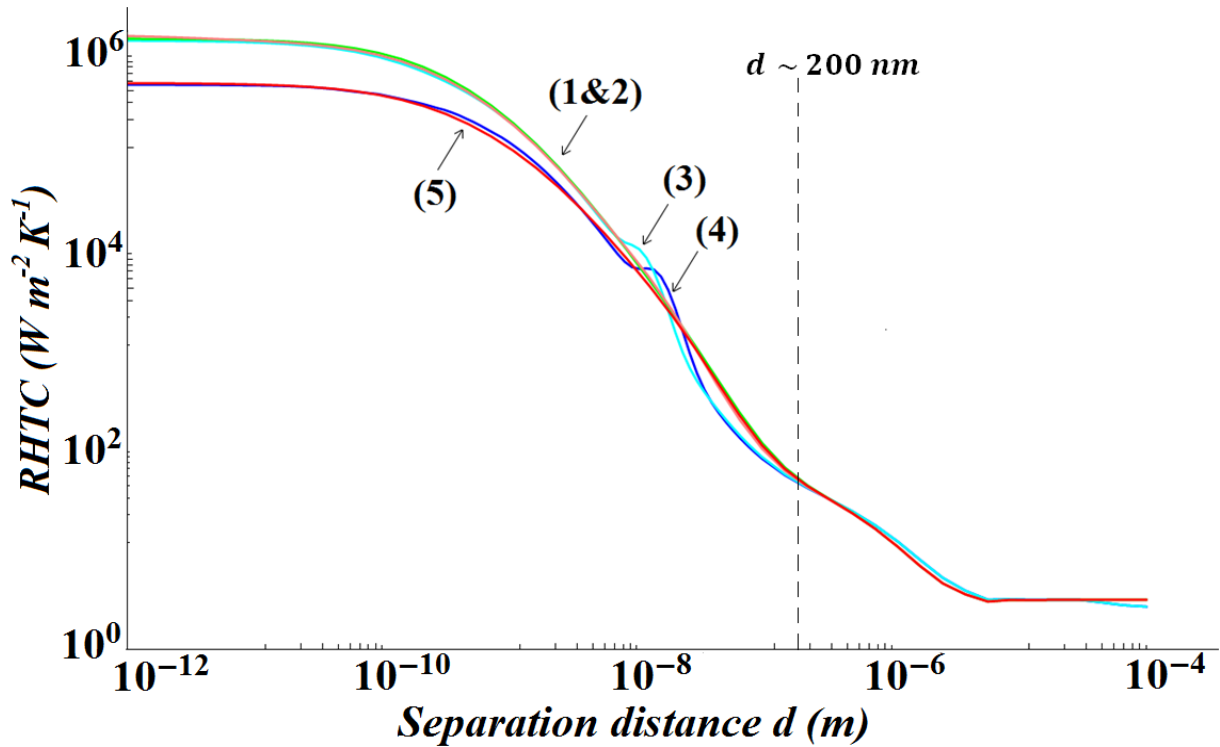


Figure 4.8: Variation of the total radiative heat transfer coefficient (RHTC) between two semi-infinite 6H-SiC parallel planes of average temperature $T=300K$, for the nonlocal model with the five different sets of the ABC; (1): Rimbey–Mahan, (2): Agarwal et al., (3): Ting et al., (4): Kliewer–Fuchs, (5): Pekar.

We observe from Fig. 4.8 that in the far field, i.e. at large distances ($d > 200 \text{ nm}$) the graphs of the five nonlocal models overlap, and from Fig. 4.9 we observe that for the same distance range the nonlocal graphs coincide with that of the local case.

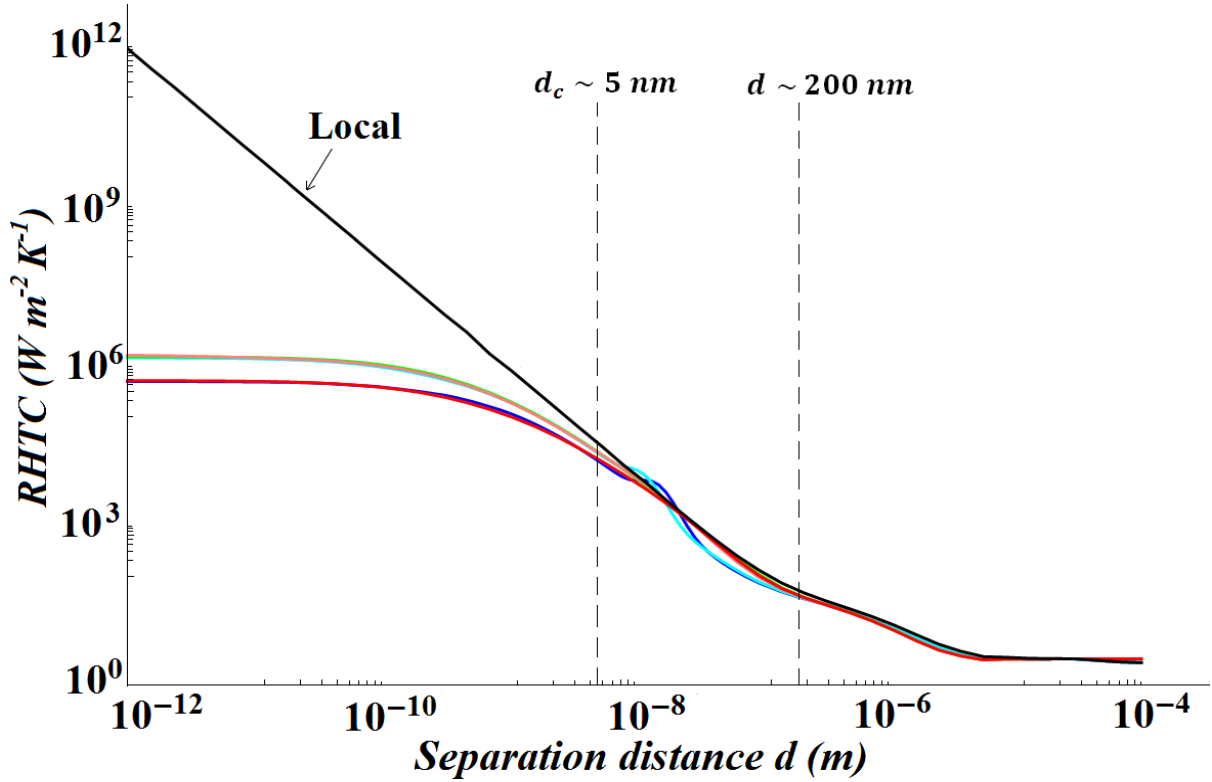


Figure 4.9: Variation of the total RHTC between two semi-infinite 6H-SiC parallel planes of average temperature $T=300\text{K}$ for the nonlocal model with the five different sets of the ABC, in comparison with the local model.

This behavior is expected in this distance range as it is the domain of the local regime of the RHT, where a nonlocal dielectric function has the same behavior as the local one. For distances $10 \text{ nm} < d < 200 \text{ nm}$ we observe that the RHTC increases as the curves of Ting et al. and Kliewer–Fuchs ABC sets no more coincide with the other graphs. At distances of the order of 10^{-8} m , the nonlocal graphs deviate from the $1/d^2$ asymptote and saturate at finite values. We observe that starting from this distance the graphs of Rimbey–Mahan, Agarwal et al., and Ting et al. coincide and reach the same saturation values, while those of Kliewer and Fuchs and Pekar coincide to saturate at smaller values. Obtaining saturation at small distances implies that for sufficiently large k , the reflection coefficient will tend to zero contrary to the local case, and by this we can say that the transfer is controlled by a critical wavevector limit and not by the inverse of the separation distance. Let us consider $k \sim 2\pi/d$ at a certain

distance d and the condition $Dk^2 \gg \omega_T^2$ in the denominator of Eq. (4.1), we find a critical distance $d_c \sim \sqrt{D4\pi^2/\omega_T^2}$ approximately equal to 5 nm for which the nonlocal behavior will be dominant. This distance can be seen as the distance travelled by the resonant heat carriers during an oscillation period at ω_T . By studying the variation of the real and the imaginary parts of the dielectric permittivity function $\varepsilon(\omega, K)$ in the (ω, K) plane (see Fig. 4.10), we notice that their values are maximum for all frequencies of the order of ω_T . The spectrums obtained show no change in values as K increases until reaching a wavevector value of the order of the inverse of the critical distance $K \approx 1/d_c \approx 2 \times 10^{-8} \text{ m}^{-1}$ where a cutoff takes place. We therefore conclude two main points from this discussion. The first point is that the diffusion parameter D and more precisely the additional term Dk^2 act as a cutoff for the infinite divergence of the RHTC; in other words, the $1/d^2$ divergence was replaced by a saturation depending on $1/D$. As a matter of fact, one can show that the distance at which saturation of the contribution to the RHTC of the p -polarized evanescent waves start to occur is of the order of the distance for which the high spatial frequencies would make Dk^2 dominant in the denominator of the expression of the nonlocal dielectric function (see Eq. (4.1)). The second point is that the nonlocal behavior occurs at distances of few nanometers, for which in principle quantum effects are still non dominant since these effects have been reported at sub nanometer scale [30-33]. In this modeling, the discrete nature of the atoms is not taken into account which will appear for typical sizes of the order of the atomic size i.e. in the angstrom range. This implies that the modeling will lose its pertinence for spatial frequencies larger than $2\pi/10^{-10}$ or separation distances smaller than a fraction of a nanometer. In the graphs representing the nonlocal model with the ABC of Ting et al. and Kliewer and Fuchs, we note two bumps in the graphs at distances $d_1 \approx 10 \text{ nm}$ and $d_2 = 20 \text{ nm}$, respectively. It is not trivial to link these distances to the optical parameters. We intended then to study the influence of varying the values of the plasmon frequency, the diffusion parameter and the losses parameter on the bump. For this reason, we increased and decreased the values of these parameters by few percentages and we recalculated the contribution of the p -polarized EM evanescent wave to the RHTC in each case, using Kliewer and Fuchs, and Ting et al. ABC sets. Figs. 4.11–4.16 show the curves obtained in each case.

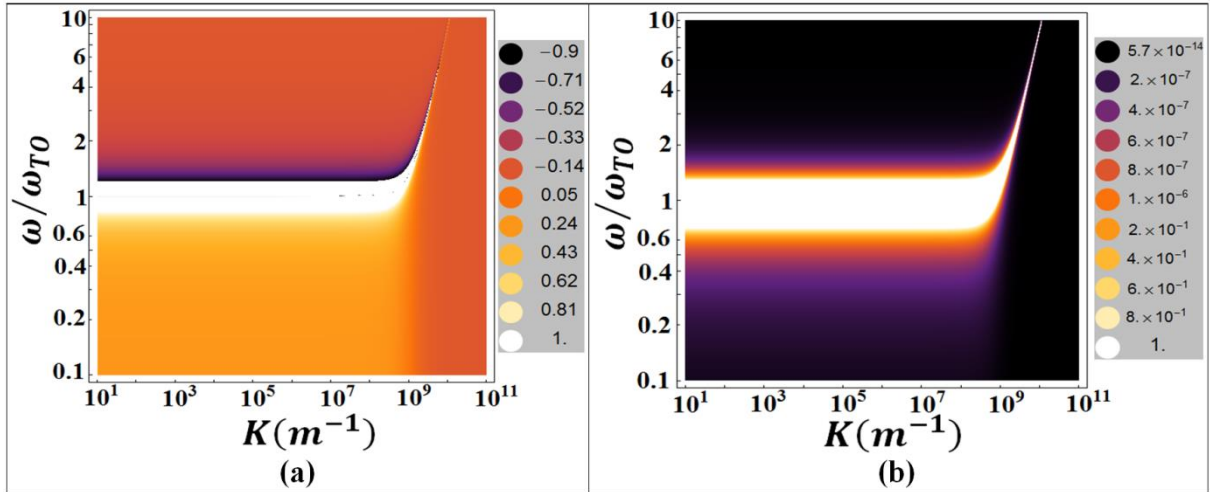


Figure 4.10: Plot of the real part (a) and the imaginary part (b) of the nonlocal dielectric permittivity function $\varepsilon(\omega, K)$ in the plane (ω, K) . The cutoff of the spectrums take place at $K \approx 1/d_c$.

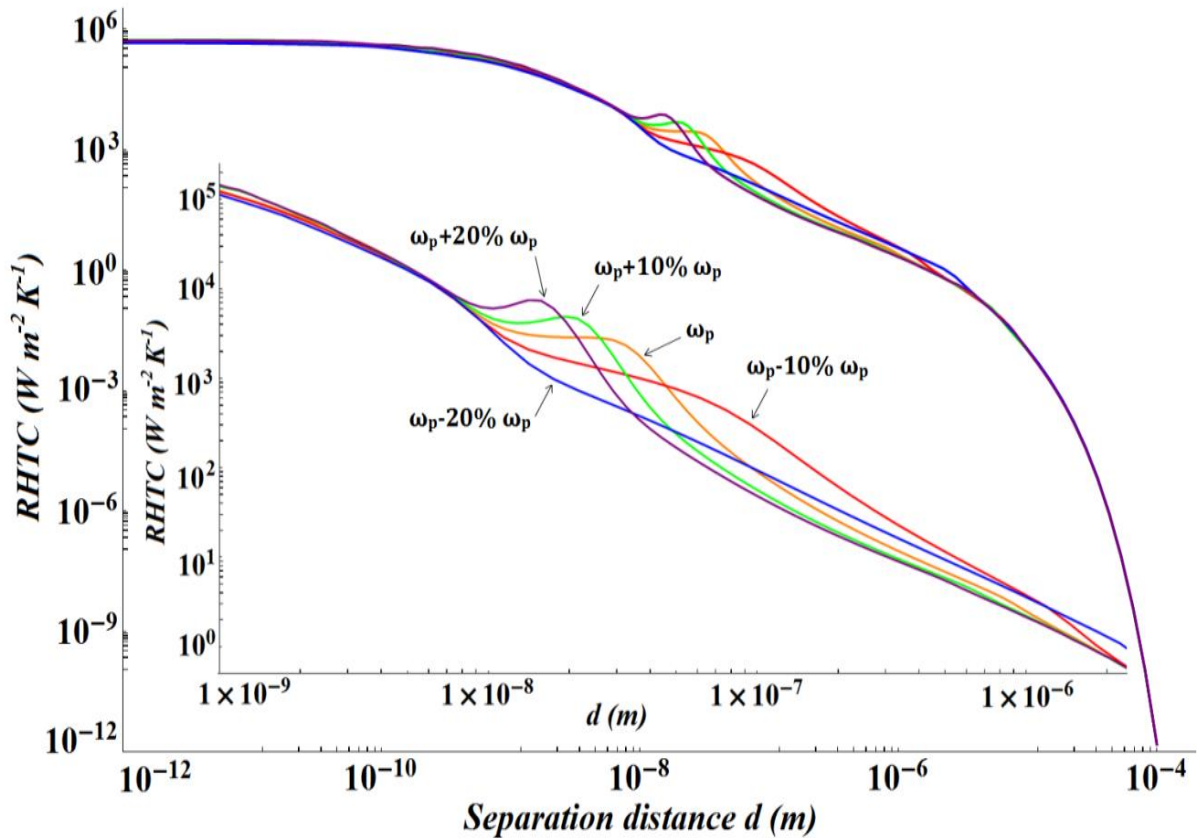


Figure 4.11: Variation of the bump in the curve of the contribution of the p -polarized evanescent EM waves to the RHTC between two semi-infinite 6H-SiC parallel planes of average temperature $T=300\text{K}$, as the value of ω_p changes for the nonlocal model of Kliever–Fuchs ABC. Inset: zoom of the plot for $10^{-9}\text{m} \leq d \leq 10^{-6}\text{m}$.

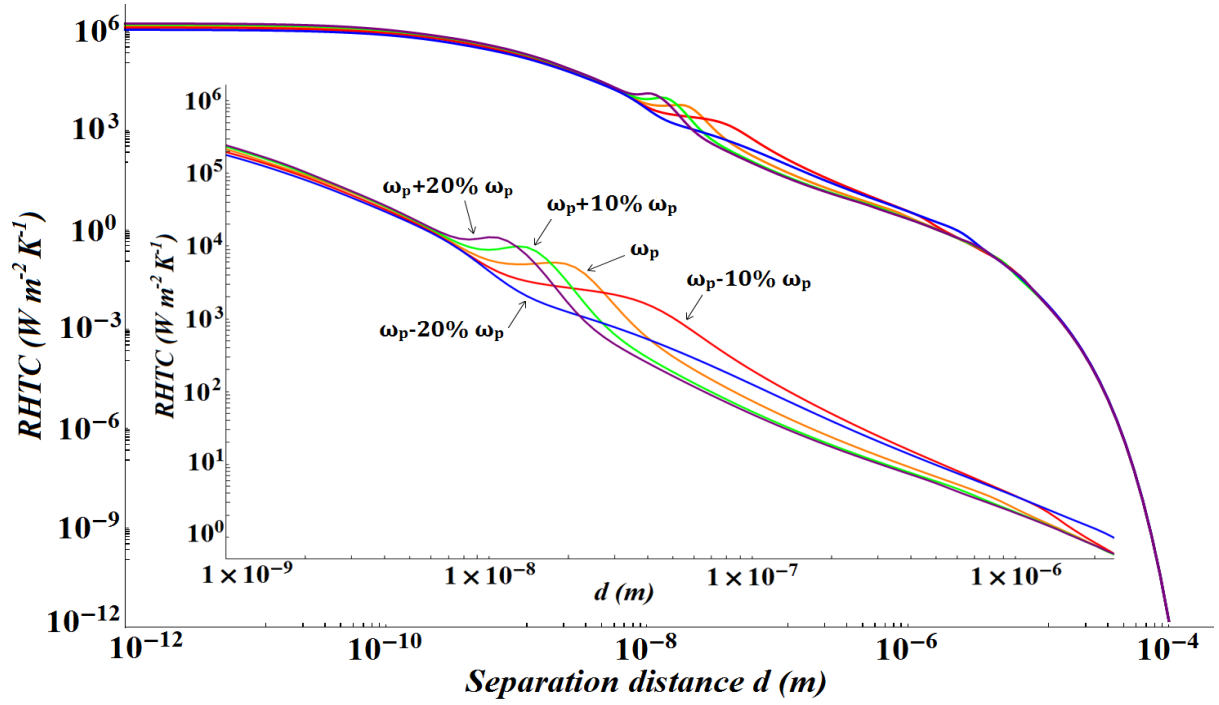


Figure 4.12: Variation of the bump in the curve of the contribution of the p -polarized evanescent EM waves to the RHTC between two semi-infinite 6H-SiC parallel planes of average temperature $T=300\text{K}$, as the value of ω_p changes for the nonlocal model of Ting ABC. Inset: zoom of the plot for $10^{-9}\text{m} \leq d \leq 10^{-6}\text{m}$.

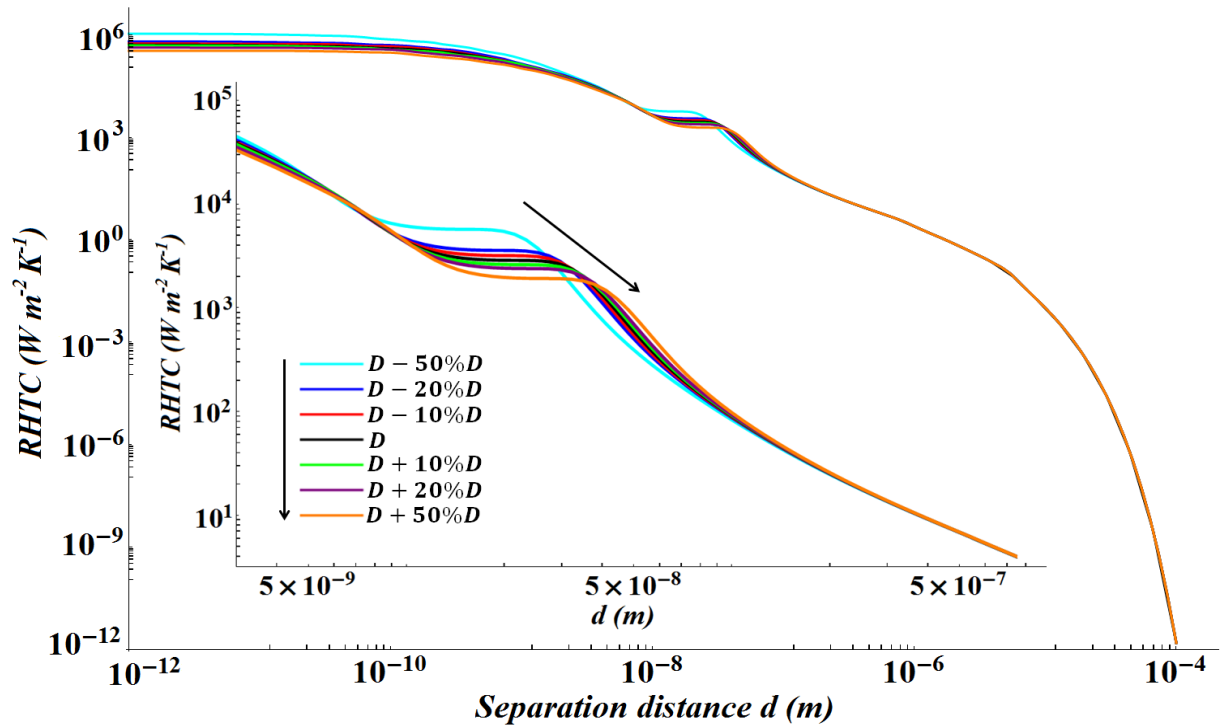


Figure 4.13: Variation of the bump in the curve of the contribution of the p -polarized evanescent EM waves to the RHTC between two semi-infinite 6H-SiC parallel planes of average temperature $T=300\text{K}$, as the value of the diffusion parameter D changes for the nonlocal model of Kliewer-Fuchs ABC. The arrow indicates the increasing order of the value of D , as well as the order of the corresponding graphs. Inset: zoom of the plot for $5 \times 10^{-9}\text{m} \leq d \leq 5 \times 10^{-7}\text{m}$.

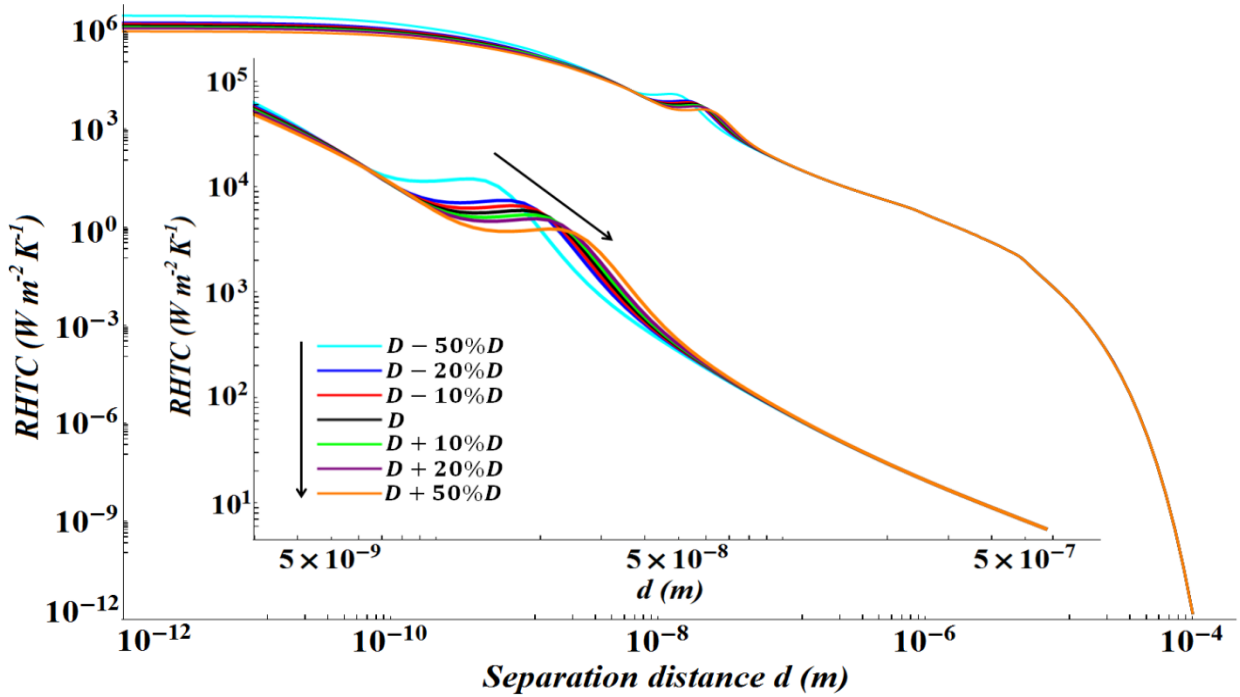


Figure 4.14: Variation of the bump in the curve of the contribution of the p -polarized evanescent EM waves to the RHTC between two semi-infinite 6H-SiC parallel planes of average temperature $T=300\text{K}$, as the value of the diffusion parameter D changes for the nonlocal model of Ting ABC. The arrow indicates the increasing order of the value of D , as well as the order of the corresponding graphs. Inset: zoom of the plot for $5 \times 10^{-9}\text{m} \leq d \leq 5 \times 10^{-7}\text{m}$.

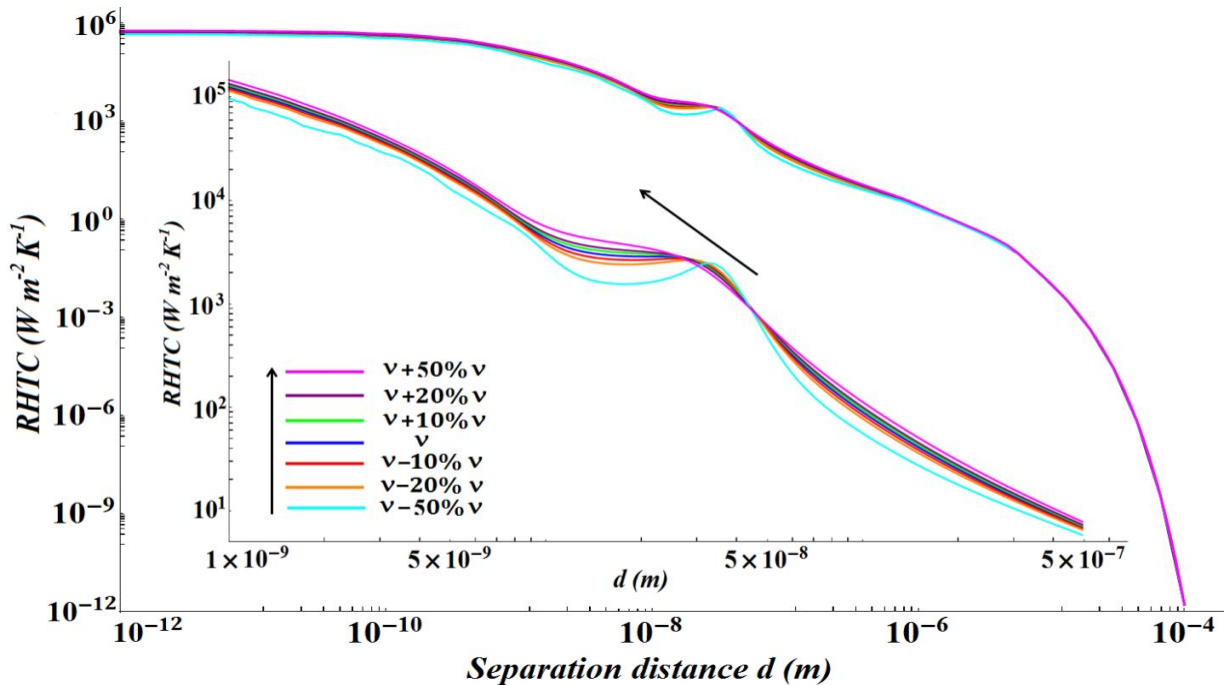


Figure 4.15: Variation of the bump in the curve of the contribution of the p -polarized evanescent EM waves to the RHTC between two semi-infinite 6H-SiC parallel planes of average temperature $T=300\text{K}$, as the value of the losses parameter ν change for the nonlocal model of Kliewer-Fuchs ABC. The arrow indicates the increasing order of the value of ν , as well as the order of the corresponding graphs. Inset: zoom of the plot for $10^{-9}\text{m} \leq d \leq 5 \times 10^{-7}\text{m}$.

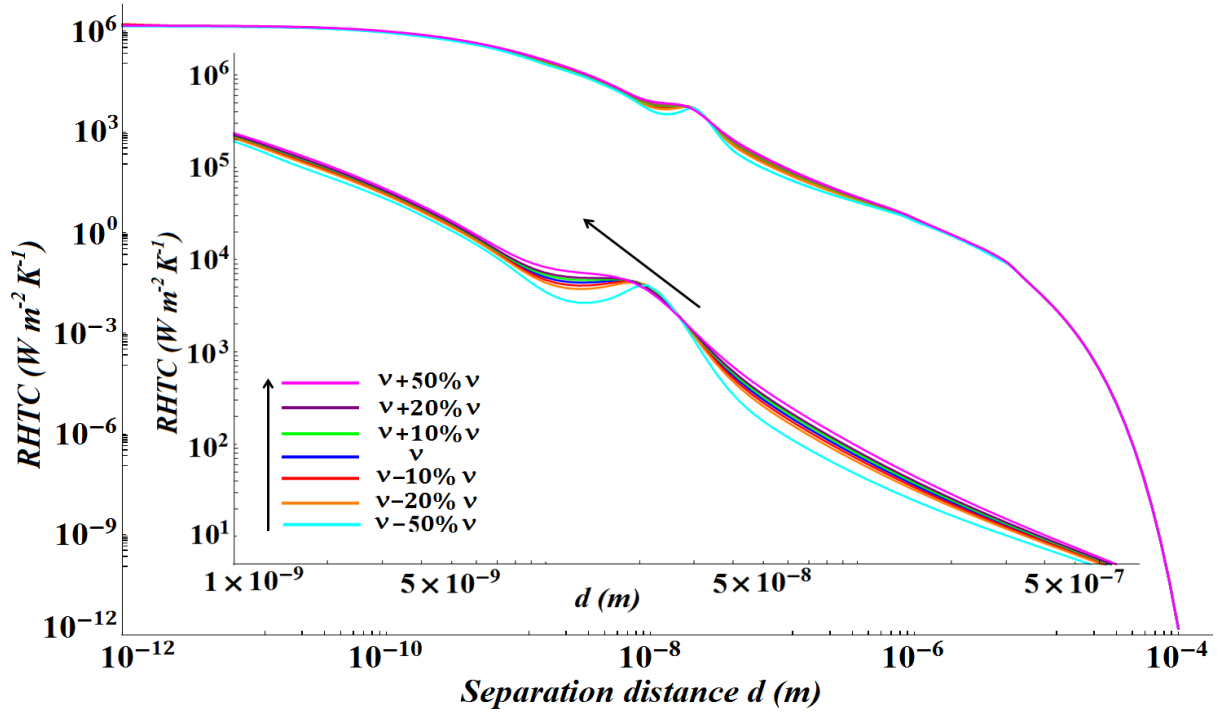


Figure 4.16: Variation of the bump in the curve of the contribution of the p -polarized evanescent EM waves to the RHTC between two semi-infinite 6H-SiC parallel planes of average temperature $T=300\text{K}$, as the value of the losses parameter ν change for the nonlocal model of Ting ABC. The arrow indicates the increasing order of the value of ν , as well as the order of the corresponding graphs. Inset: zoom of the plot for $1 \times 10^{-9}\text{m} \leq d \leq 5 \times 10^{-7}\text{m}$.

Figs. 4.11 and 4.12 show that for the ABC of Kliewer and Fuchs and Ting et al., the bump position and width are closely related to the value of ω_p . It is clear that as the value of ω_p increases, the width of the bump decreases and its position shifts to smaller distances. On the other hand, when the value of ω_p decreases, the width of the bump increases and its position shifts to larger distances. Figs. 4.13 and 4.14 show that when the value of D increases, the position of the bump shifts to larger distances and its width increases. On the other hand, Figs. 4.15 and 4.16 show that the width of the bump increases as the value of the losses parameter increases and decrease as the values of the latter decreases. We notice also that the position of the bump is almost insensitive to the value of the losses parameter except for the case where ν decreases by 50 %, the bump shifts significantly to larger distances.

As we mentioned above, Fig. 4.7 shows that at sub-nanometric separation distances, the calculated RHTC obtained with different ABC exhibit very similar behaviors. They all saturate to a certain value that can be considered as the ultimate radiative conductance between two semi-infinite parallel planes of 6H-SiC. This conductance is around $10^6 \text{Wm}^{-2}\text{K}^{-1}$, which is much smaller than the one obtained in conduction if we make a “rough approximation” by calculating the ratio of the thermal conductivity of SiC ($\kappa =$

$400 \text{ Wm}^{-2}\text{K}^{-1}$) on the size of the typical distance between atoms in SiC (Si – C $\approx 1.88 \text{ \AA}$, Si – Si $\approx 2.5 \text{ \AA}$). This means that heat transfer by radiation is always smaller than conduction heat transfer in the matter. This also means that when the distances are going to reduce as small as 1 nm , other effects such as quantum effects, that are completely different from EM effects described here have to be taken into account to describe the full heat transfer process. As this work limits itself to radiative heat transfer, this quantum treatment is beyond the scope of this thesis.

The saturation value of the thermal radiation can also be interpreted in terms of the number of modes coupled. Heat transfer can actually be written using Landauer formalism as a summation over the system eigenmodes of the product of the number of modes by the mean energy carried by each mode and by the transmission coefficient of the mode through the cavity. Each mode of the system is determined by the angular frequency and the parallel wavevector and the summation is performed over these two quantities. The transmission coefficients are given by the following equations for the propagative and evanescent contributions, respectively.

$$\left\{ \begin{array}{l} h_{rad}(T, d) = \sum_{\alpha=S,P} \int_0^{+\infty} d\omega h^0(T, \omega) \int_0^{\infty} \frac{KdK}{k_0^2} \tau(\omega, K) \\ \tau(\omega, K < \omega/c) = \frac{(1 - |r_{31}^\alpha|^2)(1 - |r_{32}^\alpha|^2)}{|1 - r_{31}^\alpha r_{32}^\alpha e^{2i\gamma_3 d}|^2} \\ \tau(\omega, K > \omega/c) = \frac{4\text{Im}(r_{31}^\alpha)\text{Im}(r_{32}^\alpha)e^{2i\gamma_3 d}}{|1 - r_{31}^\alpha r_{32}^\alpha e^{2i\gamma_3 d}|^2} \end{array} \right\} \quad (4.43)$$

Finally, after integration over ω and K , the RHTC can be seen as the total number of coupled modes per surface unit multiplied by the quantum of the thermal conductance $g_0 = \pi^2 k_b^2 T / 3h$; this value represents the rate at which heat is transported by a bosonic carrier channel. Therefore the number of modes per surface unit at 300 K can be estimated and is around 3×10^{15} coupled modes per m^2 .

In order to understand which modes contribute to the RHT when the two SiC surfaces are approached one to another, we plot the transmission coefficient for the evanescent EM waves of p polarization $4(\text{Im}(r_{31}^P))^2 e^{2i\gamma_3 d} / |1 - (r_{31}^P)^2 e^{2i\gamma_3 d}|^2$ at different separation distances for the local model and the nonlocal models with the five different ABC sets. The transmission coefficient plots in the (ω, K) plane are reported in Figs., 4.17–4.21. We observe from the above figures that all the curves of the nonlocal models show similar behavior. For a separation distance of 100 nanometers, the transmission coefficients in the nonlocal cases and

the local case have similar tendencies. The modes very well coupled ($\tau = 1$) are the ones corresponding to coupled surface phonon-polaritons of SiC in the cavity. For the local dielectric modeling case, the transmission coefficient map has a similar shape when the separation distance is reduced except that more and more modes contribute to the transfer. We see that the same map shape is obtained as long as we increase the parallel wavevector scale as the inverse of the separation distance. This explains why the transfer increases as $1/d^2$ and why the spectral contributions to the transfer are always occurring at the same frequencies. Indeed, as the separation distance decreases, the shape of the transfer spectrum does not change except that the scale increases as $1/d^2$ which explains the infinite divergence obtained of the plot of the RHTC. This spectrum is narrow and the transfer occurs around surface-polaritons frequencies.

On the other hand, the cases of the nonlocal modeling of the dielectric function show a somewhat different behavior. We note that most of the transfer still occurs around phonon-polariton angular frequencies. However, by decreasing the distance, the transmission coefficient map starts to show a clear cut-off in the parallel wavevector. Contrary to the local case, for separation distances below 1 nanometer, the transmission coefficient maps do not change. We note that the angular frequency domain at which the transfer occurs broadens. Moreover, there are no modes able to well couple for parallel wavevector larger than few hundreds of k_0 .

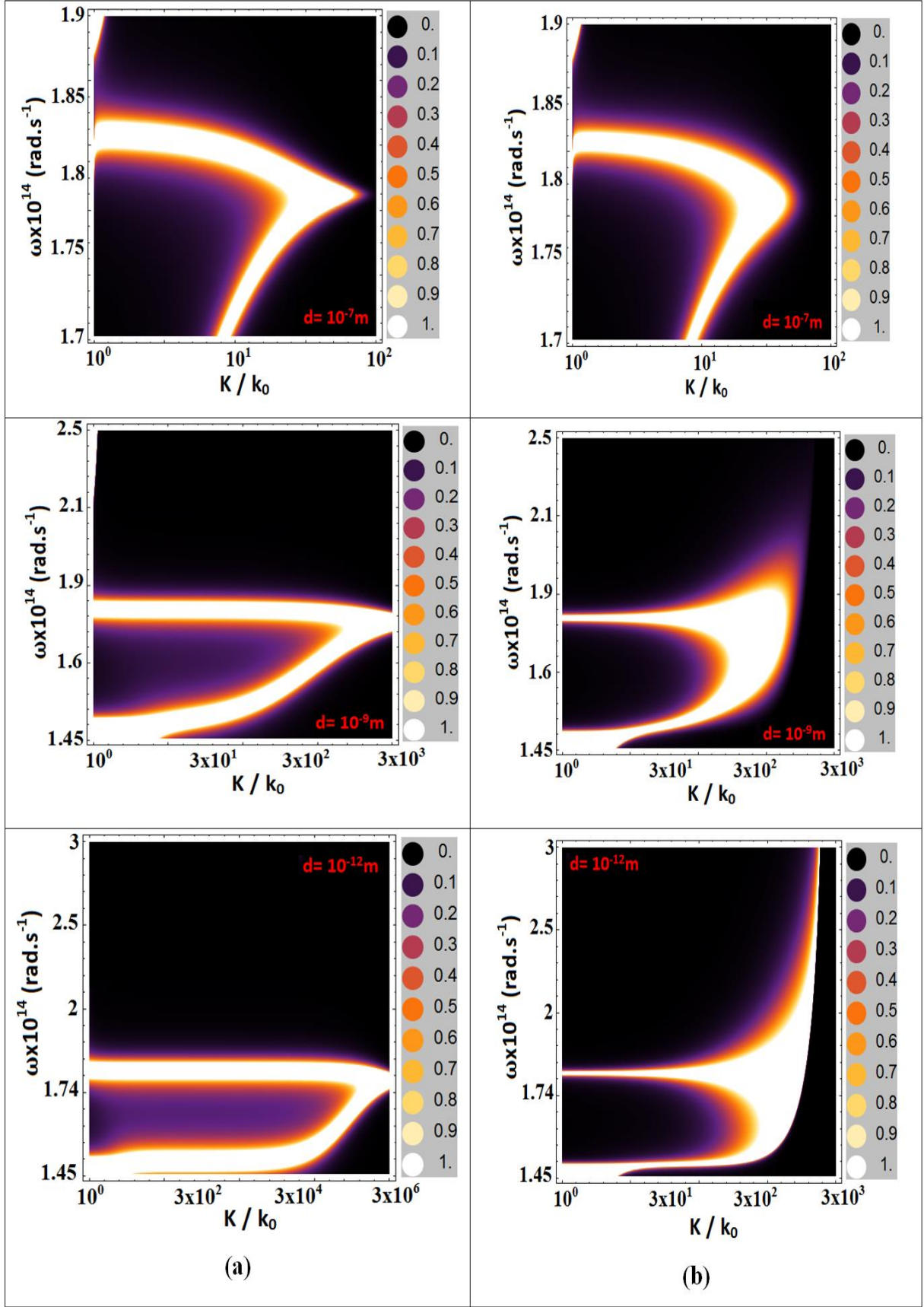


Figure 4.17: Plot of the transmission coefficient $4(\text{Im}(r_{31}^P))^2 e^{2i\gamma_3 d} / |1 - (r_{31}^P)^2 e^{2i\gamma_3 d}|^2$ of the p -polarized evanescent EM waves in the plane (ω, K) for the local model (a) and the nonlocal model of Rimbey–Mahan ABC (b) at different separation distances d .

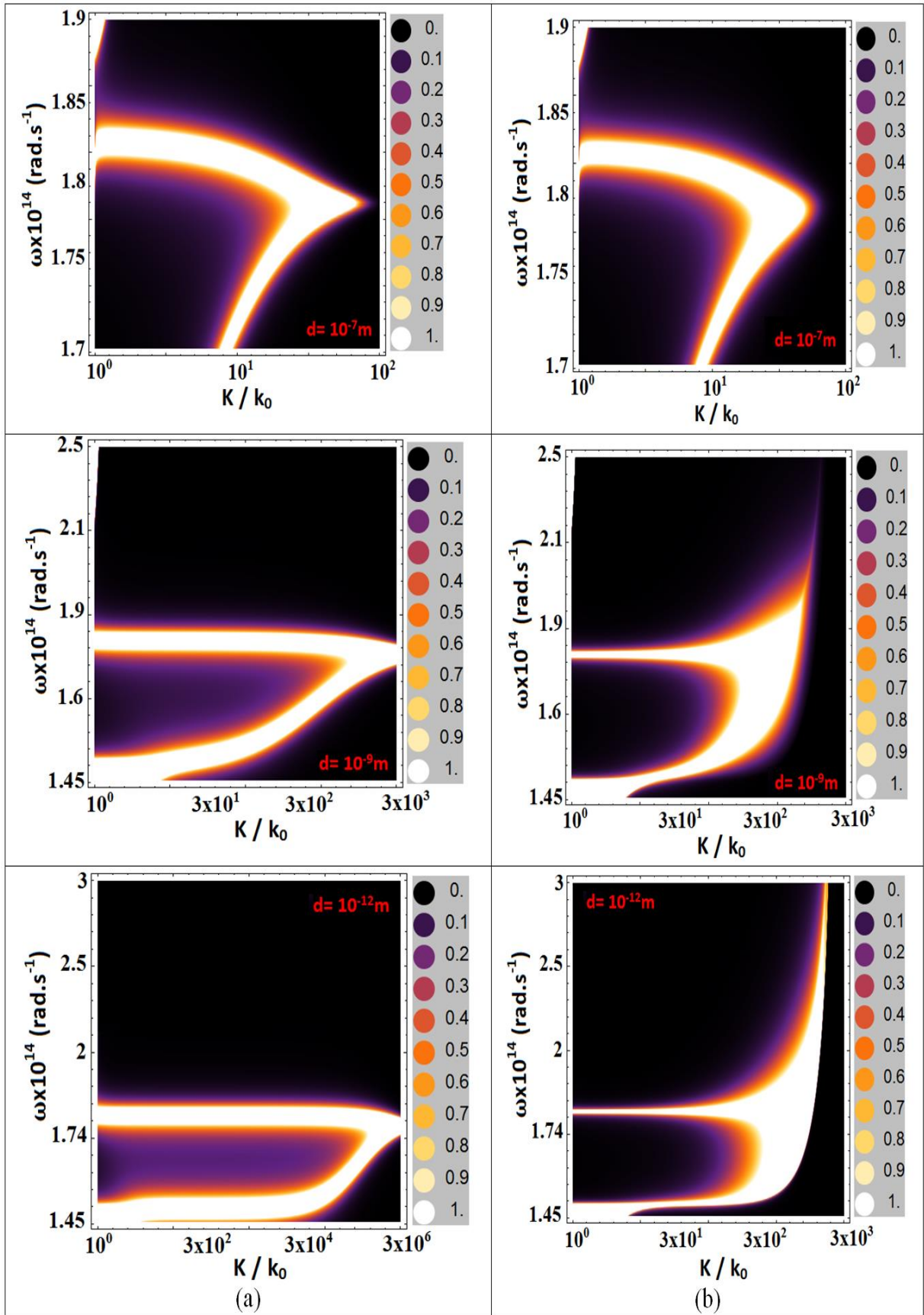


Figure 4.18: Plot of the transmission coefficient $4(\text{Im}(r_{31}^P))^2 e^{2i\gamma_3 d} / |1 - (r_{31}^P)^2 e^{2i\gamma_3 d}|^2$ of the p -polarized evanescent EM waves in the plane (ω, K) for the local model (a) and the nonlocal model of Agarwal ABC (b) at different separation distances d .

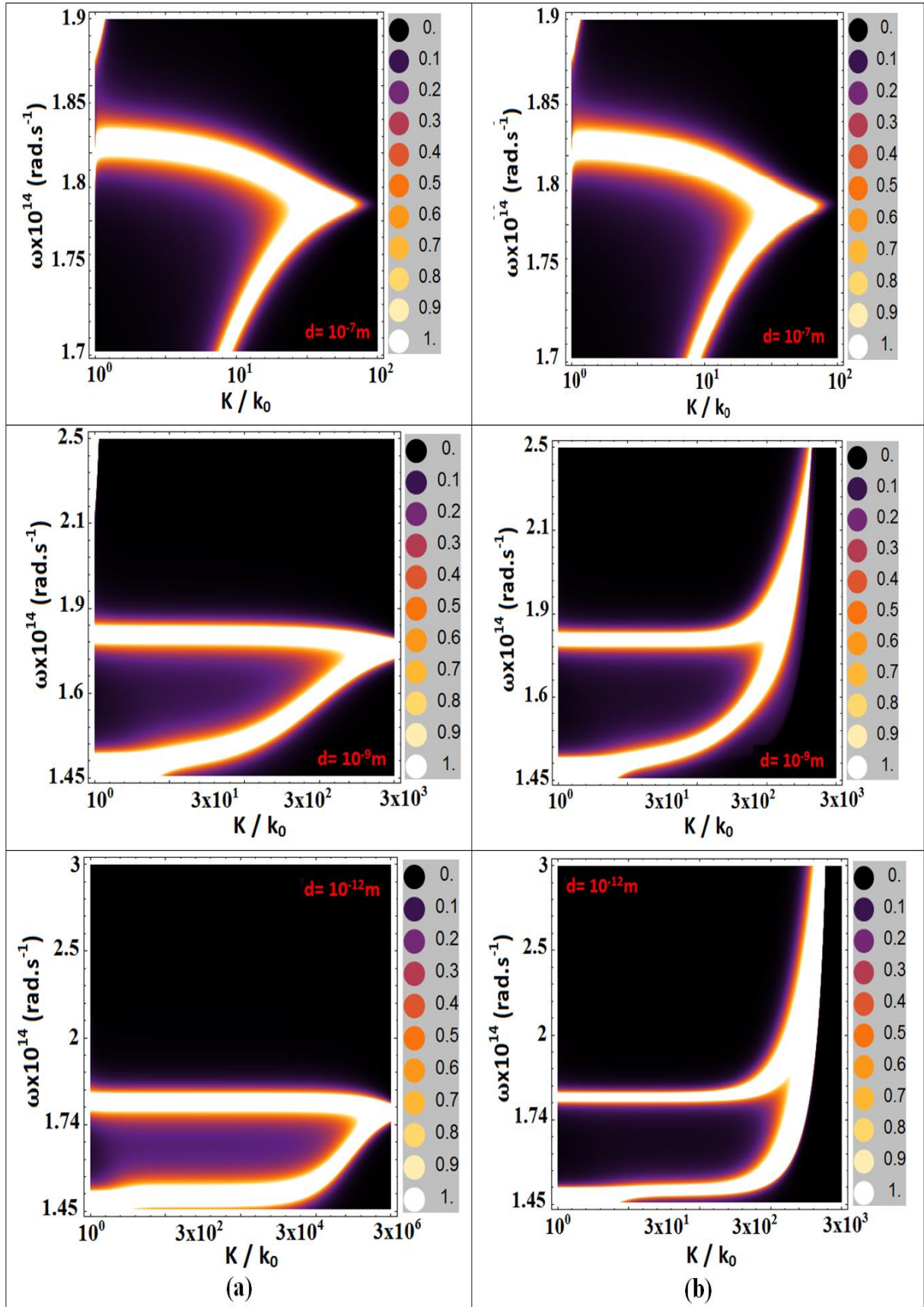


Figure 4.19: Plot of the transmission coefficient $4(\text{Im}(r_{31}^P))^2 e^{2i\gamma_3 d} / |1 - (r_{31}^P)^2 e^{2i\gamma_3 d}|^2$ of the p -polarized evanescent EM waves in the plane (ω, K) for the local model (a) and the nonlocal model of Ting ABC (b) at different separation distances d .

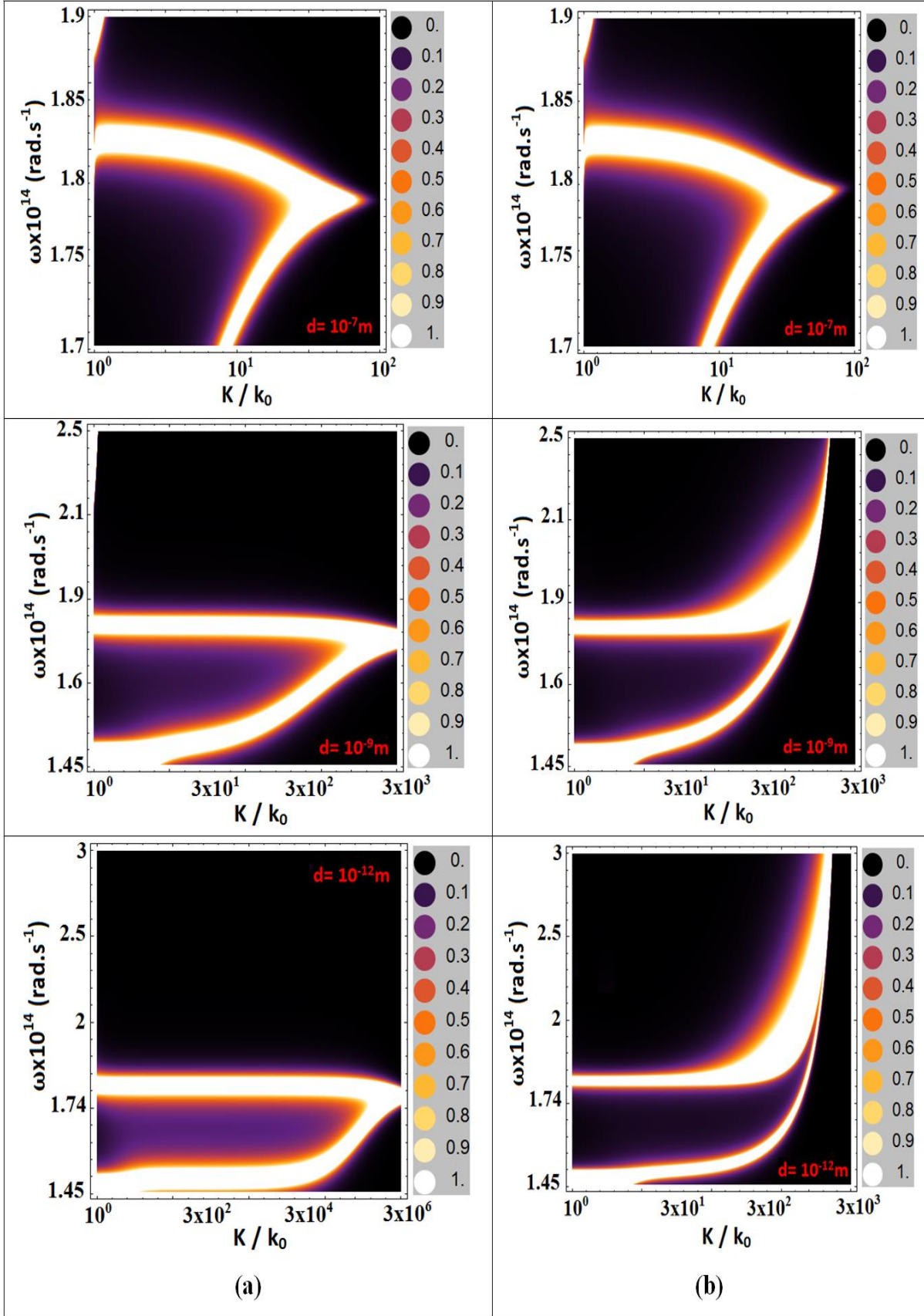


Figure 4.20: Plot of the transmission coefficient $4(\text{Im}(r_{31}^P))^2 e^{2i\gamma_3 d} / |1 - (r_{31}^P)^2 e^{2i\gamma_3 d}|^2$ of the p - polarized evanescent EM waves in the plane (ω, K) for the local model (a) and the nonlocal model of Kliever and Fuchs ABC (b) at different separation distances d .

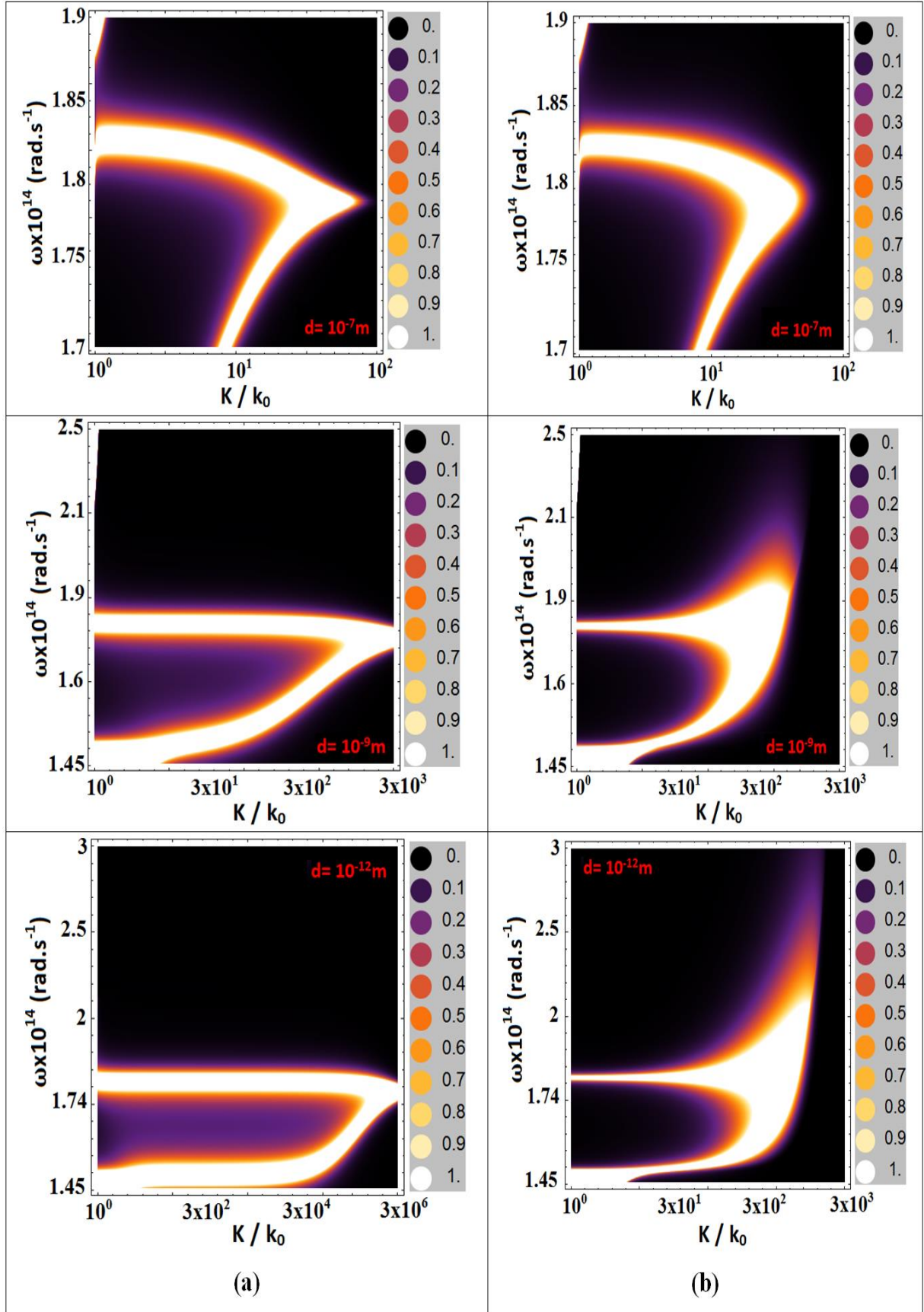


Figure 4.21: Plot of the transmission coefficient $4(\text{Im}(r_{31}^P))^2 e^{2i\gamma_3 d} / |1 - (r_{31}^P)^2 e^{2i\gamma_3 d}|^2$ of the p -polarized evanescent EM waves in the plane (ω, K) for the local model (a) and the nonlocal model of Pekar ABC (b) at different separation distances d .

4.4 Study of the radiative transfer spectrum and the electromagnetic energy density

We studied the variation of the radiative transfer spectrum and the EM energy density (the 1–surface case) for each case of the nonlocal model, Figs. 4.22–4.26. From these figures we observe that the spectra broaden and saturate as the distance is reduced, contrary to the plots obtained for the local case in chapter 1 (Fig. 1.8) where the width of the graph shortens and shows a narrow peak around the angular frequency of the surface waves. We also show that the radiative heat transfer spectrum is very similar to the energy density spectrum. This is not surprising since this last quantity is directly proportional to the local density of EM states (LDOS) and the radiative heat transfer spectrum is also related to the LDOS [5]. For the nonlocal models of Kliewer and Fuchs and Ting et al. ABC, the plot of the spectral energy flux at distances $d = 10^{-9}m$ and $10^{-12}m$, show a bump at an angular frequency less than that of the surface waves. This feature is definitely related to the bump obtained in the curves of the RHTC. By comparing the spectra of the different nonlocal models with the ones of the local model, one may advance that taking into account the nonlocality of the dielectric permittivity function decreases the degree of coherence of the radiated EM field in the near field. After showing the importance of the parameter D in the saturation of the RHTC at small distances where it acts as a cutoff of the divergence, we aimed to study the effects of changing the value of the D on the energy density spectra. We present in Figs. 4.27– 4.31 the plots of the spectral energy flux and the spectral EM energy density of the p -polarized evanescent EM waves at distance $d = 10^{-12}m$ as D changes values for the nonlocal cases of the five different ABC.

By comparing the magnitudes and the widths of the obtained graphs of the spectral energy flux, we note that for all the ABC, the spectral energy density is inversely proportional to D . In other words, as the value of D increases, the magnitude and the width of the spectral flux decrease. We also notice that for any D , the bump shown in the plots of the RHTC and the Kliewer–Fuchs and Ting et al. ABC is shown in the plots of the spectral energy flux for any D , which is consistent with the results shown in Figs. 4.12 and 4.13. The same argument applies for the spectral EM energy density for all the ABC sets considered. By normalizing the magnitudes of the graphs of the spectral energy flux of Kliewer and Fuchs ABC, we are able to retrieve one single graph corresponding to the original value of D . This means that the heat transfer saturation value is also inversely proportional to D .

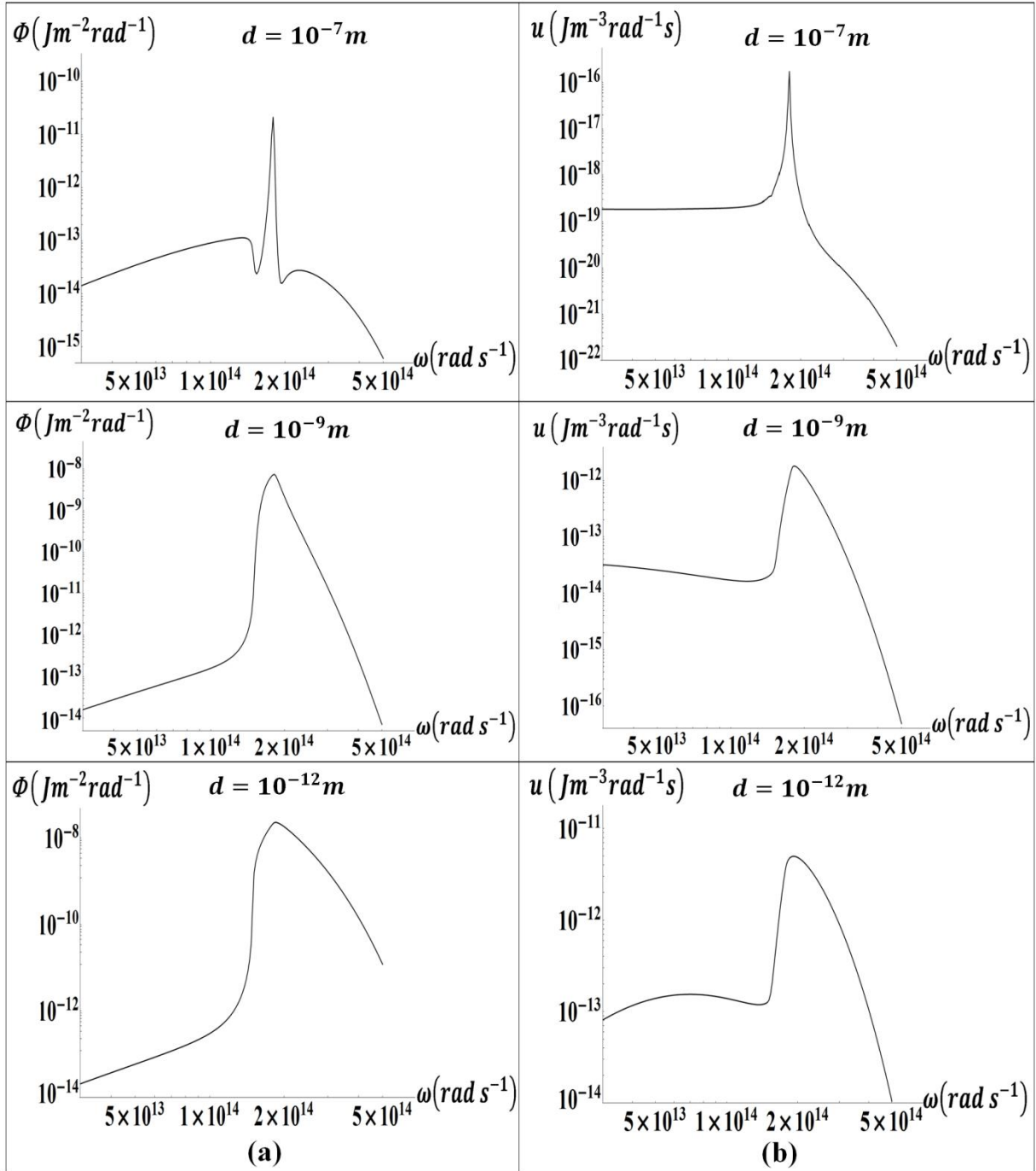


Figure 4.22: Plots of the spectral energy flux (a) and the spectral EM energy density (b) of the p -polarized evanescent EM waves as function of the angular frequency for the nonlocal model of Rimbeý–Mahan ABC at different distances d and average temperature $T=300\text{K}$.

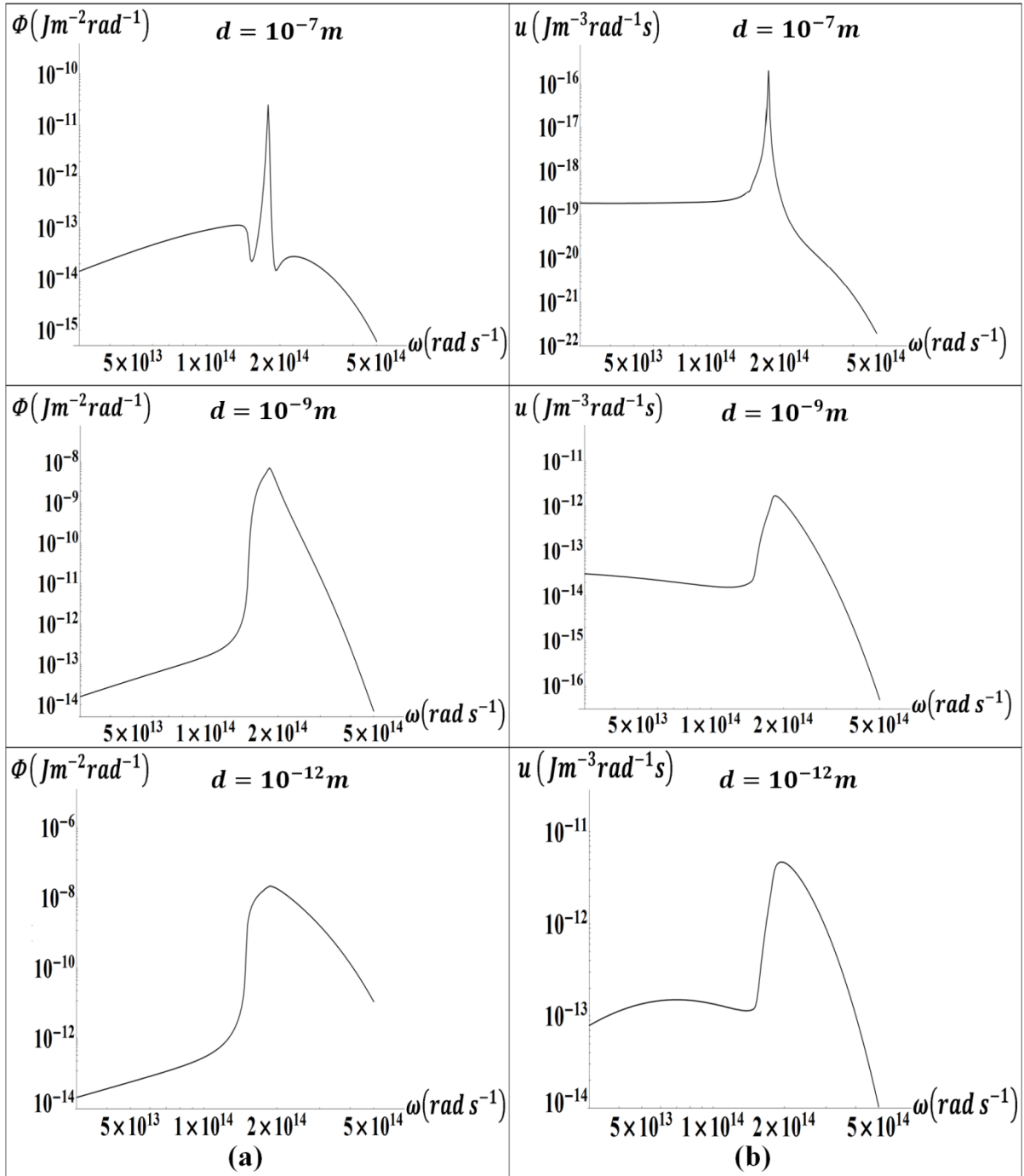


Figure 4.23: Plots of the spectral energy flux (a) and the spectral EM energy density (b) of the p -polarized evanescent EM waves as function of the angular frequency for the nonlocal model of Agarwal ABC at different distances d of average temperature $T=300K$.

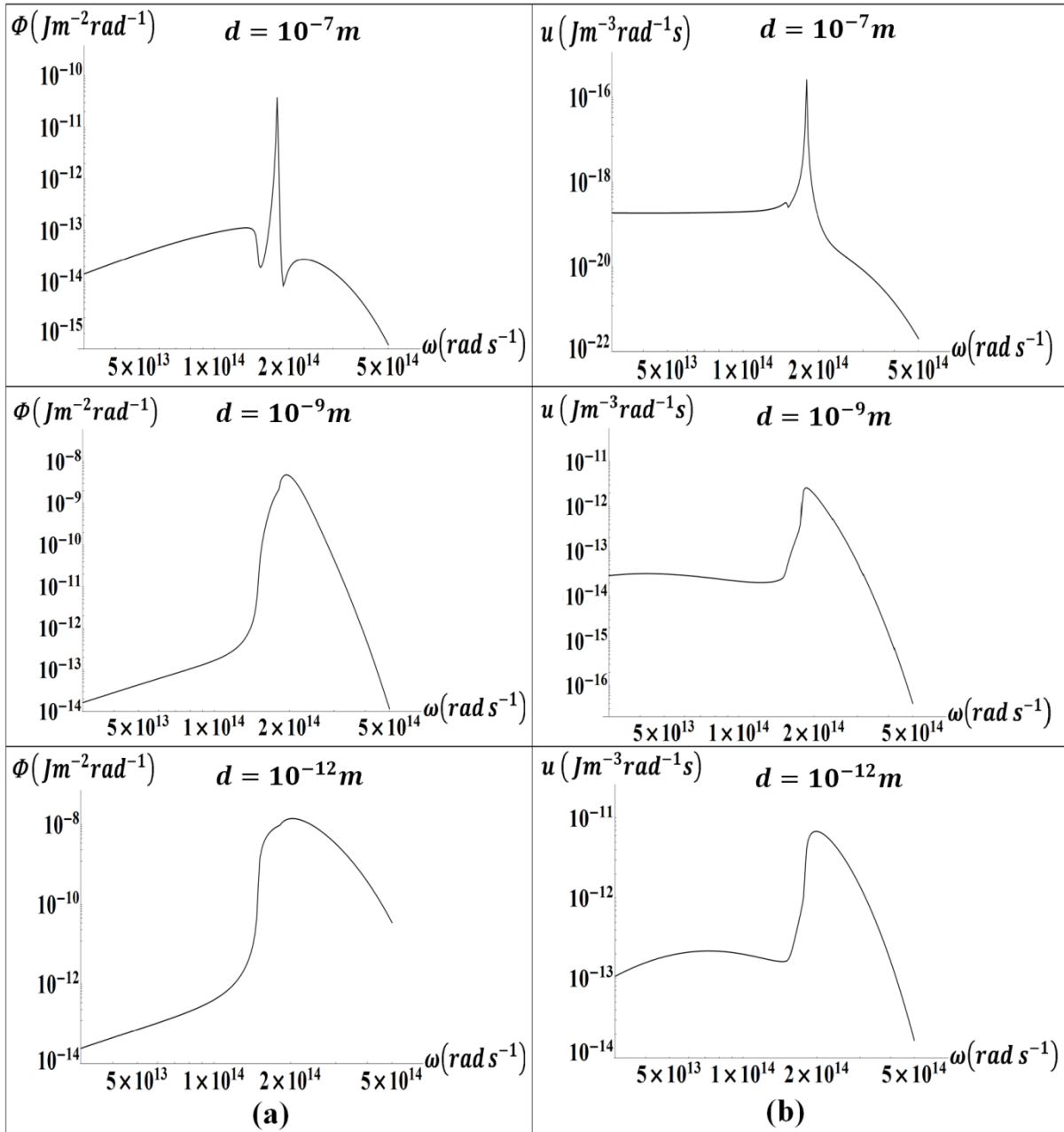


Figure 4.24: Plots of the spectral energy flux (a) and the spectral EM energy density (b) of the p -polarized evanescent EM waves as function of the angular frequency for the nonlocal model of Ting ABC at different distances d and average temperature $T=300K$.

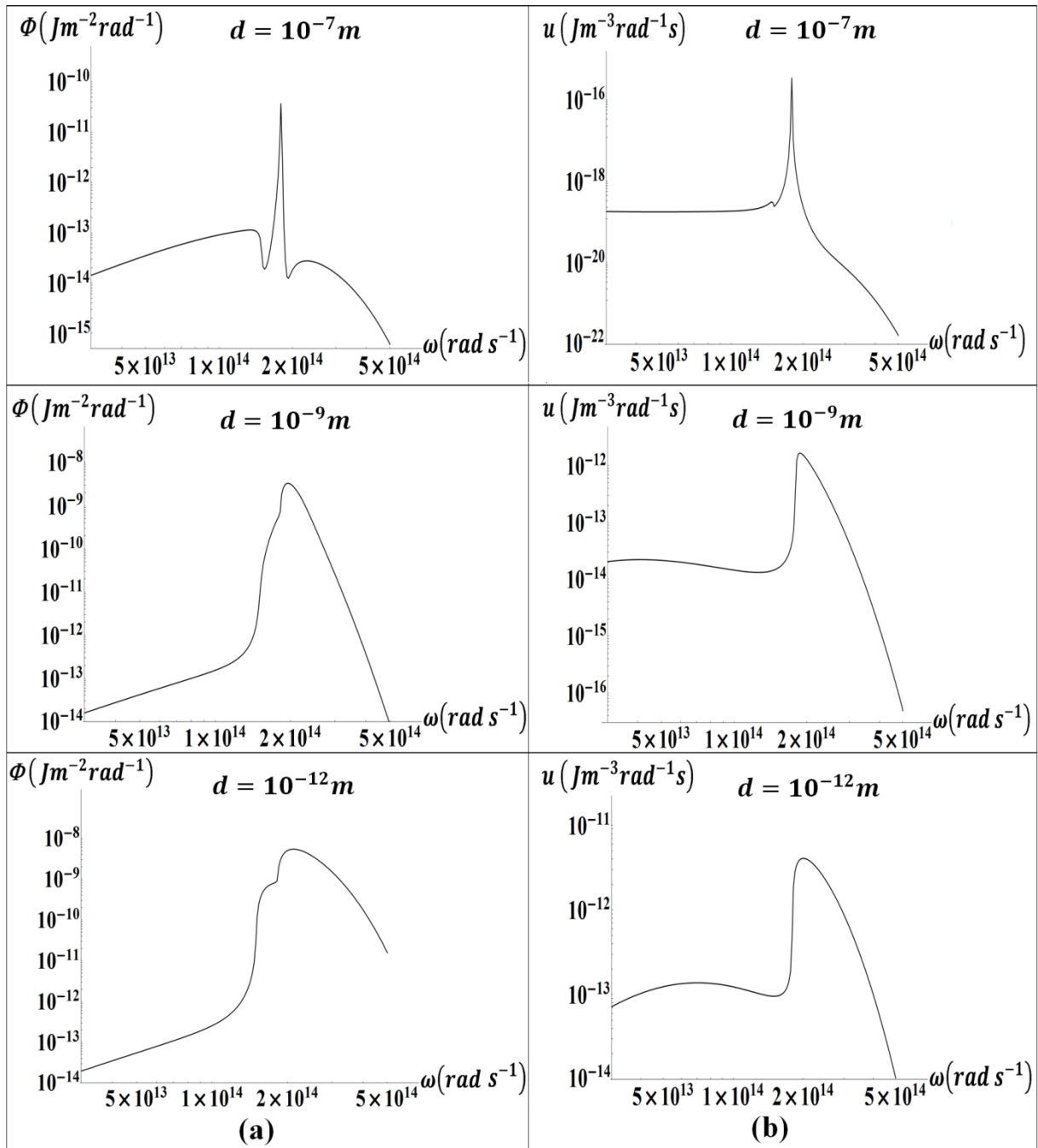


Figure 4.25: Plots of the spectral energy flux (a) and the spectral EM energy density (b) of the p -polarized evanescent EM waves as function of the angular frequency for the nonlocal model of Kliewer–Fuchs ABC at different distances d and average temperature $T=300\text{K}$.

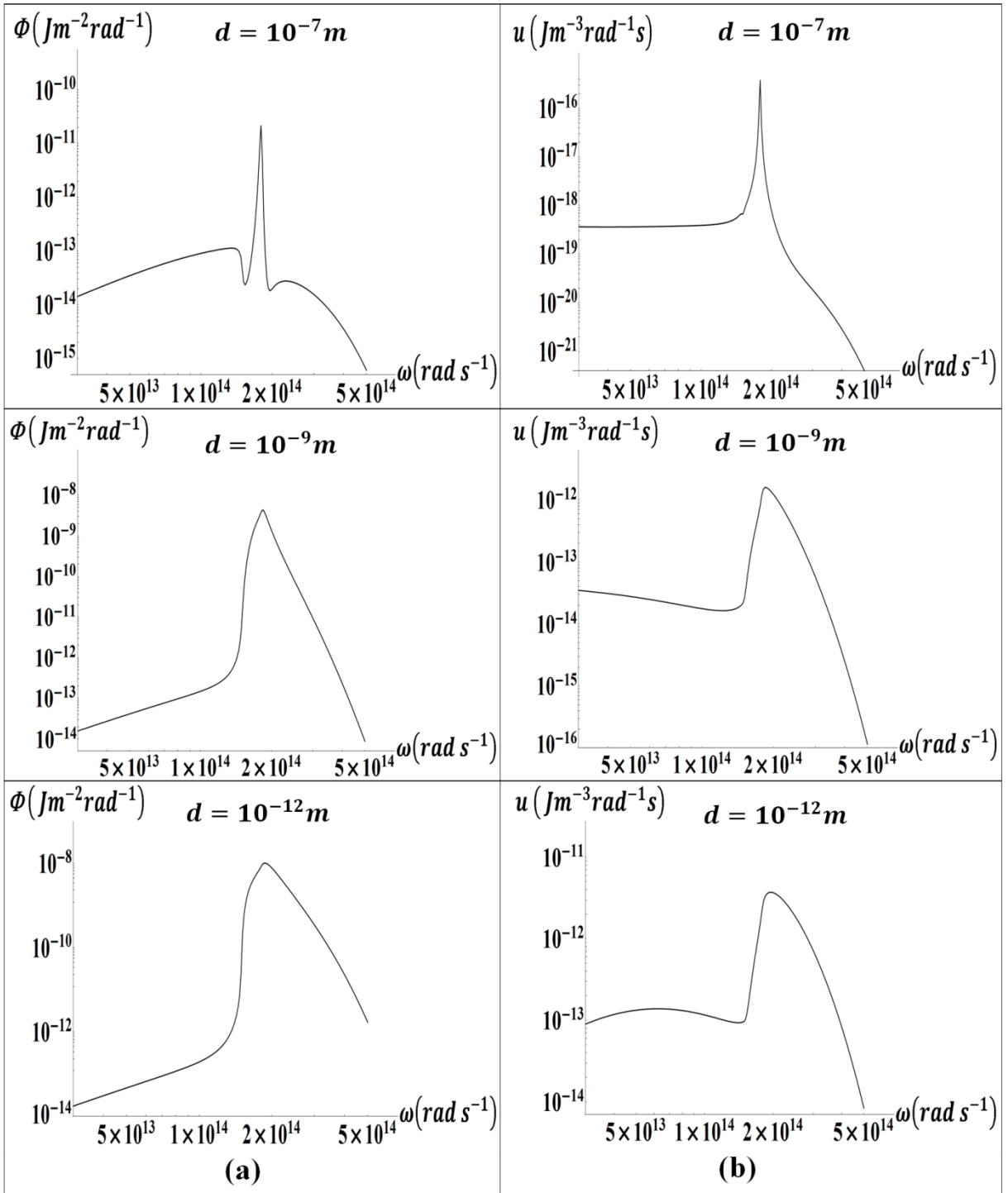


Figure 4.26: Plots of the spectral energy flux **(a)** and the spectral EM energy density **(b)** of the p -polarized evanescent EM waves as function of the angular frequency for the nonlocal model of Pekar ABC at different distances d and average temperature $T=300K$.

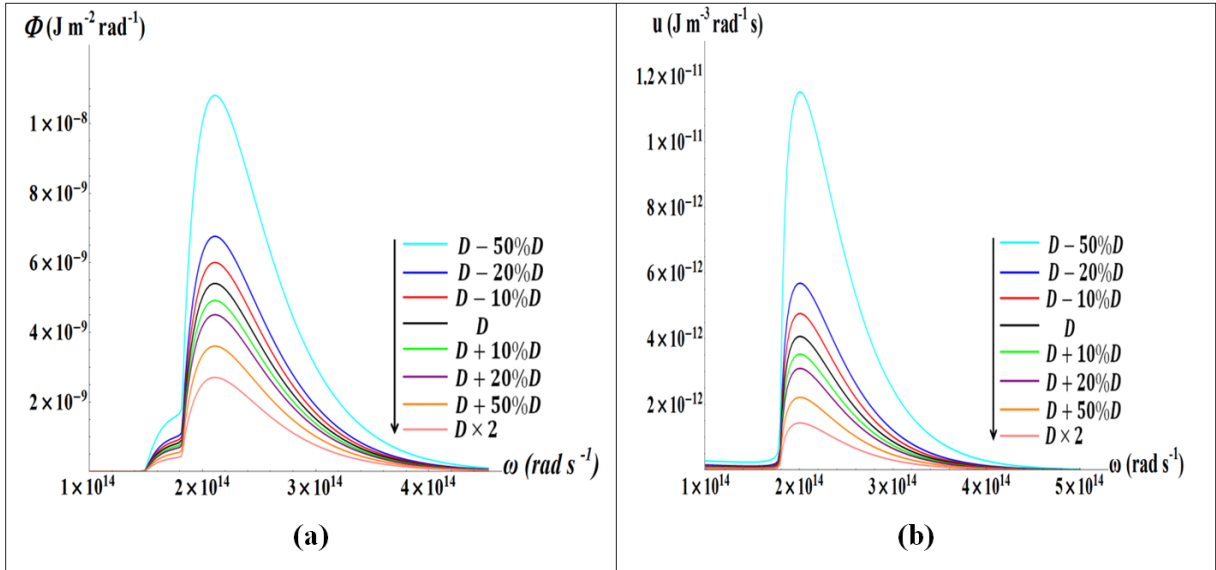


Figure 4.27: Plots of the spectral energy flux (a) and the spectral EM energy density (b) of the p -polarized evanescent EM waves as functions of the angular frequency, at $d = 10^{-12}m$ and $T=300K$, for different values of the parameter D for the nonlocal model of Kliewer–Fuchs ABC. The curves show that the energy densities are inversely proportional to D . The arrow indicates the increasing order of the value of D , as well as the order of the corresponding curves.

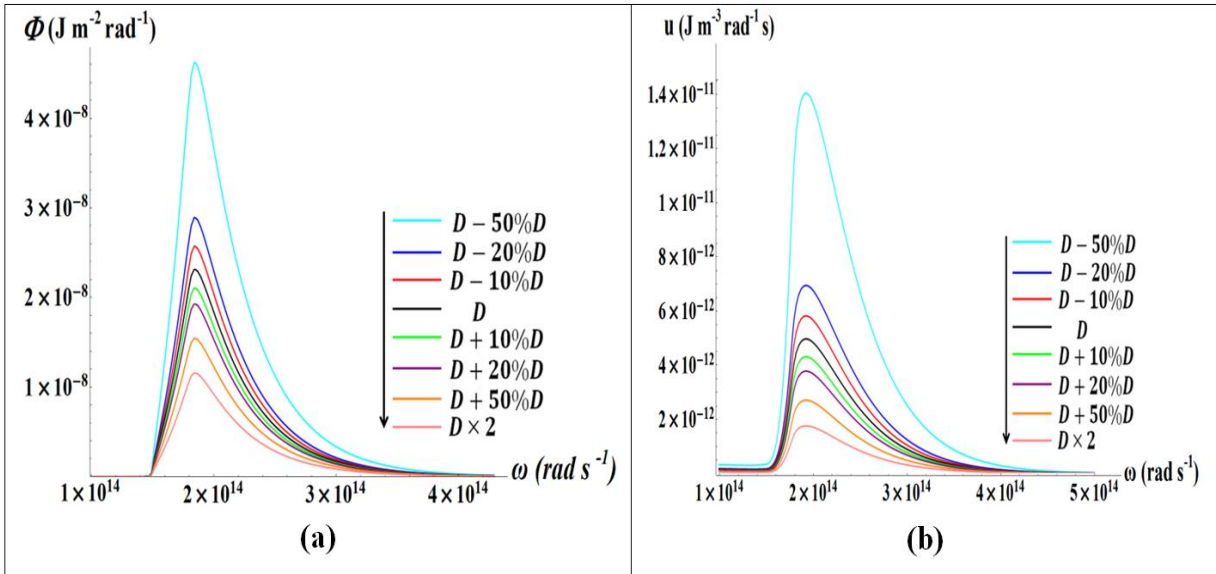


Figure 4.28: Plots of the spectral energy flux (a) and the spectral EM energy density (b) of the p -polarized evanescent EM waves as functions of the angular frequency, at $d = 10^{-12}m$ and $T=300K$, for different values of the parameter D for the nonlocal model of Rimbey–Mahan ABC. The graphs show that the energy densities are inversely proportional to D . The arrow indicates the increasing order of the value of D , as well as the order of the corresponding curves.

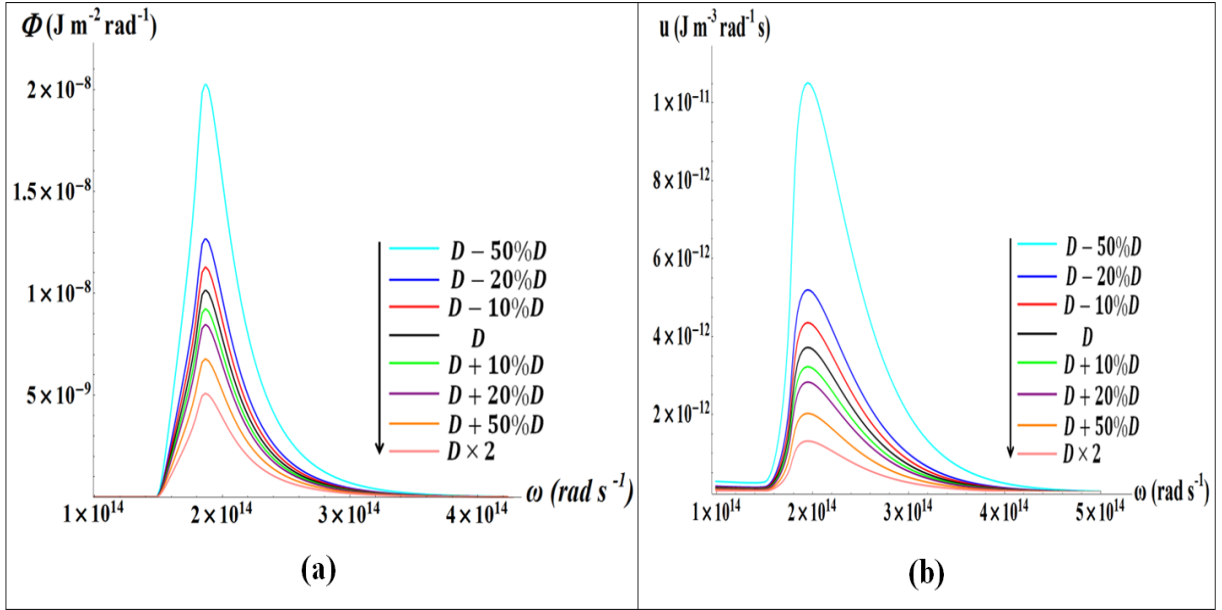


Figure 4.29: Plots of the spectral energy flux (a) and the spectral EM energy density (b) of the p -polarized evanescent EM waves as functions of the angular frequency, at $d = 10^{-12}m$ and $T=300K$, for different values of the parameter D for the nonlocal model of Pekar ABC. The curves show that the energy densities are inversely proportional to D . The arrow indicates the increasing order of the value of D , as well as the order of the corresponding curves.

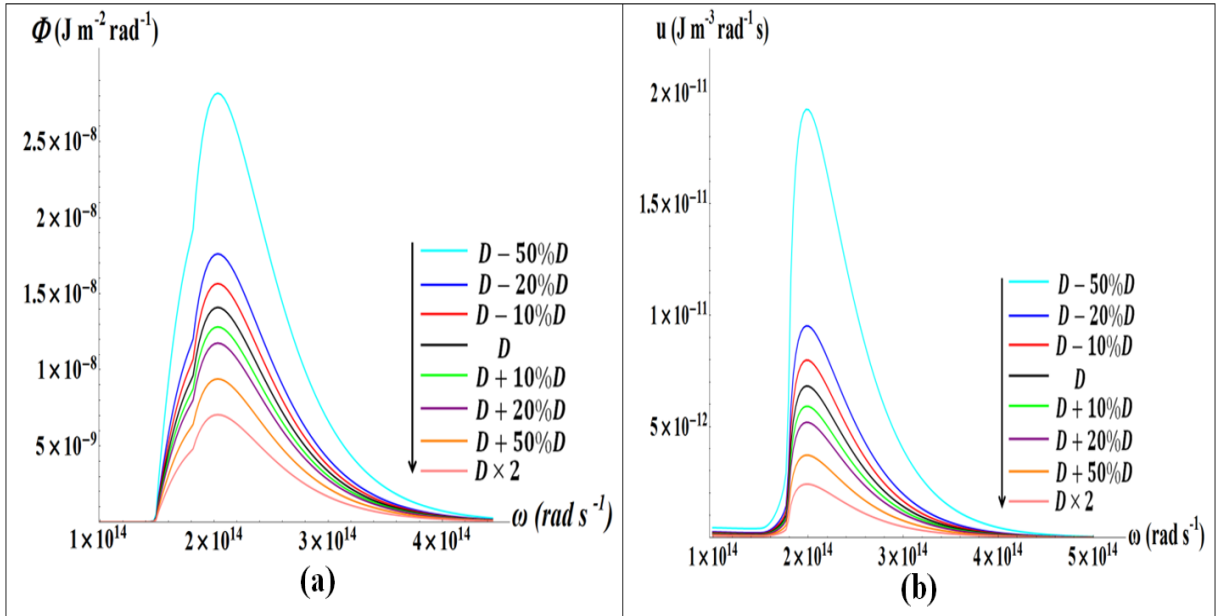


Figure 4.30: Plots of the spectral energy flux (a) and the spectral EM energy density (b) of the p -polarized evanescent EM waves as functions of the angular frequency, at $d = 10^{-12}m$ and $T=300K$, for different values of the parameter D for the nonlocal model of Ting ABC. The curves show that the energy densities are inversely proportional to D . The arrow indicates the increasing order of the value of D , as well as the order of the corresponding curves.

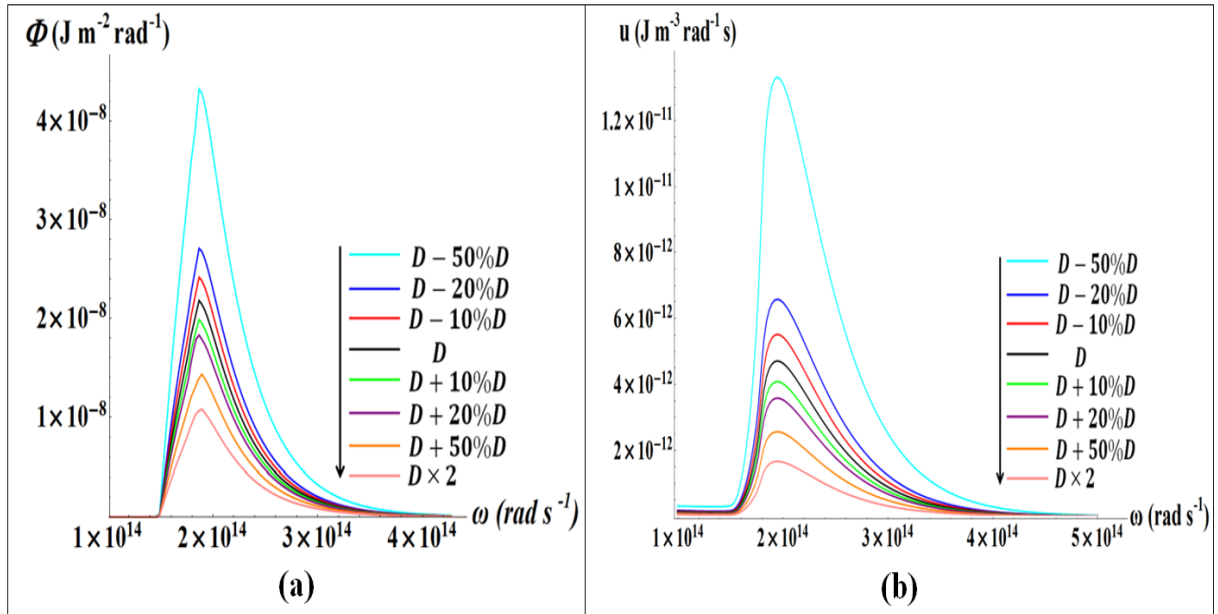


Figure 4.31: Plots of the spectral energy flux (a) and the spectral EM energy density (b) of the p -polarized evanescent EM waves as functions of the angular frequency, at $d = 10^{-12} \text{m}$ and $T=300\text{K}$, for different values of the parameter D for the nonlocal model of Agarwal ABC. The curves show that the energy densities are inversely proportional to D . The arrow indicates the increasing order of the value of D , as well as the order of the corresponding curves.

Conclusions

We have studied in this chapter RHT between two semi-infinite parallel dielectric 6H-SiC planes taking into account the nonlocal corrections in the material optical properties. We chose to follow Halevi and Fuchs nonlocal dielectric permittivity function theory that considers scattering of the EM excitation at the surface of the dielectric material. This assumption leads to defining additional boundary conditions (ABC) needed to solve the transmission problem in Maxwell's equations. Different ABC were considered and they appear as additional surface scattering parameters in the derived expressions of the surface impedances and reflection factors.

Taking into account the spatial dispersion that is given as an additional term depending on the square of the total wavevector and multiplied by a diffusion parameter D in the dielectric permittivity function, we studied the different nonlocal cases to calculate the RHTC between the 6H-SiC planes. We showed that for separation distances between few nanometers and few hundreds of nanometers, the RHTC follows a $1/d^2$ dependence law identical for both nonlocal and local material optical responses. On the other hand, at distances of few nanometers, the RHTC calculated with nonlocal modeling deviates from the $1/d^2$ law and saturation starts taking place. The heat transfer spectrum is also broadened when compared to the local case and we were able to show that the diffusion parameter D acts as a cutoff for the divergence of the RHTC obtained using the local model case.

Different features are revealed from the RHTC plots, as two bumps appeared for the cases of Kliewer and Fuchs and Ting et al. ABC. We studied the effects of varying the values of the different parameters of the model on the position and the width of these bumps by demonstrating the related plots. We showed that as the value of ω_p increases, the width of the bump decreases and its position shifts to smaller distances; while as the value of ω_p decreases, the width of the bump increases and its position shifts to larger distances. On the other hand, when the value of D increases, the position of the bump shifts to larger distances and its width increases. We also showed that the width of the bump increases as the value of the losses parameter increases, and decreases as the values of the latter decreases. We noticed also that the value of the losses parameter did not affect the position of the bump, except for the case where ν decreases by 50 %, the bump shifts significantly to larger distances. One of the most important features of our study is that the saturation of the radiative heat flux in the

nonlocal case is obtained for distances much smaller than the atomic size where the modeling presented here more likely ceases to be valid. At sub nanometer scale, heat transfer by electromagnetic waves probably ceases to be the dominant transfer modes and quantum effects enter into play leading to a transition between radiation and conduction.

We also studied the variation of the spectral energy flux and the EM energy density at different distances for the nonlocal models of the five different sets of the ABC considered and we showed that the energy densities increase as the distances decrease and the transfer spectrum broadens; the transfer is proportional to the LDOS. On the other hand, we studied the effect of varying the value of the diffusion parameter D on the variation of the energy densities by demonstrating their plots for each case. We showed that the energy densities are inversely proportional to the diffusion parameter.

In future works, we will have to compare our theoretical results with experimental measurements of near field thermal radiation. This would allow us to determine at the same time the distance at which the RHT stops to be the dominant heat transfer mode (below 1 nanometer) as well as the distance where local medium approximation becomes not valid (few nanometers). Experimental measurements could also be a way to choose between the different ABC that are suggested in the literature. The existence or non-existence of “bumps” could eliminate some of the modeling approaches and suggest a consistent nonlocal model for the dielectric permittivity function of dielectric materials.

References

1. P. Halevi and R. Fuchs, *J. Phys. C: Solid State Phys.* **17**, 3869 (1984).
2. N. W. Ashcroft and N. D. Mermin, “*Solid State Physics*”, Holt, Rinehart and Winston, New York, (1976).
3. J. J. Hopfield and D. G. Thomas, *Phys. Rev.* **132**, 563 (1963).
4. E. Palik, *Handbook of Optical Constants*, Vol. **1** (1985).
5. K. Joulain, J.-P. Mulet, F. Marquier, R. Carminati, and J.-J. Greffet, *Surf. Sci. Rep.* **57**, 59-112 (2005).
6. K. L. Kliewer and R. Fuchs, *Phys. Rev.* **172**, 607 (1968).
7. R. Fuchs and K. L. Kliewer, *Phys. Rev. B* **3**, 2270 (1971).
8. B. Fischer and H. Queisser, *Solid State Commun.* **16**, 1125 (1975).
9. C. Ting, M. Frankel and J. Birman, *Solid State Commun.* **17**, 1285 (1975).
10. R. Ruppin, *J. Opt. Soc. Am.* **71**, 755 (1981).
11. P. Rimbey and G. Mahan, *Solid State Commun.* **15**, 35 (1974).
12. P. Rimbey, *Phys. Statu Solidi* **68**, 617 (1975).
13. D. Johnson and P. Rimbey, *Phys. Rev. B* **15**, 5087 (1976).
14. P. Rimbey, *Phys. Rev. B* **15**, 1215 (1977).
15. P. Rimbey, *Phys. Rev. B* **18**, 971 (1978).
16. S. Pekar, *Sov. Phys. JETP* **6**, 785 (1958).
17. S. Pekar, *Sov. Phys. JETP* **7**, 813 (1958).
18. S. Pekar, *J. Phys. Chem. Solids* **5**, 11 (1958).
19. S. Pekar, *Sov. Phys. JETP* **9**, 314 (1959).
20. G. Agarwal, D. Pattanayak and E. Wolf, *Phys. Rev. Lett.* **27**, 1022 (1971).
21. G. Agarwal, D. Pattanayak and E. Wolf, *Opt. Commun.* **4**, 255 (1971).
22. G. Agarwal, *Opt. Commun.* **4**, 221 (1972).
23. J. Birman and J. Sein, *Phys. Rev. B* **6**, 2482 (1972).
24. G. Agarwal, *Phys. Rev. B* **8**, 4768 (1973).
25. A. Maradudin and D. Mills, *Phys. Rev. B* **7**, 2787 (1973).
26. J. Birman and R. Zeyher, “*Polaritons*”, ed. E. Burstein and F. DeMartini (New York: Pergamon), p. 161 (1974).

27. D. Mills, “*Polaritons*”, ed. E. Burstein and F. DeMartini (New York: Pergamon), p. 147 (1974).
 28. J. Foley and A. Devaney, *Phys. Rev. B* **12**, 3104 (1975).
 29. M. Bishop, A. Maradudin and D. Mills, *Phys. Rev. B* **14**, 4744 (1976).
 30. H. Duan , A. I. Fernández-Domínguez, M. Bosman, S. A. Maier and J. K. W. Yang, *Nano Lett.* **12**, 1683 (2012).
 31. J.A. Scholl, A.I. Koh and J.A. Dionne, *Nature* **483**, 421 (2012).
 32. F. Javier Garcia de Abajo, *Nature* **483**, 417 (2012).
- S. Xiong, K. Yang, Y. A. Kosevich, Y. Chalopin, R. D’Agosta, P. Cortona and S. Volz, *Phys. Rev. Lett.* **112**, 114301 (2014).

Chapter 5

5. Lindhard–Mermin nonlocal model for n-doped semiconductors

Introduction

In this chapter we study the RHTC between two semi-infinite parallel solid planes of n-doped Si when the distance between them tends to zero. We conduct this study by using first the local model of the dielectric permittivity where we show, as shown and discussed in previous chapters, that the infinite divergence is obtained due to the contribution of the p -polarized evanescent EM waves. Then we will repeat our calculations by considering a nonlocal model of the dielectric permittivity and for this reason, we will apply the Lindhard–Mermin nonlocal theory of the dielectric permittivity to our system. We will show that saturation of the RHTC is obtained at very small distances, in contrary to the results obtained for the local case.

One particular characteristic acquired by the n-doped Si material is the possibility of tuning its dielectric permittivity by modifying the carrier concentration N [1]. This allows to tune the plasma frequency and therefore the frequency where the material enters into resonance, leading to important different applications in different technological domains. Being n-doped, this Si material acquires extra electrons in its conduction band resulting in changing its properties to approach those of metals.

Due to the fact that the n-doped Si characteristics are very close to those of metals, we apply the same dielectric permittivity model we apply to metals (Chapter 2) in our study of the RHTC between two semi-infinite parallel planes of n-doped Si as the distance between them tends to zero. By repeating the study for different doping levels, our results show saturation of the RHTC upon applying this nonlocal model which lead us to conclude that the radiation is driven by the plasmons at the surface and the saturation starts at distances of the order of the Thomas–Fermi length.

5.1 Theory of the local model of the dielectric permittivity

In this section, we present the theory of the local dielectric permittivity used in the study of the RHT between the two heavily n-doped Si planes (see Fig. 1.5) of average temperature $T=300K$ ($T_1 = 300.5K$ and $T_2 = 299.5K$). In the infrared domain, the local dielectric permittivity of n-doped Si is given by the well-known Drude expression [1]:

$$\varepsilon(\omega) = \varepsilon_\infty \left(1 - \frac{\omega_p^2}{\omega(\omega + i/\tau)} \right) \quad (5.1)$$

$\varepsilon_\infty = 11.7$ is the static permittivity, ω_p is the plasmon frequency given by $\omega_p^2 = Ne^2/m^*\varepsilon_\infty\varepsilon_0$, where $\varepsilon_0 = 8.854 \times 10^{-12} F.m^{-1}$ is the vacuum permittivity, N is the doping concentration, $m^* = 0.27 \times m_0$ is the electron effective mass, $m_0 = 9.109 \times 10^{-31} Kg$ is the free electron mass, $e = 1.602 \times 10^{-19} C$ is the electron charge. τ is the relaxation time or the inverse of the loss factor ν defined as $\nu = 1/\tau = Ne^2\rho/m^*$ where ρ is the electric resistivity of the doped Si [1].

5.1.1 Formalism

In our calculations we considered three different values of the doping concentration: $N = 10^{19} cm^{-3}$, $10^{20} cm^{-3}$ and $10^{21} cm^{-3}$, and the values of the electric resistivity ρ were obtained graphically from the graphs given by references [1,2] as the resistivity depends on the value of N . We therefore deduced the value of τ for each concentration Fig. 5.1.

To calculate the RHTC between the two n-doped Si given by Eq. (1.13), we should first substitute with the expressions of the reflection factors at the surface. As we did in all the local theories we studied, we consider the reflection factors given by Fresnel equations and defined in chapter 1: Eqs. (1.18).

5.1.2 Calculation of the radiative heat transfer coefficient

For each value of N , we substituted with the equations of the dielectric permittivity Eq. (5.1) and the reflection factors Eqs. (1.15) in Eqs. (1.13) to calculate the RHTC for both s and p -polarized EM waves. In Figs. 5.2, 5.3, and 5.4 we show the plots of the different contributions to the RHTC between the two n-doped Si semi-infinite parallel planes.

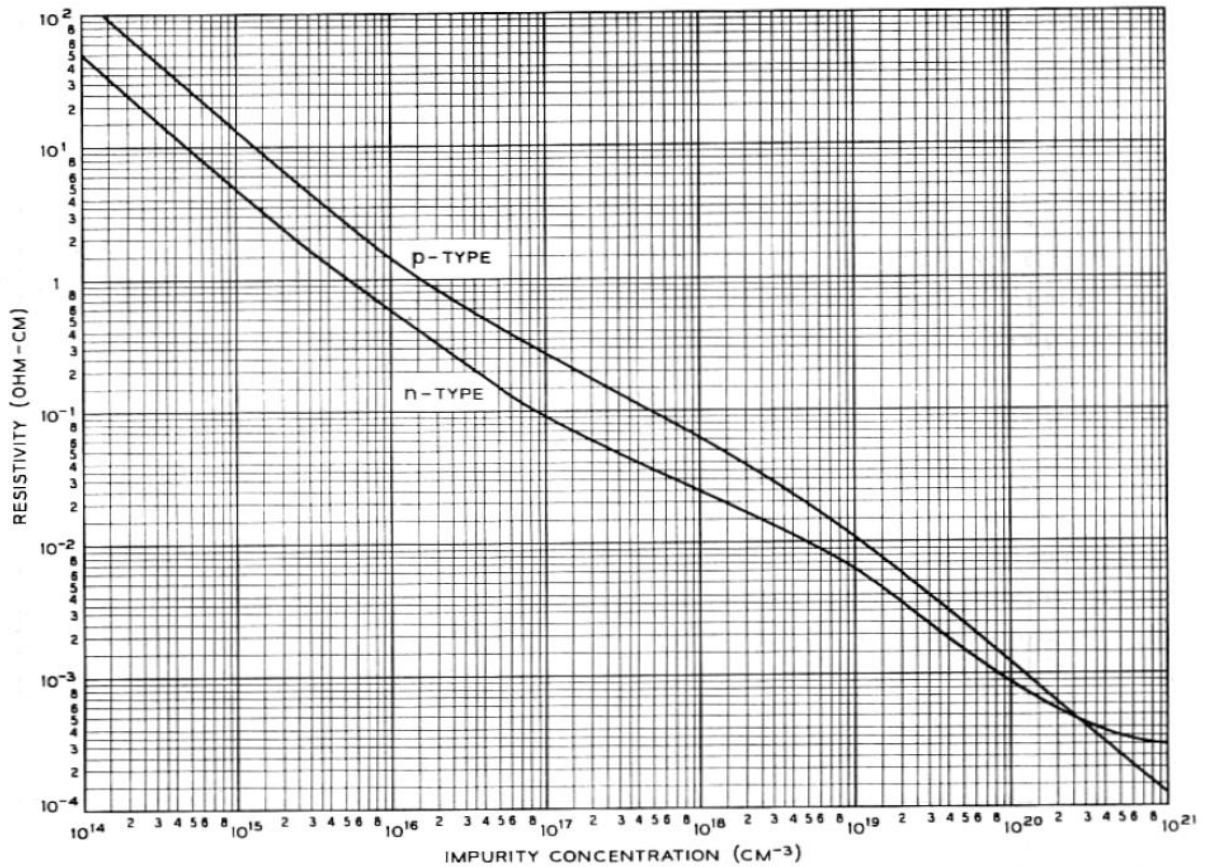


Figure 5.1: Resistivity of Si at $T=300\text{K}$ as a function of acceptor and donor concentration [2].

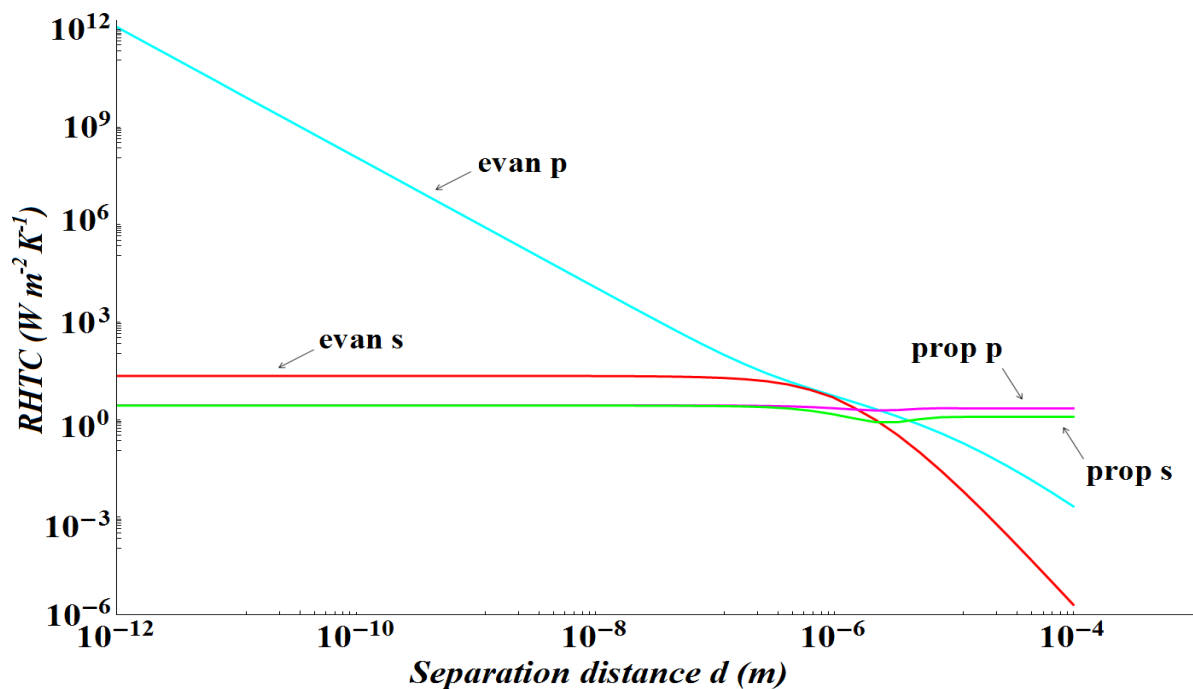


Figure 5.2: Variation of the RHTC (contributions of the evanescent and propagative EM waves of s and p polarizations) as function of the distance between two semi-infinite n-doped Si parallel planes of doping concentration $N = 10^{19}\text{cm}^{-3}$ and average temperature $T=300\text{K}$, for the local model case.

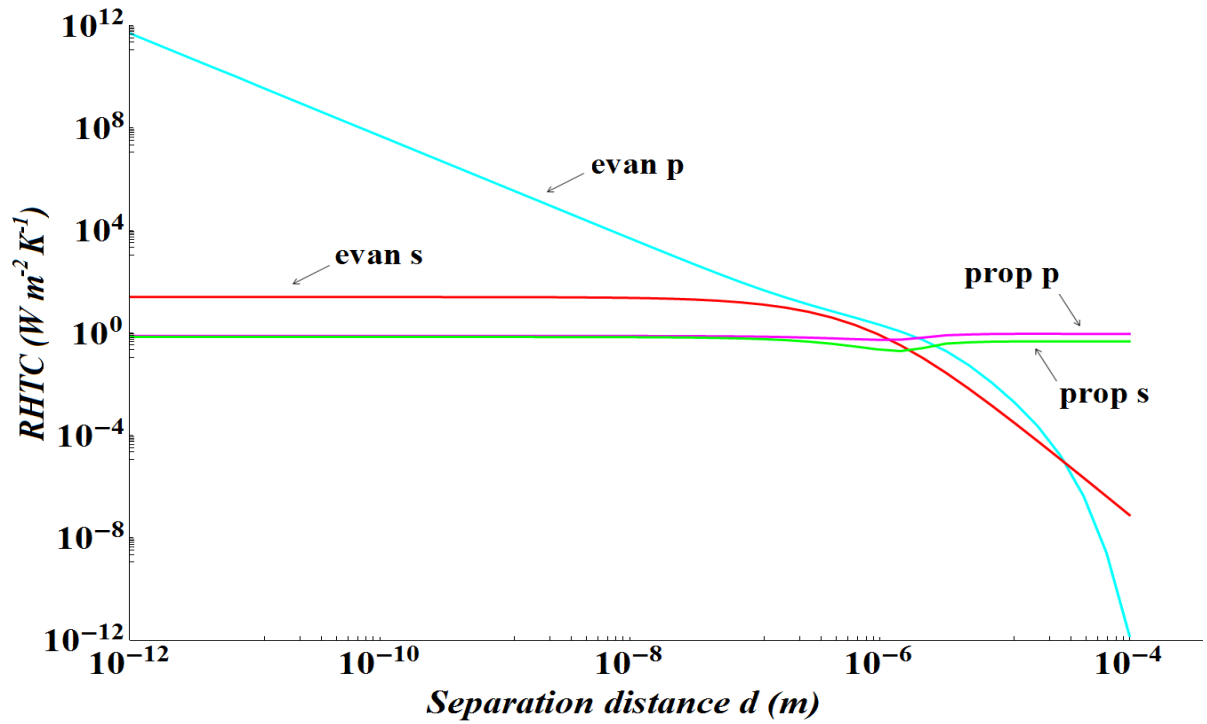


Figure 5.3: Variation of the RHTC (contributions of the evanescent and propagative EM waves of s and p polarizations) as function of the distance between two semi-infinite n-doped Si parallel planes of doping concentration $N = 10^{20} \text{ cm}^{-3}$ and average temperature $T=300\text{K}$, for the local model case.

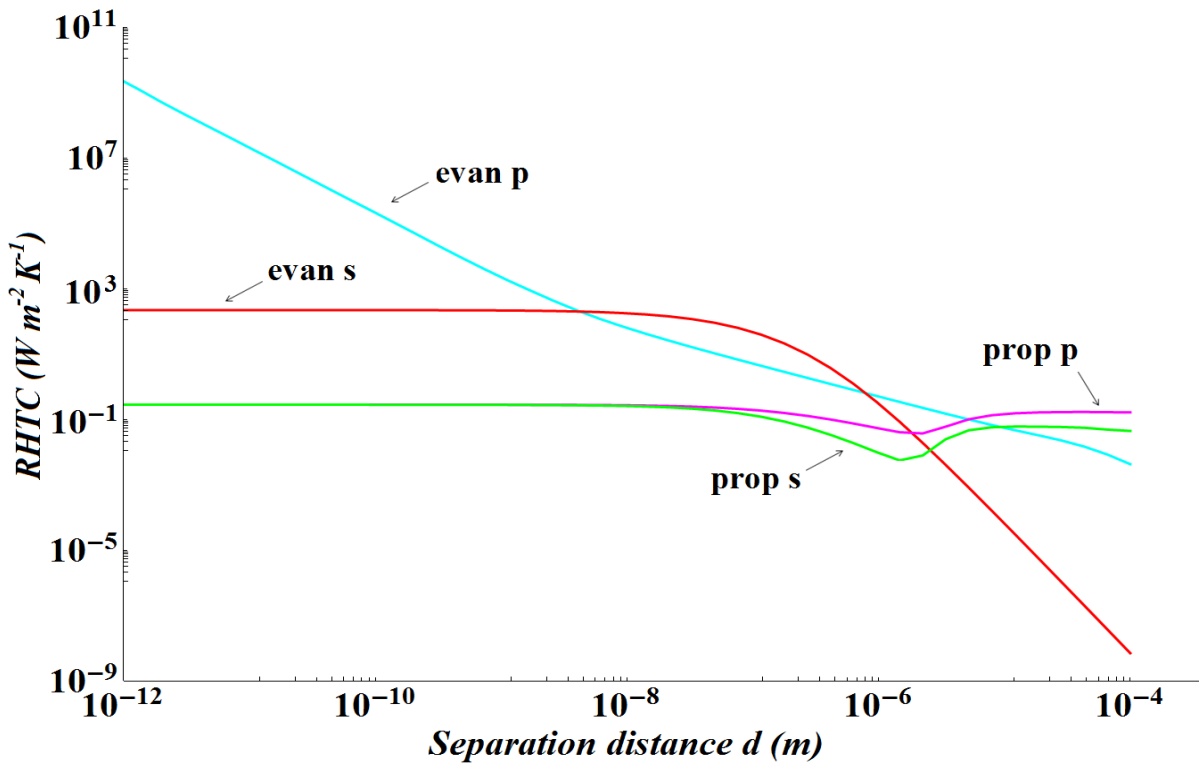


Figure 5.4: Variation of the RHTC (contributions of the evanescent and propagative EM waves of s and p polarizations) as function of the distance between two semi-infinite n-doped Si parallel planes of doping concentration $N = 10^{21} \text{ cm}^{-3}$ and average temperature $T=300\text{K}$, for the local model case.

From these figures we notice that the evanescent contribution of the EM waves of p -polarization increases infinitely as d decreases in all the cases, and it dominates the transfer at very short distances. The values reached by this contribution at short distances decrease, as the value of the doping concentration increases. Concerning interpretation of the behavior of this contribution, as well as the other contributions (and the distance ranges at which they dominate), the argument given for the case of Aluminum (chapter 1) applies for them with the note here that the resonance frequency at which the surface plasmon-polaritons are excited is $\approx \omega_p$. By comparing the variations of the propagative s and p -polarized contributions in the different cases, we notice that their values decrease as N increases. The evanescent contribution of the s -polarized EM waves showed relatively equal magnitudes for the cases $N = 10^{19} \text{cm}^{-3}$ and 10^{20}cm^{-3} , but it increased by almost an order for ten for the case $N = 10^{21} \text{cm}^{-3}$. These results show the dependence of the RHTC on the value of the doping concentration which could be also concluded from the dependence of ω_p on N . The contribution of the evanescent waves of p -polarization also varied with the doping concentration N and since this contribution dominates the transfer at small distances, we plot in Fig. 5.5 the total contributions to the RHTC for the different values of N .

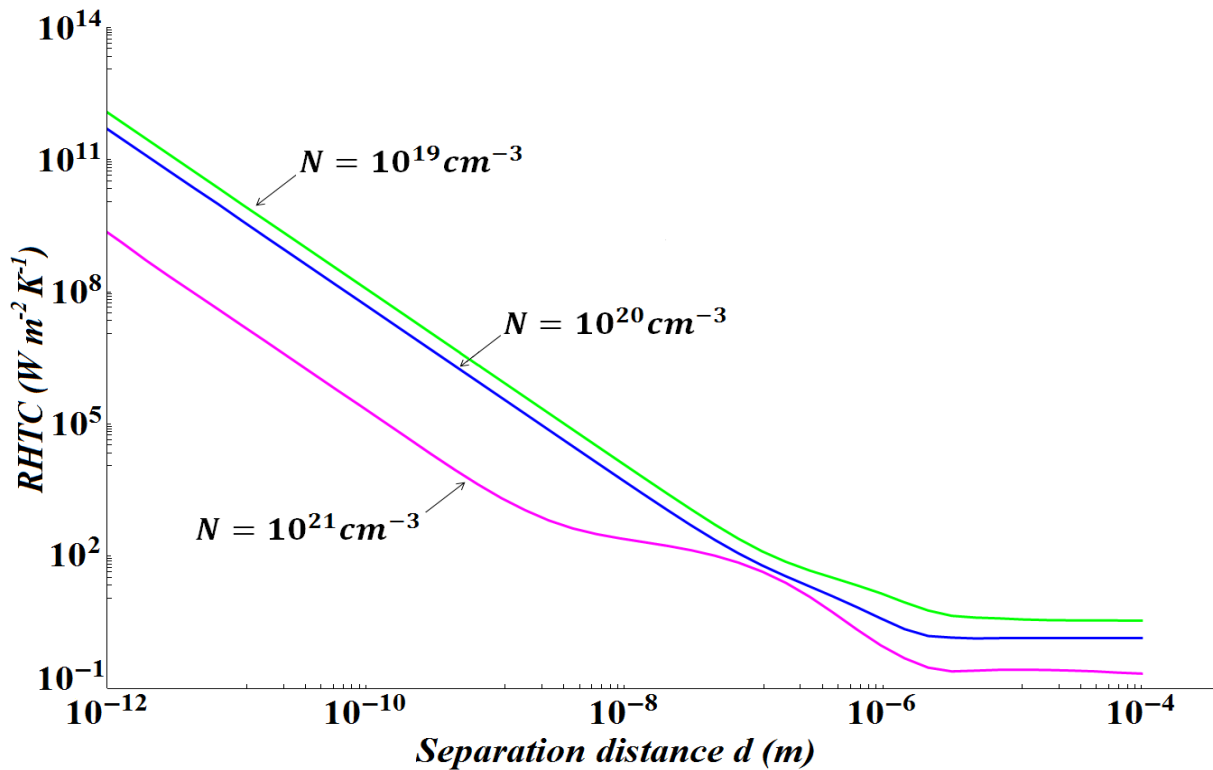


Figure 5.5: Variation of the total RHTC (summation of the contributions of the evanescent and propagative EM waves of s and p polarizations) as function of the distance between two semi-infinite n-doped Si parallel planes of average temperature $T=300\text{K}$ and of doping concentration $N = 10^{19} \text{cm}^{-3}$, 10^{20}cm^{-3} and 10^{21}cm^{-3} , for the local model case.

We notice in Fig. 5.5 that at large distances the total contribution to the RHTC decreased as N increased in value. As the distance decreased we notice that the maximum contribution was attained for the case where $N = 10^{19} \text{cm}^{-3}$, and the minimum contribution was attained for the case where $N = 10^{21} \text{cm}^{-3}$. We interpret these observations by examining the dependence of the plasmon frequency on the doping level N . For each value of N corresponds a different value of ω_p . It is clear from the relation between them that ω_p increases as the value of N increases. This implies that as the value of ω_p vary within the Planck range, the corresponding spectrum shows a similar behavior as Planck spectrum; i.e. the spectrum will increase as the value of ω_p increases, until reaching a maximum, after which it decreases in magnitude. For this reason, we observed that the highest values of the RHT are attained for the doping level $N = 10^{20} \text{cm}^{-3}$, after which the spectrum decreases as N increases in values.

5.2.3 Study of the contribution of the surface-plasmon polaritons

Rousseau et al. [3,4] studied the contribution of the surface-plasmon polaritons to the RHTC between two highly n-doped Si planes h_{rad}^{spp} , and they were able to derive an accurate asymptotic expression of this contribution at nanometric distances where the electrostatic limit is valid Eqs. (5.2) [3,4]. They were also able to specify the doping concentration N needed to maximize the RHTC between the two planes [4].

$$\left\{ \begin{array}{l} h_{rad}^{spp}(u, T, d) = \frac{\delta G(T, N)}{d^2} \\ \delta G(T, N) = \frac{k_B^2 T}{2\pi h} \int_0^\infty du \frac{u^2 e^u}{(e^u - 1)^2} \frac{Im(\tilde{r}_{31}^p) Im(\tilde{r}_{32}^p)}{Im(\tilde{r}_{31}^p \tilde{r}_{32}^p)} Im[L_{i2}(\tilde{r}_{31}^p \tilde{r}_{32}^p)] \end{array} \right\} \quad (5.2)$$

where L_{i2} is the polylogarithm function of second order (check Appendix E), and

$$\left\{ \begin{array}{l} u = \frac{\hbar \omega}{k_B T} \\ \tilde{r}_{3m}^p = \frac{\varepsilon(u) - 1}{\varepsilon(u) + 1} \end{array} \right\} \quad (5.3)$$

Since our system consists of two identical planes, $\delta G(T, N)$ becomes:

$$\delta G(T, N) = \frac{k_B^2 T}{2\pi h} \int_0^\infty du \frac{u^2 e^u}{(e^u - 1)^2} \frac{[Im(\tilde{r}_{3m}^p)]^2}{Im(\tilde{r}_{3m}^p)^2} Im[L_{i2}(\tilde{r}_{3m}^p)^2] \quad (5.4)$$

Since the dielectric permittivity, and consequently the reflection factor are dependent on the doping concentration N , Rousseau et al. [4] plotted the variation of $\delta G(T, N)$ as a function of

N and T . We also plotted the behavior of $\delta G(T, N)$ as T varies for different N (Fig. 5.6) and as N varies for different T (Fig. 5.7).

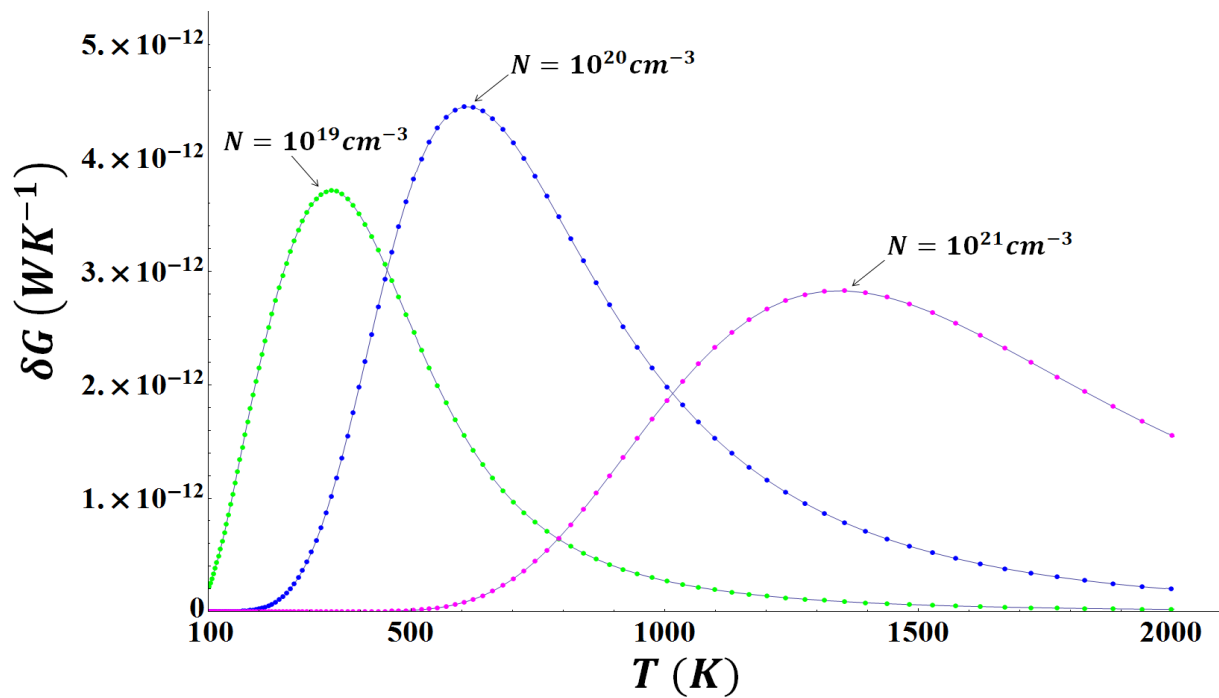


Figure 5.6: Variation of $\delta G(T, N)$ as the average temperature T varies for the three different doping concentrations considered in the calculation of the RHTC between the n-doped Si semi-infinite parallel planes.

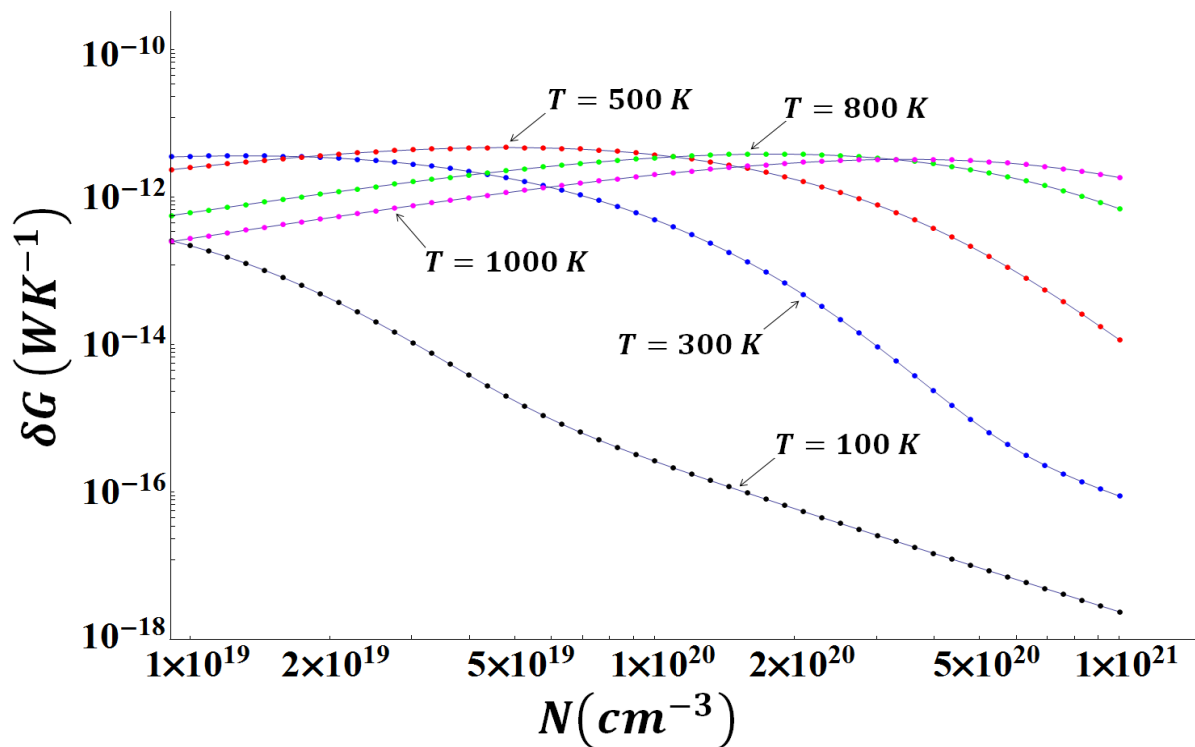


Figure 5.7: Variation of $\delta G(T, N)$ as the doping concentration varies for different average temperatures T .

Fig. 5.6 shows the variation of $\delta G(T)$ as a function of the temperature T for the cases where $N = 10^{19} \text{ cm}^{-3}$, 10^{20} cm^{-3} and 10^{21} cm^{-3} . By comparing the curves we notice that for each doping concentration, $\delta G(T, N)$ increases as T increases until reaching a maximum value after which it starts to decrease. We notice that the maximum point shifts to the right as the doping concentration increases, i.e. the temperature at which the maximum of $\delta G(T, N)$ occurs increases with the increase of N . We observe for the case $N = 10^{21} \text{ cm}^{-3}$ that the magnitude of the graph is less than those of the other graphs.

In Fig. 5.7 we observe that for temperature $T=100\text{K}$ and 300K , $\delta G(T, N)$ decreases as N increases. For the case where $T=500\text{K}$, the graph increases in values till reaching its maximum at $N \approx 5 \times 10^{19} \text{ cm}^{-3}$, after which it decreases. The same behavior is observed for the graph corresponding to the case where $T=800\text{K}$, except that the maximum of this graph is reached at $N \approx 2 \times 10^{20} \text{ cm}^{-3}$. For the case where $T=1000\text{K}$, the curve increases till reaching its maximum at large doping concentration, $N \approx 5 \times 10^{20} \text{ cm}^{-3}$, after which the values decrease only slightly. Rousseau et al. [4] plotted such a curve for the case where $T=300\text{K}$ and our results are similar. We notice that the concentration at which $\delta G(T, N)$ attains its maximum value shifts to the right, i.e. to higher values as the temperature increases. We can therefore conclude that for any temperature T and doping level N , corresponds a plasmon frequency that lies in the spectral range, and relates to the optimum resonance and the maximum transfer.

We have shown in this section that the RHTC between two n-doped Si semi-infinite parallel planes diverges at small distances upon considering a local model of the dielectric permittivity; and for this reason, we will repeat our calculations in the following section by considering a nonlocal model of the dielectric permittivity.

5.2 Theory of the nonlocal model of the dielectric permittivity: Lindhard–Mermin nonlocal model

In this section, we aim to repeat the calculation of the RHTC between two n-doped Si semi-infinite parallel planes by considering a nonlocal model of the dielectric permittivity in our study. As we mentioned in the introduction, the highly n-doped Si acquire characteristics similar to those of metals, and for this reason, we chose to apply the Lindhard-Mermin nonlocal model of the dielectric permittivity [5-8].

5.2.1 Formalism

In chapter 2 we mentioned that the Lindhard-Mermin model of the nonlocal dielectric permittivity is the most studied nonlocal model for the case of metals and we used it in the studying the case of Aluminum.

For our system consisting of two semi-infinite parallel solid n-doped Si planes, the equations of the longitudinal and transverse components of the nonlocal dielectric permittivity are given as follows:

$$\left\{ \begin{array}{l} \varepsilon_{LM}^l(\omega, z) = \varepsilon_\infty + \frac{3 \varepsilon_\infty \omega_p^2}{\omega + i\nu} \frac{u^2}{\{\omega + i\nu [f_l(z, u)/f_l(z, 0)]\}} \\ \varepsilon_{LM}^t(\omega, z) = \varepsilon_\infty - \frac{\varepsilon_\infty \omega_p^2}{\omega^2(\omega + i\nu)} \{\omega [f_t(z, u) - 3z^2 f_l(z, u)] + i\nu [f_t(z, 0) - 3z^2 f_l(z, 0)]\} \end{array} \right\} \quad (5.5)$$

With

$$\left\{ \begin{array}{l} z = k/2k_F \\ u = (\omega + i\nu)/kv_F \\ v_F = \sqrt{\frac{2}{m^*} k_B T \log \frac{N}{N_c}} \\ N_c = 2(m^* k_B T / 2\pi \hbar^2)^{3/2} \\ k_F = m^* v_F / \hbar \\ f_l(z, u) = \frac{1}{2} + [1 - (z - u)^2 / 8z] \ln(z - u + 1/z - u - 1) + \\ \quad [1 - (z + u)^2 / 8z] \ln(z + u + 1/z + u - 1) \\ f_t(z, u) = \frac{3}{8} (z^2 + 3z^2 + 1) - \{3 [1 - (z - u)^2]^2 / 32z\} \ln(z - u + 1/z - u - 1) - \\ \quad \{3 [1 - (z + u)^2]^2 / 32z\} \ln(z + u + 1/z + u - 1) \\ f_l(z, 0) = \frac{1}{2} + (1 - z^2 / 4z) \ln|z + 1/z - 1| \\ f_t(z, 0) = \frac{3}{8} (z^2 + 1) - [3(1 - z^2)^2 / 16z] \ln|z + 1/z - 1| \end{array} \right\} \quad (5.6)$$

where v_F is the Fermi velocity, k_F is the Fermi wavevector, and N_c is the density of the carriers in the conduction band. For $T=300\text{K}$, $N_c \approx 3.5 \times 10^{18} \text{cm}^{-3}$. It is important to note here that the main difference between applying the Lindhard-Mermin model for metals and applying it for n-doped Si is the dependence of the Fermi velocity v_F on the doping concentration N in the case of Si, where for metals it is a constant. This constitutes the main reason for us to predict the strong dependence of the results we obtain on the concentration level N .

5.2.2 Calculation of the radiative heat transfer coefficient

The reflection factors needed to calculate the RHTC in this case, are given by the general equations Eqs. (1.15), and the equations of the surface impedances are also given by the general forms Eqs. (1.16). By substituting these equations in the RHTC equations (Eqs. (1.13)), we obtained the different contributions to the RHTC as the distance d decreases, for the cases where $N = 10^{19} \text{ cm}^{-3}$, 10^{20} cm^{-3} and 10^{21} cm^{-3} . The results are reported in Figs. 5.8, 5.9, and 5.10. The most significant result shown in these figures is the saturation of the contribution of the evanescent p -polarized EM waves at small distances. The contributions of the propagative waves were the same in the local and the nonlocal cases, and this is expected because, as we mentioned in all our previous studies, these contributions dominate in the far-field regime where nonlocal effects are not important. In the near-field regime the evanescent contributions dominate; and as for the s -polarized contribution, we notice that for the cases where $N = 10^{19} \text{ cm}^{-3}$ and 10^{20} cm^{-3} it was the same for both the local and the nonlocal case. For the case where $N = 10^{21} \text{ cm}^{-3}$, this contribution changed significantly in the nonlocal case where the values dropped by a factor of ten, in comparison with the values obtained in the local case. We notice also from these plots that the values attained by the saturating contribution of the p -polarized EM evanescent waves are not equal.

To better compare between them we plot the curves of the total contribution to the RHTC for all the cases in Fig. 5.11. We observe in this figure that the saturation values attained by the curves are not equal, and they increase as the value of the doping concentration N increases from 10^{19} cm^{-3} to 10^{20} cm^{-3} . However for the case where $N = 10^{21} \text{ cm}^{-3}$, the saturation value decreased. We added to this figure the values of the Thomas-Fermi screening length calculated for each value of N and given by $l_{TF} = \vartheta_F / \omega_p$, where it is clear from this formula the dependence of l_{TF} on N as both ϑ_F and ω_p are dependent on N . For each curve, we notice that the distance at which its saturation starts to take place is smaller than the value of l_{TF} . In other words, the deviation of each curve from the infinite sharp divergence takes place at distances of the order of l_{TF} , after which saturation takes place. This is also shown clearly in Fig. 5.12 where we compare between the curves of the total contributions to the RHTC in the local and the nonlocal cases.

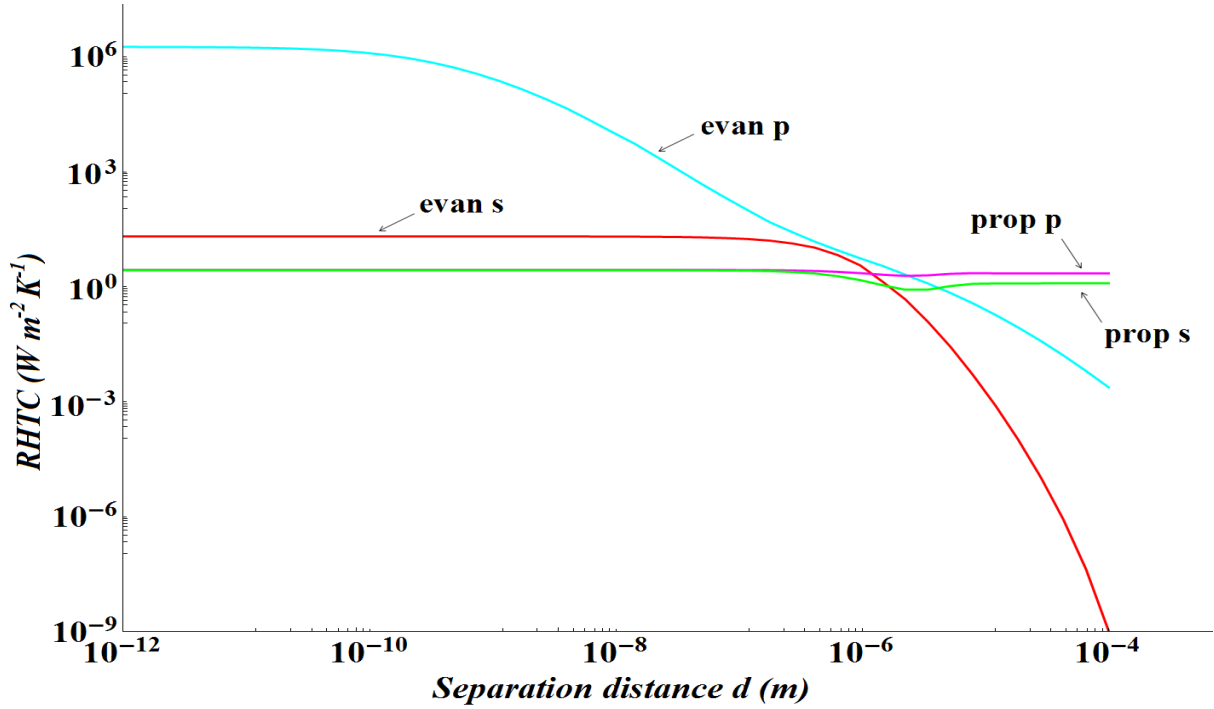


Figure 5.8: Variation of the radiative heat transfer coefficient (contributions of the evanescent and propagative EM waves of p and s polarizations) as function of the distance between two semi-infinite n-doped Si parallel planes of doping concentration $N = 10^{19}\text{cm}^{-3}$ and average temperature $T=300\text{K}$, for the nonlocal model case.

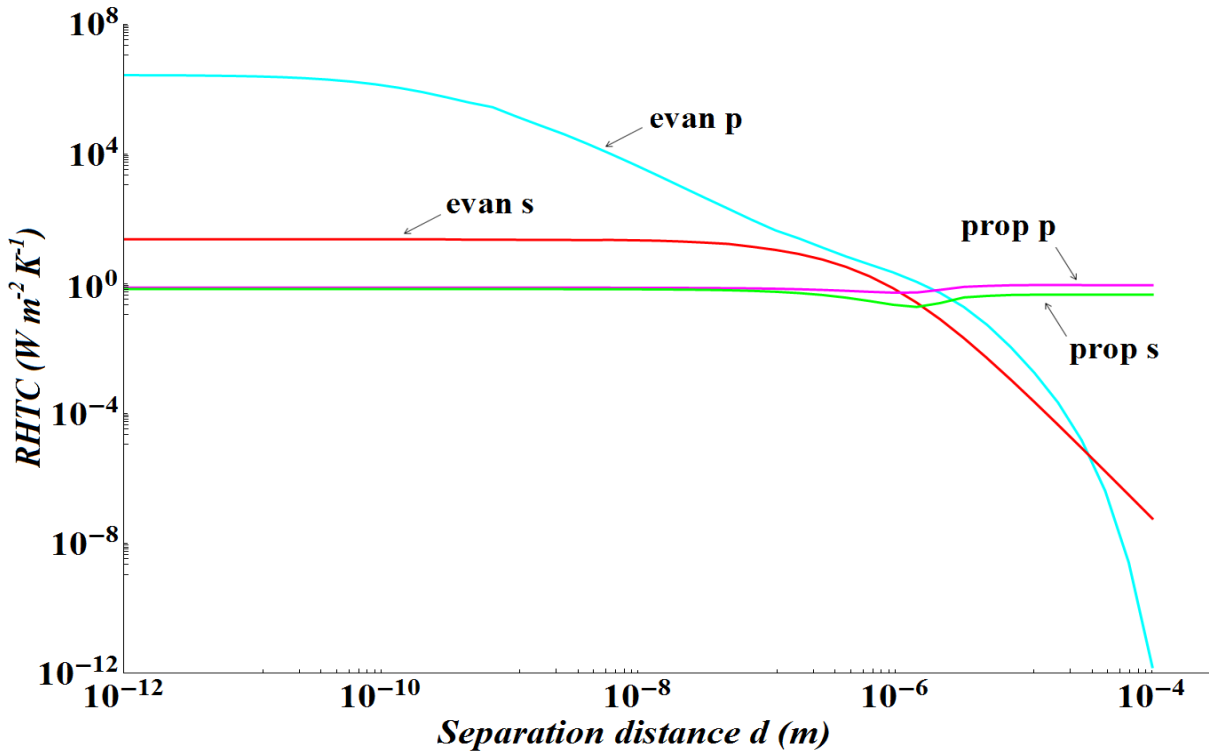


Figure 5.9: Variation of the radiative heat transfer coefficient (contributions of the evanescent and propagative EM waves of p and s polarizations) as function of the distance between two semi-infinite n-doped Si parallel planes of doping concentration $N = 10^{20}\text{cm}^{-3}$ and average temperature $T=300\text{K}$, for the nonlocal model case.

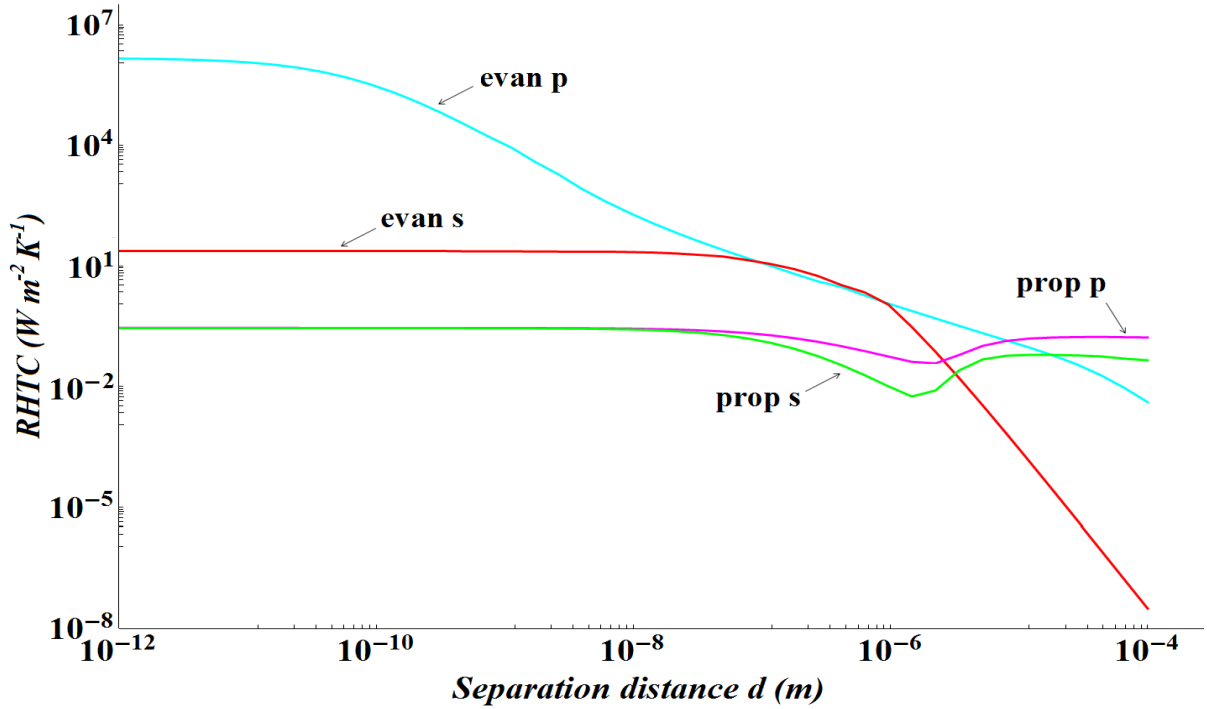


Figure 5.10: Variation of the radiative heat transfer coefficient (evanescent and propagative contributions of p and s polarizations) as function of the distance between two semi-infinite n-doped Si parallel planes of doping concentration $N = 10^{21} \text{ cm}^{-3}$ and average temperature $T=300\text{K}$, for the nonlocal model case.

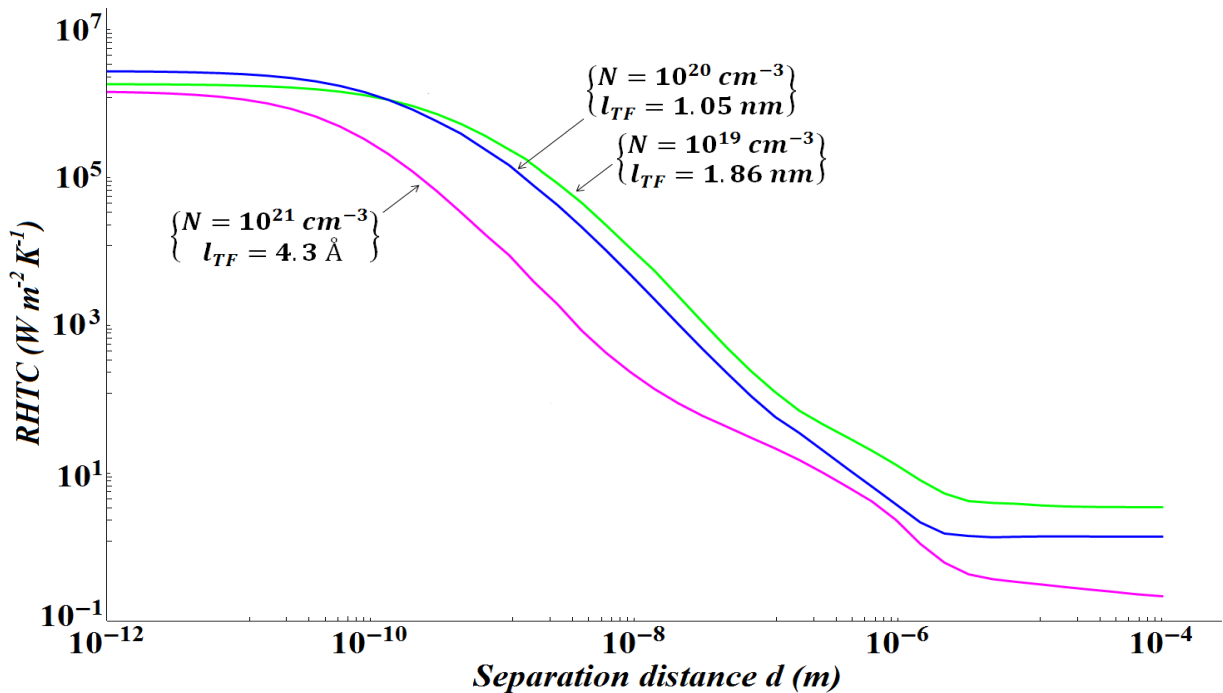


Figure 5.11: Variation of the total radiative heat transfer coefficient (summation of the contributions of the evanescent and propagative EM waves of s and p polarizations) as function of the distance between two semi-infinite n-doped Si parallel planes of doping concentration $N = 10^{19} \text{ cm}^{-3}$, 10^{20} cm^{-3} and 10^{21} cm^{-3} , for the nonlocal model case. The inset shows the values of the Thomas-Fermi length calculated for each value of the doping concentration N . For each graph, we notice that the distance at which its saturation starts to take place is smaller than the value of l_{TF} .

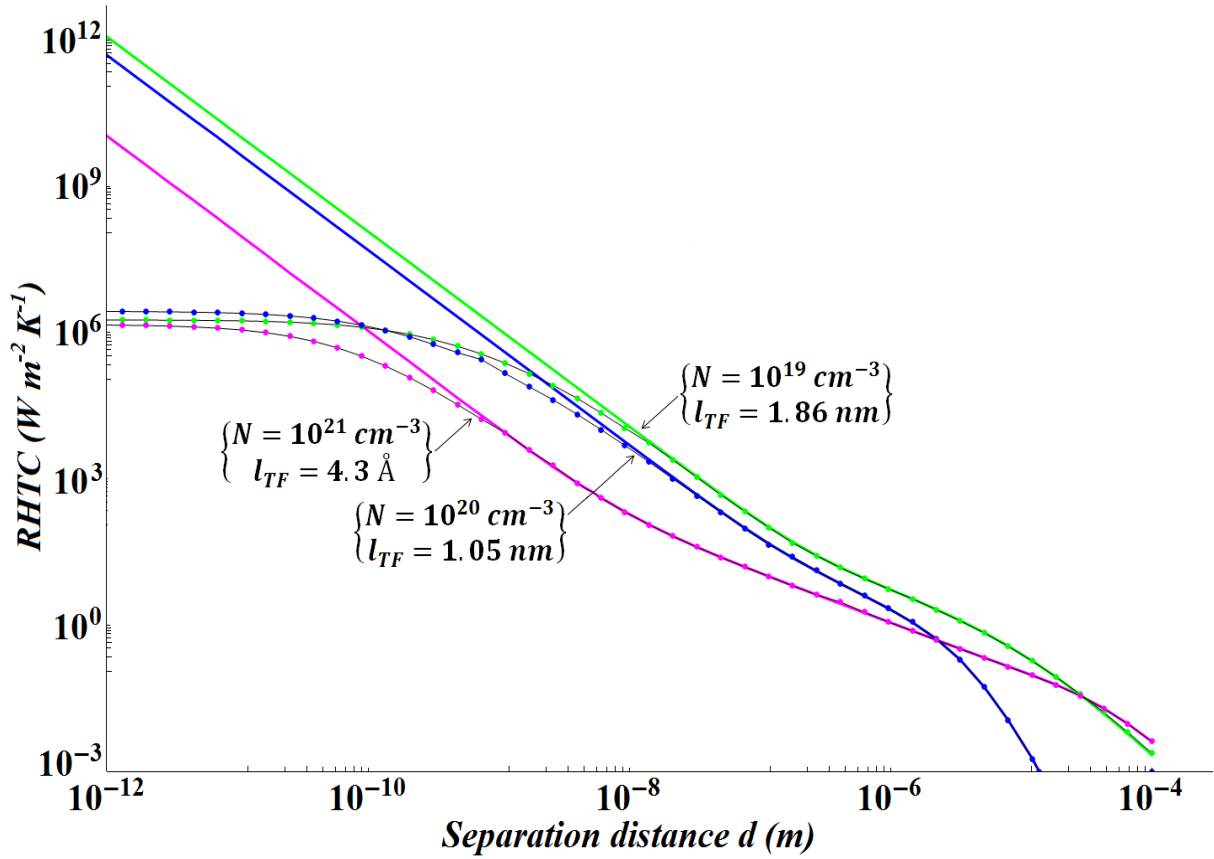


Figure 5.12: Variation of the total radiative heat transfer coefficient (summation of the contributions of the evanescent and propagative EM waves of s and p polarizations) as function of the distance between two semi-infinite n-doped Si parallel planes of doping level $N = 10^{19} \text{ cm}^{-3}$, 10^{20} cm^{-3} and 10^{21} cm^{-3} and average temperature $T=300\text{K}$, for the local and the nonlocal model cases. The graphs of the nonlocal model saturate at distances of the order of the Thomas-Fermi length l_{TF} , below which saturation takes place.

From Fig. 5.12 we notice that the curves of the nonlocal model deviate from the diverging slope at distances of the order of the Thomas-Fermi length and saturation then takes place for smaller distances. Since for metals, and eventually for highly doped materials that exhibit metallic-like characteristics, nonlocal effects appear at distances smaller than the Thomas-Fermi length [9], it is expected that the saturation takes place at distances smaller than l_{TF} . Taking into account the nonlocal effects in the dielectric permittivity equations allows to represent correctly the optical response at small distances and lead finally to the saturation of the RHTC. We wanted to study the variation of the saturation values of the contribution of the p -polarized EM evanescent waves to the RHTC as the doping level N varies, and for this reason we plotted in Fig. 5.13 the obtained saturation values of the RHTC as N takes the values between 10^{19} cm^{-3} and 10^{21} cm^{-3} where the average temperature of the system was considered $T=300 \text{ K}$.

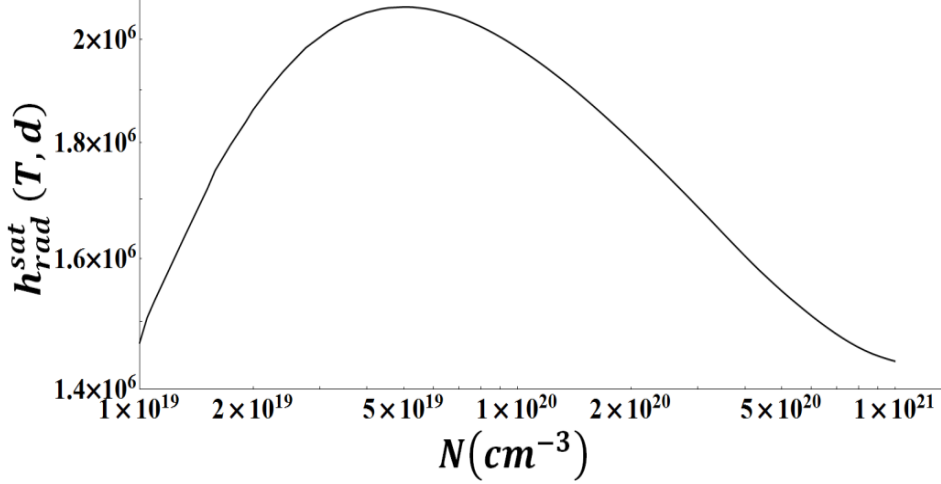


Figure 5.13: Variation of the saturation value of the RHTC graph as the doping concentration varies between 10^{19} cm^{-3} and 10^{21} cm^{-3} for the nonlocal model case where the average temperature of the system is considered $T=300\text{K}$.

We observe in Fig. 5.13 that the saturation value of the RHTC increases as N increases until reaching its maximum value for about $N = 9 \times 10^{19} \text{ cm}^{-3}$, after which it decreases for further increase of the doping concentration level N . This emphasizes the discussion we presented in the previous section. We explained that since for any N , corresponds a plasmon frequency that lies in the Planck range, we obtain a spectrum that varies in a way that mimics the Planck spectrum. This means that the spectrum increases in values until reaching a maximum, after which it decreases. For this reason we observe in Fig. 5.13 that the saturation value of the RHTC increases as N increases until reaching a maximum, apparently for about $N = 9 \times 10^{19} \text{ cm}^{-3}$, after which it starts to decrease as the value of N continues to increase.

We also study the variation of the transmission factor $4(Im(r_{31}^P))^2 e^{2i\gamma_3 d} / |1 - (r_{31}^P)^2 e^{2i\gamma_3 d}|^2$ of the p -polarized EM evanescent waves, for the local and the nonlocal models, by plotting it in the (ω, K) plane for different doping concentrations, and at different distances (Figs. 5.14, 5.15, and 5.16). We notice from the spectrums of the local model (a) that at any d , the transmission factor increases in magnitude as K increases, and as the distance decreases the maximum is reached at larger K values. This implies that more modes are able to couple well to the transmission as K increases, which explains the infinite increase attained by the RHTC in the previous figures. From the figures of the nonlocal model (b), we notice that the transmission factor increases as K increases until reaching a cutoff after which the transmission factor tends to zero where no modes are able to be transmitted.

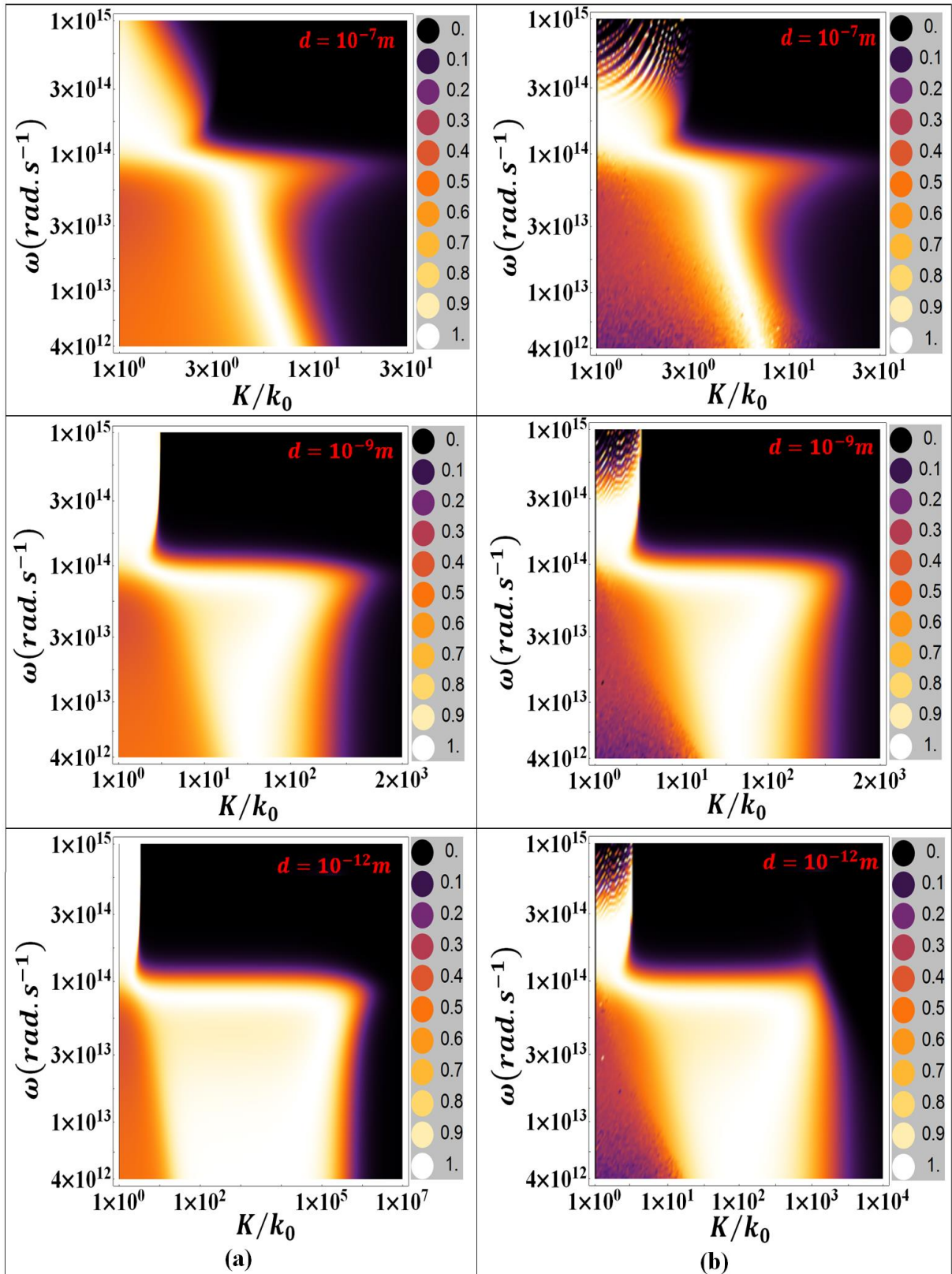


Figure 5.14: Plot of the transmission coefficient $4(\text{Im}(r_{31}^P))^2 e^{2i\gamma_3 d} / |1 - (r_{31}^P)^2 e^{2i\gamma_3 d}|^2$ of the p -polarized EM evanescent waves in the plane (ω, K) for the local case (a) and the nonlocal case (b) for the doping level $N = 10^{19} \text{ cm}^{-3}$ and at different separation distances d .

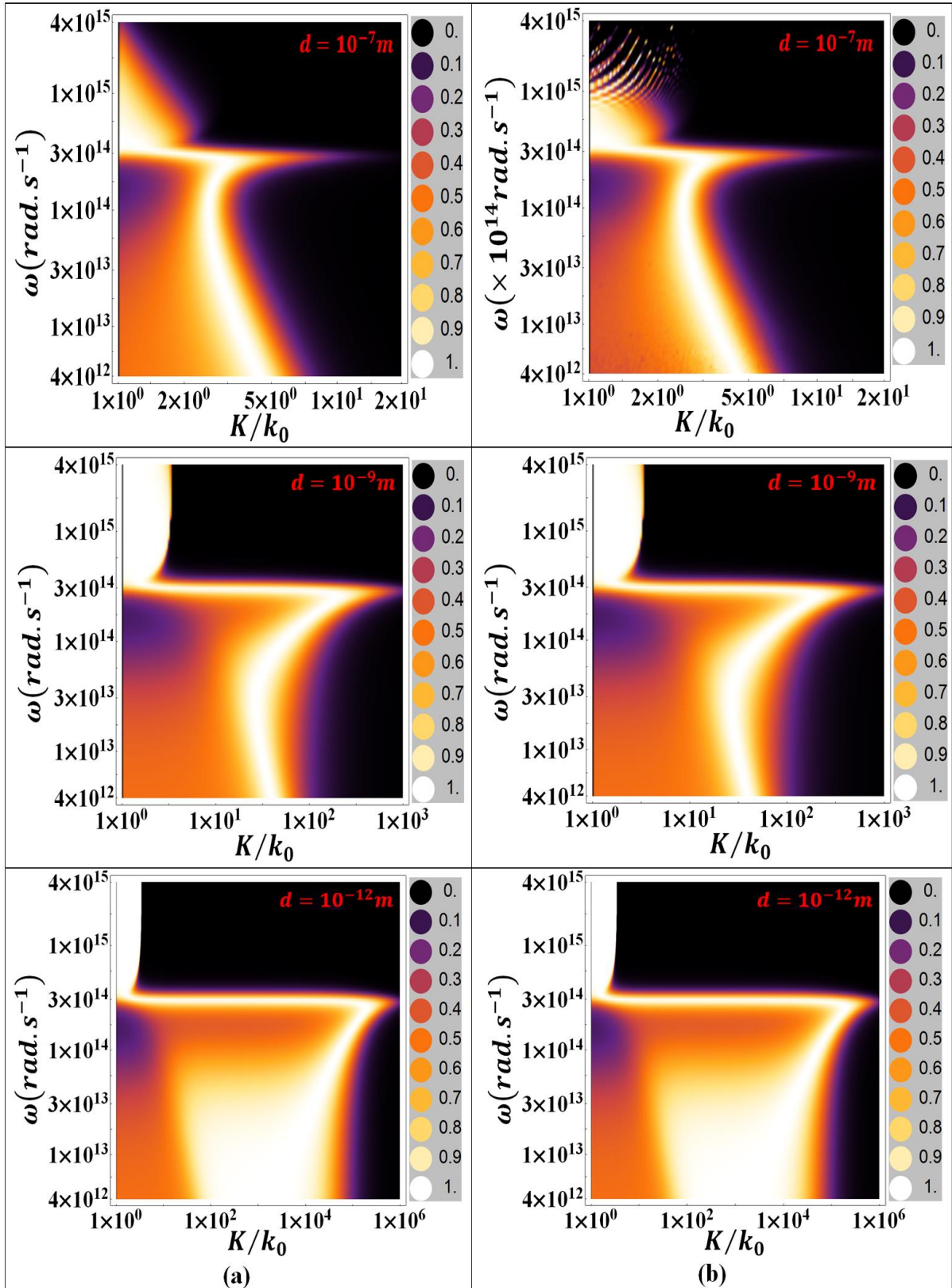


Figure 5.15: Plot of the transmission coefficient $4(Im(r_{31}^p))^2 e^{2i\gamma_3 d} / |1 - (r_{31}^p)^2 e^{2i\gamma_3 d}|^2$ of the p -polarized EM evanescent waves in the plane (ω, K) for the local case (a) and the nonlocal case (b) for the doping level $N = 10^{20} \text{ cm}^{-3}$ and at different separation distances d .

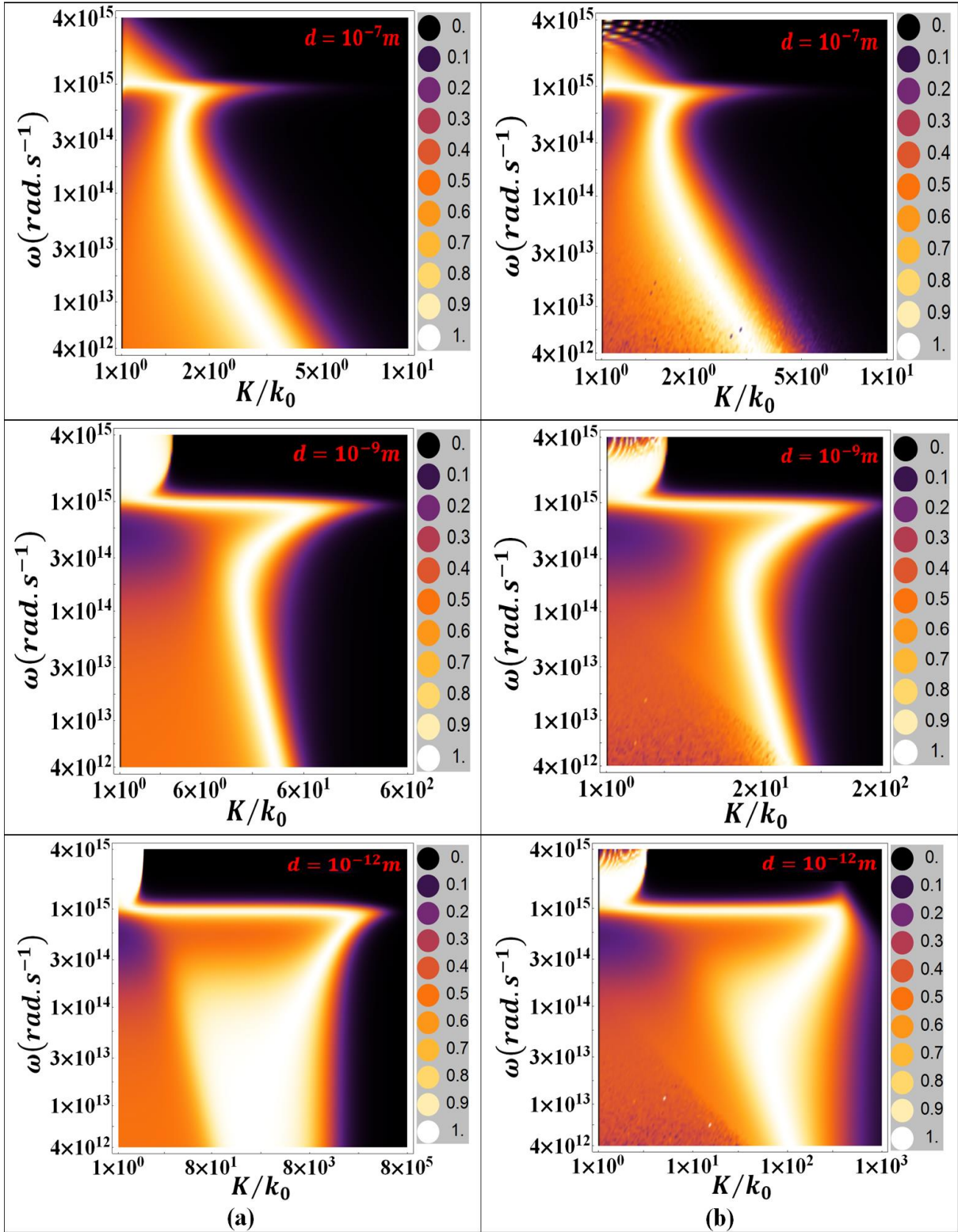


Figure 5.16: Plot of the transmission coefficient $4(\text{Im}(r_{31}^P))^2 e^{2i\gamma_3 d} / |1 - (r_{31}^P)^2 e^{2i\gamma_3 d}|^2$ of the p -polarized EM evanescent waves in the plane (ω, K) for the local case (a) and the nonlocal case (b) for the doping level $N = 10^{21} \text{ cm}^{-3}$ and at different separation distances d .

We also notice that as the distance decreases, the transmission factor attains its maximum at higher K values, and in each case the cutoff takes place at K value larger than the inverse of the Thomas-Fermi length $1/l_{TF}$. This result is consistent with the results obtained in the previous figures where we noticed that the saturation of the RHTC starts to take place at distances just below the Thomas-Fermi length. By comparing the plots of the transmission factors of the nonlocal case for different N with the graphs of the local case, we notice that at large distances, i.e. $d = 10^{-7}m$, the curves are quite similar. This is expected as for large distances, i.e. in the far-field regime the nonlocal effects are negligible and the results obtained in the local and the nonlocal case would be the same. As the separation distance decreases we notice that the local plots do not saturate and they reach their maximum values at K values larger in many orders than the K values of the nonlocal graphs. This demonstrates the difference between the infinite divergence observed at small distances in the local case, and the saturation obtained in the nonlocal cases. We would like to note that the differences observed in the interferences range of the spectrum (at very small K values) of the local model and the nonlocal models seem to be due to an artifact in the used simulation code.

5.2.3 Study of the spectral radiative heat transfer flux

We present in Fig. 5.17 the variation of the spectral radiative heat transfer flux Φ of the p -polarized EM evanescent waves for Lindhard–Mermin nonlocal model at $d = 10^{-12}m$.

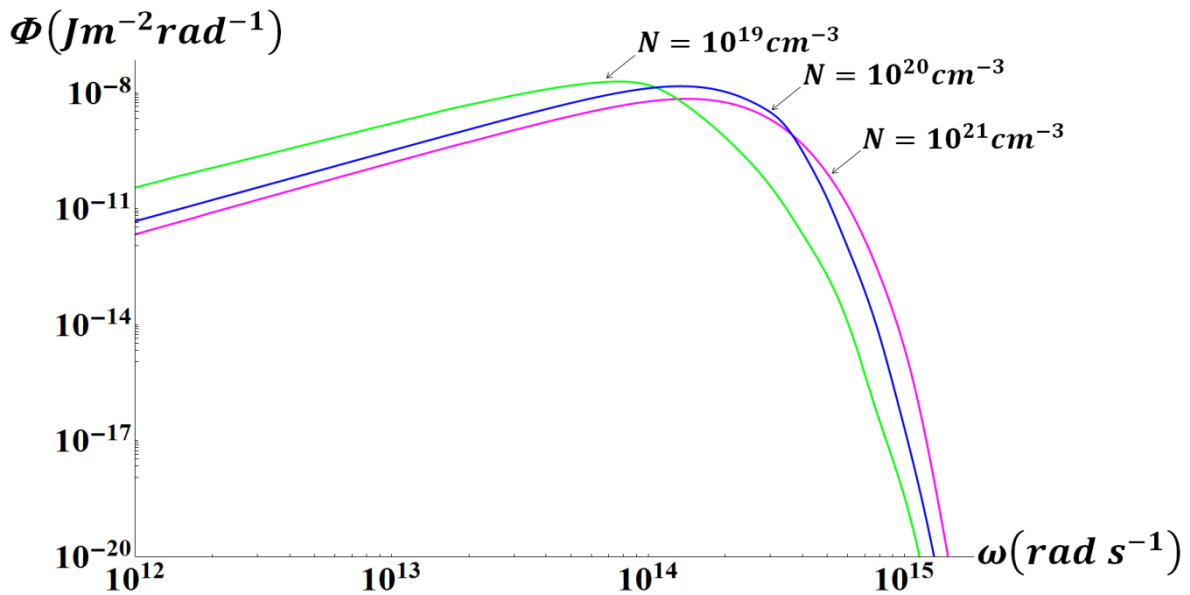


Figure 5.17: Variation of the spectral radiative heat transfer flux Φ of the p -polarized EM evanescent waves as ω varies for the different doping concentrations N considered in the calculation of the RHTC in the nonlocal model case and for a separation distance $d = 10^{-12}m$ and average temperature $T=300K$.

We observe in Fig. 5.17 that for any doping concentration N , the spectral radiative heat transfer flux Φ increases and reaches a maximum value for $\omega \approx \omega_p$ where a relatively wide peak is obtained, after which it decreases. This corresponds to the enhancement of the radiative heat transfer due to the excitation of the surface plasmon polaritons. We also notice that the peak values attained by Φ is the highest for $N = 10^{20} \text{cm}^{-3}$ and the least for $N = 10^{21} \text{cm}^{-3}$. This is consistent with the variation of the values of the saturating RHTC at extremely small distances, where we noticed a small difference in the saturation value that was the highest for $N = 10^{20} \text{cm}^{-3}$ and the least for $N = 10^{21} \text{cm}^{-3}$. The features observed emphasize the results obtained before, i.e. the relation between the variation of the RHTC and the variation of the corresponding plasmon frequency in the Planck range. We would like to note that the peaks of the plots obtained for the metallic-like materials are not as sharp as those obtained for the dielectric materials.

Conclusions

In this chapter we studied the RHTC between two n-doped Si semi-infinite parallel planes as the distance between them decreases. We divided our study into two parts where in the first part we used the local Drude model of the dielectric permittivity upon considering different values of the doping concentration $N = 10^{19}\text{cm}^{-3}$, 10^{20}cm^{-3} and 10^{21}cm^{-3} . The results obtained in this study show non-physical divergence of the contribution of the p -polarized evanescent EM waves as the distance decreases, due to the presence of the surface-plasmon polaritons. We noticed that the variation of the RHT spectrum shows a maximum as a function of N . This is due to the corresponding plasmon frequency that depends on the value of N and that is found in the Planck range and leads to the optimization of the resonance and the radiative transfer at a certain value. Rousseau et al. [13] have studied the RHT between similar planes and they derived a general specific form of the surface-plasmon polaritons contribution to the RHTC depending on the distance d , the temperature T and the doping concentration N : $h_{rad}^{spp}(T, d) = \delta G(T, N)/d^2$. They also studied the variation of $\delta G(T, N)$ as N and T vary, respectively and they plotted the corresponding graphs. We plotted the variation of $\delta G(T, N)$ as T varies and we showed that for any N , $\delta G(T, N)$ increases in value as T increases and reaches a maximum after which the values of $\delta G(T, N)$ decrease. This maximum point shifts to higher temperatures as N increases. Similarly, the plot of $\delta G(T, N)$ for any T as N varies showed that $\delta G(T, N)$ increases as N increases and reaches a maximum point after which it decreases; and this maximum point shifts to higher densities as the temperature increases. These studies show that for any system considered of specified N (or specified T) there is a specific temperature (and specific concentration) that maximizes the value of $\delta G(T, N)$.

In the second part we repeated the calculation of the RHTC between the n-doped Si planes by applying the Lindhard-Mermin nonlocal dielectric model [15-17]. This is the same model we used in our study of the Aluminum planes in chapter 2. We showed that the contribution of the evanescent p -polarized waves saturates as the distance decreases, in contrary to the divergence obtained in the local case. We showed that the saturation in each case starts to occur at distances smaller than the Thomas-Fermi screening length l_{TF} . This is consistent with the fact that for metals and materials with metallic-like properties the nonlocal effects appear at distances smaller than l_{TF} . Therefore, the nonlocality of the dielectric

permittivity equations, lead to saturation of the RHTC at these distance scales. Studying the variation of the saturation value shows that it increases as N increases and it reaches its maximum for the value $N = 2 \times 10^{19} \text{cm}^{-3}$, after which it decreases. This implies that for this doping level and its corresponding value of the plasmon frequency the resonance is optimized and the radiative spectrum is maximized. We also studied the plot of the transmission factor in the plane (ω, K) for the local and the nonlocal cases when considering $d = 10^{-7} \text{m}, 10^{-9} \text{m}$ and 10^{-12}m . By comparing the obtained curves we noticed that in the local case the values of the transmission factor increase as K increases while the curves of the nonlocal case showed saturation at K values larger than the inverse of the Thomas-Fermi length for small distances. At large distances they showed the same the behavior as the local curves, as in the far-field the nonlocal effects are negligible.

References

1. F. Marquier , K. Joulain, J.P. Mulet, R. Carminati, J.J. Greffet, *Opt. Commun.* **237**, 379 (2004).
2. J. Irvin, *Bell Syst Tech. J.* **XLI**, 387 (1961).
3. E. Rousseau, M. Laroche, and J.-J. Greffet, *Appl. Phys. Lett.* **95**, 231913 (2009).
4. E. Rousseau, M. Laroche, and J.-J. Greffet, *J. Appl. Phys.* **111**,014311 (2012).
5. N. D. Mermin, *Phys. Rev. B* **1**, 2362 (1970).
6. J. Lindhard, Kgl. Danske Videnskab. Selskab, *Mat.-Fys. Medd.* **28**, 8 (1954).
7. G. W. Ford and W. H. Weber, *Phys. Rep.* **113**, 195 (1984). We note a mistake in formula 2.29 corrected, for example, in Ref. 8.
8. R. Esquivel and V. B. Svetovoy, *Phys. Rev. A* **69**, 062102 (2004).
9. P. Ben-Abdallah and K. Joulain, *Phys. Rev.B* **82**, 121419, (2010).

Conclusions

In this thesis, we studied the validity of four nonlocal models of the dielectric permittivity in the calculation of the RHTC between two semi-infinite parallel dielectric planes separated by a vacuum gap of width d .

Starting with the description of the thermal energy and the radiative heat transfer, we shed the light on the importance of studying the RHT between two bodies separated by a distance d . We then showed that in the far-field study where d is much larger than Wien's wavelength, the RHT is dependent on the difference of the temperatures of the bodies, to the power four. On the other hand, in the near-field, the RHT depends on the distance d due to the existence and domination of different physical phenomena at these distance scales, such as the tunneling evanescent waves that exist at the surface and decay exponentially in the perpendicular direction away from the surface. To better highlight the difference between the two studies, we derived the expression of the radiative heat flux using the radiometry approach in the far field, and the expression of the RHTC between two semi-infinite parallel planes using the fluctuation dissipation theorem. We showed that the latter consists of two terms related to the contributions of the evanescent and propagative EM waves. We then showed that studying the variation of the RHTC between two semi-infinite parallel planes of 6H-SiC using Lorentz-Drude local model of the dielectric permittivity leads to a non-physical result as the contribution of the p -polarized EM evanescent waves diverged as $1/d^2$ when the distance d decreases. Studying the variation of the spectral energy flux and the spectral EM energy density of the p -polarized EM evanescent waves showed us that the excitation of surface phonon-polariton waves is responsible of the increase of the RHT.

We repeated the study of the RHTC for two semi-infinite parallel aluminum planes separated by a vacuum gap of width d . When we considered the local Drude model, the evanescent term of p polarization diverged as $1/d^2$ in an unphysical infinite tendency while all other contributions saturated as the distance d decreased. The saturation of the contribution of the evanescent waves of s polarization started at a distance of the order of the skin depth. When we used the Lindhard-Mermin nonlocal model for the dielectric permittivity, we obtained saturation of the evanescent p term at distances smaller than Thomas-Fermi length; while all other terms showed no significant change in values. The comparison between the

plots of the transmission factors of the evanescent p terms in both the local and the nonlocal cases highlighted the differences between them. The spectrum of the local model increases as K increases because the number of modes contributing to the transfer continually increases while the spectrum of the nonlocal model increases till reaching a cutoff at a K value of the order of the inverse of the Thomas-Fermi length.

For the case of 6H-SiC planes, we suggested three different nonlocal models of the dielectric permittivity and we used them in calculating the RHTC for a system of two semi-infinite parallel 6H-SiC planes. The first and the second nonlocal models were inspired from the model of Kliewer and Fuchs. The value of the longitudinal and the transverse components of the dielectric permittivity differed, depending on the value of the wavevector with respect to the limit of the first Brillouin zone (FBZ). The results of these models were similar and the values of the RHTC due to the contribution of the evanescent EM waves of p -polarization deviated from the infinite divergence obtained in the local case, as it showed a logarithmic divergence as the distance d decreases. We noticed that the limit of the FBZ affects the distance at which this deviation takes place where in the first model it starts at distances of the order of the lattice constant, and in the second model it starts at distances just smaller than the lattice constant. The plots of the transmission factors in the (ω, K) plane for $d=0$ confirmed the obtained results. The third suggested nonlocal model was inspired from the work of Henkel and Joulain [11] where we considered the EM field above the dielectric medium to acquire a coherence length l of the order of or larger than the lattice constant. We showed that introducing this length in the correlation equation of the fluctuating currents leads to a RHTC equation that depends on l . We then showed that the RHTC saturated at distances of the order of this coherence length l . Upon changing the value of l the saturation distance changed but in all cases it was equal to l . We deduced also that this saturation value is inversely proportional to l^2 with a T -dependent coefficient. On the other hand, we showed that the EM energy density is dependent on l and saturates as $1/l^3$ at very small distances.

We continued by suggesting a fourth nonlocal model of the dielectric permittivity for dielectrics. Considering Halevi–Fuchs nonlocal dielectric permittivity function theory, we repeated the study of the RHT for the 6H-SiC system. In this theory, the spatial dispersion is given as an additional term depending on the square of the total wavevector and multiplied by a diffusion parameter D in the dielectric permittivity function; the nonlocal corrections in the material optical properties are accounted for, and scattering of the EM excitation at the surface of the dielectric material is considered. This leads to defining additional boundary

conditions (ABC) needed to solve the transmission problem in Maxwell's equations. Different ABC were considered and they appear as additional surface scattering parameters (SSP) in the derived expressions of the surface impedances and reflection factors. We showed that at distances of few nanometers, the RHTC calculated with this nonlocal model deviates from $1/d^2$ law and saturation takes place. We also found that the heat transfer spectrum is broadened as compared to the local model, and the diffusion parameter D acts as a cutoff for the divergence of the RHTC obtained using the local model. Even though the saturation of the RHTC in the nonlocal case is obtained for distances much smaller than the atomic size, we are aware that at sub nanometer scale, heat transfer by EM waves probably ceases to be the dominant transfer modes and quantum effects must be taken into consideration as to assure a complete study of the RHT. One of the features observed in this nonlocal study is the appearance of two bumps for the cases of the ABC modelled by Kliewer and Fuchs and Ting et al. We studied the effects of varying the values of the different parameters of the model on the position and the width of these bumps by performing a parametric study. On the other hand, we showed that the EM energy densities are inversely proportional to the diffusion parameter D .

The last part of our work involved studying the RHT between two highly n-doped dielectric planes. By using the local Drude model of the dielectric permittivity upon considering different values of the doping concentration $N = 10^{19}\text{cm}^{-3}, 10^{20}\text{cm}^{-3}$ and 10^{21}cm^{-3} , we showed that the contribution of the p -polarized evanescent EM waves diverged as the distance decreases, due to the presence of the surface-plasmon polaritons. The variation of the RHT spectrum showed a maximum as a function of N . This is due to the corresponding plasmon frequency that depends on the value of N and that is found in the Planck range and leads to the optimization of the resonance and the radiative transfer at a certain value. By studying as function of N and T , the variations of the general form of the surface-plasmon polaritons contribution to the RHTC derived by Rousseau et al., we showed that for any system considered there exists a specific temperature (and specific concentration) that maximizes the value of this contribution. We then repeated the calculation of the RHTC between the n-doped Si planes by applying the Lindhard-Mermin nonlocal dielectric model. We showed that the contribution of the evanescent p -polarized waves saturated, and that for any N , the saturation starts to take place at distances smaller than the Thomas-Fermi screening length l_{TF} . We explained that this is expected due to the fact that for metals and materials with metallic-like properties, the nonlocal effects appear at distances smaller than l_{TF} . We

also showed that for a fixed T , the saturation value shows a maximum at a certain value of N which implies that for this doping level and its corresponding value of the plasmon frequency the resonance is optimized and the radiative spectrum is maximized. The plots of the transmission factor in the plane (ω, K) for the local and the nonlocal cases supported our results.

In future works, we will have to compare our theoretical results with experimental measurements of near field thermal radiation. This would allow us to determine at the same time the distance at which the radiative heat transfer stops to be the dominant heat transfer process (below 1 nm) as well as the distance where local medium approximation becomes not valid (few nanometers). Experiment measurement could also be a way to choose between the different ABC that are suggested in the literature. The existence or non-existence of “bumps” could eliminate some of the modeling approaches and suggest a consistent nonlocal dielectric permittivity function model for dielectrics.

Appendix A

A. Derivation of the radiative heat transfer coefficient of a system of two interfaces

A.1 Geometry of the system

We consider our system to consist of two semi-infinite parallel solid planes (1) and (2) of temperatures T_1 and T_2 . They are characterized by dielectric permittivities $\varepsilon_1(\omega)$ and $\varepsilon_2(\omega)$, respectively. They are separated by a third medium of width d and dielectric permittivity $\varepsilon_3(\omega)$ (in our work it will be considered as vacuum) Fig. A.1.

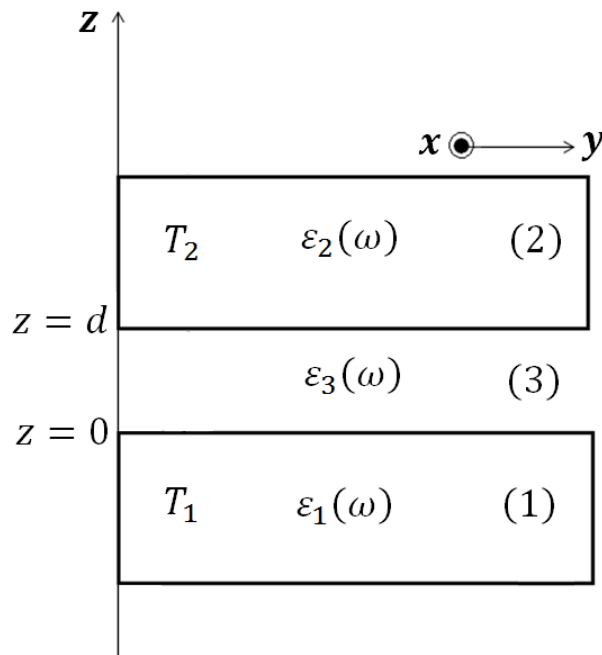


Figure A.1: Geometry of the system considered.

The three media are considered linear, homogeneous, isotropic and non-magnetic. Since medium (3) is considered vacuum, $\varepsilon_3(\omega) = 1$.

A.2 Sipe formalism for a system of two interfaces: Vectors and notations

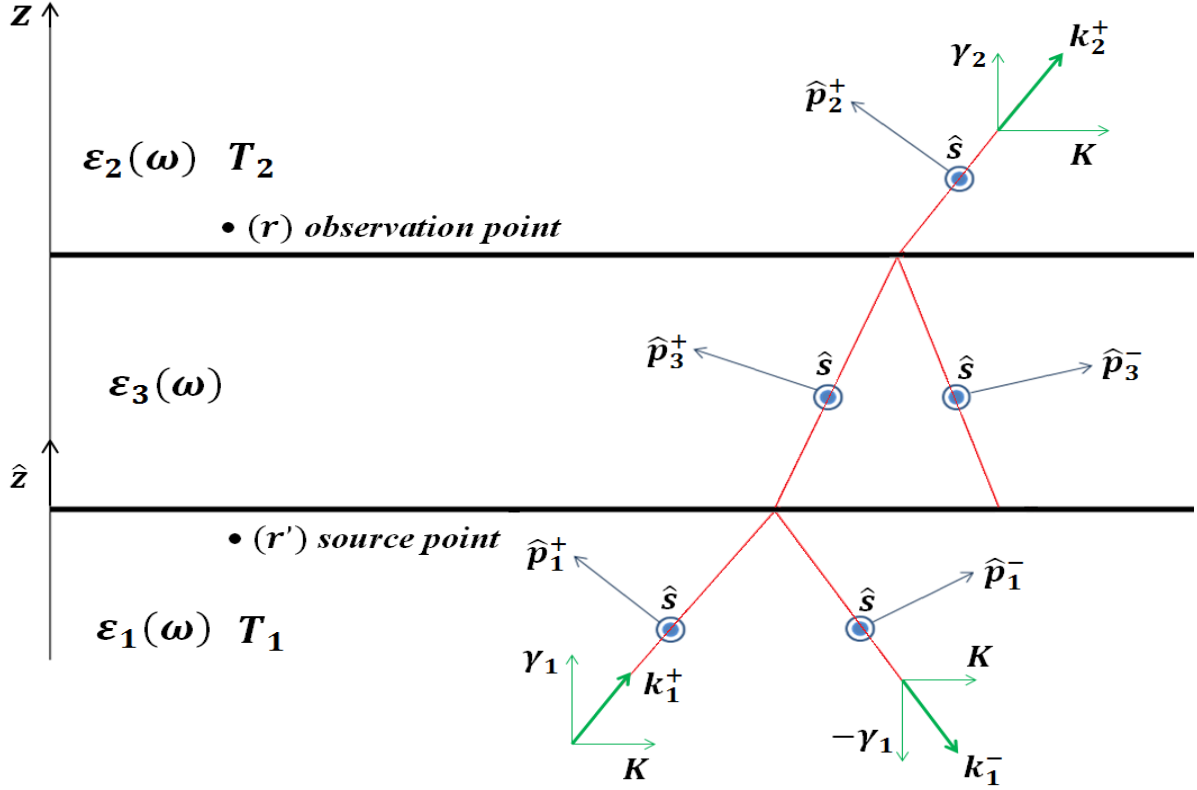


Figure A.2: Presentation of the different vectors of the EM waves of s and p polarizations, introduced in the formalism of Sipe in 1987 for the considered system.

Using the formalism of Sipe introduced in 1987, we define the unitary vectors:

$$\left\{ \begin{array}{l} \hat{\mathbf{x}} = \begin{pmatrix} 1 \\ 0 \\ 0 \end{pmatrix} \\ \hat{\mathbf{y}} = \begin{pmatrix} 0 \\ 1 \\ 0 \end{pmatrix} \\ \hat{\mathbf{z}} = \begin{pmatrix} 0 \\ 0 \\ 1 \end{pmatrix} \end{array} \right\} \quad (\text{A.1})$$

The (total) wavevector is defined as:

$$\mathbf{k}_l^\pm = (\mathbf{K}, \pm\gamma_l) \quad l = 1, 2, 3 \quad (\text{A.2})$$

where \mathbf{K} and γ_l are the parallel wavevector and the perpendicular wavevector, respectively. They are defined as:

$$\left\{ \begin{array}{l} \mathbf{K} = K_x \hat{\mathbf{x}} + K_y \hat{\mathbf{y}} \\ \gamma_l = \sqrt{k_0^2 \varepsilon_l - K^2} \end{array} \right\} \quad (\text{A.3})$$

where $k_0^2 = \omega^2/c^2$ is the velocity of light in vacuum, and $K = |\mathbf{K}|$.

It follows that the unit vector of \mathbf{K} is defined as:

$$\hat{\mathbf{K}} = \begin{pmatrix} K_x/K \\ K_y/K \\ 0 \end{pmatrix} \quad (\text{A.4})$$

We continue by defining the following unit vectors of the s and p -polarized EM waves:

$$\left\{ \begin{array}{l} \hat{\mathbf{s}} = \hat{\mathbf{K}} \times \hat{\mathbf{z}} \\ \hat{\mathbf{p}}_l^\pm = \frac{1}{k_0 n_l} (|\mathbf{K}| \hat{\mathbf{z}} \mp \gamma_l \hat{\mathbf{K}}) \end{array} \right\} \quad (\text{A.5})$$

where $n_l = \sqrt{\varepsilon_l}$ is the optical index of medium l .

A.3 Fresnel reflection and transmission factors

According to the system and the geometry presented in Figs. A.1 and A.2, we consider a plane wave incident on the interface between media (1) and (3) to be defined by the wavevector $\mathbf{k}_1^+ = (\mathbf{K}, \gamma_1)$. This wave is transmitted into medium (3) with the wavevector $\mathbf{k}_3 = (\mathbf{K}, \gamma_3)$. It propagates till reaching the interface of media (3) and (2), after which it is transmitted in medium (2) with the wavevector $\mathbf{k}_2^+ = (\mathbf{K}, \gamma_2)$. If the incident wave in medium (1) is s -polarized, the transmitted wave in medium (2) will have a transmission amplitude denoted by t_{12}^s ; similarly if the incident wave is p -polarized, the transmitted wave will have a transmission amplitudes denoted by t_{12}^p . These amplitudes are given as:

$$\left\{ \begin{array}{l} t_{12}^s = \frac{t_{13}^s t_{32}^s e^{2i\gamma_3 d}}{1 - r_{13}^s r_{32}^s e^{2i\gamma_3 d}} \\ t_{12}^p = \frac{t_{13}^p t_{32}^p e^{2i\gamma_3 d}}{1 - r_{13}^p r_{32}^p e^{2i\gamma_3 d}} \end{array} \right\} \quad (\text{A.6})$$

where r_{lm}^s and r_{lm}^p are Fresnel reflection factors between media l and m , t_{lm}^s and t_{lm}^p are Fresnel transmission factors between media l and m .

$$\left\{ \begin{array}{l} r_{lm}^s = (\gamma_l - \gamma_m)/(\gamma_l + \gamma_m) \\ r_{lm}^p = (\varepsilon_m \gamma_l - \varepsilon_l \gamma_m)/(\varepsilon_m \gamma_l + \varepsilon_l \gamma_m) \\ t_{lm}^s = (2\gamma_l)/(\gamma_l + \gamma_m) \\ t_{lm}^p = (2n_l n_m \gamma_l)/(\varepsilon_m \gamma_l + \varepsilon_l \gamma_m) \end{array} \right\} \quad l, m = 1, 2, 3 \quad (\text{A.7})$$

A.4 Green tensors of a system of two interfaces

As shown in Fig. A.2, we consider $\mathbf{r}'(\mathbf{R}', z')$ as a “source point” situated in the plane (1) and $\mathbf{r}(\mathbf{R}, z)$ an observation point situated in plane (2). For the electric field \mathbf{E} and the magnetic field \mathbf{H} , $\vec{\mathbf{G}}^E(\mathbf{r}, \mathbf{r}', \omega)$ and $\vec{\mathbf{G}}^H(\mathbf{r}, \mathbf{r}', \omega)$ denote the Green tensors of the medium. Therefore, the Green function equations of transmission from medium (1) to medium (2), used to link the EM field at the point \mathbf{r} to the current density at point \mathbf{r}' are defined as follows:

$$\left\{ \begin{array}{l} \vec{\mathbf{G}}^E_{12}(\mathbf{r}, \mathbf{r}', \omega) = \int \frac{d^2\mathbf{K}}{4\pi^2} \vec{\mathbf{g}}^E_{12}(\mathbf{K}, z, z', \omega) \exp[i\mathbf{K} \cdot (\mathbf{R} - \mathbf{R}')] \\ \vec{\mathbf{G}}^H_{12}(\mathbf{r}, \mathbf{r}', \omega) = \int \frac{d^2\mathbf{K}}{4\pi^2} \vec{\mathbf{g}}^H_{12}(\mathbf{K}, z, z', \omega) \exp[i\mathbf{K} \cdot (\mathbf{R} - \mathbf{R}')] \end{array} \right\} \quad (\text{A.8})$$

where

$$\left\{ \begin{array}{l} \vec{\mathbf{g}}^E_{12}(\mathbf{K}, z, z') = \frac{i}{2\gamma_1} (\hat{\mathbf{s}} t_{12}^s \hat{\mathbf{s}} + \hat{\mathbf{p}}_2^+ t t_{12}^p \hat{\mathbf{p}}_1^+) \exp[i\{\gamma_2(z-d) - \gamma_1 z'\}] \\ \vec{\mathbf{g}}^H_{12}(\mathbf{K}, z, z') = \frac{k_0 n_2}{2\gamma_1} (\hat{\mathbf{p}}_2^+ t t_{12}^s \hat{\mathbf{s}} - \hat{\mathbf{s}} t_{12}^p \hat{\mathbf{p}}_1^+) \exp[i\{\gamma_2(z-d) - \gamma_1 z'\}] \end{array} \right\} \quad (\text{A.9})$$

A.5 Derivation of the Poynting vector from medium (1) to medium (2) and the radiative heat transfer coefficient

We start by the main assumption where we consider that the EM radiation at the point \mathbf{r} due to an ensemble of fluctuating currents sources at point \mathbf{r}' characterized by the current volume density $\mathbf{j}_f(\mathbf{r}', \omega)$. By this, $\mathbf{E}(\mathbf{r}, \omega)$ and $\mathbf{H}(\mathbf{r}, \omega)$ denote the electric and the magnetic fields, respectively, radiated at the point \mathbf{r} with angular frequency ω . These fields are related to the fluctuating current density $\mathbf{j}(\mathbf{r}', \omega)$ through the following relations:

$$\left\{ \begin{array}{l} \mathbf{E}(\mathbf{r}, \omega) = i\omega\mu_0 \int \vec{\mathbf{G}}^E(\mathbf{r}, \mathbf{r}', \omega) \cdot \mathbf{j}_f(\mathbf{r}', \omega) d^3\mathbf{r}' \\ \mathbf{H}(\mathbf{r}, \omega) = \int \vec{\mathbf{G}}^H(\mathbf{r}, \mathbf{r}', \omega) \cdot \mathbf{j}_f(\mathbf{r}', \omega) d^3\mathbf{r}' \end{array} \right\} \quad (\text{A.10})$$

The Poynting vector is defined as:

$$\langle \pi(\mathbf{r}, \omega) \rangle = 4 \times \left\{ \frac{1}{2} \text{Re}[\mathbf{E}(\mathbf{r}, \omega) \mathbf{H}^*(\mathbf{r}, \omega)] \right\} \quad (\text{A.11})$$

where the symbol $\langle \dots \rangle$ indicates that we are considering a statistical ensemble average over all realizations of the system. It is worth mentioning here that this definition of the Poynting vector is four times greater than the usual definition, as we are considering analytical signals in our work.

The RHTC is defined as:

$$h_{\omega}^R(d, T_1) = \lim_{T_2 \rightarrow T_1} \frac{P(d, \omega, T_1, T_2)}{T_2 - T_1} \quad (\text{A.12})$$

where

$$P(d, \omega, T_1, T_2) = \langle \pi_z(d^+, \omega) - \pi_z(0^-, \omega) \rangle \quad (\text{A.13})$$

$\langle \pi_z(d^+, \omega) \rangle$ is the z component of the Poynting vector calculated in the plane $z=d$ of medium (2). It represents the thermal radiation radiated from medium (1) towards medium (2), where in this case point \mathbf{r}' is situated in medium (1), and \mathbf{r} in medium (2). Similarly, we should calculate $\langle \pi_z(0^-, \omega) \rangle$, the z component of the Poynting vector calculated in the plane $z=0$ of medium (1). It represents the thermal radiation radiated from medium (2) towards medium (1), where in this case \mathbf{r}' is situated in medium (2), and \mathbf{r} in medium (1).

We will proceed by calculating $\langle \pi_z(d^+, \omega) \rangle$ in details, and the calculation of $\langle \pi_z(0^-, \omega) \rangle$ would be done in a similar way.

The developed form of the Poynting vector is given by:

$$\langle \Pi_z(\mathbf{r}, \omega) \rangle = 2 \langle \text{Re} [E_x(\mathbf{r}, \omega) H_y^*(\mathbf{r}, \omega) - H_x^*(\mathbf{r}, \omega) E_y(\mathbf{r}, \omega)] \rangle \quad (\text{A.14})$$

Using eqs. (A.10):

$$\begin{aligned} & \langle E_x H_y^* \rangle \\ &= \left\langle \left\{ i\omega\mu_0 \int \vec{\mathbf{G}}_{12x\alpha}^E(\mathbf{r}, \mathbf{r}', \omega) \cdot \mathbf{j}_{f\alpha}(\mathbf{r}', \omega) d^3\mathbf{r}' \right\} \times \left\{ \int \vec{\mathbf{G}}_{12y\beta}^H(\mathbf{r}, \mathbf{r}'', \omega) \cdot \mathbf{j}_{f\alpha}(\mathbf{r}'', \omega) d^3\mathbf{r}'' \right\}^* \right\rangle \\ &= \iint G_{12x\alpha}^E(\mathbf{r}, \mathbf{r}', \omega) G_{12y\beta}^{H*}(\mathbf{r}, \mathbf{r}'', \omega) \langle j_{f\alpha}(\mathbf{r}', \omega) j_{f\beta}^*(\mathbf{r}'', \omega) \rangle d^3\mathbf{r}' d^3\mathbf{r}'' \quad (\text{A.15}) \end{aligned}$$

where $\alpha, \beta = x, y, z$ and Einstein convention on repeated indices is applied.

Using the fluctuation-dissipation theorem for the fluctuating currents in medium (1) which is considered at local thermodynamic equilibrium:

$$\langle j_{f\alpha}(\mathbf{r}', \omega) j_{f\beta}^*(\mathbf{r}'', \omega) \rangle = \frac{\omega \varepsilon_0}{\pi} \varepsilon_1''(\omega) \Theta(\omega, T_1) \delta_{\alpha\beta} \delta(\mathbf{r}' - \mathbf{r}'') \quad (\text{A.16})$$

where $\langle \dots \rangle$ indicate an ensemble average, $\varepsilon_0 = 8.85417 \times 10^{-12} \text{ F.m}^{-1}$ is the dielectric permittivity of vacuum and $\varepsilon_1''(\omega)$ is the imaginary part of the material's dielectric permittivity. $\delta_{k,l}$ is Kronecker symbol and δ is Dirac delta function. $\Theta(\omega, T) = \frac{\hbar\omega}{2} + \frac{\hbar\omega}{(e^{\hbar\omega/k_B T} - 1)}$ is the mean energy of the harmonic oscillator of frequency ω at temperature T and $\frac{\hbar\omega}{2}$ is the vacuum energy, called the zero-point energy.

Using this equation, we obtain:

$$\langle E_x H_y^* \rangle = \frac{i\omega^2 \varepsilon_1''(\omega) \Theta(\omega, T_1)}{\pi c^2} \int G_{12x\alpha}^E(\mathbf{r}, \mathbf{r}', \omega) G_{12y\alpha}^{H*}(\mathbf{r}, \mathbf{r}', \omega) d^3\mathbf{r}' \quad (\text{A.17})$$

with

$$\begin{aligned} & \int G_{12x\alpha}^E(\mathbf{r}, \mathbf{r}', \omega) G_{12x\alpha}^{H*}(\mathbf{r}, \mathbf{r}', \omega) d^3\mathbf{r}' \\ &= \int \frac{d^2k}{4\pi c^2} \left\{ \int_{-\infty}^0 dz' g_{12x\alpha}^E(\mathbf{K}, z, z', \omega) g_{12y\alpha}^{H*}(\mathbf{K}, z, z', \omega) \right\} \quad (\text{A.18}) \end{aligned}$$

Taking into consideration that:

$$\left\{ \begin{aligned} g_{12x\alpha}^E(\mathbf{K}, z, z', \omega) &= g_{12x\alpha}^E(\mathbf{K}, z, \omega) \exp(-i\gamma_1 z') \\ g_{12y\alpha}^{H*}(\mathbf{K}, z, z', \omega) &= g_{12y\alpha}^{H*}(\mathbf{K}, z, \omega) \{ \exp(-i\gamma_1 z') \}^* \end{aligned} \right\} \quad (\text{A.19})$$

this implies that:

$$\begin{aligned} & g_{12x\alpha}^E(\mathbf{K}, z, z', \omega) g_{12y\alpha}^{H*}(\mathbf{K}, z, z', \omega) \\ &= g_{12x\alpha}^E(\mathbf{K}, z, \omega) g_{12y\alpha}^{H*}(\mathbf{K}, z, \omega) \exp[(-i\gamma_1' + \gamma_1'')z'] \exp[(i\gamma_1' + \gamma_1'')z'] \\ &= g_{12x\alpha}^E(\mathbf{K}, z, \omega) g_{12y\alpha}^{H*}(\mathbf{K}, z, \omega) \exp(2\gamma_1'' z') \quad (\text{A.20}) \end{aligned}$$

where γ_1' and γ_1'' denote the real and the imaginary parts of γ_1 , respectively.

The integral on the right-hand side of Eq. (A.18) becomes:

$$\begin{aligned}
& \int_{-\infty}^0 dz' g_{12x\alpha}^E(\mathbf{K}, z, z', \omega) g_{12y\alpha}^{H*}(\mathbf{K}, z, z', \omega) \\
&= \int_{-\infty}^0 dz' g_{12x\alpha}^E(\mathbf{K}, z, \omega) g_{12y\alpha}^{H*}(\mathbf{K}, z, \omega) \exp(2\gamma_1'' z') \\
&= \frac{1}{2\gamma_1''} g_{12x\alpha}^E(\mathbf{K}, z, \omega) g_{12y\alpha}^{H*}(\mathbf{K}, z, \omega) \quad (A.21)
\end{aligned}$$

It follows that:

$$\langle E_x H_y^* \rangle = \frac{ik_0^2 \varepsilon_1''(\omega) \Theta(\omega, T_1)}{\pi} \int \frac{d^2 \mathbf{K}}{4\pi} \frac{1}{2\gamma_1''} g_{12x\alpha}^E(\mathbf{K}, z, \omega) g_{12y\alpha}^{H*}(\mathbf{K}, z, \omega) \quad (A.22)$$

and

$$\begin{aligned}
\langle \pi_z(d^+, \omega) \rangle &= 2Re \left\{ \frac{ik_0^2 \varepsilon_1''(\omega) \Theta(\omega, T_1)}{\pi} \int \frac{d^2 \mathbf{K}}{4\pi^2} \frac{1}{2\gamma_1''} [g_{12x\alpha}^E(\mathbf{K}, d^+, \omega) g_{12y\alpha}^{H*}(\mathbf{K}, d^+, \omega) \right. \\
&\quad \left. - g_{12x\alpha}^{H*}(\mathbf{K}, d^+, \omega) g_{12y\alpha}^E(\mathbf{K}, d^+, \omega)] \right\} \quad (A.23)
\end{aligned}$$

We continue by calculating the term:

$$\begin{aligned}
& g_{12x\alpha}^E(\mathbf{K}, d^+, \omega) g_{12y\alpha}^{H*}(\mathbf{K}, d^+, \omega) - g_{12x\alpha}^{H*}(\mathbf{K}, d^+, \omega) g_{12y\alpha}^E(\mathbf{K}, d^+, \omega) \\
&= g_{xx}^E g_{yx}^{H*} + g_{xy}^E g_{yy}^{H*} + g_{xz}^E g_{yz}^{H*} - g_{xx}^{H*} g_{yx}^E + g_{xy}^{H*} g_{yy}^E + g_{xz}^{H*} g_{yz}^E \quad (A.24)
\end{aligned}$$

We now use the definition:

$$\left\{ \begin{aligned} g_{12}^E &= \frac{i}{2\gamma_1} (\hat{\mathbf{s}} t_{12}^s \hat{\mathbf{s}} + \hat{\mathbf{p}}_2^+ t_{12}^p \hat{\mathbf{p}}_1^+) = \frac{i}{2\gamma_1} (t_{12}^s \hat{\mathbf{s}} \hat{\mathbf{s}} + t_{12}^p \hat{\mathbf{p}}_2^+ \hat{\mathbf{p}}_1^+) \\ g_{12}^{H*} &= \left\{ \frac{k_0 n_2}{2\gamma_1} (\hat{\mathbf{p}}_2^+ t_{12}^s \hat{\mathbf{s}} - \hat{\mathbf{s}} t_{12}^p \hat{\mathbf{p}}_1^+) \right\}^* = \frac{k_0 n_2^*}{2\gamma_1^*} (t_{12}^{s*} \hat{\mathbf{p}}_2^{+*} \hat{\mathbf{s}}^* - t_{12}^{p*} \hat{\mathbf{s}}^* \hat{\mathbf{p}}_1^{+*}) \end{aligned} \right\} \quad (A.25)$$

Using the vectors given in Sipe notation and defined in section A.1 we obtain:

$$\left\{ \begin{array}{l} \hat{\mathbf{s}} = \begin{pmatrix} K_y/K \\ -K_x/K \\ 0 \end{pmatrix} \\ \hat{\mathbf{p}}_1^+ = \frac{1}{k_0 n_1} \begin{pmatrix} -\gamma_1 K_x/K \\ -\gamma_1 K_y/K \\ K \end{pmatrix} \\ \hat{\mathbf{p}}_2^+ = \frac{1}{k_0 n_2} \begin{pmatrix} -\gamma_2 K_x/K \\ -\gamma_2 K_y/K \\ K \end{pmatrix} \end{array} \right\} \quad (\text{A.26})$$

This leads to the following expressions:

$$\begin{aligned} g_{12}^E = \frac{i}{2\gamma_1} & \left\{ t_{12}^s \begin{pmatrix} K_y^2/|K|^2 & -K_x K_y/|K|^2 & 0 \\ -K_x K_y/|K|^2 & K_x^2/|K|^2 & 0 \\ 0 & 0 & 0 \end{pmatrix} \right. \\ & \left. + \frac{t_{12}^p}{k_0^2 n_1 n_2} \begin{pmatrix} \gamma_1 \gamma_2 K_x^2/|K|^2 & \gamma_1 \gamma_2 K_x K_y/|K|^2 & -\gamma_1 K_x \\ \gamma_1 \gamma_2 K_x K_y/|K|^2 & \gamma_1 \gamma_2 K_y^2/|K|^2 & -\gamma_2 K_y \\ -\gamma_1 K_x & -\gamma_1 K_y & |K|^2 \end{pmatrix} \right\} \quad (\text{A.27}) \end{aligned}$$

$$\begin{aligned} g_{12}^{H*} = \frac{k_0 n_2^*}{2\gamma_1^*} & \left\{ \frac{t_{12}^{s*}}{k_0 n_2^*} \begin{pmatrix} -\gamma_2^* K_x K_y/|K|^2 & \gamma_2^* K_x^2/|K|^2 & 0 \\ -\gamma_2^* K_y^2/|K|^2 & \gamma_2^* K_x K_y/|K|^2 & 0 \\ K_y & -K_x & 0 \end{pmatrix} \right. \\ & \left. - \frac{t_{12}^{p*}}{k_0 n_1^*} \begin{pmatrix} -\gamma_1^* K_x K_y/|K|^2 & -\gamma_1^* K_y^2/|K|^2 & K_y \\ \gamma_1^* K_y/|K|^2 & \gamma_1^* K_x K_y/|K|^2 & -K_x \\ 0 & 0 & 0 \end{pmatrix} \right\} \quad (\text{A.28}) \end{aligned}$$

Using these equations and performing trivial simplifying steps, we arrive at the following equation:

$$g_{x\alpha}^E g_{y\alpha}^{H*} - g_{x\alpha}^{H*} g_{y\alpha}^E = \frac{-in_2^*}{4|\gamma_1|^2} \left[\frac{\gamma_2^*}{n_2^*} |t_{12}^s|^2 + \frac{\gamma_2(|\gamma_1|^2 + |K|^2)}{k_0^2 n_2 |n_1|^2} |t_{12}^p|^2 \right] \quad (\text{A.29})$$

Using eq. (A.29) and the following equation:

$$\int \frac{d^2 \mathbf{K}}{4\pi^2} = \iint \frac{dK_x dK_y}{(2\pi)^2} = \int_0^\infty \int_0^{2\pi} \frac{K dK d\theta}{(2\pi)^2} \rightarrow \int_0^\infty \frac{K dK}{2\pi} \quad (\text{A.30})$$

We obtain:

$$\langle \pi_z(d^+, \omega) \rangle = \frac{\Theta(\omega, T_1)}{8\pi^2} \int K dK \operatorname{Re} \left[\frac{k_0^2 \varepsilon_1''(\omega) \gamma_2^*}{\gamma_1'' |\gamma_1|^2} |t_{12}^s|^2 + \frac{\varepsilon_1''(\omega) n_2^* \gamma_2 (|\gamma_1|^2 + |K|^2)}{\gamma_1'' |\gamma_1|^2 n_2 |n_1|^2} |t_{12}^p|^2 \right] \quad (\text{A. 31})$$

Using now the following relations:

$$\left\{ \begin{array}{l} k_0^2 \varepsilon'' = 2\gamma' \gamma'' \\ |\gamma_1|^2 + |K|^2 = k_0^2 (\varepsilon \gamma^*)' / \gamma' \end{array} \right\} \quad (\text{A. 32})$$

Eq. (A.31) becomes:

$$\langle \pi_z(d^+, \omega) \rangle = \frac{\Theta(\omega, T_1)}{4\pi^2} \int K dK \left[\gamma_1' \gamma_2' \frac{|t_{12}^s|^2}{|\gamma_1|^2} + (\varepsilon_1 \gamma_1^*)' (\varepsilon_2 \gamma_1^*)' \frac{|t_{12}^p|^2}{|\gamma_1|^2 |n_1|^2 |n_2|^2} \right] \quad (\text{A. 33})$$

The integration over K is divided into two domains: the first domain is for all values $K \leq k_0$ i.e. propagative waves, and the second domain is for all $K > k_0$, i.e. evanescent waves.

We taking into consideration that

$$\frac{\Theta(\omega, T)}{4\pi^2} = \frac{\pi L_\omega^0(T)}{k_0^2} \quad (\text{A. 34})$$

where $L_\omega^0(T) = \hbar \omega^3 / [4\pi^3 c^2 (e^{\hbar \omega / k_B T} - 1)]$ is the monochromatic specific intensity of radiation of a blackbody of temperature T as given by Planck's law.

For propagative waves :

$$\left\{ \begin{array}{l} \gamma_1' \gamma_2' \frac{|t_{12}^s|^2}{|\gamma_1|^2} = \frac{(1 - |r_{31}^s|^2)(1 - |r_{32}^s|^2)}{|1 - r_{31}^s r_{32}^s e^{2i\gamma_3 d}|^2} \\ (\varepsilon_1 \gamma_1^*)' (\varepsilon_2 \gamma_1^*)' \frac{|t_{12}^p|^2}{|\gamma_1|^2 |n_1|^2 |n_2|^2} = \frac{(1 - |r_{31}^p|^2)(1 - |r_{32}^p|^2)}{|1 - r_{31}^p r_{32}^p e^{2i\gamma_3 d}|^2} \end{array} \right\} \quad (\text{A. 35})$$

while for evanescent waves:

$$\left\{ \begin{array}{l} \gamma_1' \gamma_2' \frac{|t_{12}^s|^2}{|\gamma_1|^2} = \frac{4 \operatorname{Im}(r_{31}^s) \operatorname{Im}(r_{32}^s) e^{-2\gamma_3'' d}}{|1 - r_{31}^s r_{32}^s e^{-2\gamma_3'' d}|^2} \\ (\varepsilon_1 \gamma_1^*)' (\varepsilon_2 \gamma_1^*)' \frac{|t_{12}^p|^2}{|\gamma_1|^2 |n_1|^2 |n_2|^2} = \frac{4 \operatorname{Im}(r_{31}^p) \operatorname{Im}(r_{32}^p) e^{-2\gamma_3'' d}}{|1 - r_{31}^p r_{32}^p e^{-2\gamma_3'' d}|^2} \end{array} \right\} \quad (\text{A. 36})$$

We obtain the following final form of $\langle \pi_z(d^+, \omega) \rangle$:

$$\begin{aligned} \langle \pi_z(d^+, \omega) \rangle = \pi L_\omega^0(T_1) & \left\{ \int_0^{k_0} \frac{KdK}{k_0^2} \left[\frac{(1 - |r_{31}^s|^2)(1 - |r_{32}^s|^2)}{|1 - r_{31}^s r_{32}^s e^{2i\gamma_3 d}|^2} + \frac{(1 - |r_{31}^p|^2)(1 - |r_{32}^p|^2)}{|1 - r_{31}^p r_{32}^p e^{2i\gamma_3 d}|^2} \right] \right. \\ & + \int_{k_0}^\infty \frac{KdK}{k_0^2} \left[\frac{4 \operatorname{Im}(r_{31}^s) \operatorname{Im}(r_{32}^s) e^{-2\gamma_3'' d}}{|1 - r_{31}^s r_{32}^s e^{-2\gamma_3'' d}|^2} \right. \\ & \left. \left. + \frac{4 \operatorname{Im}(r_{31}^p) \operatorname{Im}(r_{32}^p) e^{-2\gamma_3'' d}}{|1 - r_{31}^p r_{32}^p e^{-2\gamma_3'' d}|^2} \right] \right\} \quad (\text{A. 37}) \end{aligned}$$

Following the same procedure to calculate $\pi_z(0^-, \omega)$ and replacing $L_\omega^0(T_1)$ by $L_\omega^0(T_2)$, we obtain:

$$\begin{aligned} P(d, \omega, T_1, T_2) = \pi [L_\omega^0(T_1) \\ - L_\omega^0(T_2)] & \left\{ \int_0^{k_0} \frac{KdK}{k_0^2} \left[\frac{(1 - |r_{31}^s|^2)(1 - |r_{32}^s|^2)}{|1 - r_{31}^s r_{32}^s e^{2i\gamma_3 d}|^2} + \frac{(1 - |r_{31}^p|^2)(1 - |r_{32}^p|^2)}{|1 - r_{31}^p r_{32}^p e^{2i\gamma_3 d}|^2} \right] \right. \\ & + \int_{k_0}^\infty \frac{KdK}{k_0^2} \left[\frac{4 \operatorname{Im}(r_{31}^s) \operatorname{Im}(r_{32}^s) e^{-2\gamma_3'' d}}{|1 - r_{31}^s r_{32}^s e^{-2\gamma_3'' d}|^2} \right. \\ & \left. \left. + \frac{4 \operatorname{Im}(r_{31}^p) \operatorname{Im}(r_{32}^p) e^{-2\gamma_3'' d}}{|1 - r_{31}^p r_{32}^p e^{-2\gamma_3'' d}|^2} \right] \right\} \quad (\text{A. 38}) \end{aligned}$$

Therefore:

$$\begin{aligned} h_\omega^R(d, T) = \pi \frac{\partial L_\omega^0(T)}{\partial T} & \left\{ \int_0^{k_0} \frac{KdK}{k_0^2} \left[\frac{(1 - |r_{31}^s|^2)(1 - |r_{32}^s|^2)}{|1 - r_{31}^s r_{32}^s e^{2i\gamma_3 d}|^2} + \frac{(1 - |r_{31}^p|^2)(1 - |r_{32}^p|^2)}{|1 - r_{31}^p r_{32}^p e^{2i\gamma_3 d}|^2} \right] \right. \\ & + \int_{k_0}^\infty \frac{KdK}{k_0^2} \left[\frac{4 \operatorname{Im}(r_{31}^s) \operatorname{Im}(r_{32}^s) e^{-2\gamma_3'' d}}{|1 - r_{31}^s r_{32}^s e^{-2\gamma_3'' d}|^2} \right. \\ & \left. \left. + \frac{4 \operatorname{Im}(r_{31}^p) \operatorname{Im}(r_{32}^p) e^{-2\gamma_3'' d}}{|1 - r_{31}^p r_{32}^p e^{-2\gamma_3'' d}|^2} \right] \right\} \quad (\text{A. 39}) \end{aligned}$$

where

$$\pi \frac{\partial L_\omega^0(T)}{\partial T} = h^0(T, \omega) = \frac{1}{T} \frac{\hbar \omega}{k_B T} \frac{\hbar \omega^3}{4\pi^2 c^2} \frac{e^{\hbar \omega / k_B T}}{(e^{\hbar \omega / k_B T} - 1)} \quad (\text{A. 40})$$

The final form of the RHTC is:

$$\left\{ \begin{array}{l} h_{rad}(T, d) = \sum_{\alpha=S,P} \int_0^{+\infty} d\omega [h_{prop}^{\alpha}(T, d, \omega) + h_{evan}^{\alpha}(T, d, \omega)] \\ h_{prop}(T, d, \omega) = h^0(T, \omega) \times \int_0^{k_0} \frac{KdK (1 - |r_{31}^{\alpha}|^2)(1 - |r_{32}^{\alpha}|^2)}{k_0^2 |1 - r_{31}^{\alpha} r_{32}^{\alpha} e^{2i\gamma_3 d}|^2} \\ h_{evan}(T, d, \omega) = h^0(T, \omega) \times \int_{k_0}^{+\infty} \frac{KdK 4Im(r_{31}^{\alpha})Im(r_{32}^{\alpha})e^{2i\gamma_3 d}}{k_0^2 |1 - r_{31}^{\alpha} r_{32}^{\alpha} e^{2i\gamma_3 d}|^2} \end{array} \right\} \alpha = s, p \quad (A.41)$$

Appendix B

B. The electromagnetic energy density above an interface

B.1 Geometry of the system

We consider our system to consist of a semi-infinite parallel solid planes (1) of temperature $T > 0$ and dielectric permittivity $\epsilon_2(\omega)$, above which vacuum is situated with dielectric permittivity $\epsilon_2(\omega) = 1$ Fig. B.1.

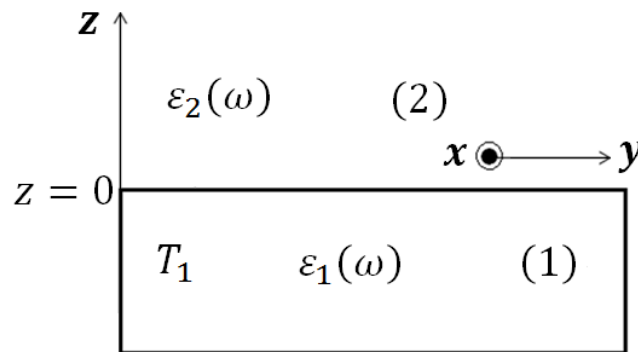


Figure B.1: Geometry of the system considered.

B.2 Sipe formalism for a system of one interface: vectors and notations

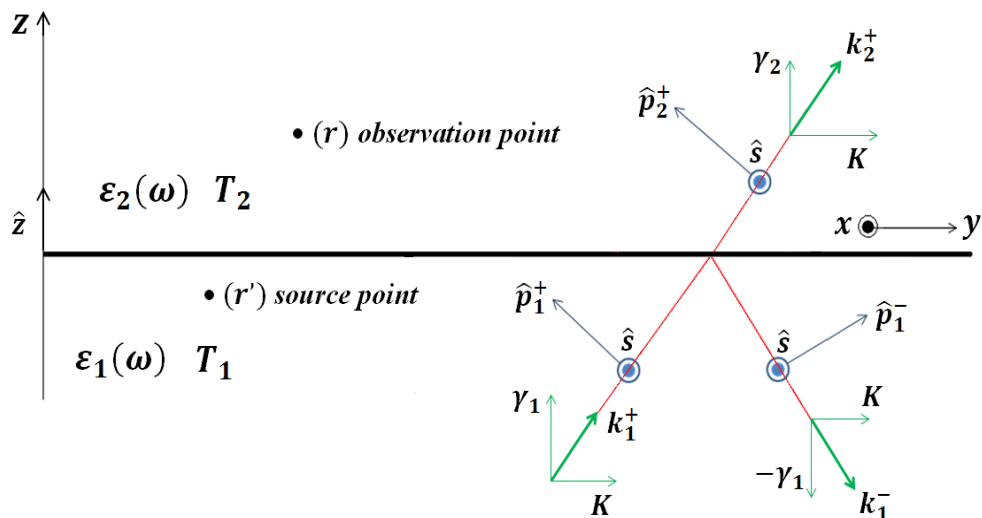


Figure B.2: Presentation of the different vectors introduced in the formalism of Sipe in 1987 for the considered system.

The vectors shown in Fig. B.2 introduced by Sipe 1987 for this 1-interface system are defined in the same way as in Appendix A.2, i.e. Eqs. (A.1), (A.2), (A.3), (A.4) and (A.5) will be used in this section also.

B.3 Fresnel reflection and transmission factors

According to the system and the geometry presented in Fig. B.2, we consider a plane wave of amplitude E_{inc} , incident on the interface between media (1) and (2), to be defined by the wavevector $\mathbf{k}_1^+ = (\mathbf{K}, \gamma_1)$. This wave will be reflected in medium (1) with a wavevector $\mathbf{k}_1^- = (\mathbf{K}, -\gamma_1)$ and an amplitude $E_{ref}^s = r_{12}^s E_{inc}$ if the incident wave is s-polarized ($E = E_{inc} \hat{\mathbf{s}}$), or with an amplitude $E_{ref}^p = r_{12}^p E_{inc}$ if the incident wave is p-polarized, i.e. $E = E_{inc} \hat{\mathbf{p}}_1^+$. On the other hand, this wave is also transmitted inside medium (2) with the wavevector $\mathbf{k}_2 = (\mathbf{K}, \gamma_2)$ with an amplitude $E_{tran}^s = t_{12}^s E_{inc}$ if the incident wave is s-polarized, or with an amplitude if the incident wave is p-polarized $E_{tran}^p = t_{12}^p E_{inc}$. The different Fresnel reflection and transmission factors are defined as follows, for both the s and p polarizations:

$$\left\{ \begin{array}{l} r_{12}^s = (\gamma_1 - \gamma_2)/(\gamma_1 + \gamma_2) \\ r_{12}^p = (\varepsilon_2 \gamma_1 - \varepsilon_1 \gamma_2)/(\varepsilon_2 \gamma_1 + \varepsilon_1 \gamma_2) \\ t_{12}^s = (2\gamma_1)/(\gamma_1 + \gamma_2) \\ t_{12}^p = (2n_1 n_2 \gamma_1)/(\varepsilon_2 \gamma_1 + \varepsilon_1 \gamma_2) \end{array} \right\} \quad (B.1)$$

B.4 Green tensors of a system of one interface

As shown in Fig. B.2, we consider $\mathbf{r}'(\mathbf{R}', z')$ as a ‘‘source point’’ situated in medium (1) and $\mathbf{r}(\mathbf{R}, z)$ an observation point situated in medium (2), i.e. vacuum. Similarly to the definitions presented in Appendix A.4, for the electric field \mathbf{E} and the magnetic field \mathbf{H} , $\vec{\mathbf{G}}^E(\mathbf{r}, \mathbf{r}', \omega)$ and $\vec{\mathbf{G}}^H(\mathbf{r}, \mathbf{r}', \omega)$ denote the Green tensors of the medium.

Therefore, the Green function equations of transmission from medium (1) to medium (2), used to link the EM field at the point \mathbf{r} to the current density at point \mathbf{r}' are defined as given by Eqs. (A.8), (A.9) and (A.10).

B.5 Deriving the EM energy density above an interface

The EM energy density, denoted by $u_{EM}(\mathbf{r}, \omega, T)$ and associated with an EM field represented by the fields $\mathbf{E}(\mathbf{r}, \omega)$ and $\mathbf{H}(\mathbf{r}, \omega)$ at point \mathbf{r} , is given by:

$$u_{EM}(\mathbf{r}, \omega, T) = 2 \times \left[\frac{\varepsilon_0}{2} \langle \mathbf{E}(\mathbf{r}, \omega) \cdot \mathbf{E}(\mathbf{r}, \omega)^* \rangle + \frac{\mu_0}{2} \langle \mathbf{H}(\mathbf{r}, \omega) \cdot \mathbf{H}(\mathbf{r}, \omega)^* \rangle \right] \quad (B.2)$$

where the factor 2 is due to the fact that we consider analytic signals.

The EM energy density is consisted of two contributions. The first is the electric contribution represented by the following electric term, and the second is the magnetic contribution represented by the magnetic term. They are denoted $u_E(\mathbf{r}, \omega, T)$ and $u_M(\mathbf{r}, \omega, T)$, respectively :

$$\left\{ \begin{array}{l} u_E(\mathbf{r}, \omega, T) = 2 \times \frac{\varepsilon_0}{2} \langle \mathbf{E}(\mathbf{r}, \omega) \cdot \mathbf{E}(\mathbf{r}, \omega)^* \rangle \\ u_M(\mathbf{r}, \omega, T) = 2 \times \frac{\mu_0}{2} \langle \mathbf{H}(\mathbf{r}, \omega) \cdot \mathbf{H}(\mathbf{r}, \omega)^* \rangle \end{array} \right\} \quad (B.3)$$

Where $\mathbf{E}(\mathbf{r}, \omega)$ and $\mathbf{H}(\mathbf{r}, \omega)$ are given by Eqs. (A.10).

In what follows, we will derive the $u_E(\mathbf{r}, \omega, T)$ in details and the derivation of $u_M(\mathbf{r}, \omega, T)$ would be done in a similar way.

$$\begin{aligned} \langle \mathbf{E}(\mathbf{r}, \omega) \cdot \mathbf{E}(\mathbf{r}, \omega)^* \rangle &= \left\langle \left| i\omega\mu_0 \int d^3\mathbf{r}' \vec{\mathbf{G}}_{13}^E(\mathbf{r}, \mathbf{r}', \omega) \cdot \mathbf{j}_f(\mathbf{r}', \omega) \right|^2 \right\rangle \\ &= \omega^2 \mu_0^2 \int d^3\mathbf{r}' \int d^3\mathbf{r}'' \sum_{l,m,n} G_{13l,m}^E(\mathbf{r}, \mathbf{r}', \omega) G_{13l,n}^{E*}(\mathbf{r}, \mathbf{r}'', \omega) \\ &\quad \times \langle j_m^f(\mathbf{r}', \omega) j_n^{f*}(\mathbf{r}'', \omega) \rangle \quad l, m, n = x, y, z \quad (B.4) \end{aligned}$$

The currents correlation function is given by the fluctuation-dissipation theorem as explained in Appendix A.5:

$$\langle j_m^f(\mathbf{r}', \omega) j_n^{f*}(\mathbf{r}'', \omega) \rangle = \frac{2\omega\varepsilon_0}{\pi} \varepsilon''(\omega) \Theta(\omega, T) \delta_{mn} \delta(\mathbf{r}' - \mathbf{r}'') \quad l, m, n = x, y, z \quad (B.5)$$

Using Eq. (B.5) and the relation $\mu_0\varepsilon_0c^2 = 1$:

$$\varepsilon_0 \langle \mathbf{E}(\mathbf{r}, \omega) \cdot \mathbf{E}(\mathbf{r}, \omega)^* \rangle = \frac{2\omega^3 \varepsilon''(\omega)}{\pi c^4} \Theta(\omega, T) \int d^3\mathbf{r}' G_{13l,m}^E(\mathbf{r}, \mathbf{r}', \omega) G_{13l,m}^{E*}(\mathbf{r}, \mathbf{r}', \omega) \quad (B.6)$$

To calculate the volume integral on the right-hand side of Eq.(B.6),we substitute with Eqs. (A.8):

$$\begin{aligned}
& \int d^3 \mathbf{r}' G_{13l,m}^E(\mathbf{r}, \mathbf{r}', \omega) G_{13l,m}^{E*}(\mathbf{r}, \mathbf{r}', \omega) \\
&= \iint \frac{d^2 \mathbf{K}}{4\pi^2} \frac{d^2 \mathbf{K}'}{4\pi^2} \exp[i(\mathbf{K} - \mathbf{K}') \cdot \mathbf{R}] \\
&\times \int_{-\infty}^0 dz' g_{13l,m}^E(\mathbf{K}, z, z', \omega) g_{13l,m}^{E*}(\mathbf{K}, z, z', \omega) \int d^2 \mathbf{R}' \exp[-i(\mathbf{K} - \mathbf{K}') \\
&\cdot \mathbf{R}'] \quad (B.7)
\end{aligned}$$

Taking into consideration that :

$$\int d^2 \mathbf{R}' \exp[-i(\mathbf{K} - \mathbf{K}') \cdot \mathbf{R}'] = 4\pi^2 \delta(\mathbf{K} - \mathbf{K}') \quad (B.8)$$

Eq. (B.7) becomes:

$$\begin{aligned}
& \int d^3 \mathbf{r}' G_{12l,m}^E(\mathbf{r}, \mathbf{r}', \omega) G_{13l,m}^{E*}(\mathbf{r}, \mathbf{r}', \omega) \\
&= \int \frac{d^2 \mathbf{K}}{4\pi^2} \int_{-\infty}^0 dz' g_{12l,m}^E(\mathbf{K}, z, z', \omega) g_{12l,m}^{E*}(\mathbf{K}, z, z', \omega) \quad (B.9)
\end{aligned}$$

Considering:

$$\vec{g}_{12}^E(\mathbf{K}, z, z', \omega) = \vec{g}_{12}^E(\mathbf{K}, \omega) \exp[i(\gamma_2 z - \gamma_1 z')] \quad (B.10)$$

and since medium (2) is vacuum, γ_2 will be denoted by γ_0 , we deduce that:

$$\left\{ \begin{aligned} g_{12x\alpha}^E(\mathbf{K}, z, z', \omega) &= g_{12x\alpha}^E(\mathbf{K}, \omega) \exp[i(\gamma_0 z - \gamma_1 z')] \\ g_{12y\alpha}^{E*}(\mathbf{K}, z, z', \omega) &= g_{12y\alpha}^{E*}(\mathbf{K}, \omega) \exp[-i(\gamma_0 z - \gamma_1 z')] \end{aligned} \right\} \quad (B.11)$$

and

$$\begin{aligned}
& g_{12x\alpha}^E(\mathbf{K}, z, z', \omega) g_{12y\alpha}^{E*}(\mathbf{K}, z, z', \omega) \\
&= g_{12x\alpha}^E(\mathbf{K}, z, \omega) g_{12y\alpha}^{E*}(\mathbf{K}, z, \omega) \exp(-2\gamma_0'' z) \exp(2\gamma_1'' z') \quad (B.12)
\end{aligned}$$

Therefore:

$$\begin{aligned}
& \int d^3 \mathbf{r}' G_{13l,m}^E(\mathbf{r}, \mathbf{r}', \omega) G_{13l,m}^{E*}(\mathbf{r}, \mathbf{r}', \omega) \\
&= \int \frac{d^2 \mathbf{K}}{4\pi^2} g_{12l,m}^E(\mathbf{K}, \omega) g_{13l,m}^{E*}(\mathbf{K}, \omega) \exp(-2\gamma_3'' z) \int_{-\infty}^0 dz' \exp(-2\gamma_1'' z') \quad (B.13)
\end{aligned}$$

It follows that :

$$\int_{-\infty}^0 dz' \exp(-2\gamma_1'' z') = \frac{1}{\gamma_1''} \quad (B.14)$$

Then :

$$\begin{aligned} & \int d^3 \mathbf{r}' G_{12l,m}^E(\mathbf{r}, \mathbf{r}', \omega) G_{12l,m}^{E*}(\mathbf{r}, \mathbf{r}', \omega) \\ &= \int \frac{d^2 \mathbf{K}}{4\pi^2} \frac{\exp(-2\gamma_1'' z)}{2\gamma_1''} g_{12l,m}^E(\mathbf{K}, \omega) g_{12l,m}^{E*}(\mathbf{K}, \omega) \end{aligned} \quad (B.15)$$

We should now proceed by calculating $g_{12l,m}^E(\mathbf{K}, \omega) g_{12l,m}^{E*}(\mathbf{K}, \omega)$.

Using Eqs. (A.9):

$$\begin{aligned} g_{12}^E &= \frac{i}{2\gamma_1} (\hat{\mathbf{s}} t_{12}^s \hat{\mathbf{s}} + \hat{\mathbf{p}}_3^+ t_{13}^p \hat{\mathbf{p}}_1^+) = \frac{i}{2\gamma_1} (t_{13}^s \hat{\mathbf{s}} \hat{\mathbf{s}} + t_{13}^p \hat{\mathbf{p}}_3^+ \hat{\mathbf{p}}_1^+) \\ &= \frac{i}{2\gamma_1} \left\{ t_{13}^s \begin{pmatrix} K_y^2/K^2 & -K_x K_y/K^2 & 0 \\ -K_x K_y/K^2 & K_x^2/K^2 & 0 \\ 0 & 0 & 0 \end{pmatrix} \right. \\ &\quad \left. + \frac{t_{13}^p}{k_0^2 n_1 n_3} \begin{pmatrix} \gamma_1 \gamma_3 K_x^2/K^2 & \gamma_1 \gamma_3 K_x K_y/K^2 & -\gamma_1 K_x \\ \gamma_1 \gamma_3 K_x K_y/K^2 & \gamma_1 \gamma_3 K_y^2/K^2 & -\gamma_3 K_y \\ -\gamma_3 K_x & -\gamma_1 K_y & K^2 \end{pmatrix} \right\} \end{aligned} \quad (B.16)$$

Consequently :

$$\begin{aligned} g_{13}^{E*} &= \frac{i}{2\gamma_1^*} \left\{ t_{13}^{s*} \begin{pmatrix} K_y^2/K^2 & -K_x K_y/K^2 & 0 \\ -K_x K_y/K^2 & K_x^2/K^2 & 0 \\ 0 & 0 & 0 \end{pmatrix} \right. \\ &\quad \left. + \frac{t_{13}^{p*}}{k_0^2 n_1^* n_3^*} \begin{pmatrix} \gamma_1^* \gamma_3^* K_x^2/K^2 & \gamma_1^* \gamma_3^* K_x K_y/K^2 & -\gamma_1^* K_x \\ \gamma_1^* \gamma_3^* K_x K_y/K^2 & \gamma_1^* \gamma_3^* K_y^2/K^2 & -\gamma_3^* K_y \\ -\gamma_3^* K_x & -\gamma_1^* K_y & K^2 \end{pmatrix} \right\} \end{aligned} \quad (B.17)$$

Taking into consideration that $n_2 = 1$, we obtain:

$$g_{13l,m}^E(\mathbf{K}, \omega) g_{13l,m}^{E*}(\mathbf{K}, \omega) = \frac{1}{4} \left\{ \frac{|t_{13}^s|^2}{|\gamma_1|^2} + \left[\frac{(|\gamma_1|^2 + K^2) + (|\gamma_3|^2 + K^2)}{k_0^4 |n_1|^2} \right] \frac{|t_{13}^p|^2}{|\gamma_1|^2} \right\} \quad (B.18)$$

Therefore Eq. (B.3) becomes:

$$u_E(z, \omega, T) = \frac{2\omega^3 \varepsilon_1''(\omega) \Theta(\omega, T)}{\pi c^4} \int \frac{d^2 \mathbf{K}}{4\pi^2} \frac{\exp(-2\gamma_3'' z)}{2\gamma_1''} \\ \times \frac{1}{4} \left\{ \frac{|t_{13}^s|^2}{|\gamma_1|^2} + \left[\frac{(|\gamma_1|^2 + K^2) + (|\gamma_3|^2 + K^2)}{k_0^4 |n_1|^2} \right] \frac{|t_{13}^p|^2}{|\gamma_1|^2} \right\} \quad (B.19)$$

Taking into consideration equation (A.30) and the following equations:

$$\left\{ \begin{array}{l} \varepsilon'' = \frac{2}{k_0^2} \gamma' \gamma'' \\ u_\omega^0(T) = \frac{\omega^2 \Theta(\omega, T)}{\pi^2 c^3} \end{array} \right\} \quad (B.20)$$

We obtain :

$$u_E(z, \omega, T) = \frac{u_\omega^0(T)}{4} \int_0^\infty \frac{K dK}{k_0} \gamma_1' \left\{ \frac{|t_{13}^s|^2}{|\gamma_1|^2} \right. \\ \left. + \left[\frac{(|\gamma_1|^2 + K^2) + (|\gamma_3|^2 + K^2)}{k_0^4 |n_1|^2} \right] \frac{|t_{13}^p|^2}{|\gamma_1|^2} \right\} \exp(-2\gamma_3'' z) \quad (B.21)$$

The integration over K is divided into two domains: the first domain is for all values $K \leq k_0$ i.e. propagative waves, and the second domain is for all $K > k_0$, i.e. evanescent waves.

Considering:

$$|\gamma_1|^2 + K^2 = \frac{k_0^2 (\varepsilon_1 \gamma_1^*)'}{\gamma_1'} \quad (B.22)$$

And for the propagative waves:

$$\left\{ \begin{array}{l} |\gamma_3|^2 + K^2 = k_0^2 \\ \gamma_3 \approx \gamma_3' \approx |\gamma_3| \\ \gamma_1' \frac{|t_{13}^s|^2}{|\gamma_1|^2} = \frac{1 - |r_{13}^s|^2}{|\gamma_3|} \\ \frac{(\varepsilon_1 \gamma_1^*)' |t_{13}^p|^2}{|n_1|^2 |\gamma_1|^2} = \frac{1 - |r_{13}^p|^2}{|\gamma_3|} \end{array} \right\} \quad (B.23)$$

while for the evanescent waves:

$$\left\{ \begin{array}{l} |\gamma_3|^2 + K^2 = \left(\frac{2K^2}{k_0^2} - 1 \right) \\ \gamma_3 \approx i\gamma_3'' \approx i|\gamma_3| \\ \gamma_1' \frac{|t_{13}^s|^2}{|\gamma_1|^2} = \frac{2 \operatorname{Im}(r_{13}^s)}{|\gamma_3|} \\ \frac{(\varepsilon_1 \gamma_1^*)' |t_{13}^p|^2}{|n_1|^2 |\gamma_1|^2} = \frac{2 \operatorname{Im}(r_{13}^p)}{|\gamma_3|} \end{array} \right\} \quad (B.24)$$

We obtain the final form of the electric energy density:

$$u_e(z, \omega, T) = \frac{\omega^2 \Theta(\omega, T)}{\pi^2 c^3} \left\{ \frac{1}{2} \int_0^{k_0} \frac{K dK}{k_0 |\gamma_3|} \left[\frac{(1 - |r_{31}^s|^2) + (1 - |r_{31}^p|^2)}{2} \right] \right. \\ \left. + \frac{1}{2} \int_{k_0}^{\infty} \frac{K dK}{k_0 |\gamma_3|} \left[\operatorname{Im}(r_{31}^s) + \left(\frac{2K^2}{k_0^2} - 1 \right) \operatorname{Im}(r_{31}^p) \right] e^{-2\gamma_3'' z} \right\} \quad (B.25)$$

Following the same procedure for the magnetic energy density we obtain finally:

$$u_m(z, \omega, T) = \frac{\omega^2 \Theta(\omega, T)}{\pi^2 c^3} \left\{ \frac{1}{2} \int_0^{k_0} \frac{K dK}{k_0 |\gamma_3|} \left[\frac{(1 - |r_{31}^s|^2) + (1 - |r_{31}^p|^2)}{2} \right] \right. \\ \left. + \frac{1}{2} \int_{k_0}^{\infty} \frac{K dK}{k_0 |\gamma_3|} \left[\left(\frac{2K^2}{k_0^2} - 1 \right) \operatorname{Im}(r_{31}^s) + \operatorname{Im}(r_{31}^p) \right] e^{-2\gamma_3'' z} \right\} \quad (B.26)$$

By adding the two contributions to the energy density we obtain the following final form of the EM energy density:

$$u_{EM}(z, \omega, T) = \frac{\omega^2 \Theta(\omega, T)}{\pi^2 c^3} \left\{ \int_0^{k_0} \frac{K dK}{k_0 |\gamma_3|} \left[\frac{(1 - |r_{31}^s|^2) + (1 - |r_{31}^p|^2)}{2} \right] \right. \\ \left. + 4 \int_{k_0}^{\infty} \frac{K^3 dK}{k_0^3 |\gamma_3|} \left[\frac{\operatorname{Im}(r_{31}^s) + \operatorname{Im}(r_{31}^p)}{2} \right] e^{-2\gamma_3'' z} \right\} \quad (B.27)$$

Appendix C

C. Electrostatic limits of Fresnel reflection factors

C.1 The general case

The system considered is that of Appendix B, where medium (1) in this section is 6H-SiC, and medium (2) is vacuum. The geometry is similar to the one presented in Fig. (B.1)

The general equation of Fresnel factors are that r_{12}^S is that given in Eqs. (B.).

C.1.1 *s*-polarized EM waves

Starting from Eqs.(B.1) we obtain the following developed form of Fresnel reflection factor of *s*-polarized EM waves:

$$\begin{aligned} r_{12}^S &= \frac{\gamma_1 - \gamma_2}{\gamma_1 + \gamma_2} = \frac{\gamma_1^2 - \gamma_2^2}{(\gamma_1 + \gamma_2)^2} \\ &= \frac{(\varepsilon_1 k_0^2 - K^2) - (k_0^2 - K^2)}{(\varepsilon_1 k_0^2 - K^2)^2 + 2\sqrt{(\varepsilon_1 k_0^2 - K^2)(k_0^2 - K^2)} + (k_0^2 - K^2)^2} \end{aligned} \quad (C.1)$$

In the electrostatic limit $K \gg k_0$, which implies that:

$$r_{12}^S \approx \frac{\varepsilon_1 - 1}{(\varepsilon_1 - 1) + 2\frac{K^2}{k_0^2} + 2\frac{K^2}{k_0^2}} \quad (C.2)$$

Therefore we obtain finally :

$$r_{12}^S \approx \frac{\varepsilon_1 - 1}{4(K/k_0)^2} \quad (C.3)$$

C.1.2 *p*-polarized EM waves

Starting from Eqs. (B.1), we obtain the following developed form of Fresnel reflection factor of *p*-polarized EM waves:

$$\begin{aligned}
r_{12}^p &= \frac{\varepsilon_1 \gamma_2 - \varepsilon_2 \gamma_1}{\varepsilon_1 \gamma_2 + \varepsilon_2 \gamma_1} = \frac{\varepsilon_1 \sqrt{k_0^2 - K^2} - \varepsilon_2 \sqrt{\varepsilon_1 k_0^2 - K^2}}{\varepsilon_1 \sqrt{k_0^2 - K^2} + \varepsilon_2 \sqrt{\varepsilon_1 k_0^2 - K^2}} \\
&= \frac{\varepsilon_1 - \varepsilon_2 \sqrt{\left[K^2 \left(\frac{\varepsilon_1 k_0^2}{K^2} - 1 \right) \right] / \left[K^2 \left(\frac{k_0^2}{K^2} - 1 \right) \right]}}{\varepsilon_1 + \varepsilon_2 \sqrt{\left[K^2 \left(\frac{\varepsilon_1 k_0^2}{K^2} - 1 \right) \right] / \left[K^2 \left(\frac{k_0^2}{K^2} - 1 \right) \right]}} \quad (C.4)
\end{aligned}$$

In the electrostatic limit where $K \gg k_0$:

$$r_{12}^p \approx \frac{\varepsilon_1 - \varepsilon_2}{\varepsilon_1 + \varepsilon_2} \quad (C.5)$$

For the case where medium (2) is vacuum, i.e. $\varepsilon_2 = 1$, Eq. (C.5) reduces to:

$$r_{12}^p \approx \frac{\varepsilon_1 - 1}{\varepsilon_1 + 1} \quad (C.6)$$

C.2 Case of aluminum

The local dielectric permittivity of aluminum is that of Drude's model:

$$\varepsilon(\omega) = \varepsilon_b - \frac{\omega_p^2}{\omega(\omega + i\nu)} \quad (C.7)$$

where ω_p is the plasma frequency which is a material property that is based on the number density of conduction electrons. ε_b is a corrective constant that accounts for the background electron screening at high frequency and $\nu = 1.22 \times 10^{14} \text{s}^{-1}$ is the damping factor accounting for losses as it represents the scattering frequency of the electron as it travels through the metal.

C.2.1 s-polarized EM waves

The electrostatic limit of Fresnel reflection factor is given by Eq. (C.3). Starting from this equation, we substitute with the expression of the dielectric permittivity:

$$r_{12}^s \approx \frac{k_0^2}{4K^2} \left(\varepsilon_b - \frac{\omega_p^2}{\omega(\omega + i\nu)} \right) \quad (C.8)$$

By developing we obtain :

$$r_{12}^s \approx \frac{k_0^2}{4K^2} \left[\frac{(\varepsilon_b - \omega_p^2 - \omega^2) + i(\varepsilon_b \omega \nu - \omega \nu)}{\omega^2 + i\omega \nu} \right] \quad (C.9)$$

Then :

$$r_{12}^s \approx \frac{k_0^2}{4K^2} \left[\frac{(\varepsilon_b - \omega_p^2 - \omega^2)(\omega^2 - i\omega \nu) + i(\varepsilon_b \omega \nu - \omega \nu)(\omega^2 - i\omega \nu)}{\omega^4 + \omega^2 \nu^2} \right] \quad (C.10)$$

Therefore the imaginary part of r_{12}^s is:

$$Im(r_{12}^s) \approx \frac{k_0^2}{4K^2} \frac{\omega_p^2 \nu}{\omega(\omega^2 + \nu^2)} \quad (C.11)$$

C.2.2 *p*-polarized EM waves

Starting from the final form of the electrostatic limit of Fresnel reflection factor of *p*-polarized EM waves Eq. (C.5), we substitute with the expression of the dielectric permittivity:

$$r_{12}^p \approx \frac{\left(\varepsilon_b - \frac{\omega_p^2}{\omega(\omega + i\nu)} \right) - \varepsilon_2}{\left(\varepsilon_b - \frac{\omega_p^2}{\omega(\omega + i\nu)} \right) - \varepsilon_2} \quad (C.12)$$

By developing we obtain :

$$r_{12}^p \approx \frac{(\varepsilon_b \omega^2 - \omega_p^2 - \varepsilon_2 \omega^2) + i(\omega \nu \varepsilon_b - \omega \nu \varepsilon_2)}{(\varepsilon_b \omega^2 - \omega_p^2 + \varepsilon_2 \omega^2) + i(\omega \nu \varepsilon_b \omega \nu \varepsilon_2)} \quad (C.13)$$

It follows that by developing, the imaginary part of r_{12}^p is:

$$Im(r_{12}^p) \approx \frac{2\omega \nu \omega_p^2 (\varepsilon_b - \varepsilon_2)}{\omega^4 (\varepsilon_b + \varepsilon_2)^2 + \omega^2 [-2\omega_p^2 + \nu^2 (\varepsilon_b + \varepsilon_2)^2] + \omega_p^4} \quad (C.14)$$

which implies that :

$$Im(r_{12}^p) \approx \frac{2\omega \nu \omega_p^2 (\varepsilon_b - \varepsilon_2) / (\varepsilon_b + \varepsilon_2)^2}{\left[\frac{\omega_p^2}{(\varepsilon_b + \varepsilon_2)} - \omega^2 \right] + \omega^2 \nu^2} \quad (C.15)$$

Therefore we obtain finally:

$$\left\{ \begin{array}{l} \text{Im}(r_{12}^p) \approx \frac{\omega \nu \omega_{sp}^2 (R - 1)}{(\omega_{sp}^2 - \omega^2)^2 + \omega^2 \nu^2} \\ \omega_{sp}^2 = \omega_p^2 / (\varepsilon_b + \varepsilon_2) \\ R = (\varepsilon_b - \varepsilon_2) / (\varepsilon_b + \varepsilon_2) \end{array} \right\} \quad (C.16)$$

For the special case where medium (2) is vacuum:

$$\left\{ \begin{array}{l} \text{Im}(r_{12}^p) \approx \frac{\omega \nu \omega_{sp}^2 (R - 1)}{(\omega_{sp}^2 - \omega^2)^2 + \omega^2 \nu^2} \\ \omega_{sp}^2 = \omega_p^2 / (\varepsilon_b + 1) \\ R = (\varepsilon_b - 1) / (\varepsilon_b + 1) \end{array} \right\} \quad (C.17)$$

Appendix D

D. Henkel–Joulain approach

D.1 The correlation equation of the fluctuating currents

In this section the system and the geometry considered are those of Appendix A (Fig. A.1 and A.2).

The work presented in section 3 of chapter 3 is inspired from Henkel and Joulain approach [11]. This approach is based on the idea that the minimum value of the coherence length of the thermal EM field near a planar surface is related to the nonlocal dielectric response of the material. Therefore, Henkel and Joulain [11] defined a parameter l as being the coherence length of the EM field. This parameter is introduced l as a correlation distance in the correlation equation Eq. (A.16) of the fluctuating currents that generate the radiation field in the medium:

$$\langle j_{f\alpha}(\mathbf{r}', \omega) j_{f\beta}^*(\mathbf{r}'', \omega') \rangle = 2 \omega \varepsilon_0 \varepsilon_1''(\omega) \frac{e^{-(\mathbf{r}' - \mathbf{r}'')^2 / l^2}}{\pi^{3/2} l^3} \Theta(\omega, T_1) \delta_{kl} \delta(\omega' - \omega') \quad (D.1)$$

where it is clear that this equation differs from Eq. (A.16) by the additional multiplied term, $\frac{e^{-(\mathbf{r}' - \mathbf{r}'')^2 / l^2}}{\pi^{3/2} l^3}$. This term is replacing the spatial delta function in the fluctuation-dissipation theorem. It introduces a spatial correlation length for the currents below which the currents are indeed correlated

D.2 Derivation of the Poynting vector from medium (1) to medium (2) and the radiative heat transfer coefficient

We aim to repeat the derivation of the Poynting vector as to obtain at the end the RHTC for this system. We will carry out this derivation in a general way, i.e. using general notations so as to focus on the impact of the additional term (which is a function of l) throughout this calculation,; and eventually throughout any other derivation (Poynting vector, EM energy density,...).

In the local case, i.e. in the case where $l=0$, upon using Green's Functions we were required to solve integrals of the form (as we saw in Appendices A and B):

$$A_i B_j^* = cst \int d^3 \mathbf{r}' \int d^3 \mathbf{r}'' \int d^2 \mathbf{K} d^2 \mathbf{K}' A_{ik} B_{jk}^* e^{i\mathbf{K} \cdot (\mathbf{R} - \mathbf{R}')} \\ \times e^{i\gamma_1(z-d)} e^{-i\gamma_2 z'} e^{-i\mathbf{K}' \cdot (\mathbf{R} - \mathbf{R}'')} e^{-i\gamma_1^*(z-d)} e^{+i\gamma_2^* z''} \quad (D.2)$$

where \mathbf{A} and \mathbf{B} denote Green tensors (of the electric field \mathbf{E} and/or the magnetic field \mathbf{H}).

In the nonlocal case, i.e. for $l \neq 0$, we obtain:

$$A_i B_j^* = cst * \frac{2 \omega \varepsilon_0 \varepsilon_1''(\omega)}{\pi} \frac{1}{\pi^{1/2} l^3} \int d^3 \mathbf{r}' \int d^3 \mathbf{r}'' \int d^2 \mathbf{K} d^2 \mathbf{K}' A_{ik} B_{jk}^* e^{-(\mathbf{r}' - \mathbf{r}'')^2 / l^2} e^{i\mathbf{K} \cdot (\mathbf{R} - \mathbf{R}')} \times \\ e^{i\gamma_1(z-d)} e^{-i\gamma_2 z'} e^{-i\mathbf{K}' \cdot (\mathbf{R} - \mathbf{R}'')} e^{-i\gamma_1^*(z-d)} e^{+i\gamma_2^* z''} \quad (D.3)$$

where

$$\int d^3 \mathbf{r}'' e^{-(\mathbf{r}' - \mathbf{r}'')^2 / l^2} e^{-i\mathbf{K}' \cdot (\mathbf{R} - \mathbf{R}'')} e^{+i\gamma_2^* z''} \\ = \int d^2 \mathbf{R}'' e^{-(\mathbf{R}' - \mathbf{R}'')^2 / l^2} e^{-i\mathbf{K}' \cdot (\mathbf{R}' - \mathbf{R}'')} \int dz'' e^{-(z' - z'')^2 / l^2} e^{+i\gamma_2^* z''} \quad (D.4)$$

and

$$\int d^2 \mathbf{R}'' e^{-(\mathbf{R}' - \mathbf{R}'')^2 / l^2} e^{-i\mathbf{K}' \cdot (\mathbf{R}' - \mathbf{R}'')} \\ = \int dx'' e^{-(x' - x'')^2 / l^2} e^{-iK'_x(x' - x'')} \int dy'' e^{-(y' - y'')^2 / l^2} e^{-iK'_y(y' - y'')} \quad (D.5)$$

We will start by solving the on the right hand side, which we denote by:

$$X = \int dx'' e^{-(x' - x'')^2 / l^2} e^{-iK'_x(x' - x'')} = e^{-iK'_x x} \int dx'' e^{-(x' - x'')^2 / l^2} e^{iK'_x x''} \quad (D.6)$$

Using the change of variable $u = x' - x''$, we obtain:

$$X = -e^{-iK'_x x} \int du e^{-u^2 / l^2} e^{iK'_x(x' - u)} = -e^{-iK'_x(x' - x)} \int du e^{-\frac{1}{l^2}(u^2 + iK'_x l^2 u)} = \\ = -e^{iK'_x(x' - x)} e^{-K_x'^2 l^2 / 4} \int du e^{\left(u + \frac{iK'_x l^2}{2}\right)^2 / l^2} \quad (D.7)$$

Using the change of variable $b = (u + ia)/l$ where $a = iK'_x l^2/2$, and the Gaussian integral given by:

$$\int_{-\infty}^{+\infty} dy e^{-y^2} = \sqrt{\pi} \quad (D.8)$$

Eq. (D.7) becomes:

$$X = -l\sqrt{\pi} e^{iK'_x(x'-x)} e^{-K_x'^2 l^2/4} \quad (D.9)$$

Solving the second integral on the right-hand side of Eq. (D.5) with similar steps, we obtain:

$$Y = \int dy'' e^{-(y'-y'')^2/l^2} e^{-iK'_y(y'-y'')} = -l\sqrt{\pi} e^{iK'_y(y'-y)} e^{-K_y'^2 l^2/4} \quad (D.10)$$

which imply that:

$$\int d^2 \mathbf{R}'' e^{-(\mathbf{R}'-\mathbf{R}'')^2/l^2} e^{-i\mathbf{K}'\cdot(\mathbf{R}'-\mathbf{R}'')} = l^2 \pi e^{iK'_x(x'-x)} e^{iK'_y(y'-y)} e^{-\frac{l^2}{4}(K_x'^2+K_y'^2)} \quad (D.11)$$

Therefore Eq. (D.3) becomes:

$$\begin{aligned} A_i B_j^* &= cst * \frac{2 \omega \varepsilon_0 \varepsilon_1''(\omega)}{\pi} * \frac{l^2 \pi}{\pi^{\frac{1}{2}} l^3} \int d^3 \mathbf{r}' \int d^2 \mathbf{K} d^2 \mathbf{K}' \int dz'' A_{ik} B_{jk}^* e^{-K^2 l^2/4} e^{i\mathbf{K}\cdot(\mathbf{R}-\mathbf{R}')} \\ &\quad \times e^{i\gamma_1(z-d)} e^{-i\gamma_2 z'} e^{-i\mathbf{K}'\cdot(\mathbf{R}-\mathbf{R}'')} e^{-i\gamma_1^* (z-d)} e^{+i\gamma_2^* z''} \quad (D.12) \end{aligned}$$

Now, the volume integral:

$$\begin{aligned} \int d^3 \mathbf{r}' e^{i\mathbf{R}'\cdot(\mathbf{K}-\mathbf{K}')} &= \int d^2 \mathbf{R}' \int dz' e^{i\mathbf{R}'\cdot(\mathbf{K}-\mathbf{K}')} = 2\pi \int \mathbf{R}' d\mathbf{R}' \int dz' e^{i\mathbf{R}'\cdot(\mathbf{K}-\mathbf{K}')} \\ &= 4\pi^2 \delta(\mathbf{K} - \mathbf{K}') \int dz' \quad (D.13) \end{aligned}$$

It follows that :

$$\begin{aligned} A_i B_j^* &= cst * \frac{2 \omega \varepsilon_0 \varepsilon_1''(\omega)}{\pi} * \frac{l^2 \pi}{\pi^{\frac{1}{2}} l^3} \\ &\quad * 4\pi^2 \int dz' dz'' \int d^2 \mathbf{K} A_{ik} B_{jk}^* e^{-K^2 l^2/4} e^{-i\gamma_2 z'} e^{-i(z'-z'')^2/l^2} e^{+i\gamma_2^* z''} \quad (D.14) \end{aligned}$$

We should proceed by solving the integral:

$$Z = \int dz' dz'' e^{-i\gamma_2 z'} e^{+i\gamma_2^* z''} e^{-i(z'-z'')^2/l^2} \quad (D.15)$$

Using the following change of variables:

$$\begin{cases} u = \frac{z' - z''}{2} \\ v = \frac{z' + z''}{2} \end{cases} \quad (D.16)$$

We obtain:

$$Z = \int_{-\infty}^{+\infty} dv e^{2\gamma_2'' v} \int_{-\infty}^{+\infty} du e^{-i\gamma_2' u} e^{-u^2/l^2} \quad (D.17)$$

Again, using Gaussian integral Eq. (D.8):

$$Z = l\sqrt{\pi} e^{-(\gamma_2')^2/l^2} \int_{-\infty}^{+\infty} dv e^{2\gamma_2'' v} = \frac{l\sqrt{\pi} e^{-(\gamma_2')^2/l^2}}{2\gamma_2''} \quad (D.18)$$

Therefore:

$$\begin{aligned} A_i B_j^* &= cst * \frac{2 \omega \varepsilon_0 \varepsilon_1''(\omega)}{\pi} * \frac{l^2 \pi}{\pi^{\frac{1}{2}} l^3} \\ &* 4\pi^2 \int_{-\infty}^0 dv e^{2\gamma_2'' v} l \pi^{\frac{1}{2}} e^{-Re^2(\gamma_2)l^2/4} \int d^2 \mathbf{K} A_{ik} B_{jk}^* e^{-K^2 l^2/4} \end{aligned} \quad (D.19)$$

It follows that the final form of Eq. (D.3) is:

$$A_i B_j^* = C * \frac{1}{2\gamma_2''} \int d^2 \mathbf{K} A_{ik} B_{jk}^* * e^{-Re^2(\gamma_2)l^2/4} e^{-K^2 l^2/4} \quad (D.20)$$

From this equation we conclude that we would obtain the same expression as in the local case, multiplied by the exponential term $e^{-Re^2(\gamma_2)l^2/4} e^{-K^2 l^2/4}$. This implies that the RHTC equation in this nonlocal case would be given as follows:

$$\left\{ \begin{aligned} h_{rad}(T, d) &= \sum_{\alpha=S,P} \int_0^{+\infty} d\omega [h_{prop}^\alpha(T, d, \omega) + h_{evan}^\alpha(T, d, \omega)] \\ h_{prop}(T, d, \omega) &= h^0(T, \omega) \times \int_0^{k_0} \frac{K d K (1 - |r_{31}^\alpha|^2)(1 - |r_{32}^\alpha|^2) \times e^{-[Re^2(\gamma_2)+K^2]l^2/4}}{k_0^2 |1 - r_{31}^\alpha r_{32}^\alpha e^{2i\gamma_3 d}|^2} \\ h_{evan}(T, d, \omega) &= h^0(T, \omega) \times \int_{k_0}^{+\infty} \frac{K d K 4Im(r_{31}^\alpha)Im(r_{32}^\alpha) e^{2i\gamma_3 d} \times e^{-[Re^2(\gamma_2)+K^2]l^2/4}}{k_0^2 |1 - r_{31}^\alpha r_{32}^\alpha e^{2i\gamma_3 d}|^2} \end{aligned} \right\} \quad (D.21)$$

Similarly, the expressions of the EM energy density, and any of the electric and the magnetic contributions to it in the nonlocal case, will be the same as obtained in Appendix B, multiplied by the exponential term $e^{-[Re^2(\gamma_2)+K^2]l^2/4}$.

Appendix E

E. The polylogarithm function $Li_s(z)$

The polylogarithm $Li_s(z)$ is the function defined as follows:

$$\left\{ \begin{array}{l} Li_s(z) = \sum_{k=1}^{\infty} \frac{z^k}{k^s} \\ Li_{s+1}(z) = \int_0^z \frac{Li_s(t)}{t} dt \end{array} \right\} \quad (E.1)$$

Therefore the polylogarithm function of second order is defined as:

$$Li_2(z) = \int_0^z \frac{Li_1(t)}{t} dt \quad (E.2)$$

where

$$Li_1(z) = z + z^2 + \dots \quad (E.3)$$